Université d'Aix-Marseille
Ecole Doctorale 352 : Physique et Science de la Matière

Pour obtenir le grade de
DOCTEUR DE l'UNIVERSITE AIX-MARSEILLE
Spécialité : Physique théorique et Mathématique
par

Ritesh MOHUN

RAMAN SPECTROSCOPY FOR THE CHARACTERIZATION OF DEFECTIVE SPENT NUCLEAR FUELS DURING INTERIM STORAGE IN POOLS

Soutenue le 07 Novembre 2017

Membres du jury:

Nathalie MONCOFFRE	Directrice de Recherche IPNL, Lyon	Rapporteur
Michel MERMOUX	Directeur de Recherche CNRS, Grenoble	Rapporteur
David SHOESMITH	Professeur des Universités, Ontario	Examinateur
Dario MANARA	Directeur de Recherche ITU, Karlsruhe	Examinateur
Lionel DESGRANGES	Expert Senior CEA, Cadarache	Directeur de thèse
Patrick SIMON	Directeur de recherche CNRS, Orléans	Co-encadrant
Christophe JEGOU	Expert Senior CEA, Marcoule	Co-encadrant
Antoine AMBARD	Ingénieur de Recherches, EDF	Invité

CEA CADARACHE 2014-2017

Acknowledgements

This research work was carried out in the framework of the PRECCI project, with EDF as the main industrial partner, and was performed at the French Alternative Energies and Atomic Energy Commission (CEA) within the Laboratoire des Lois de Comportement du Combustible (LLCC) at Cadarache.

The preparation and completion of this research project would have never been possible without the contributions and assistances of the people who were directly/indirectly involved in my work. I would like to seize this opportunity to express my outmost gratefulness for their generous support and cooperation during the past 3 years.

First of all, I would like to express my deepest gratitude to my supervisor Lionel Desgranges, to whom I owe everything. I consider myself as extremely lucky to have a supervisor who showed a constant availability to discuss the experimental findings and explaining the scientific theory behind those. Under his guidance, I was inspired to pursue my goals with dedication and hard work. Beyond his scientific insights, I also thanked him for his friendly approach and I truly appreciate and value all the lessons that I have learned from him.

During my thesis, I had the opportunity to conduct several experiments at CNRS, Orléans. I am indebted to Patrick Simon for co-ordinating all my trips and organizing all my irradiation and characterization campaigns, when he was probably up to neck in work. Thanks to his joyful personality and caring character, I felt at ease and enjoyed my time at Orléans. I also had a great experience working with a fine team of colleagues, all of whom I will sorely miss. I want to thank Aurélien Canizares, Nicole Raimboux, Florian Duval, Ammar Mohamed-Ramzi, Rachelle Omnee and David Chaulin for all experimental technical assistances. In addition, Marie-France Barthe, Pierre Desgradin and Chenwei He were really instrumental for the position annihilation spectroscopy measurements that were performed in this work.

I would also acknowledge the strong support of Christophe Jégou, Sandrine Miro and Magali Magnin at CEA, Marcoule. Their constructive remarks and numerous discussions were vital to develop suitable nuclear fuel dissolution mechanisms. I am grateful to Veronique Broudic-Oliver and Caroline Marques who were responsible for the chemical analysis of the water solutions. I would also like to thank Nicolas Dacheux and Nicolas Clavier at CNRS-University of Montpellier for the fabrication of the mixed oxide samples used in this work.

I am really grateful to Nathalie Moncoffre at IPNL, Lyon and Michel Mermoux at CNRS, Grenoble for carefully reviewing this manuscript. My sincere appreciation also goes to David Shoesmith at Western University, Ontario and Dario Manara at ITU, Karlshure for agreeing to be members of the jury during my defence. I would also like to thank Antoine Ambard at EDF, Fontainebleau and Chantal Cappelaere at CEA, Saclay for all the discussions that allowed us to orientate our experimental results towards the industrial need of the PRECCI project.

My experience working with the members of the LLCC and LCU laboratory was intellectually exciting and positive. I would like to acknowledge the great support of Gérald Jomard, Marjorie Bertolus, Jacques Lechelle, Serge Maillard, Claire Onofri, Gaelle Carlot, Doris Drouan, Hélène Rouquette and not forgetting Catherine Tanguy. A special thought goes to Jean-Michel Escleine for his dark and twisted sense of humour and Armande Berthelot who always found the right words to help me get back on track whenever things were not going as expected.

I want to thank my wonderful friends; Jean-Eric, Vincent, Sarah, Dan, Karl, Eric, Ibrahim, Martin, Adrien among others, for the good moments spent together to provide a much needed escape from my studies. However, a special mention goes to Arno and Shi Lei whom I spent the first two years of my thesis. It was amazingly funny how their presence had been giving me comfort and increased my devotion towards my work. Their absence was deeply felt and I wish them much success in their careers.

Finally, this thesis would have never been possible without the invaluable support of my parents. Thanks Mom for always keeping an eye on your favourite child. Thanks Dad for supporting me through the best and worst years of my life. Sis, thanks for being the best friend I can confide in. It didn’t matter how many miles separated us, you showed a constant presence. Thank you all for believing in me and for *everything* that helped me get to this day.

List of Abbreviations

a.u	Arbitrary Units
Bq	Becquerel
CEMHTI	Conditions Extrêmes et Matériaux : Haute température et Irradiation
CNRS	Centre National de la Recherche Scientifique
EDF	Électricité de France
I.D	Irradiation defects
F.A	Fuel assembly
FCC	Face cubic centered
GWd	Gigawatt-day
H_2O_2	Hydrogen peroxide
LET	Linear Energy Transfer
MIMAS	Micronized master blend
MOX	Mixed oxide fuel
PRECCI	Programme de recherche sur l'évolution à long terme des colis de combustible irradié
PuO_2	Plutonium oxide
SEM	Scanning Electron Microscope
SFP	Spent fuel pools
SIMFUEL	Chemical simulant of SNF
SNF	Spent nuclear fuel
t_{HM}	metric ton of heavy metals
UOX	Uranium oxide fuel
XRD	X-ray Diffraction

Table of Contents

General Introduction

The safe disposal of spent nuclear fuels (SNF) remains one of the key issues facing the modern nuclear industry and a major international effort is currently underway in order to propose suitable safe management and disposal procedures. The management of irradiated fuels depends on the type of fuel cycle adopted by the nuclear power plants. Nuclear fuel cycle can be categorized either as open (once-through) or closed fuel cycle. In the open fuel cycle, the irradiated fuels are not recycled to be re-used in nuclear reactors. Instead, they are disposed to repository sites once their radioactivity has sufficiently decreased. From an economical viewpoint, the open fuel cycle is not viewed as sustainable considering that SNF still contains 98% of reusable materials.

In contrast, the closed fuel cycle aims to recover the reusable materials and contain the SNF sustainably to reduce the amount of waste destined for final disposal. For instance, both fertile (U-238) and fissile isotopes (U-235 and Pu-239) are recovered for the fabrication of Mixed Oxide (MOX) fuels. The closed fuel cycle has been adopted at the very beginning of the French nuclear program which was governed by the limited amount of domestic uranium and the willingness to employ an independent energy strategy.

The use of MOX fuels in French reactors has largely been motivated as indicated by the implementation of the *"MOX Parity Fuel Management"* project which aims to achieve parity between MOX and UOX fuels in terms of fuel performance. The French nuclear industry remains committed to the recycling policy considering that they have a strong capability to manage all the processes involved in the closed fuel cycle. However due the current slow pace of reprocessing, the French utility EDF (Électricité de France) has accumulated a large backlog of unprocessed SNF. It is considered as more suitable to extend the interim storage of irradiated nuclear fuels in spent fuel pools (SFP) until they are recycled in the forthcoming commercialization of the next generation reactors, which are basically long-term projects. Hence, it is essential to evaluate the long-term performance of UOX and MOX fuel rods under SFP conditions.

The extended interim storage of SNF poses no significant risk, but an incidental scenario of a damaged fuel rod stored in the SFP should be studied. A physical cladding failure creates a pathway through which water is allowed to interact with the irradiated fuel matrix. The fuel matrix-water interaction and the physico-chemical properties of the SFP lead to the formation of radiolytic species and in particular hydrogen peroxide (H_2O_2). These radiolytic products are known to enhance the fuel surface alteration mechanisms, accelerate the dissolution rate and favor the precipitation of secondary U(VI) phases. The formation of secondary phases can

further stress a damaged fuel rod at the defect level leading to a pronounced opening of the fuel cladding over the years.

The oxidative dissolution of UO_2 and MOX in the presence of irradiation (alpha, beta and gamma) has extensively been studied in the literature; however the oxidative dissolution mechanisms of nuclear fuels need to be further investigated. Previous studies were mainly devoted to characterize the oxidation of the fuel matrix, the uranium and plutonium release rate and the effect of H_2O_2 on the nuclear fuel dissolution rate, but little is known about the behavior of irradiation defects within the spent fuels during a potential fuel matrix-water interaction. Hence, it is important to elucidate the role of irradiation defects during SNF dissolution in order to successfully predict the final properties of the irradiated fuels before they are considered for subsequent reprocessing.

A fundamental joint project, involving EDF and CEA (French Alternative Energies and Atomic Energy Commission), has recently been initiated for the experimental study of an actual defective fuel rod which has been stored in SFP aqueous conditions during several years. Among the different characterization tools considered, Raman spectroscopy remains one of the techniques that can reveal important information about the alteration of the nuclear fuel matrix mainly due to its proven reliability for the identification of secondary U(VI) phases. In addition, Raman spectroscopy has recently attributed a specific signature, referred as the “triplet defect bands”, corresponding to the presence of irradiation defects. Although much effort have been devoted to the study of the Raman triplet defect bands, more precise information are still required to sanction a better interpretation of the irradiation-induced Raman bands.

This thesis is devoted to provide an in-depth analysis of the Raman triplet defect bands and to investigate how this Raman signature can be used to characterize actual SNF stored in pools. For the purpose of this study, **three main objectives** were identified which were based on the ionic implantation of nuclear fuels and MOX surrogate compounds to simulate irradiation-induced damages. The main fields of study can be described as follows:

1. Identify the type of irradiation defects responsible for the apparition of the Raman triplet defect bands
2. Investigate the behavior of the Raman triplet defect bands during UO_2 leaching under oxidizing conditions
3. Study the effect of chemical doping and microstructure on the Raman triplet defect bands

In attempt to bring relevant information in regards to the targeted objectives, this manuscript is structured into **six main chapters**. The first three chapters aim to present a detailed literature review and the methodology employed in this work. The findings obtained from the experimental studies are presented in the last three chapters. A summary of the different chapters are as follows:

Chapter 1 provides an overview of the data reported in the literature for a good understanding of the works performed in this thesis. In this context, the state of the art about the irradiation-induced effects in nuclear fuels is presented. In addition, a non-exhaustive summary of the different studies focused on the leaching behavior of nuclear fuels under/without irradiation is then provided.

Chapter 2 presents the fundamentals of Raman scattering. This chapter compiles the current knowledge and information about the application of Raman spectroscopy for the characterization of irradiation damages in nuclear fuels and the identification of secondary U(VI) phases. The ultimate objectives and motivation of the current study are then described.

Chapter 3 aims to present the experimental methodology. The different steps involved in the fabrication of the samples considered in this study (in the form of disk and half-disk) are initially presented. A full description of the ion-implantation facilities (electron and alpha sources) is also provided. The fundamentals of the experimental characterization techniques (Raman, Positron annihilation spectroscopy & X-ray diffraction) that were employed for the measurement of the samples are then described.

Chapter 4 is devoted to the identification of the type of irradiation defects that are consistent with the Raman triplet defect bands. The experimental results obtained during the UO_2 electron irradiation experiment are presented to illustrate the effect of electron energy on the intensity of the Raman defect bands. The findings are then compared with the Positron annihilation spectroscopy measurements in order to provide a better interpretation of the irradiation-induced Raman triplet defect bands. The study was extended to investigate the ageing of an electron-irradiated UO_2 disk under ambient-air conditions. The results are discussed and interpreted to develop a suitable ageing mechanism involving the role of irradiation defects.

Chapter 5 is focused on the behavior of the Raman triplet defect bands during UO_2 leaching experiment under oxidizing conditions. The first part of this chapter is dedicated to the study of the alpha irradiation-induced defects in UO_2 under different interfaces (inert & reactive environment). A complete description of the *in situ* experimental set-up and the selected irradiation parameters employed to measure the formation kinetics of irradiation defects are presented. A detailed analysis of the UO_2 leaching behavior is discussed in the second part of the chapter. The chemistry of the irradiated water solution is analyzed to identify the oxidative UO_2 dissolution mechanisms.

Finally, **Chapter 6** aims to investigate the effect of chemical doping and microstructure on the irradiation-induced Raman triplet defect bands. The alpha irradiation experiments of both heterogeneous (U, Ce)O_2 and homogeneous (U, Th)O_2 mixed oxides are described and the results obtained from the Raman measurements are presented. The experimental findings are analyzed to determine their consistency in regards to actual MOX fuels.

Finally, the conclusions and perspectives are presented in the final section of this manuscript.

Chapter 1

Context and literature review

1.1 Introduction

In France, the interim storage of unprocessed irradiated fuels in water pools over a few decades remains the reference scenario before they can be reprocessed. Some rods fail during normal operation in reactor due to various causes (debris, wear, corroded weld). They are wet stored before reprocessing and it is of interest to investigate the behaviour of these fuel rods during this stage.

The presence of a defect at the cladding level creates a pathway through which water is allowed to contact the spent fuel matrix. Due to the high radiation field of the used nuclear fuel and the physico-chemical conditions of aerated water pools, the fuel matrix-water interaction leads to the formation of radiolytic species which can significantly alter the fuel interface to a state that is different to that expected in the absence of the radiation field. It is therefore necessary to identify and understand the basic mechanisms that occur at the UO_X/water interface under the influence of irradiation. This chapter reviews the studies of the effects of irradiation-induced water radiolysis on model interfaces.

The first part of this chapter is devoted to provide an overview of the back-end fuel cycle to describe the management of SNF in France. The principal properties of UO_2 and its evolution under irradiation are also described. The irradiation-induced water radiolysis mechanisms and their influence on UO_2 dissolution are then discussed. The final part of this chapter summarizes the effect of the different types of irradiation on the spent fuel alteration and the precipitation of secondary phases based on the data available in the literature.

1.2 Spent nuclear fuels

Post irradiation, the safe disposal of SNF remains one of the key issues facing the modern nuclear industry and a major international effort is currently underway in order to propose suitable safe management and disposal procedures. The management of irradiated fuels depends on the type of fuel cycle adopted by the nuclear power plants. Nuclear fuel cycle can be categorized either as open (also referred as "once-through") or closed fuel cycle. In the open fuel cycle, the SNF is considered as the final waste. After nuclear operations, the irradiated fuels are stored as spent nuclear rods in a suitable cooling medium, kept away from reprocessing, recycling and possibly arms proliferation. When the radioactivity of the SNF has been sufficiently decreased, they are disposed to repository sites. However from an economical viewpoint, this methodology is not viewed as sustainable since the SNF still contains 98% of reusable materials.

The closed fuel cycle is considered as an alternative to manage SNF and aims to recover the usable materials, contain the waste sustainably and reduce the total amount of ultimate waste destined for final disposal. Thus, both fertile (U-238) and fissile isotopes (U-235 and Pu-239) are recovered for the fabrication of MOX fuels as illustrated in Figure 1.1. It is important to note that the quantity of reusable materials depends on the final composition of the SNF. For instance according to Ewing [1], a burnup of 30 GWd/t_{HM} results in the conversion of 4 atomic percent (at.%) of uranium to around 3 at.% fission products and 1 at.% transuranium elements.

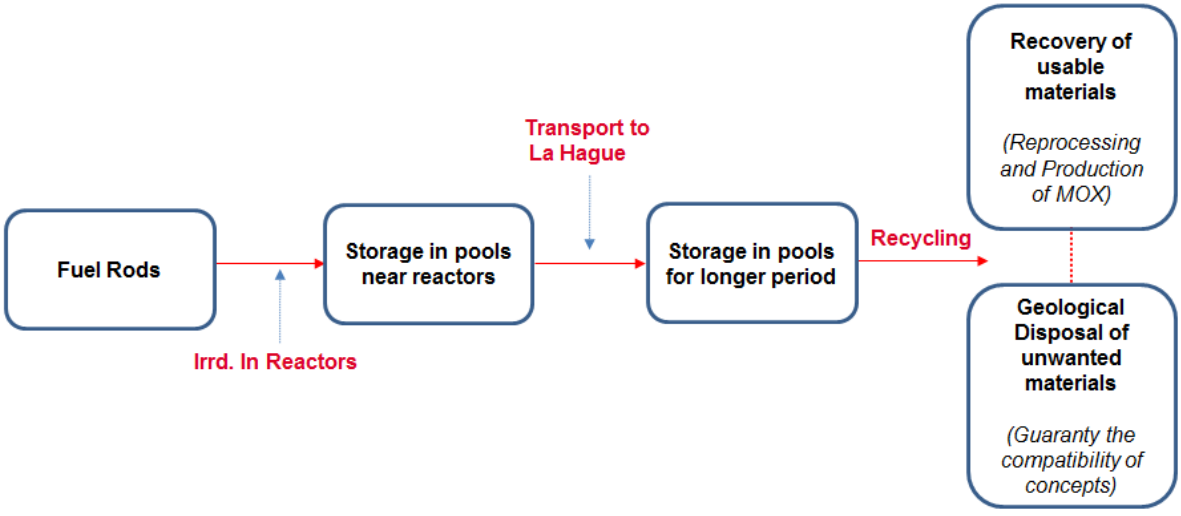

Figure 1.1: Simplified diagram illustrating the management of SNF in France

The closed nuclear fuel cycle has been adopted at the very beginning of the French nuclear program which was governed by the limited amount of domestic uranium and the willingness to employ an independent energy strategy. Statistics show that out of the 1200 tons of SNF discharged every year from the French reactors; about 850-1050 tons/yr are reprocessed [2]**.** The recovered U-235 isotopes are used for UOX fuel fabrication while plutonium isotopes are recycled in 21 out of the 34 PWRs 900 MWe to assemble MOX fuels. The latter has a fabrication rate of around 120 tons MOX/yr, which is equivalent to around 10 tons Pu recycled per year [3]. Compared to UOX fuels, the in-core MOX ratio is restricted to 30% (48 fuel assemblies (FA) per core) in order to maintain the neutronic design and safety aspects of the core during nuclear operations [4].

At the very beginning, MOX FA were principally used in power plants which operated at full power in the base load with a fuel reloading rate every 3 years or so. Advanced R&D activities and accumulated experience have largely contributed to improve the utilization of MOX fuels which has led to the implementation of the "*MOX Parity Fuel Management*" project licensed in December 2006. The project aims to increase the burnup of MOX fuels in order to achieve parity in regards to UOX fuels in terms of fuel performance [5]. The Pu content in the new design has been increased from 7.08% to 8.65% which can be translated to an increase in burnup from 42 GWd/t_{HM} to a maximum of 52 GWd/t_{HM} [6].

The French nuclear industry is strongly committed to the recycling policy as they have a strong capability to master all the different processes involved in the closed fuel cycle. However at the current pace of reprocessing, EDF has accumulated a backlog of around 12 kilotons of SNF, three-quarters of which are stored at la Hague reprocessing plant [2]. It is viewed as more suitable to temporarily store the irradiated FA in suitable water pools over a longer timescale until they are recycled in the forthcoming commercialization of the next generation reactors. During the long-term wet storage, the evolution of the SNF matrix is to be expected. In this sense, the following sections will explore the different processes that are more likely to occur during the heat dissipation phase of irradiated nuclear fuels.

1.3 Composition of spent nuclear fuels

The composition and characteristics of nuclear fuels change during in-reactor operation as a result of fission and capture nuclear reactions. The fission of U-235 and Pu-239 in a thermal reactor is immediately followed by the instantaneous formation of fission products which can exist in both gaseous form and oxide precipitates. Gaseous products such as Krypton (Kr), Xenon (Xe) and Iodine (I) are highly radioactive and can degrade the fuel performance. In contrast, capture nuclear reactions and sequential decay chain processes of unstable actinides lead to an increase concentration of transuranic isotopes, such as U-238 and Pu-239.

The final composition of SNF depends on the initial fuel type, level of enrichment and burnup. For example after an average burnup of 60 GWd/t_{HM}, around 6.5 at.% of the uranium atoms are directly burned or involved in capture reactions to produce transuranium elements or fissile plutonium. An illustration of the microstructure and fission products distribution in such a SNF matrix is illustrated in Figure 1.2. The figure shows the formation of the RIM structure which is a porous region enriched with Pu-239 isotopes. It also contains fission products in the form of oxide precipitates of Rubidium (Rb), Cesium (Cs), Barium (Ba), Molybdenum (Mo), Niobium (Nb) and Zirconium (Zr). Gaseous fission products (Xe, Kr and I) occur as finely dispersed bubbles in the UO_2 grains. In addition, solid products tend to form metallic precipitates of Technetium (Tc), Ruthenium (Ru), Rhodium (Rh) and Palladium (Pd).

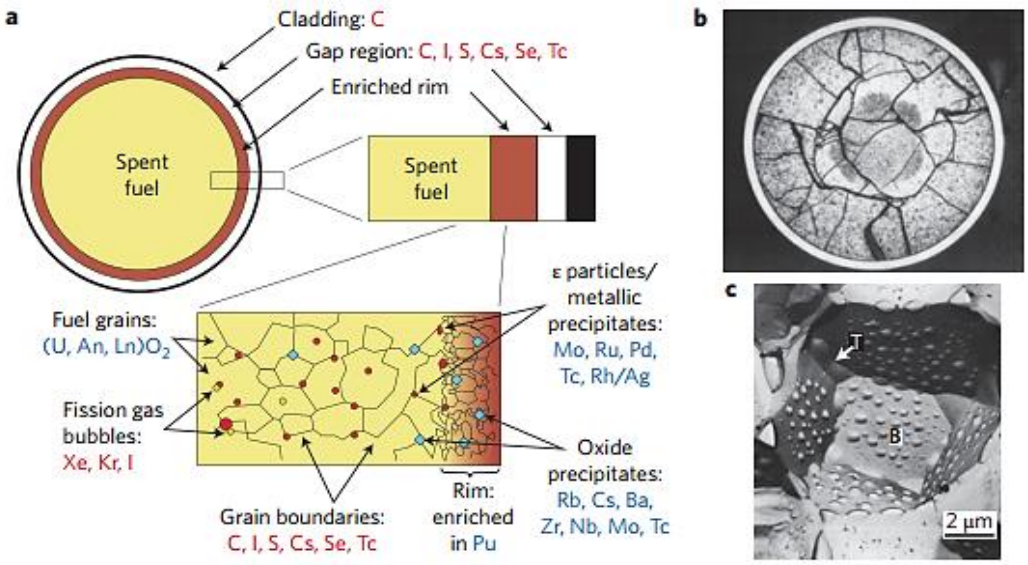

Figure 1.2: Schematic representation of the *(a)* SNF matrix, *(b)* Cross section of the irradiated fuel showing the fractures created by the temperature difference between the center and the edge of the RIM side, *(c)* Segregation of the fission gaseous products in the grains of the UO_2 pellet (T: Grain edge and B: Bubbles) [1]

From Figure 1.2 (a), the heterogeneous distribution profile of the chemical form of the fission products is due to the temperature gradient between the center (1100°C) and the periphery (400°C) of the pellet. The thermal excursion can cause extensive macro-fracturing as displayed in Figure 1.2 (b) and coarsening of the grain size. The high temperature at the center of the pellet favors the migration of volatile fission gases (Cs, Tc, I and Selenium (Se)) to the grain boundaries, fractures and fuel-cladding gap. Some of these volatile gases segregate themselves on the pellet surface and become part of the fractions which are instantaneously release in case of a cladding failure (Figure 1.2 (c)).

The overall characteristic of irradiated fuels remains very complex. The physical and chemical properties of the SNF are expected to change over time; therefore it is of primordial importance to fully understand these aspects in order to develop suitable back-end management strategies. Major intrinsic evolutions of the irradiated FA, both at the microscopic and macroscopic levels, are expected to occur during their cooling phase. This can be largely attributed to the decay series of unstable radioactive actinides contained in the irradiated fuel matrix.

At the point where they are removed from the reactors, the radiation field of the SNF is approximately a hundred thousand (10^6 GBq/Mt) times higher than that of unirradiated UO_2 [7]. The decay of short-lived fission products is responsible for both the radioactivity and the large amount of heat released during the initial stages of storage. As illustrated in Figure 1.3, the decay heat tends to decrease with increasing storage time and the radiation field of the SNF matrix is then governed by long-lived radionuclides on the long term.

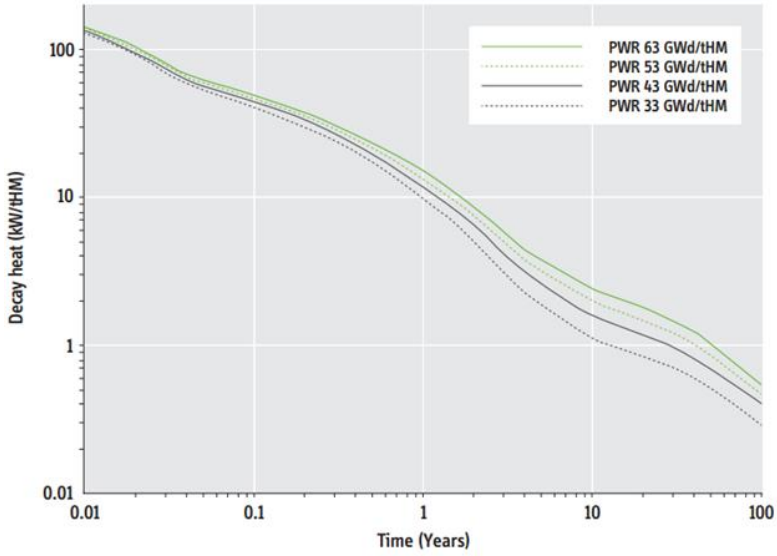

Figure 1.3: Decay heat as a function of time from 0.01 years (about 4 days) to 100 years for low enriched uranium spent-fuel with burnups of 33, 43, 53 and 63 GWd/t_{HM} [7]

During the first 100 years of cooling, the radioactivity of the SNF will be primarily dominated by beta and gamma radiation due to the decay of two main fission products: Strontium (Sr)-90 and Cs-137. After hundreds years of storage, the beta and gamma radiation field will then be relayed by alpha radiation, principally due to the alpha decay behavior of elements such as plutonium, americium, neptunium and curium. The low solubility of alpha ions impacts the physico-chemical properties of the irradiated fuel matrix. These ions may induce additional microstructural defects and can also result in a high accumulation of helium bubbles in the fuel rods as indicated in Figure 1.4 (a) and Figure 1.4 (b) respectively.

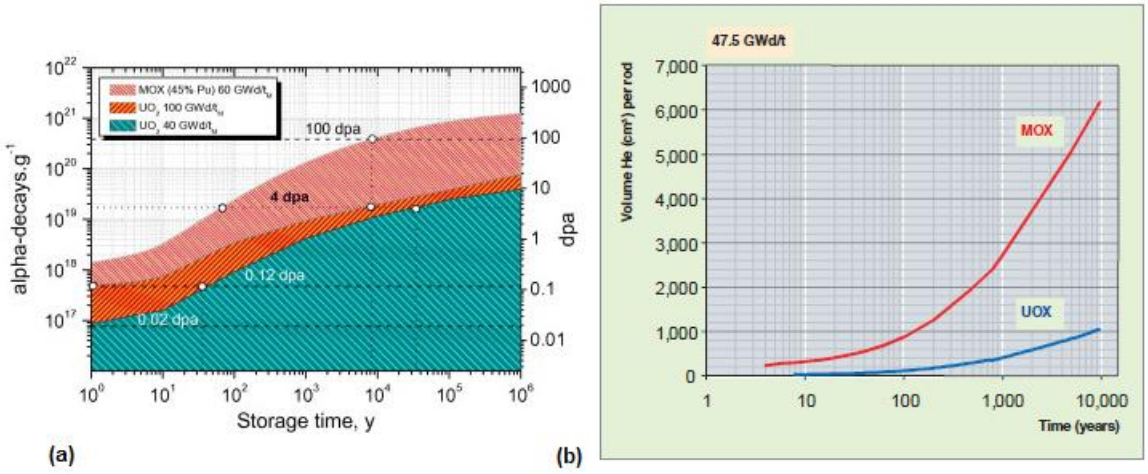

Figure 1.4: Evolution of the irradiated nuclear fuels during storage time *(a)* Atomic displacements caused by alpha particles as a function of time in different nuclear materials *(b)* Volume of helium produced by α decay in UOX and MOX fuels during 10 000 years of storage [8]

During alpha decay, an energetic recoil nucleus of 0.1 MeV and a helium particle with a kinetic energy of 5 MeV are released. According to Staicu *et al.* [9], the helium particle loses around 99.9% of its energy to the bound electrons while the recoil atom is mostly involved in ballistic interactions with UO_2 target atoms. The latter is capable of producing around 295 uranium and 1180 oxygen displacements respectively. In doing so, the helium particle contributes to additional atomistic defects to the already irradiated fuels.

On the other hand, helium bubbles may also engender macroscopic swelling of the fuels. The increase in volume can induce the disintegration/cracking of the pellets, thus allowing the helium bubbles and other pressurized gases to diffuse in the free spaces of the fuel rods.

1.4 Back-end fuel management

The back-end management starts when the irradiated fuels are removed from nuclear reactors and stored intermediately in wet conditions to allow the dissipation of residual heat and a significant decrease in terms of their radioactivity. During the cooling phase, SNF can either be stored in SFP located in the reactor building or in a site devoted to the extended storage given that it has the required infrastructural development.

In France, the reactor buildings have enough capacity to accommodate around 7500 tU and are only able to store the fuels for around 9-12 months. Beyond this timescale, the FAs are transported to Valognes Station and finally to la Hague reprocessing plant. The fuels are then stored for several years in the massive cooling pools at la Hague station. The facility has a capacity extending over 14 400 tU with a specific density of 3 tU/m^2 and can store one irradiated FA for around 20 years [10]. In recent years, the spent fuel storage capacity of the four massive SFP at La Hague has been increased through re-racking to dense packing from 13,600 to 17,600 tons [11]**.**

Over its entire operational period, la Hague reprocessing plant has recycled about 26 550 tons of irradiated fuels originating from France, Germany and Japan with the aim to recover usable materials that can be used again as fresh fuels [2].

1.5 Mixed Oxide fuels

During nuclear operations, along with fission reactions, U-238 undergoes neutron capture processes to form several plutonium isotopes such as Pu-239, Pu-240 & Pu-241, amongst others. Pu-239 and Pu-241 are fissionable materials and can be reused for the next operation cycles through recycling and processing. The reprocessing of SNF and recovery of usable materials such as uranium and plutonium has the general aim to produce MOX fuel. The latter is an intimate mixture of plutonium oxide in a depleted or natural uranium oxide matrix. As 95% of the MOX fuel is composed of UO_2, both fuels share similar characteristic properties.

In France, 21 nuclear reactors are currently using MOX fuel which represents 10% share of its total electrical generation. The French industrial protocol for the MOX fuel fabrication is based on the MIMAS (MIcronized MASter blend) process. The latter involves two major blending steps: a first ball-milling process of UO_2 and PuO_2 powders results in a master blend with an initial enrichment of 20-30%. The process is then followed by a secondary blend to reach an enrichment of about 5-10%. Although MOX pellets share similar macroscopic properties with unirradiated UO_2 fuels, they have a unique microstructure characteristic.

According to Oudinet *et al.* [12], microscopic examinations of a standard MOX MIMAS fuel reveal the existence of three distinct phases.

- A Pu-rich agglomerate phase with a high plutonium content (24% Pu). The latter is rich in fissile Pu-239 and Pu-241 isotopes, which offer greater fission cross sections. Phase segmentation shows that the plutonium agglomerate phase occupies 13% of MOX specific surface area.
- A U-rich phase (0.5% Pu) largely dominated by fertile U-238. Very little fission is expected in this region during the initial stage of irradiation but neutron capture reactions convert U-238 into Pu-238, thus increases the local fission density. The surface fraction of the uranium phase is about 36% of the total specific surface area.
- A coating phase with a Pu content (5.7% Pu) intermediate between the U-rich phase and the enriched Pu clusters. The coating phase covers the remaining 51% of the MOX surface area.

Bouloré *et al.* [13] used the Electron Microprobe Analysis method (EPMA) to analyze the microstructure of a typical MIMAS MOX fuel. Figure 1.5 shows the presence of the three different phases in the pellet matrix, namely the solid solution (U, Pu)O_2 aggregates (Red color), UO_2 matrix (Blue color) and the coating phase (Green color).

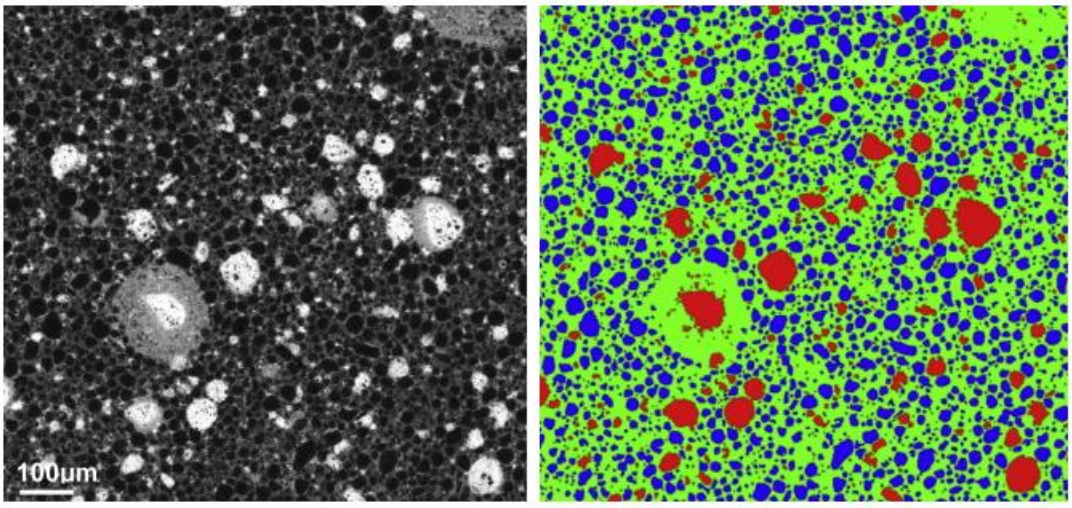

Figure 1.5: EPMA X-ray image mapping indicating the heterogeneity nature of MIMAS MOX fuel

1.6 Uranium dioxide

Most of the commercial nuclear power plants use uranium dioxide (UO_2) for the production of electricity. After irradiation, the majority of the SNF remains in the form of UO_2 (95%), while the remaining 5% is distributed amongst fission products and transuranic elements. Hence, it can be considered that the UO_2 solubility will govern the release of the radionuclides from the SNF matrix. The following section intends to use the known properties of UO_2 fuels in order to predict their expected dissolution mechanisms based on an electrochemical model. In addition, the dissolution behavior of both UO_2 and SNF in the presence of radiolytic species resulting from the interaction of ionizing particles with water will also be discussed.

1.6.1 Crystallographic structure of UO_2

UO_2 has a dark grey/black color and share the characteristics of being extremely stable in environment and nearly insoluble in water. These properties make them suitable for nuclear operations and also allowed them to be stored in a suitable phase during their interim storage as well as final disposal. UO_2 has a cubic structure of the fluorite (CaF_2) type, belonging to the Fm3m space group. In an ideal crystal, the uranium (IV) atoms are cubically coordinated to the oxygen (II) atoms as shown in Figure 1.6. In addition to UO_2, it is to be noted that this thesis also deals with other compounds, such as PuO_2, CeO_2 and ThO_2, which also share the CaF_2 crystallographic structure.

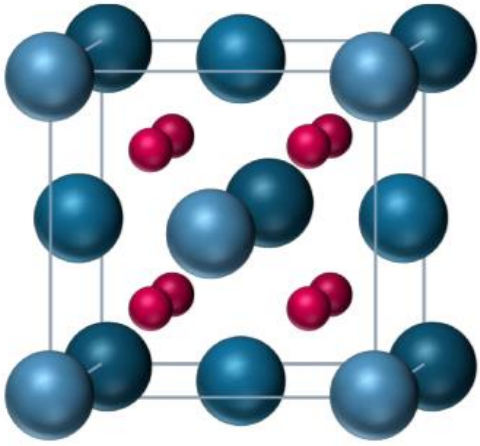

Figure 1.6: Fluorite structure (CaF_2) showing the cations (blue atoms) and anions (red atoms) respectively (in the case of UO_2, uranium and oxygen atoms) [14]

1.6.2 Stoichiometry of UO_2 compounds

UO_2 fuels can exist either as hypo-stoichiometric or hyper-stoichiometric when the oxygen content diverts from ideality. The stoichiometry in ceramic UO_2 is determined by the conditions applied during the sintering process, whereby the oxide fuel pellets are heated at high temperature under reducing environment with the aim to reach a suitable oxygen to uranium ratio. The main advantage of using stoichiometric UO_2 is that it enhances the thermo-mechanical performance of the fuel.

1.6.3 Oxidation of UO_2 compounds

Stoichiometric UO_2 is very reactive and oxidizes rapidly at low temperature in air. According to Blackburn *et al.* [15], UO_2 can be transformed into three other stable forms; namely U_4O_9, U_3O_8, and UO_3 depending on the oxygen partial pressure. UO_2 is the only stable oxide in a reducing atmosphere while UO_3 is mostly stable in oxidizing environment. During the oxidation process, U(IV) ions are oxidized to +V or +VI oxidation states as illustrated in Figure 1.7.

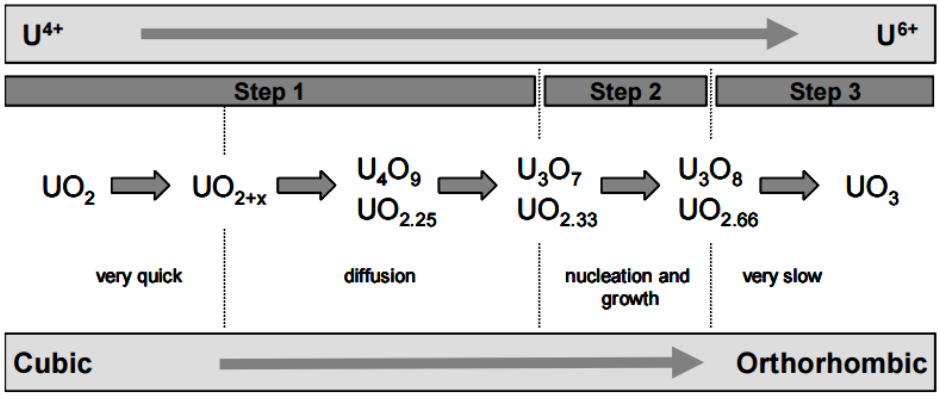

Figure 1.7: Oxidation transitions between UO_2 and UO_3 [15]

1.6.4 U_4O_9/U_3O_7 structures

A lattice contraction of the UO_2 structure is observed during its oxidation process. According to Leinders *et al.* [16], the excess oxygen interstitials are incorporated onto positions which are slightly displaced from the interstitial sites and vacancies appear at some of the regular oxygen sites which results in a local, but random, reorganization of the anion sublattice. Although intermediate oxidation products have been reported [[15], [17] & [18]], McEachern *et al.* [19] used the term U_4O_9/U_3O_7 to designate the products formed during the initial stages of UO_2 oxidation.

U_4O_9 phase can be described as a crystalline superstructure represented by an ordering of cuboctahedral oxygen clusters, which is a way to stabilize oxygen interstitials as lattice defects in UO_{2+x}. There exits three phases of U_4O_9, namely α-U_4O_9, cubic β-U_4O_9 and cubic γ-U_4O_9. The main difference among the three U_4O_9 phases relies on the re-arrangement of the cuboctahedral oxygen clusters [20].

U_3O_7 phase, on the other hand, is principally formed during the air oxidation of UO_2 powders at high temperature. Studies carried out on U_3O_7 powders showed that uranium atoms retained their positions in the fluorine structure and that the majority of changes with respect to UO_2 occurred in the oxygen sublattice [21]. The early stages of UO_2 oxidation lead to the formation of the α-U_3O_7 phase which then proceed to form the β-U_3O_7 compound. The main difference between α-U_3O_7 and β-U_3O_7 is their c/a ratio, which is 0.989 and 1.031 respectively.

1.6.5 U_3O_8 crystallographic structure

The final stages of UO_2 oxidation involve the formation of the U_3O_8 and UO_3 compounds. Both have orthorhombic structures. The O/U ratio of U_3O_8 compounds vary depending on the oxidation temperature. For instance under ambient temperature, the O/U ratio remains close to 2.33 but can reach 2.35 when the oxidation temperature is higher than 507°C. Hoekstra *et al.* [17] and Westrum *et al.* [22] reported that U_3O_8 can exist either as α-U_3O_8 or β-U_3O_8, depending on their crystallographic orientations.

According to Zhang *et al*. [23], α-U_3O_8 is a stable compound with cell parameters (a=6.71 Å, b=11.96 Å & c= 4.14 Å). The latter can be obtained by UO_2 oxidation in air at 800°C followed by slow cooling. Figure 1.8 illustrates the α-U_3O_8 crystallographic structure. On the other hand, β-U_3O_8 (a=7.07 Å, b=11.45 Å & c= 8.30 Å) is formed when α-U_3O_8 is heated above 1350°C in air or oxygen followed by slow cooling to room temperature [24].

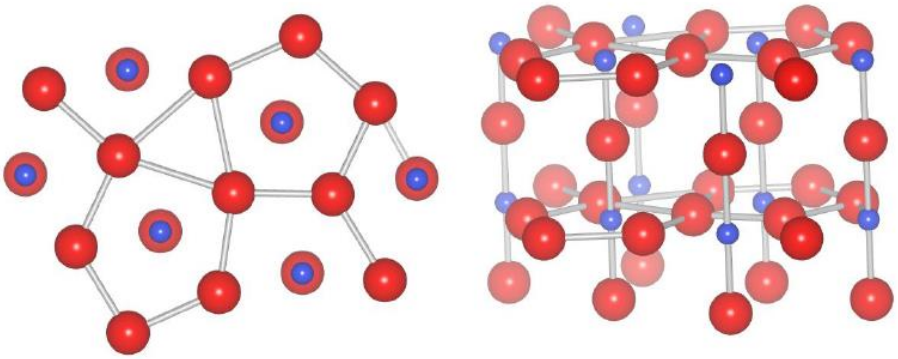

Figure 1.8: Representation of the crystallographic structure of α-U_3O_8 (Red atom: uranium and blue atoms: oxygen)

1.7 Irradiation effects on microstructure

As discussed in Section 1.3, the decay of heavy and unstable actinides during the back-end fuel cycle can significantly impact the physico-chemical properties of the SNF. For instance, the macroscopic swelling of the FA due to alpha decay may affect the fuel cladding integrity. In addition, the 5 MeV alpha ions may also induce atomic displacements in the fuel matrix. The following sections aim to discuss the main phenomenology behind the irradiation-induced atomic damages in nuclear fuels.

1.7.1 Stopping power

During irradiation, the incident ions gradually lose their kinetic energy due to their interactions with the target atoms. The energy loss is defined by the stopping power of the target material (-dE/dx). The minus sign corresponds to the energy loss and x is the penetration depth of the ions. The unit of stopping power is usually given as MeV.cm^2/g.

The stopping power can be divided into electronic and nuclear stopping power. However, the radiative stopping power also needs be considered when the energy of the charged incident ions is very high. The radiative stopping power is defined as the bremsstrahlung emission in the electric field of the material. Thus, the overall stopping power of a material can be described as:

$$-\frac{dE}{dx} = S_{Elec.} + S_{Nucl.} + S_{Rad.} \quad (1.1)$$

Where:

-dE/dx: Total stopping power of a material (MeV.cm^2/g)
$S_{Elec.}$: Electronic stopping power
$S_{Nucl.}$: Nuclear stopping power
$S_{Rad.}$: Radiative stopping power

Figure 1.9 shows the variation of the electronic and nuclear stopping power when UO_2 is irradiated with a 25 MeV alpha ion beam. The calculation was performed using SRIM software [25].

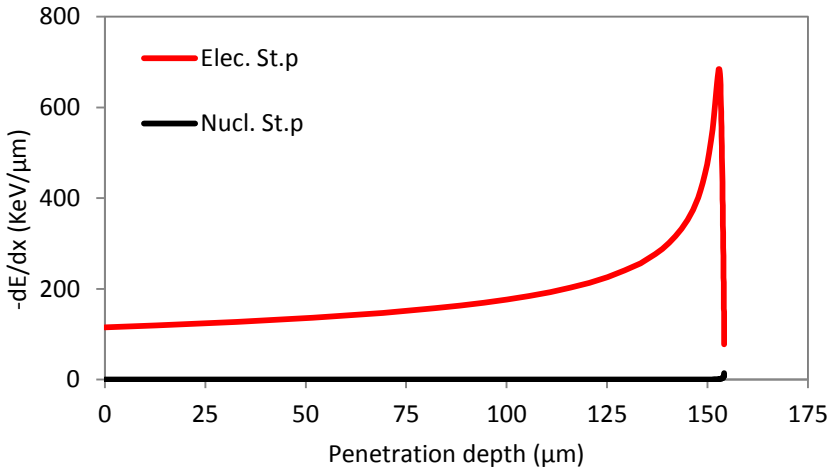

Figure 1.9: Electronic (Elec. St.p) and Nuclear (Nucl. St.p) stopping power of UO_2 during the implantation of 25 MeV alpha ions

1.7.2 Electronic stopping power

Electronic stopping, denoted by $-(dE/dx)_E$, is due to the inelastic collisions that take place between the incident ions and the bound electrons in the target material. The energy transferred to the electrons can cause their excitations to higher energy levels, thus resulting in electron-hole pairs. The electronic stopping power can be estimated by the Bethe and Bloth equation [26]. The latter gives the mean rate of energy loss (stopping power) for a heavy charged particle ($m_0 >> m_e$) and is defined as:

$$-\left(\frac{\mathrm{dE}}{dx}\right)_E = K\,(z_1{}^2)\,\frac{Z_2}{A}\,\frac{1}{\beta^2}\left[\frac{1}{2}\,In\,\frac{2m_e\,c^2\beta^2\,T_{max}}{I^2} - \beta^2 - \frac{\delta(\beta\gamma)}{2}\right] \qquad (1.2)$$

Where:

A: atomic mass of absorber
N_A: Avogadro's number (6.023×10^{23} mol^{-1})
m_ec^2: electron mass x c^2 (0.511 MeV)
r_e: classical electron radius ($e^2/4\pi\epsilon_0 mec^2$: 2.818 fm)
K/A: $4\pi N_A r_e{}^2 m_e c^2/A$ = 0.307075 MeV.cm^2/g, for A = 1 g/mol
Z_1: atomic number of incident particle
Z_2: atomic number target material
I: characteristic ionization constant (depends on the material)
$\delta(\beta\gamma)$: density effect correction to ionization energy loss

1.7.3 Nuclear stopping power

When the projectile has lost most of its energy and when the screening of the nucleus of the incident projectile due to the capture of the electrons becomes important, the nuclear component starts to compete with the electronic stopping. The nuclear stopping power refers to the energy loss involves in the elastic collisions between the atoms of the incident ion and the target atoms. As shown in Figure 1.9, the nuclear stopping power is more important when the energy of the projectile becomes sufficiently low.

1.7.4 Defects in UO_2 structure

1.7.4.1 Electronic defects

In solids, electron-hole pair excitations give rise to electronic defects. These defects can also occur in non-stoichiometric compounds as they help to maintain the electrical neutrality. In hypo-stoichiometric UO_2, the lack of oxygen atoms is compensated by uranium atoms sitting on uranium lattice sites carrying a negative charge, denoted by U'_U (electron type). On the other hand, the excess oxygen interstitials in hyper-stoichiometric UO_2 are compensated by uranium atoms sitting on uranium lattice sites carrying a positive charge, $U^{\cdot}_U$ (hole type). Thus, the stoichiometry defines the concentration of electronic defects in the crystal.

1.7.4.2 Point defects

During elastic collisions, lattice atoms are displaced off their original positions when the energy transferred by the projectile is greater than the energy binding the atoms in their lattice sites. The displaced atoms, referred as Primary Knock-On atoms (PKA), can cause a series of other atomic collisions if they have high enough kinetic energy thus resulting in a succession of cascade displacement to form point defects. Point defects can be sub-categorized as Frenkel pair and Schottky defect.

In UO_2, a Frenkel pair defect arises when a lattice atom is pushed to an interstitial site as a result of ballistic collision with an energetic particle or when the crystal is heated at sufficiently high temperature, provided that the energy absorbed by the atom is higher than its displacement energy. According to Olander [27], Frenkel pair defects are most commonly observed in UO_2.

Schottky defect, on the other hand, occurs when a vacant cation site is balanced by a vacant anion site [28]. In UO_2, this defect is characterized by one uranium vacancy and two oxygen vacancies; given that they are far enough to ensure that they do not interact with each other. These defects are most common in ionic compounds with high coordination number and where the cations and anions are of comparable size.

Figure 1.10 provides a better visualization of the two types of point defect.

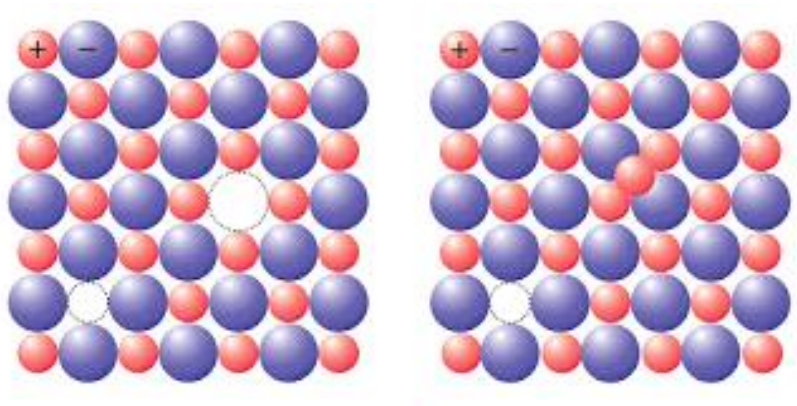

(b) Schottky defect **(a)** Frenkel defect

Figure 1.10: Differences between (a) Schottky and (b) Frenkel defects

1.7.4.3 Extended defects

The primarily focus of the current thesis rely is on zero-dimensional defects (point defects). However, it is important to note that other types of defects can also exist in UO_2. These can be categorized as one-dimensional line defects, two-dimensional planar defects and three-dimensional bulk defects.

One-dimensional defects refer mainly to dislocation linear defects. Dislocations can be defined as a line that forms a boundary between a region of a crystal that has slipped and one that has not, i.e. they correspond to areas where the atoms are out of positions in the crystal structure. There are three main types of dislocations, namely; edge, screw and mixed. Edge dislocations occur when the localized lattice distortion exists along the end of an extra half-plane of atoms. Screw dislocations result from shear distortion such that the atoms over the cut surface are shifted in a direction parallel to the dislocation line. Mixed dislocations are defects where the shift is neither parallel nor perpendicular to the dislocation line.

A schematic representation of the different types of dislocation lines is shown in Figure 1.11.

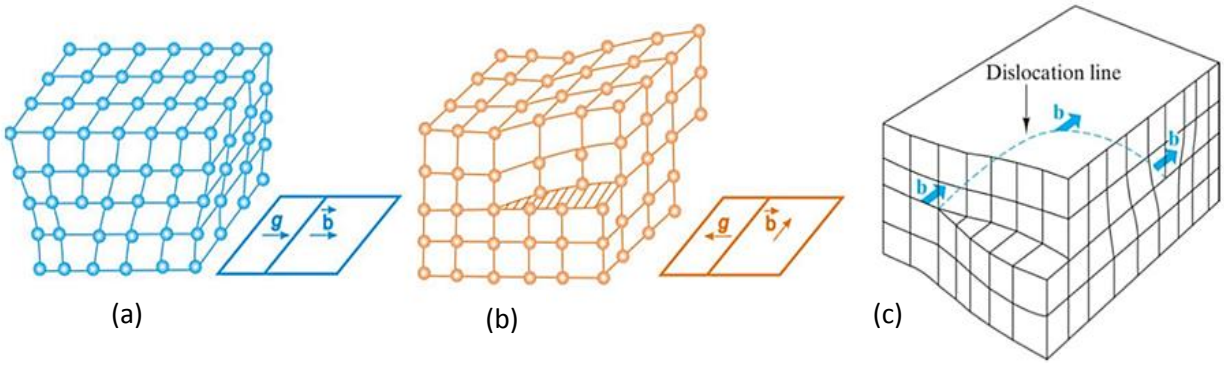

Figure 1.11: Dislocation lines in materials *(a)* Edge dislocation described as an extra half plane of atoms above the slip plane *(b)* Screw dislocation formed by a cut and a shift of atoms in a direction of parallel to the cut line *(c)* Mixed dislocation along the length of the dislocation [29]

Dislocation networks are likely to be formed in nuclear fuels due to the slowing down of fission fragments in high temperature conditions during in-reactor operations. Onofri *et al.* [30] recently conducted an extensive study to investigate the dislocation structures during the irradiation of polycrystalline UO_2 with 4 MeV gold ions at elevated temperature.

Figure 1.12 shows the microstructural changes that occur in UO_2 during heavy ion implantation at 600°C under different irradiation fluence.

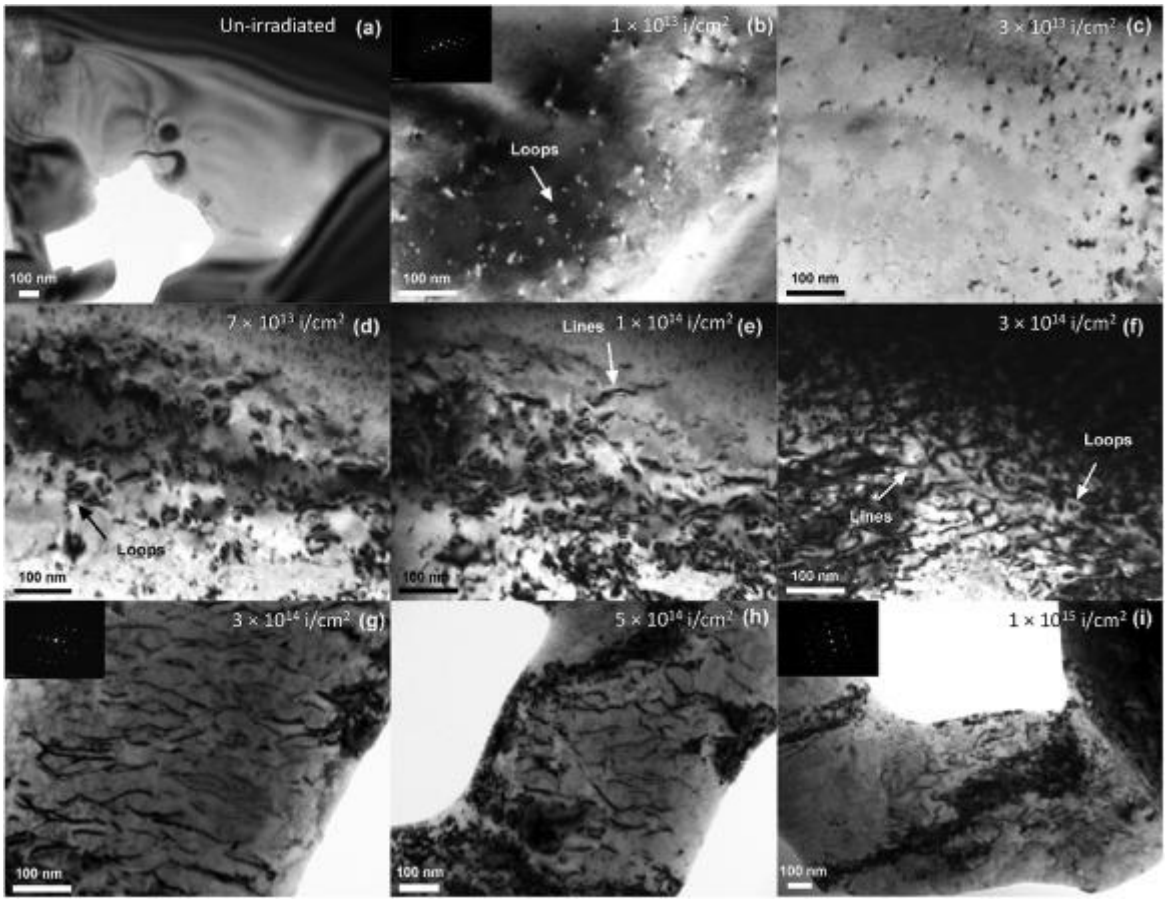

Figure 1.12: Sequential bright field Transmission Electron Microscope (TEM) images of *(a)* unirradiated polycrystalline UO_2 thin film and irradiated polycrystalline UO_2 thin film *(b)* 1×10^{13} Au/cm^2, (c) 3×10^{13} Au/cm^2, *(d)* 7×10^{13} Au/cm^2, *(e)* 1×10^{14} Au/cm^2, *(f, g)* 3×10^{14} Au/cm^2, (h) 5×10^{14} Au/cm^2, *(i)* 1×10^{15} Au/cm^2 [30]

The authors reported a significant quantity of defect clusters of a few nanometers in size and dislocation loops under the lowest fluence (1×10^{13} Au/cm^2). From the above figure, it can be observed that an increase in the irradiation fluence up to 1×10^{14} Au/cm^2 (Figure 1.12 (b-e)) causes an increase in the size of the defect clusters. In addition, the presence of dislocation lines from Figure 1.12 (e) can clearly be distinguished. Figure 1.12 (f) shows a dislocation line network and some dislocations loops when the fluence was increase up to 3×10^{14} Au/cm^2, but increasing the irradiation fluence up to $0.3\text{-}1 \times 10^{15}$ Au/cm^2 does not induce major microstructural evolution as it can observed in Figure 1.12 (g-i).

Two-dimensional defects include surfaces, grain boundaries (Figure 1.13) and crystallographically specific boundary such as twinning and stalking faults. These defects correspond to the internal interfaces that separate neighboring regions of the same crystal structure but of different orientation. These interfaces, which are usually planar, have a two-dimensional periodic atomic structure.

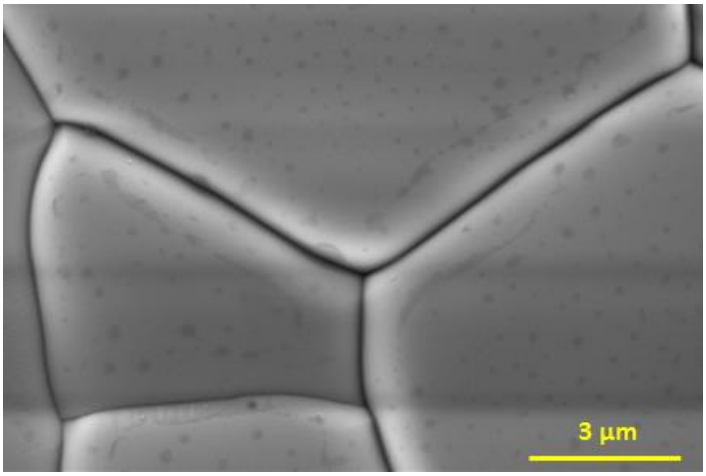

Figure 1.13: Scanning Electron Microscope (SEM) images of the grain boundaries in virgin UO_2 disk annealed at 1700°C during 24 hours

Three-dimensional defects, also referred as volume defects, include voids and bubbles. Pores are produced during the fuel fabrication process. The porosity of sintered UO_2 can be classified as (a) *open pores* which are associated to the pellet surface and (b) *closed pores* which are isolated near the center of the grains. Figure 1.14 (a) indicates the presence of pores in a virgin UO_2 disk sintered at 1400°C during 4 hours.

During nuclear operations, a large amount of insoluble gases (He, Xe and Kr) precipitate as bubbles and start to agglomerate in the fuel matrix. The behavior of these gaseous bubbles needs to be considered as they can significantly alter the physical and mechanical properties of the fuel. As an illustration in Figure 1.14 (b), Michel *et al.* [31] put into evidence the formation of a multimodal bubble population during the implantation of UO_2 thin film with Xe ions which was then followed by an annealing at 1500°C.

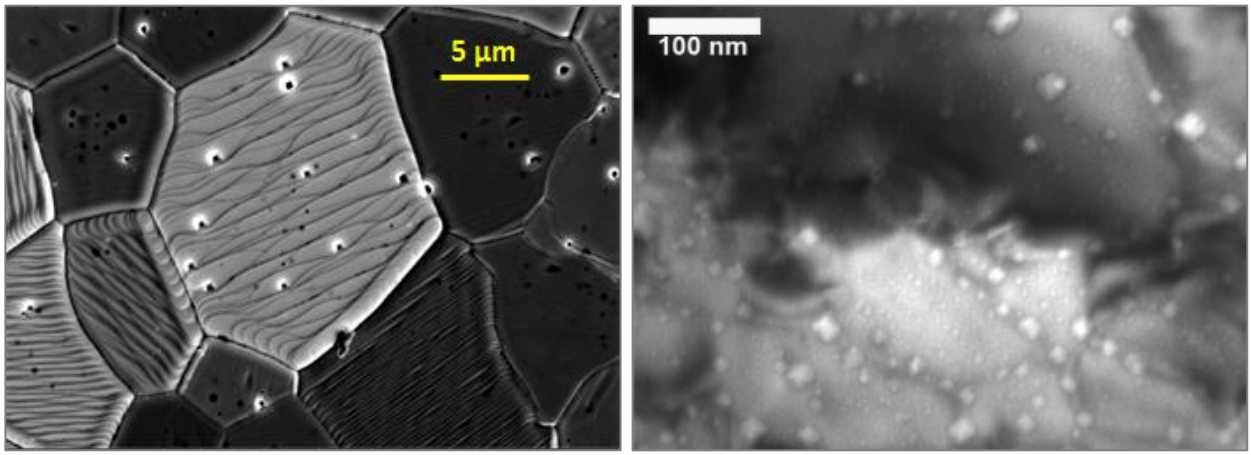

Figure 1.14: Three-dimensional defects in UO_2 fuels *(a)* SEM image of an as-fabricated UO_2 disk showing the presence of porosity *(b)* TEM image indicating the presence of gas bubbles in a UO_2 thin film implanted with 400 keV Xe ions at 7 x 10^{15} at./cm^2 after annealing at up to 1500°C during 2 hours [31]

1.8 Radiation chemistry

The radiation field of the SNF will primarily be dominated by beta and gamma radiation once they are removed from the reactor and will persist over the first 300 years during the cooling phase. After the initial beta and gamma decaying processes of the short-lived fission products, the radiation field of the irradiated fuel matrix will then be relayed by the alpha decay of unstable actinides over the long term. Figure 1.15 shows the involvement of the different isotopes contributing to the radioactivity of the SNF at different timescale.

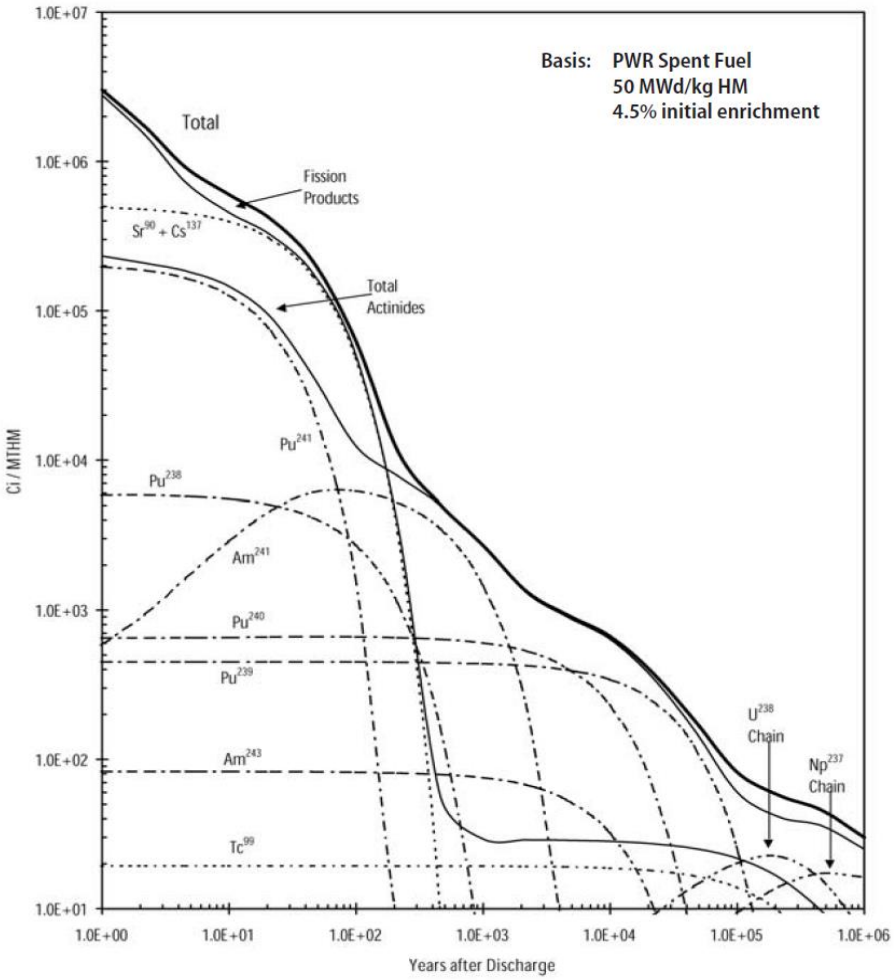

Figure 1.15: Isotopic decay heat profile of SNF [7]

The effect of beta, gamma and alpha radiation on the SNF needs to be studied separately because they interact and deposit their energies differently in the medium. This process depends on the Linear Energy Transfer (LET: -dE/dx) characteristics of the particles which defines the total energy deposited per unit path along the trajectory travelled by energetic charged particle.

Gamma and beta particles have low LET values. They tend to be very penetrating but deposit very low amount of energy along their path. The gamma spectrum of SNF lies between 600 - 1100 keV and according to Jansson *et al.* [32] at this energy range, gamma rays are involved in Compton interaction with the fuel. Therefore, gamma and beta radiation are both associated with the ejection of orbital electrons. For this reason, they will be considered to have similar impact with the irradiated fuel in this work.

High LET particles, such as alpha ions, deposit their energy densely compared to low LET radiation. For instance, Ferradini *et al.* [33] reported that the gamma radiation from a Cobalt (Co)-60 source has a LET of 0.2-0.3 keV/µm. On the contrary, the alpha decay chain results in a 5 MeV alpha particle which corresponds to 140 keV/µm.

1.8.1 Water radiolysis

When the SNF is stored under aqueous conditions, the interaction of ionizing radiation with water initiates a water radiolysis process resulting in the production of several radiolytic species. According to Obodovskiy [34], the radiolytic yield depends on parameters such as pH, water temperature, LET radiation and time. The mechanism of water radiolysis can be expressed in the form of Equation 1.3.

$$H_2O \xrightarrow{\text{Ionizing Radiation}} e^-_{aq}, HO^\bullet, H^\bullet, HO_2{}^\bullet, H_3O^+, OH^-, H_2O_2, H_2 \tag{1.3}$$

Figure 1.16 shows that water radiolysis can be categorized as a three-staged process, namely the physical stage, physico-chemical stage and chemical stage.

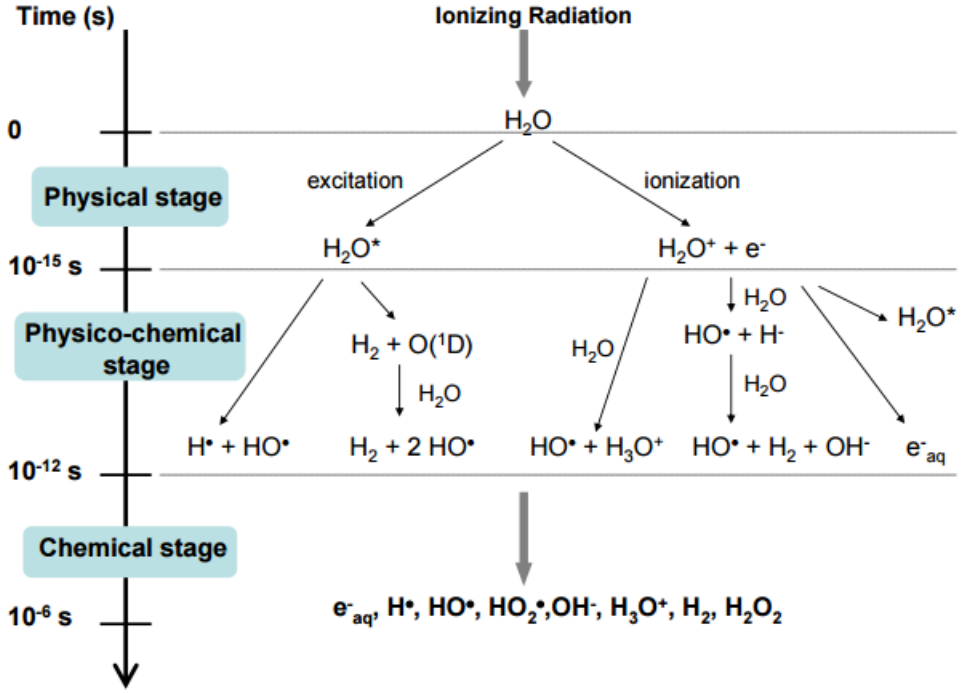

Figure 1.16: Schematic diagram describing the water radiolysis process

1. **Physical stage** ($t < 10^{-15}$ s after the radiation interact with water): the energy deposited by the radiation field produces ionized water molecules (H_2O^+), excited water molecules (H_2O^*) and sub-excitations electrons (e^-).

2. **Physico-chemical stage** ($10^{-15} < t < 10^{-12}$ s): The excited and ionized molecules from the physical stage are highly unstable. They tend to dissipate their energy to neighboring molecules. The reactions involved during this stage include ion-molecule reaction (Equation 1.4), dissociative relaxation (Equation 1.5), and thermalization of sub-excited electrons (Equation 1.6), amongst others [35].

$$H_2O^+ + H_2O \rightarrow H_3O^+ + HO^\bullet \quad (1.4)$$

$$H_2O^* \rightarrow HO^\bullet + H^\bullet \quad (1.5)$$

$$e^- \rightarrow e^-_{aqeous} \quad (1.6)$$

At the end of the physico-chemical stage, clusters of highly reactive species such as hydrated electron (e_{aq}^-), H_3O+, $H^\bullet$, $HO_2^\bullet$, H_2, H_2O_2 and OH^- are formed.

3. **Chemical stage** (10^{-12}< t <10^{-6} s): The products from stage 2 are generally produced in a heterogeneous way. They then tend to react with each other to form stable secondary radicals or molecular species. The resulting products become homogeneously distributed in the system and available for reactions with dissolved solutes in the aqueous solution.

1.8.2 Types of radiolytic products

The nature of radiolytic species produced during water radiolysis depends on the types of ionizing radiation and their corresponding LET values. According to Le Caër [35], low LET charged particles favor the formation of radiolytic products in the form of radicals such as $H^\bullet$ and $HO^\bullet$ while the concentration of molecular oxidants (O_2, H_2O_2 etc.) remains relatively low. On the contrary, high LET charged particles lead to significant amounts of molecular species. These observations are consistent with those reported by Baldacchino *et al.* [36] and Spinks *et al.* [37] and are summarized in Table 1.1.

Table 1.1: Radiolytic yields (g) obtained as a function of the type of radiation and pH

Radiation	**LET (keV/µm)**	**e^-_{aq}**	**$HO^\bullet$**	**$H^\bullet$**	**H_2**	**H_2O_2**	**$HO_2^\bullet$**
γ/β	0.23	2.63	2.72	0.55	0.45	0.68	0.008
α	93	0.04	0.1	0.16	1.7	0.3	0.3
α	108	0.42	0.54	0.27	1.11	0.07	0.07
α	200	0.13	0.44	0.14	1.17	0.11	0.11

Table 1.1 shows clearly that the LET parameter determines the yield of radiolytic products. In regards to low LET radiation, the aqueous electrons produced by gamma radiation are captured by protons to increase the concentration of hydrogen radicals in the water. At high LET values, recombination reactions increase the yield of molecular species such as H_2O_2 and H_2. For instance, H_2O_2 is produced following the reaction between hydrogen atoms and hydroxyl radicals.

1.8.3 Solubility of UO_2 matrix

The following paragraph presents the dissolution behavior of UO_2 matrix in the presence of aerated water ($[O_2]$ = 2.7 x 10^{-4} mol/L) under ambient temperature and pressure conditions (25°C and 1 atm) based on the reference model proposed by Shoesmith *et al.* [38]. The model shows that when UO_2 is in contact with water, a potential difference exists between the fuel ($E_{UO2/UO22+}$) and the aqueous medium ($E_{OX/RED}$) as shown in Figure 1.17.

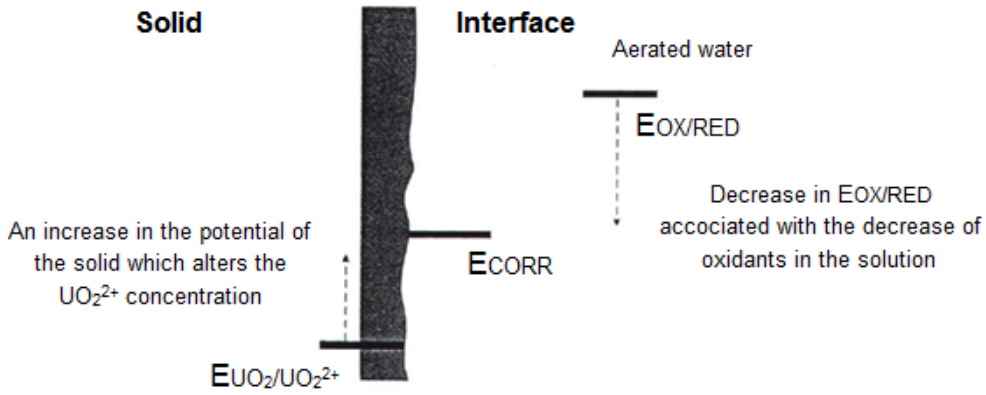

Figure 1.17: Potential difference between the UO_2 fuel and aerated contact medium [38]

The potential difference initiates an electro-chemical reaction to allow the system to reach a steady state potential at the surface boundary. The latter is referred as the corrosion potential and is represented as E_{CORR} in Figure 1.17. In order to reach the steady state, the fuel has to increase its potential from EUO_2/UO_2^{2+} to $E_{CORR.}$ In doing so, the fuel acts as an anode and undergoes oxidation to form an oxidized UO_{2+x} layer on its outer surface, whereby transfer of charged materials and matter can take place. Equation 1.7 describes the anodic oxidation process.

$$UO_2 \rightarrow UO_2^{2+} + 2e^- \tag{1.7}$$

The two electrons produced from the anodic reaction are then consumed by the aqueous medium to decrease the concentration of oxidants in the solution, thus decreasing the corrosion potential to E_{CORR}. The transition from $E_{OX/RED}$ to E_{CORR} is referred as a cathodic reaction and is represented by Equation 1.8 (Ox and Red represent a redox couple).

$$\text{Cathode (Aerated Water):}\ \mathbf{Ox} + \mathbf{2}e^- \rightarrow \mathbf{Red} \tag{1.8}$$

The cathodic reaction will only occur after the electrons are available following the anodic reaction. Hence, fuel oxidation can be viewed as the triggering process towards fuel dissolution mechanisms.

1.8.4 Oxidative dissolution of UO_2 matrix

The oxidative dissolution of UO_2 and the formation of the oxidized UO_{2+x} layer rely on the chemistry of the aqueous solution such as ionic content, presence of colloids and most importantly pH. Sunder *et al.* [39] showed that under acidic pH conditions (pH < 5), the UO_2 dissolution is enhanced in the form of uranyl ions (UO_2^{2+}) as illustrated in the solubility diagram of uranium (Figure 1.18). At low pH, the rate of oxidation equals the rate of uranium dissolution in the solution and the process occurs with little surface oxidation.

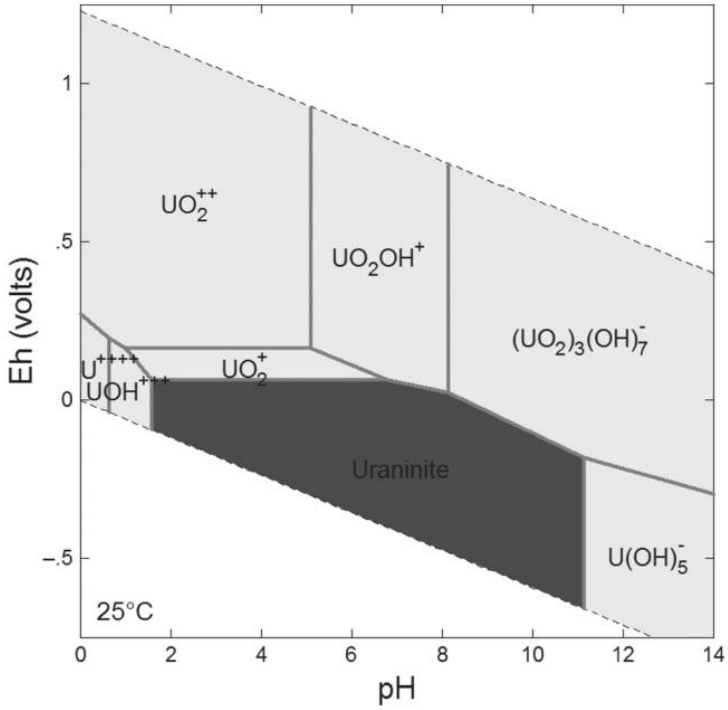

Figure 1.18: Solubility diagram of uranium in the presence of water at 25°C [40]

When the uranium concentration in the bulk solution is relatively high, the dissolved UO_2^{2+} ions precipitate as secondary oxidized phases in the form of studtite or schoepite on the fuel's surface. This is described in Equation 1.9 and illustrated in Figure 1.19 respectively.

When uranium solubility limit is reached:

$$\mathbf{UO_2} \rightarrow {UO_2}^{2+}_{adsorb} \rightarrow {UO_2}^{2+}_{surface} \rightarrow {UO_2}^{2+}_{Bulk} \rightarrow \mathbf{UO_3.z\,H_2O}_{\boldsymbol{precipitate}} \quad (1.9)$$

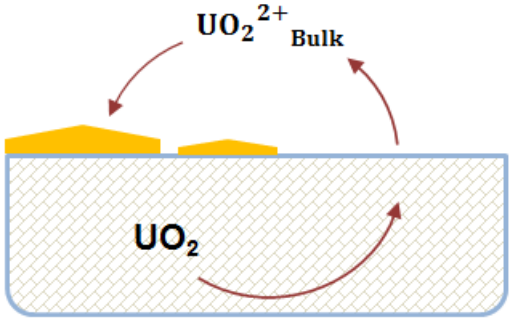

Figure 1.19: Dissolution mechanism of UO_2 and formation of secondary precipitates after reaching the solubility limit in acidic environment (pH < 5)

Under alkaline pH (pH > 10), the oxidized uranium will be involved in the formation of a UO_{2+x} layer on fuel outer surface, i.e. the rate of oxidation will be different to the rate of uranium dissolution. The amount of dissolved uranium in the solution will be fully controlled by the UO_{2+x} layer.

For an oxidation to less than $UO_{2.33}$ (i.e. x < 0.33), the process is governed by the accommodation of oxygen ions at interstitial positions (Equation 1.10). The fluorite crystallographic structure of UO_2 is not expected to change in such a case.

$$UO_2 \rightarrow UO_{2+x\ (monolayer)} \rightarrow UO_{2+x} \rightarrow UO_{2.33}\,(U_3O_7) \quad (1.10)$$

On the other hand, if the oxidation proceeds beyond $UO_{2.33}$ (i.e. x > 0.33), major structural changes are expected to occur. The UO_2 fluorite structure is destroyed and accompanied by the formation of secondary phases on the fuel surface. The oxidation continues until UO_3 is formed (Equation 1.11).

$$\mathbf{UO_{2.33}} \rightarrow {UO_2}^{2+}_{ads} \rightarrow UO_{2.5} \rightarrow UO_{2.67} \rightarrow \mathbf{UO_3} \quad (1.11)$$

The formation of the UO_3 phase results in an increase concentration of the uranyl ions in the bulk solution as illustrated in Figure 1.20.

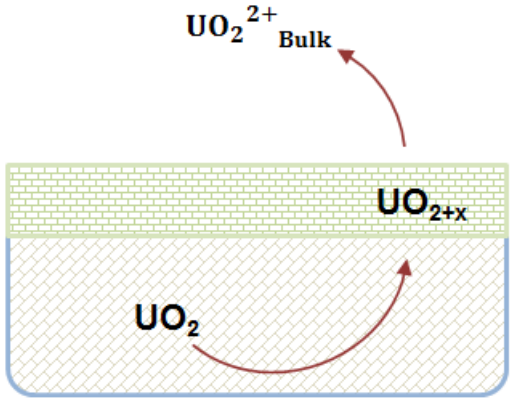

Figure 1.20: Formation of UO_{2+x} layer and uranium dissolution in the form of UO_2^{2+} ions in the bulk solution under alkaline conditions

According to Thomas *et al.* [41], the rate of uranium dissolution is lower in the pH range of 5-10. These values are usually taken as reference so as to limit the release of uranium in most SNP. For instance at la Hague treatment plant, the pH is usually kept between 5.5-6.5 [42].

1.8.5 Effect of ionization radiation on UO_2 dissolution

The previous section discussed the UO_2 fuel dissolution under aqueous conditions. However in regards to nuclear fuels, the dissolution of the UO_2 matrix will be largely affected by the inherent radioactivity of the irradiated fuel. Section 1.8.1 showed that the interaction of radiation with water produces several radiolytic species which change the redox potential of the solution. The presence of radiolytic products in the solution is more likely to drive the oxidative dissolution of UO_2. Although radiolytic products can be a mixture of both oxidants and reductants, the overall process is expected to be oxidizing because at low temperature (< 100°C), reducing radiolytic products are kinetically inert.

The different stages involved during the oxidative dissolution of UO_2 under the influence of ionizing charged particles are illustrated in Figure 1.21 below.

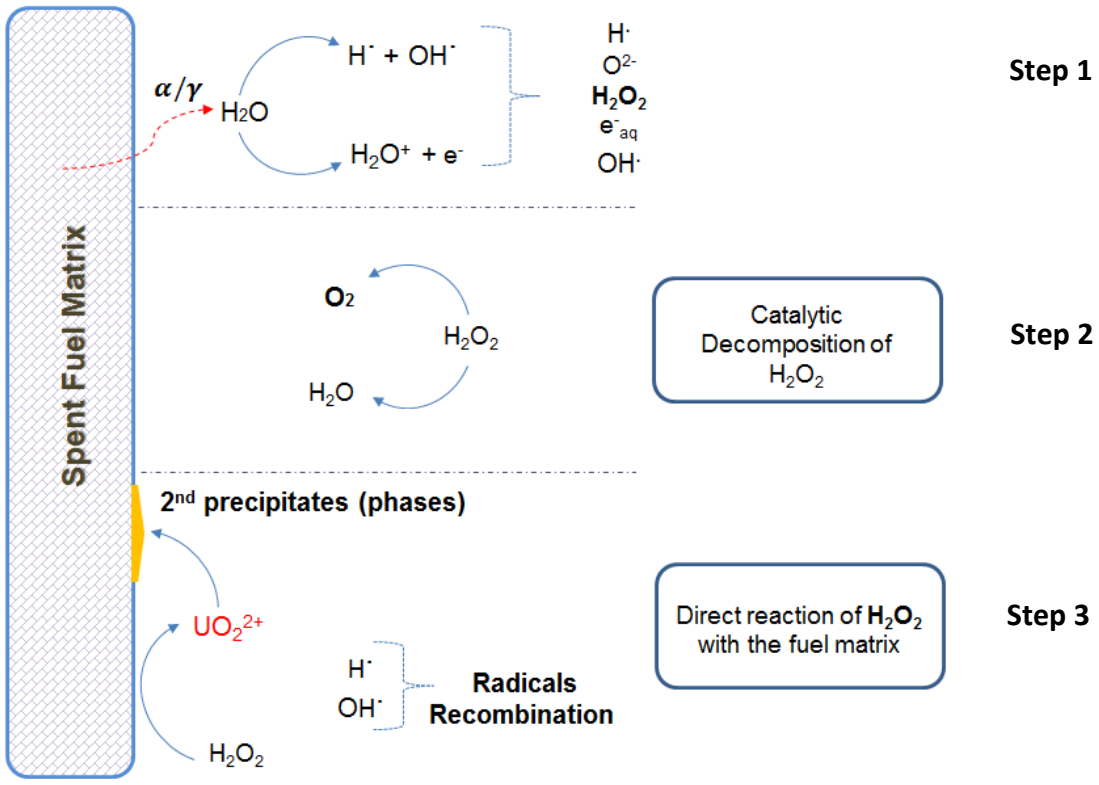

Figure 1.21: Formation of secondary phases during dissolution processes

Step 1 shows that the radiation field of the irradiated fuel firstly initiates the water radiolysis process to form different radiolytic products. Clarens *et al.* [43] showed that among the different radiolytic species, H_2O_2 remains one of the most important oxidants which, on its own, can enhance both UO_2 oxidation and the uranium dissolution rate. For example, Shoesmith *et al.* [38] showed that the rate of UO_2 oxidation in the presence of H_2O_2 is about 200 times faster than dissolved oxygen at equivalent concentration. Consequently, the fuel surface and the other redox sensitive radionuclides located near the surface will be further oxidized. H_2O_2 can react with UO_2 by two different mechanisms.

H_2O_2 can be catalytically decomposed into water and oxygen near the fuel surface and thus increases the oxygen potential of the solution as illustrated in **Step 2**. Equations 1.12-1.14 show that molecular H_2O_2 is firstly decomposed into unstable radicals. The chemical reactions continue to regenerate H_2O_2 as intermediate product and finally giving off oxygen as a by-product. In doing so, H_2O_2 does not react directly with the fuel matrix.

$$H_2O_2 + \text{Catalyst} \rightarrow 2\,HO^{\bullet} + \text{Catalyst} \quad (1.12)$$

$$O_2 \rightarrow HO_2^{\bullet} + H_2O \quad (1.13)$$

$$2\,HO_2^{\bullet} \rightarrow H_2O_2 + O_2 \quad (1.14)$$

The overall equation (1.12-1.14) can be written as:

$$\mathbf{H_2O_2 \rightarrow H_2O + \frac{1}{2}\,O_2} \quad (1.15)$$

Step 3 shows that H_2O_2 can also react directly with the fuel matrix to oxidize U(IV) to U(VI). This process favors the uranium dissolution in the solution (Equations 1.16-1.17).

$$H_2O_2 + UO_2 \rightarrow HO^{\bullet} + OH^{-} + {UO_2}^{+} \quad (1.16)$$

$$HO^{\bullet} + {UO_2}^{+} \rightarrow OH^{-} + {UO_2}^{2+} \quad (1.17)$$

Overall equation: $$\mathbf{H_2O_2 + UO_2 \rightarrow 2\,HO^{-} + {UO_2}^{2+}} \quad (1.18)$$

The two different reactions mechanisms of H_2O_2 tend to compete with each other. Water chemistry, such as pH, presence of impurities, temperature and concentration of hydrogen peroxide will determine which one of these two processes is the most predominant. Nilsson *et al.* [44] defined a dissolution yield to distinguish between the two reactions mechanisms of H_2O_2. The dissolution yield is defined as the ratio between the amount of U(VI) formed in the solvent to the total H_2O_2 consumed. For instance, Jonsson *et al.* [48] proved that H_2O_2 reacts directly with UO_2 powders and results in 80% dissolution yield. However in relevance to SNF, studies carried out with doped pellets (UO_2/Y_2O_3, UO_2/Y_2O_3/Pd & UO_2/Pd) showed that the catalytic decomposition of H_2O_2 is favored [[45], [46] & [47]].

Finally, once the solution has reached a given uranium concentration, U(VI) secondary phases (studtite or schoepite) will precipitate on the fuel outer surface. According to Hayon *et al.* [49], the unstable radicals recombine to form stable molecular species, such as H_2O or very low concentration of H_2O_2 (10^{-6} mol/L) during the later stages of the dissolution process.

1.9 Secondary altered phases

Uranium dissolution results in the formation of secondary U(VI) phases. Different types of alteration products can be formed depending on whether the SNF are stored intermediately in water pools or in geological repositories. In addition, fission products and other transuranic elements are more likely to be present near the solid/water interface. It is expected that an alteration phase chemistry involving these elements will also take place in parallel to the formation of alteration phases on the UO_2 matrix. The fission products may precipitate as additional phases on the fuel surface or they may also be incorporated in the uranium secondary phases.

1.9.1 Characteristics of secondary oxidized phases

The conditions offered during both interim storage and deep geological repository are more favorable for U(VI) compounds such as studtite and schoepite [42]. The formation of secondary phases depends on the Saturation Index (SI), which is defined as:

$$\text{SI for Studtite: } \log \frac{\frac{\left[UO_2{}^{2+}\right].[H_2O_2]}{[H^+]^2}}{Ks_{Studtite}} \tag{1.19}$$

$$\text{SI for Schoepite: } \log \frac{\frac{\left[UO_2{}^{2+}\right]}{[H^+]^2}}{Ks_{Schoepite}} \tag{1.20}$$

Conditions for the precipitation

SI = 0: solubility limit of the secondary phases
SI < 0: under-saturation (no precipitation of secondary phases)
SI > 0: over-saturation (precipitation of secondary phases is favored)

According to De Vivo *et al.* [50], schoepite ($(UO_2)_8O_2(OH)_{12}.12(H_2O)$) is a dark non-polymorphous compound which is a derivative structure of U_3O_8. It has a structure characterized by uranyl ions, which form five axial ligands with oxygen or hydroxyl ions, resulting in a layered arrangement. In schoepite, U^{6+} is 7-coordinated by two apical uranyl O-atoms and five (OH) groups or four (OH) groups and one O atom equatorially [51]. Its crystal structure shows space-group symmetry $P2_1ca$ (orthorhombic) with cell parameters (a = 14.337 Å, b = 16.813 Å and c = 14.731 Å) and has a density close to 4.8 g/cm^3 [52].

In schoepite, water molecules occupy well-defined positions and constitute parts of the H-bond linking them to the adjacent structural units (mainly OH-group). According to Finch *et al.* [52], twelve such water groups exist, but only two of them are weakly attached compared to the others. At ambient temperature, schoepite transforms slowly into metaschoepite ($UO_3.nH_2O$, n < 2). This transformation is accompanied by the removal of the two weakly bonded water molecules and by an overall rearrangement of the hydrogen bonding with the existing atoms. Forbes *et al.* [53] and Morrs *et al.* [54] stated that under increasing water radiolysis conditions, the high concentration of hydrogen peroxide will alter both schoepite and metaschoepite into a yellowish studtite compound.

Studtite, also referred as tetra hydrated uranium peroxide $[(UO_2)O_2(H_2O)_2]\cdot 2(H_2O)$, can be characterized by its mechanical weakness as it can be easily removed off the UO_2 surface by simple scratching. Burns *et al.* [55] showed that the studtite compound has a monoclinic structure with C2/c space group and cell parameters (a = 14.068 Å, b = 6.72 Å and c = 8.428 Å). The structure, as illustrated in Figure 1.22, consists of edge-sharing UO_8-polyhedra chains and water molecules are located on two different positions between these chains [56].

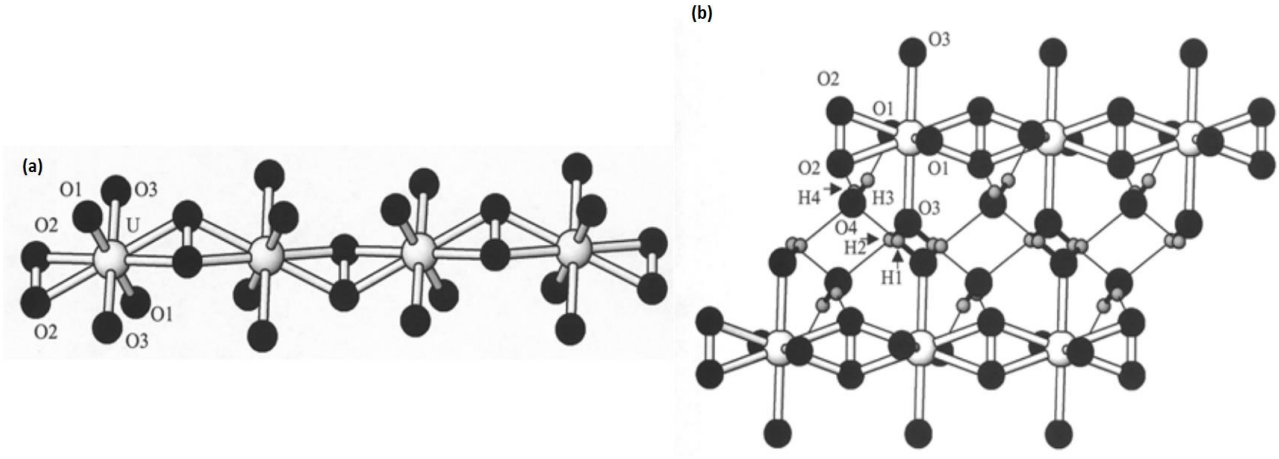

Figure 1.22: The structure of studtite *(a)* Chain of uranyl polyhedral *(b)* Polymerization of uranyl chain due to hydrogen bonding [56]

Studtite contains one symmetrically unique U^{6+} cation and four O atoms, namely O1, O2, O3 and O4. The uranium ion is bonded to two O1 atoms giving rise to a linear UO_2^{2+} ion. The uranium ion is also bonded to six other oxygen atoms; out of which four come from O2 atoms and other two are linked to O3 atoms coming from H_2O groups. A pair of O2 atoms are bonded together to form a peroxide group. The equivalent separation between the two O2 atoms has been reported to be 1.46 Å [55].

The two bonded peroxide O2 atoms play an important role during the polymerization of the uranyl polyhedral chain. These chains are linked by hydrogen bonding with an oxygen atom coming from another H_2O group, referred as O4. The latter is located in between the chains as shown in Figure 1.22 (b). The two hydrogen atoms from one O3-H_2O group both attract two oxygen atoms from two separate O4-H_2O groups. Finally, the hydrogen atoms from O4 are involved in chemical bonding with the U^{6+} cation and O2 peroxide atoms.

The formation of the oxidized secondary phases may either have an accelerating or inhibiting effect on the uranium release rate depending on the nature of the dissolution process. Shoesmith *et al.* [57] stated that if the reaction is close to equilibrium, i.e., the surface concentration of dissolved uranium is close to the solubility limit for the precipitation of the altered phases on the UO_2 surface, the dissolution of uranium tends to increase. However, the secondary phases can also act as a semi-impermeable layer between the fuel matrix and the aqueous solution. The total surface area of the fuel available for oxidation is hence reduced and the dissolution process is inhibited [58].

1.9.2 Thermal stability of secondary altered phases

According to Rey *et al.* [59], studtite remains stable up to a temperature of 50°C. At higher temperatures, it dehydrates to form metastudtite, or commonly known as dehydrated uranium peroxide. Metastudtite [$UO_2(O_2).2H_2O$] has an orthorhombic structure with cell dimensions (a = 6.50 Å, b = 8.78 Å, c = 4.21 Å) and a density of 4.67 g/cm^3 [60].

Rey *et al.* [59] also studied the thermal stability of metastudtite by using Thermogravimetry and Differential Scanning Calorimetry (DSC) with *ex situ* XRD methods upon heating in oxygen. The results showed a good stability of the metastudtite phase at a temperature close to 50°C. As temperature increases (100-700°C), it is readily transformed into U_3O_8 through four different intermediate stages as illustrated in Figure 1.23.

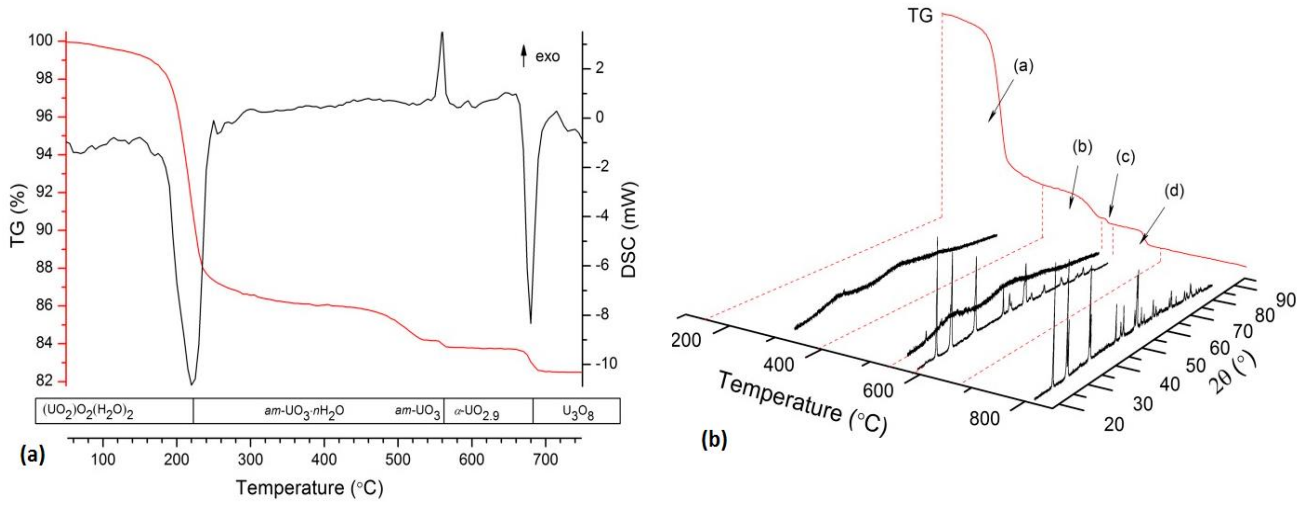

Figure 1.23: Decomposition stages of metastudtite phase *(a)* Thermogravimetry (TG) trace in red curve and DSC trace in black curve on metastudtite heating in oxygen. *(b)* TG traces on metastudtite heated in oxygen and XRD pattern for each intermediate product from decomposition steps *(a)* to *(d)*

Between 180°C and 240°C, metastudtite is converted into an amorphous phase of metaschoepite [61]. Further heating, in the range of 240°C to 500°C, causes a complete dehydration of metaschoepite to the UO_3 phase. However, the sharp rise of the DSC peak at 560°C in Figure 23 (a) indicates that the UO_3 compound loses oxygen through crystallization and ends up to form an orthorhombic $UO_{2.9}$ phase. Finally the study showed that at very high temperature, continuous heating leads to the final decomposition to U_3O_8.

1.10 Comparison study of UO_2/H_2O systems interfaces: Literature Review

The SNF matrix reacts differently in the presence of radicals and molecular oxidants. The purpose of this section is of two-folds. The first part is intended to review some of the studies carried out to understand the dissolution of irradiated nuclear fuels during the first hundreds years of storage under wet conditions, i.e. when gamma and beta radiation are predominant. The second part will focus on leaching studies conducted under the influence of alpha radiation to simulate the long term storage of SNF. The interaction of molecular species with the fuel matrix will also be discussed.

In addition, this section provides an overview of the different leaching experiments carried out under different conditions to mimic either interim storage (aerobic conditions) or final disposal of nuclear fuels (anoxic environment).

1.10.1 Effect of low LET particles on fuel dissolution

1.10.1.1 Influence of gamma radiation

The most common experimental protocol to study the effect of gamma radiation on the dissolution mechanisms consists of using external gamma sources such as Co-60, Iridium (Ir)-192 or even Cs-137. The gamma sources are placed in a closed container located just adjacent to another vessel containing the fuel immersed in the aqueous solution. The high penetrating ability of the gamma rays is efficient enough to initiate the leaching experiment in the other vessel containing the fuel/H_2O system.

Ewing *et al.* [62] reported that γ-radiation is involved in the radiolytic decomposition of nitrogen and carbon dioxide present in either air or dissolved in water, into nitric acid and carbonated radicals respectively. These radiolytic products can alter the oxidative dissolution mechanism of nuclear fuels. Gromov *et al.* [63] used a Co-60 source to simulate γ-irradiation on UO_2 and U_3O_8 samples in the presence of carbonated aqueous solution under alkaline pH. For both samples, the authors reported that the dissolution was a function of the gamma dose rate as the amount of dissolved uranium in the solvent was ten times lower when the dose rate was reduced by a factor of one hundred. The main radiolytic products involved in the leaching experiment were determined to be H_3O^+, OH^- and aqueous electrons. Furthermore, carbonate radicals obtained from the decomposition of the carbonate solution were also involved in the reactions occurring on the fuel surface. The study by Gromov *et al.* [63] proved that radiolytic radicals govern the dissolution of uranium compounds under gamma radiation.

The change in the UO_2 corrosion potential (E_{CORR}) in the presence of radicals was investigated by Sunder *et al.* [64] through the use of an external Ir-192 gamma source. The electrolyte chemistry was modified such that the effect of specific radicals could be studied. The experiment was firstly carried out under anaerobic conditions and sodium perchlorate ($NaClO_4$) solution was used to enhance the formation of HO• and aqueous electrons (e_{aq}^-). The effect of oxygen radicals was also studied by using sodium formate (HCOONa) and oxygenated $NaClO_4$ solution.

Figure 1.24 shows that the E_{CORR} increases rapidly and then reaches saturation under both aerobic and anaerobic conditions. The UO_2 oxidation can thus be defined as a two-staged process. During the first few hours of the experiment, the exponential increase of the E_{CORR} indicates the formation of an oxidized UO_{2+x} layer but the UO_2 fluorite crystallographic structure is not modified, i.e. the oxidized layer remains below $UO_{2.33}$.The steady evolution of E_{CORR} after -100 mV indicates that further oxidation subsequently results in the dissolution of uranium and also the possible precipitation of secondary phases.

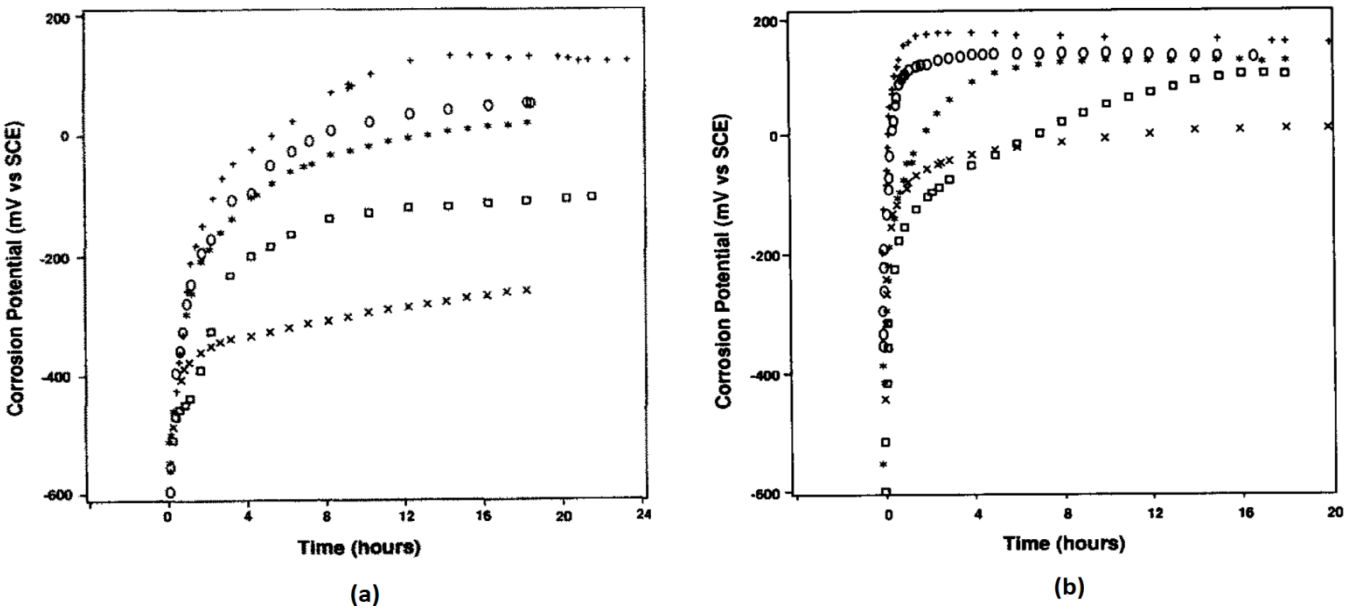

Figure 1.24: Evolution of corrosion potential of UO_2 electrode under gamma radiation in 0.1 mol/dm3 NaClO4 solution, pH: 9.5.*(a)* Under anaerobic condition with an absorbed dose (from top to bottom) of 280 Gy/h [**+**], 29 Gy/h [ʘ], 11 Gy/h [✱], 6.4 Gy/h [▫], and under no irradiation field [**x**] *(b)* Oxygenated solution with an absorbed dose of 280 Gy/h [+], 23.5 Gy/h [ʘ], 9.5 Gy/h [✱], 0.97 Gy/h [▫] [64]

The influence of external gamma radiation on a SNF segment was studied by Jegou *et al.* [65]. The experiment was also carried out under both aerated and anoxic conditions. The SNF segment considered was initially irradiated in French Gravelines 2 reactor for five cycles which corresponds to a total burnup of 60 GWd/tHM. An external Co-60 gamma source was used to deliver a dose up to 650-900 Gy/h.

Figure 1.25 shows that the concentration of both dissolved uranium and plutonium released from the SNF increases continuously, with a uranium value of 103 mg/m^2 per day under aerated conditions. The release of other actinides such as Pu-238, Pu-239, Am-241 and Cm-244 was seen to depend on the UO_2 matrix dissolution. The measured concentration of H_2O_2 in the solution was in the order of 1.2×10^{-4} mol/L.

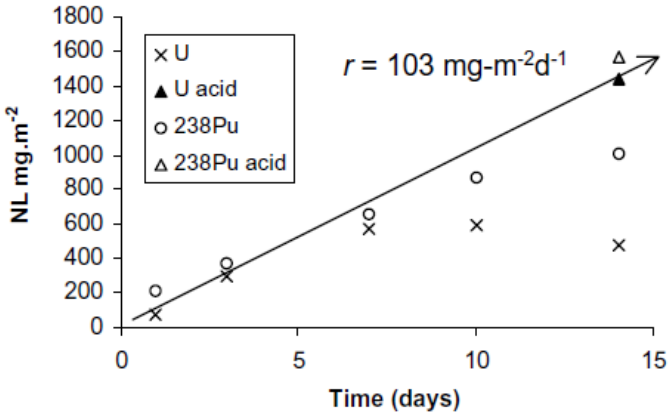

Figure 1.25: Mass loss of uranium and plutonium along with increasing leaching time in aerated water at a 650 Gy/h dose rate [65]

Cs and Sr were used as tracer elements to differentiate the dissolution behavior between fission products and actinides in the SNF matrix. The initial mass loss of Cs and Sr were chemically analyzed and reported to be 885 and 935 mg/m2 per day respectively (Figure 1.26). Comparing Figure 1.25 and Figure 1.26, Jegou *et al.* [65] concluded that the fission products are more likely to be washed away by the solvent while the majority of the actinides (U and Pu) will tend to precipitate themselves near the fuel surface.

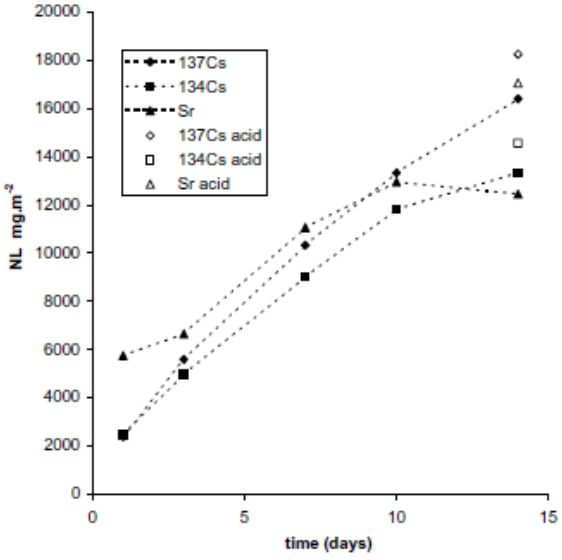

Figure 1.26: Mass loss of Cs and Sr from the spent fuel under Co-60 (650 Gy/h) [65]

However under anaerobic environment, the mean release rate of uranium and plutonium dropped to 20 mg/m^2 per day, and a similar decrease was observed for Cs and Sr (33 and 25 mg/m^2 per day). The H_2O_2 concentration was also reduced (10^{-7} mol/L) compared to the value obtained under aerated conditions (10^{-4} mol/L). These findings show that the fuel alteration process is much faster under oxidizing conditions. The study by Jegou *et al.* [65] provided important information towards the understanding of the behavior of irradiated nuclear fuels during interim wet storage.

1.10.1.2 Influence of beta radiation

The dissolution of UO_2 pellets due to beta radiation was studied by Clarens *et al.* [66]. The work was carried out under varying pH conditions and the results were then compared with simulated data using MAKSIMA software. The simulating code, developed by Carver *et al.* [67], is aimed to consider all the possible chemical reactions and species resulting from the irradiation-induced water radiolysis. The code was firstly used to estimate the concentration of hydrogen, oxygen, hydrogen peroxide and hydrogen-oxygen radicals in various parts of the primary circuit of nuclear reactors [68].

The experimental set-up consisted of an external Sr90/Yr90 pure beta source with an activity of 2.6×10^6 Bq. A vessel containing a UO_2 pellet immersed in water was placed at a given distance away from the source such that the sample acquires an accumulated dose of 1.45×10^{-3} Gy/s. This represents the total beta dose rate of a SNF with a burnup of 40 GWd/t_{HM}.

The precipitation of secondary phases having the same morphology as studtite was observed on the fuel surface under acidic pH. The change from acidic to neutral pH was accompanied by the H_2O_2 production and was consistent to the simulated results obtained with MAKSIMA code. However under alkaline pH, the concentration of H_2O_2 remained negligible. This can be attributed to a lower stability of H_2O_2 under such conditions because it tends to decompose into water and oxygen as previously reported by Watts *et al.* [69].

Figure 1.27 (a) compares the study by Clarens *et al.* [66] and relevant data regarding SNF at different pH. It can be observed that the radiation field of SNF enhances the dissolution rate (r: mol/dm^3/s) because it delivers a much higher radiation dose to the solution compared to unirradiated UO_2 pellets. Figure 1.27 (b) illustrates some of the already published data regarding the UO_2 leaching experiments under alkaline pH. It shows that the results reported by Clarens *et al.* [66] is in good agreement with those previously reported by Shoesmith *et al.* [70].

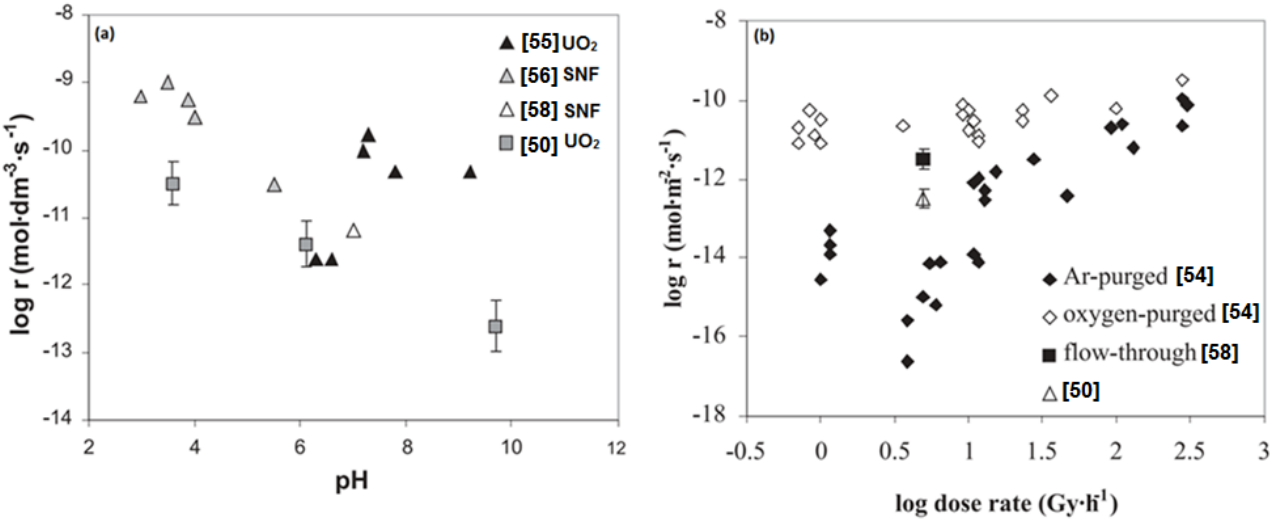

Figure 1.27: UO_2 leaching under beta irradiation *(a)* Comparison between measured UO_2 with other studies [[66], [71], [72] & [73]]. *(b)* Different published UO_2 leaching experiments under alkaline pH [[66], [70] & [74]]

1.10.2 Effect of high LET particles on fuel dissolution

The alteration of nuclear fuels and the formation of molecular corroding products such as H_2O_2, due to high LET charged particles can be investigated by three different experimental protocols:

- Using an external alpha irradiation beam generated by a cyclotron device to irradiate the fuel/water system [[74] & [75]]

- Doping UO_2 pellets with alpha emitters, such as Pu-238, Pu-239 & U-233, to simulate the alpha damage in the SNF matrix during storage [[76], [77], [78] & [79]]

- Using special electrochemical cell designed to bring an alpha source (such as Am-241 or Po-210) close to a UO_2 pellet [[80]]

External irradiation method has the main advantage to provide an on-line evaluation of the alteration process through the possibility to carry out *in situ* experiments. Doped pellets, on the other hand, are more representative in terms of total energy deposited but a given time period may be required to reach the targeted irradiation dose.

1.10.2.1 UO_2 behavior during water radiolysis induced by alpha external sources

Corbel *et al.* [81] used an external 45 MeV helium irradiation beam to irradiate a UO_2/H_2O system. The experiment consisted of a special configuration whereby the UO_2 sample was initially mounted into a leaching cell containing de-aerated water. The alpha beam energy is sufficient to allow the alpha ions to pass through the pellet and be attenuated in the aqueous solution. The thickness of the sample was chosen such that the ions reach the UO_2-water interface at 5 MeV, which is representative to the natural alpha decay behavior of SNF over the long term.

The authors showed that the radiolytic H_2O_2 concentration was proportional to the alpha energy deposited in the water and the total yield accounted for 7.4 x 10^{-8} mol/J (Figure 1.28 (a)). Figure 1.28 (b) shows that the H_2O_2 concentration produced after 4 hours of irradiation was altered up to 5.2 x 10^{-3} mol/L and the measured uranium content was 2.8 x 10^{4} µg/L.

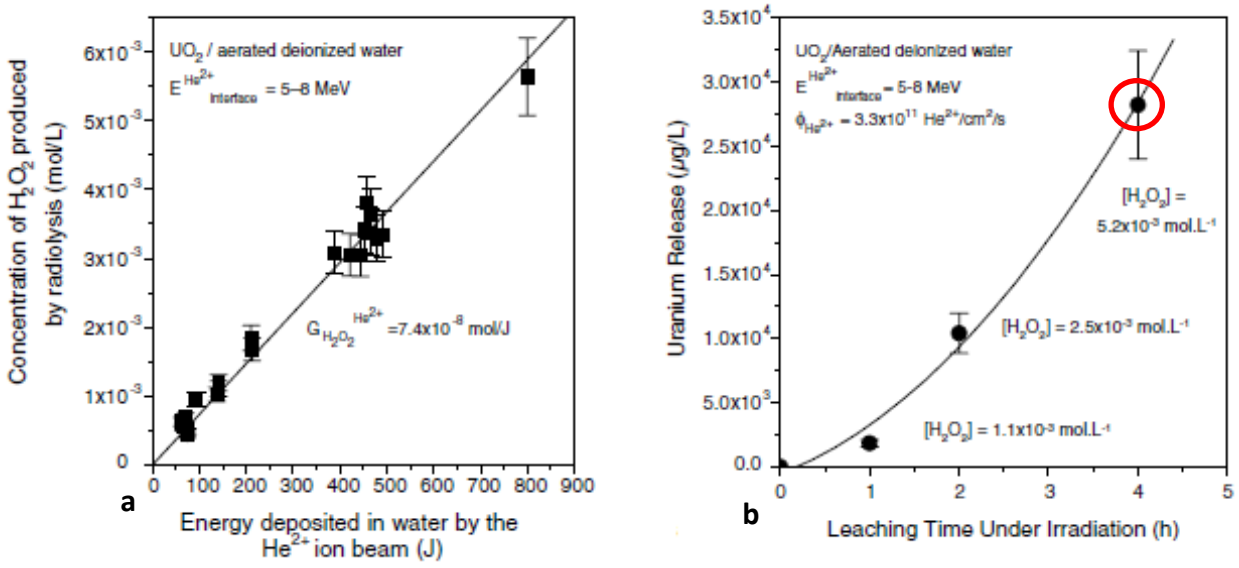

Figure 1.28: UO_2/H_2O interface irradiated with alpha beam irradiation at a flux of 3.3 x 10^{11} α/cm^2/s *(a)* The concentration of H_2O_2 produced as a result of energy deposited as the energy of the ions at the UO_2 / H_2O interface varies between 5-8 MeV *(b)* Uranium release at specific H_2O_2 concentration produced by water radiolysis indicated for each point [81]

Sattonnay *et al.* [74] investigated the alpha flux dependency on the uranium release rate. The same experimental set-up previously used by Corbel *et al.* [81] was adopted. The findings showed that the concentration of dissolved uranium tends to be higher when the dose rate is increased (Table 1.2). The alpha flux also causes an increase in the H_2O_2 concentration and a decrease in the solution pH.

Table 1.2: UO_2/water interface after 1 hour of alpha irradiation [74]

Alpha Flux ($\alpha/cm^2/s$)	[U] ($\mu g/L$)	[H_2O_2] (mol/L)	pH
3.3×10^{10}	210 ± 30	$[4.8 \pm 0.5) \times 10^{-4}$	4.9 ± 0.3
3.3×10^{11}	2280 ± 230	$(3.5 \pm 0.3) \times 10^{-3}$	3.8 ± 0.2

The concentration of dissolved uranium and radiolytic H_2O_2 reported by Corbel *et al.* [81] (Red circle in Figure 1.28 (b)) were both higher than those reported by Sattonnay *et al.* [74] (Table 1.2) even though both experiments were conducted using the same alpha flux. This discrepancy can be explained by the irradiation duration employed of irradiation in these studies. Corbel *et al.* [81] carried out an accumulated alpha flux during 4 hours, while the values reported by Sattonnay *et al.* [74] were obtained only after 1 hour of irradiation.

When the solution reaches the solubility limit for the secondary phases, the precipitation of U(VI) compounds on the fuel surface is favored according to the Equation 1.21. The protons are responsible for the decrease in pH as indicated in Table 1.2.

$$H_2O_2 + UO_2^{2+} + 4H_2O \rightleftharpoons U(VI)_{\text{secondary compounds}} + \mathbf{2H^+} \quad (1.21)$$

1.10.2.2 UO_2 behavior during water radiolysis induced by alpha emitters

Leaching experiments of UO_2 pellets doped with alpha emitters such as Pu-298 and Pu-239 under aerated conditions were carried out by Jegou *et al.* [82]. The authors used four batches of doped UO_2 pellets, three of which were of different alpha fluxes, mainly 3.30×10^4, 3.30×10^5 and 3.2×10^6 $\alpha/cm^2/s$. As the alpha activity of the SNF becomes more important over increasing storage time, the mentioned alpha fluxes correspond to 15, 1500 and 40 000 years milestones respectively in the lifetime of a SNF with a burnup of 47 GWd/t_{HM}. The fourth sample corresponded to a reference un-doped UO_2 pellet.

The leaching experiments were all carried out under pseudo-dynamic conditions, i.e., the solutions volume were renewed on an hourly basis. Five such leaching cycles were carried out and the results show that the un-doped reference sample and the batches corresponding to the 1500 years and 40 000 years of storage showed the same characteristics because they all tend towards a steady uranium release close to 5 µg/L as shown in Figure 1.29. This indicates that the amount of dissolved uranium is not affected by alpha radiation induced radiolysis. The high

uranium release from the 15-years batch samples was attributed to a microstructure effect related to the high porosity of the pellet.

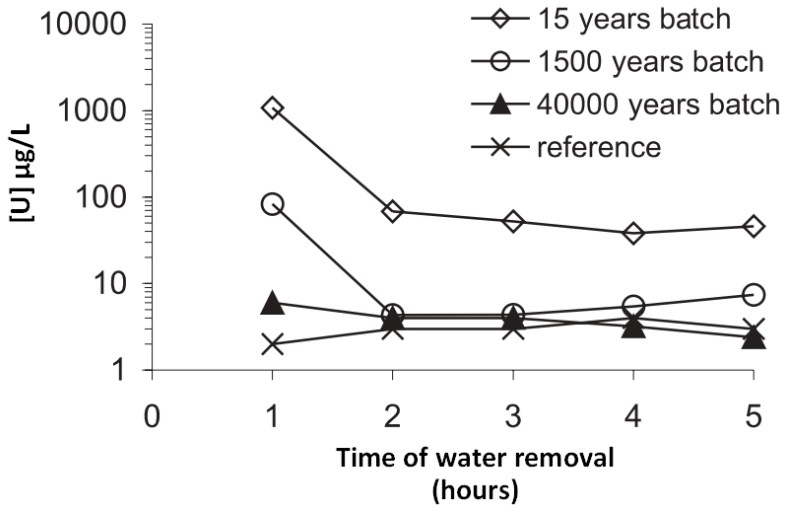

Figure 1.29: Amount of uranium dissolved in the solution after the doped pellets were stored for one week in aerated water [82]

After the first five cycles, the leaching experiment was extended for one year. The 1500 years pellet showed a higher uranium release rate than the reference and 40 000 years samples (Figure 1.30). The 1500 years sample reached a steady 25 µg/L concentration, while the reference and 40 000 years pellets remained at 5 µg/L. The 15 years batch sample exhibited the same behavior due to its high porosity as previously observed in Figure 1.29.

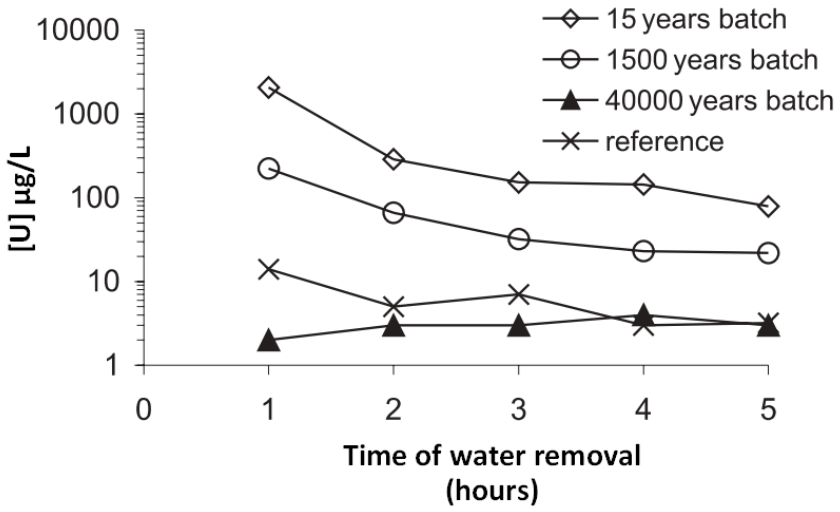

Figure 1.30: Amount of uranium dissolved in the solution after the doped pellets were stored for one year in aerated water [82]

The authors concluded that the alpha activity of the 1500 years sample enhanced oxygen diffusion. This mechanism favors both the formation of an oxidized UO_{2+x} layer and the uranium dissolution. However, the reference UO_2 and 40 000 years samples both had very long oxidation incubation time which inhibited the formation kinetics of the oxidized layer and the uranium release rate [[63]- [83]].

Rondinella *et al.* [78] and Cobos *et al.* [79] investigated the dissolution of Pu-doped UO_2 pellets under anoxic environment. The experiments were all carried out under static conditions, i.e. no sequential renewal of the solution. Instead, a given volume which is representative to the whole solution was taken off at different time intervals and analyzed. The results showed that the amount of dissolved uranium in the case of the doped samples was higher compared to a reference un-doped pellet. These findings show that alpha irradiation also influence the dissolution of nuclear fuels under reducing conditions.

1.10.3 Effect of H_2O_2 on fuel dissolution

H_2O_2 remains one of the most important radiolytic products. Stroes-Gascoyne *et al.* [84] stated that H_2O_2 can be used as a surrogate oxidant produced by radiation field to investigate the alpha-induced water radiolysis effects.

Corbel *et al.* [81] investigated the sole effect of H_2O_2 on fuel dissolution by immersing an unirradiated UO_2 sample in an aerated water solution (pH: 4) doped with 10^{-3} mol/L H_2O_2. The concentration of H_2O_2 was chosen to be close to the radiolytic H_2O_2 produced when a UO_2/H_2O interface was irradiated with an external alpha beam (Section 1.10.2.1). The concentration of dissolved uranium in the solution reported from the experiments is compared in Table 1.3.

Table 1.3: Difference in the amount of dissolved uranium under different experimental approaches

Experiments	**Solution doped with H_2O_2**	**External Alpha beam (Section 1.10.2.1)**
Quantity of Uranium (µg/L)	30	2.8×10^4

The above table shows that the uranium release due to solely H_2O_2 is much lower compared to the dissolved uranium obtained when an external irradiation beam was used. This observation is consistent with previous studies by Lucchini e*t al.* [85] and Poinssot *et al.* [86]. During irradiation, other radiolytic species are formed along with molecular H_2O_2. The presence of these radiolytic species can also participate in the oxidation/dissolution mechanisms of the UO_2 pellets. In addition, it is also important to consider that a higher concentration of H_2O_2 is

produced near the solid/water interface during irradiation while the H_2O_2 may be distributed evenly in the bulk solvent in chemically doped solution.

Shoesmith *et al.* [57] investigated the effect of H_2O_2 on UO_2 by measuring the corrosion potential (E_{CORR}) for a H_2O_2 concentration between 10^{-5} and 2 x 10^{-1} mol/L under alkaline condition. The rapid rise of E_{CORR} at low H_2O_2 concentration indicates the formation of a UO_{2+x} layer and subsequent release of uranium as illustrated in Figure 1.31. The latter shows three distinct behavior of UO_2:

1. For $[H_2O_2] < 2 \times 10^{-4}$ mol/L: The dissolution rate is relatively slow as it tends to be close to the oxidative dissolution threshold.
2. For 2×10^{-4} mol/L $< [H_2O_2] < 5 \times 10^{-3}$ mol/L: The dissolution process does not depend on the H_2O_2 concentration because the dissolution rate stays close to 0.1 µg/cm^2 per day even if the concentration of hydrogen peroxide is further increased.
3. For $[H_2O_2] > 5 \times 10^{-3}$ mol/L: the dissolution rate increases with the H_2O_2 concentration with an approximate first-order dependence.

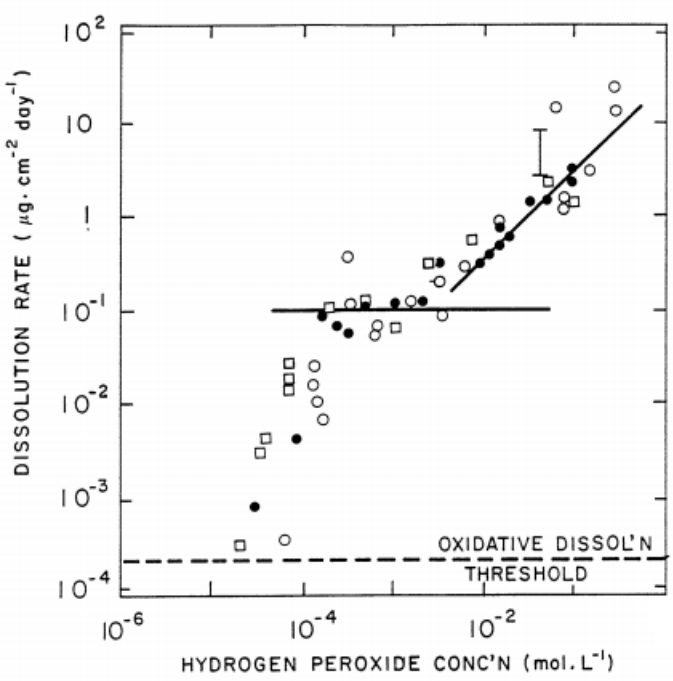

Figure 1.31: Dissolution rate of UO_2 as a function of H_2O_2 added in the solution at pH: 9

The characteristic trends of the results obtained by Shoesmith *et al.* [57] were also observed by Sunder *et al.* [87]. At higher H_2O_2 concentration, the increase in dissolution was attributed to a polarization of the anodic reactions occurring on the UO_2 surface caused by the accumulation of

dissolution product deposits, such as $UO_4.xH_2O$ and $UO_3.xH_2O$. This process leads to a more rapid dissolution of UO_2 but restricted H_2O_2 decomposition.

In another study, Nilsson *et al.* [44] compared the influence of H_2O_2 on UO_2 and SIMFUEL pellets. The aqueous solution used was bubbled with nitrogen gas to create an anaerobic condition. Table 1.4 presents the obtained results for both pellets.

Table 1.4: H_2O_2 consumption rates and dissolution rates of U(VI) in solution bubbled with nitrogen gas

Material	H_2O_2 consumption rate ($mol/m^2/s$)	Rate of U(VI) dissolution ($mol/m^2/s$)
UO_2	9.9×10^{-7}	1.4×10^{-7}
SIMFUEL	5.1×10^{-7}	9×10^{-10}

The table indicates a slight difference in H_2O_2 consumption between the two fuels. The concentration of U(VI), in the form of UO_2^{2+} ions, resulting from the leaching of SIMFUEL was lower compared to the UO_2 pellet. As explained in Section 1.8.5, H_2O_2 can be involved in two types of reaction: either it reacts directly with the fuel matrix and enhances the dissolution process, or it can be catalytically decomposed into water and oxygen. The results obtained by Nilsson *et al.* [44] show that most of the H_2O_2 were involved in catalytic decomposition reactions and is consistent with a decrease in uranium dissolution rate. Such mechanism was also reported by Trummer *et al.* [88].

1.11 Alteration of UO_2 surface during leaching studies

H_2O_2 is also involved in the formation of secondary phases on the fuel surface exposed to an aqueous environment. The precipitation of secondary phases occurs once the solution has reached a given concentration of dissolved uranium. Corbel *et al.* [81] studied the microstructural evolution of UO_2 pellet when exposed to aerated de-ionized water doped with H_2O_2 (10^{-1} mol/L) for 27 days. The findings are presented in Figure 1.32.

The leached UO_2 surface was firstly analyzed using Scanning Electron Microscopy (SEM) after 16 days of exposure. A yellow homogeneous alteration layer that displayed microcracks was observed on the fuel surface. The layer then appeared as closely packed crystalline fibers growing with an orientation perpendicular to the UO_2 surface after 27 days of leaching. The thickness of the altered layer was also seen to depend on the H_2O_2 concentration.

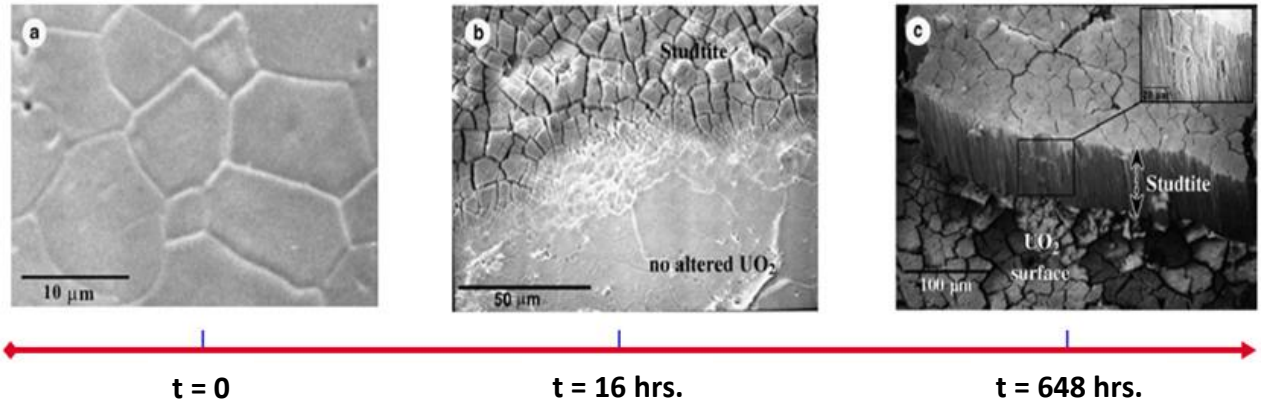

Figure 1.32: Evolution of UO_2 microstructure. *(a)* Surface before leaching experiment *(b)* After 16 hours of leaching (c) After 648 hours showing the growth of the altered layer perpendicular to the fuel surface [81]

The formation and growth of the altered layer under alpha irradiation was studied by Sattonnay *et al.* [74]. Figure 1.33 (a) shows the microstructural evolution under low alpha flux (3.3×10^{10} $\alpha/cm^2/s$). The figure shows grain boundary attack and extensive transgranular boundary corrosion. The UO_2 surface was also covered with a fine layer of alteration product and some microcracks appeared in the grains. The secondary precipitates were more visible at high alpha flux and appeared as closely packed bundles of randomly oriented crystalline rods with no specific growth direction as shown in Figure 1.33 (b). Similar results were previously observed by Amme *et al.* [89] and Hanson *et al.* [90].

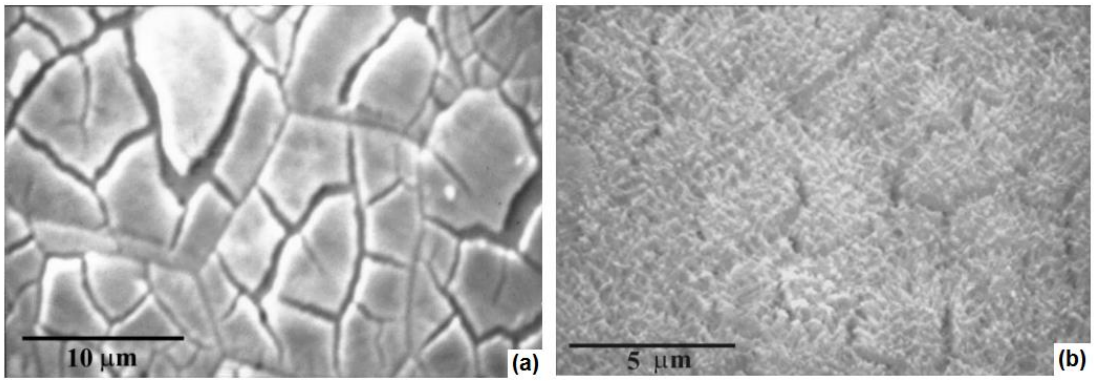

Figure 1.33: SEM images of leached UO_2 surface after irradiation with different alpha fluxes *(a)* 3.3×10^{10} $\alpha/cm^2/s$ *(b)* 3.3×10^{11} $\alpha/cm^2/s$ [74]

At the end of the leaching experiment, the irradiated pellet was analyzed by X-ray diffraction (XRD) method in order to determine the nature of the secondary phases. Figure 1.34 (a) confirmed the presence of the studtite phase on the fuel surface. Upon subsequent characterization, the studtite layer loses water molecules under vacuum and is converted into

metastudtite (Figure 1.34 (b)). According to Walenta [91], this dehydration process is irreversible.

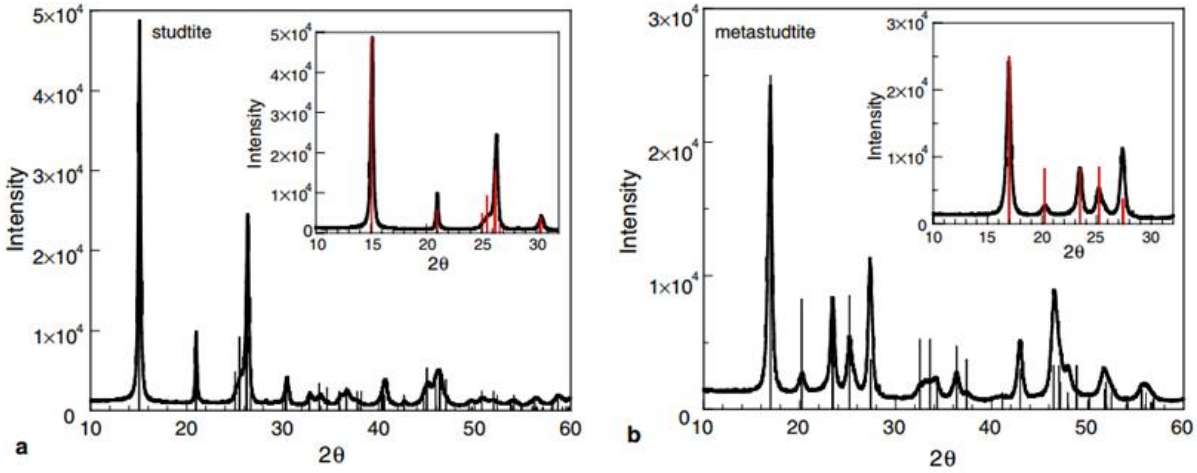

Figure 1.34: X-ray diffraction results obtained on the altered UO_2 disks for H_2O_2 addition as well as the radiolytic H_2O_2 production under alpha irradiation. *(a)* Studtite compounds just after leaching experiments, *(b)* Metastudtite formation after subsequent SEM characterization [74]

Jegou *et al.* [92] performed a similar study on fragments of SNF (60 GWd/t_{HM}) using a Co-60 source to simulate gamma irradiation. The leaching experiment, denoted as *Exp 1*, showed the initial formation of a UO_{2+x} layer and also the precipitation of needle-like studtite phase, covering parts of the fuel matrix surface.

The stability of studtite compared to the UO_{2+x} layer was also studied by leaching the samples in carbonated water under both aerated (1-5 cycles) and reducing environment (6-7 cycles). Carbonated water was used because carbonate ions act as complexing agent thus forming uranium complexes which diffuse away in the solution. This decreases the probability of uranium re-precipitation as altered products on the pellet surface. The experiment was carried out by determining the amount of tracer elements dissolved in the solution. Cs-327 was used as the tracer element because it is not involved in any type of redox reactions. This method gives a clear indication to distinguish whether the dissolution is favored either from the UO_{2+x} layer or studtite.

Figure 1.35 shows a Cs-327 to uranium ratio (Cs-327/U) value of 10 for *Exp 1*, where the formation of UO_{2+x} was more important. The subsequent post-leaching under aerated conditions gave a Cs-237/U value close to 1 for each of the 5 cycles. Therefore the dissolution of Cs-237 was much higher from the UO_{2+x} layer and this indicates that studtite is more stable under carbonated water. In regards to cycles 6 and 7, the low values of Cs-327/U suggest that the dissolution process is restricted under reducing environment.

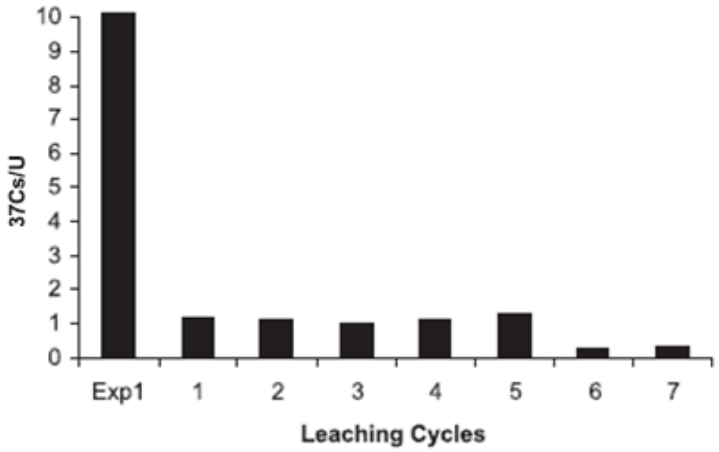

Figure 1.35: Cs-37/U ratio at the end of the reference experiment where the spent fuel was exposed to the Co-60 source. Then the post-leaching experiment under aerated (1-5 cycles) and reducing conditions (6-7 cycles) in carbonated water [92]

1.12 Conclusions

This chapter was devoted to present the main mechanisms that are likely to occur when water is allowed to react with the nuclear fuel matrix. It has been shown that the radiation field of spent nuclear fuels is strong enough to initiate a water radiolysis process, through which different radiolytic species are produced. These species, especially H_2O_2, are known to enhance surface alteration mechanisms, accelerate the dissolution rate and also allow the precipitation of secondary U(VI) phases on the fuel leached surface.

In this chapter, several studies focused on the nuclear fuel dissolution experiments have been analyzed in this literature review. It has been evidenced that most of the research was based on the understanding of UO2 fuels under both in anoxic and aerated conditions. However in regards to the French back-end fuel management policy, it is vital to acquire an overview regarding the behavior of MOX fuels under oxidizing environment, representing the interim storage conditions, for which relevant experimental data are missing in the literature.

During interim storage conditions, studtite and schoepite secondary phases are more likely to be formed. Different conventional methods, such as SEM, XRD, TEM, DSC, amongst others, can be employed for the characterization of these altered secondary phases. Raman spectroscopy, on the other hand, offers an alternative characterization approach that can be used to determine the vibrational, rotational and low frequency transitions taking place in a system based upon the interactions of photons with the sample. A detailed description of the fundamentals of Raman spectroscopy and its applications for the measurements of secondary altered phases and also irradiation defects in nuclear fuels are in the following chapter.

Chapter 2

Raman Spectroscopy

2.1 Introduction

Raman spectroscopy offers an alternate systematic non-destructive characterization approach whose principle depends on the scattering interaction of a monochromatic light source with the material. During the process, the photons will interact either elastically or inelastically before being re-emitted. Raman spectroscopy relies solely on the inelastic interactions whereby the frequency/or energy of the re-emitted photons differs from the initial monochromatic light frequency. The shift in frequency is called the Raman Effect or Raman scattering and it appears as Raman lines in the energy spectrum of scattered light [93]. These lines provide important structural information about the materials. In gases or liquids, the vibrational modes of the spectroscopy are associated with molecular motions (intra-molecular vibrations, or rotations). However, this thesis is devoted to the characterization of solids and is more related to the collective vibrational modes, defined as phonons.

In the following sections, the basic principles behind Raman spectroscopy will firstly be described. The reliability of Raman spectroscopy for the characterization of irradiation defects in nuclear fuels as well as its application for leaching experiments will then be discussed.

2.2 Basics of Raman spectroscopy

2.2.1 Interaction between photons and matter

Under the influence of an electric field, the polarization (P) of a solid is defined as the product of the magnitude E of that electric field and the polarisability tensor, defined as α, of atoms in the solid.

$$\mathrm{P} = \alpha\,\mathrm{E} \tag{2.1}$$

The polarisability tensor mainly defines the movement of the negatively charged electrons to the positive pole and the positively charged nucleus to the negative pole when submitted to the applied field. The tensor can be represented as:

$$\alpha = \begin{bmatrix} \alpha_{xx} & \alpha_{xy} & \alpha_{xz} \\ \alpha_{yx} & \alpha_{yy} & \alpha_{yz} \\ \alpha_{zx} & \alpha_{zy} & \alpha_{zz} \end{bmatrix} \tag{2.2}$$

If the electric field cannot induce a change of the polarization, the radiation emitted as a result of the induced moment oscillations will have the same frequency as the incident radiation.

When a material is subjected to a radiation from a laser of frequency v_{exc}, the electric field will vary with time such that:

$$E = E_0\, Sin\,(2\pi v_{exc} t) \tag{2.3}$$

E_0 is the amplitude of the electric field. The laser beam results in the excitation of the material, which is characterized by lattice vibration which eventually modifies the polarisability tensor. The latter is then defined as:

$$\alpha = \alpha_O + \alpha_1\, Sin\,(2\pi v_{vib} t) \tag{2.4}$$

Where α_0 is the polarisability of the atoms in the solid at equilibrium and the term $2\pi v_{vib}t$ is the rate of change of the polarisability with the vibration at equilibrium.

Therefore the induced polarization is:

$$P_{ind} = \alpha\mathrm{E} = [\alpha_O + \alpha_1\, Sin\,(2\pi v_{vib} t)\,] \times E_0\, Sin\,(2\pi v_{exc} t) \tag{2.5}$$

Using the trigonometric function:

$$Sin\ A\ Sin\ B = \frac{\mathrm{Cos}(A-B) - Cos\ (A+B)}{2} \tag{2.6}$$

The equation can be expressed as:

$$P_{ind} = \alpha_O\ E_O\ Sin\ (2\pi v_{exc} t) + \frac{\alpha_O\ E_O}{2}\ Cos(2\pi(v_{exc} - v_{vib})t) + \frac{\alpha_O\ E_O}{2}\ Cos(2\pi(v_{exc} + v_{vib})t) \tag{2.7}$$

The equation shows three main components, namely:

1. v_{exc} : Rayleigh Scattering
2. $v_{\mathrm{exc}} - v_{\mathrm{vib}}$ = Stokes Scattering
3. $v_{\mathrm{exc}} + v_{\mathrm{vib}}$ = Anti-Stokes Scattering

The equation shows clearly that without a change in the polarisability, both Stokes and anti-Stokes scattering representing the Raman Effect will not be possible as a result of which only the Rayleigh signal will appear in the spectrum.

2.2.2 Principle of Raman scattering

The photons from a laser beam produce an oscillating polarization and excite the atoms/molecules to higher (virtual) energy levels. These can be described as the continuous range of intermediate virtual energy levels (also referred as transitions) that exist between two real energy levels. The resulting oscillating polarization can couple with other possible polarizations, including vibrational and electronic excitations. In Rayleigh scattering, the induced polarization is not coupled with all the other possible polarizations and will not change the vibrational state. This means that the atoms/molecules will be excited but will finally return to their initial state or energy level as illustrated in Figure 2.1 (a). The process is said to be elastic in the sense that scattered photons will have the same frequency and energy as the initial photons from the laser source.

Raman scattering is different since the photons exchange energy with the Raman active species. The latter is promoted and then decays to a vibrational energy level located either above or below its initial energy level. The initial frequency of the photons is hence changed as shown in Figure 2.1 (b) & (c).

Stokes scattering occurs when a photon with an initial frequency, υ_{exc}, is absorbed by the Raman active molecule. Part of the photon's energy is transferred to the Raman active mode with a frequency denoted as υ_{vib}. The photons are then re-emitted with a final frequency corresponding to $\upsilon_{exc} - \upsilon_{vib}$. In anti-Stokes scattering, the Raman active species is already located in an excited vibrational level before the time of photon interaction. The extra energy of this excited atom/molecule will be released during its de-excitation to the ground level vibrational state. The resulting frequency of the scattered photons will be changed to $\upsilon_{exc} + \upsilon_{vib}$.

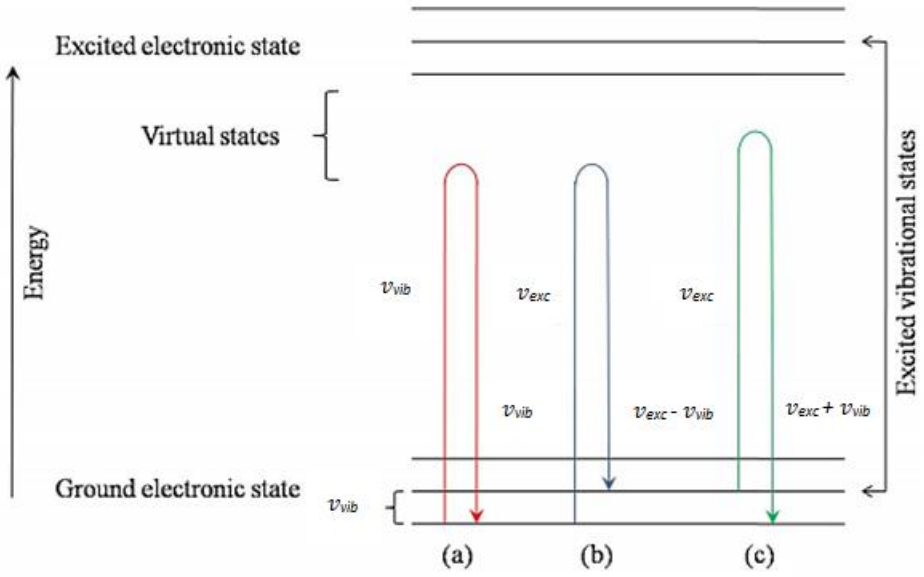

Figure 2.1: Elastic and non-elastic photons scattering behavior: (a) Rayleigh scattering (b) Stokes scattering (c) anti-Stokes scattering

Most of the incident photons that are re-emitted by Rayleigh scattering and only a small fraction undergo Raman signals with frequencies with $\upsilon_{exc} \pm \upsilon_{vib}$. At room temperature, the atoms/molecules present in the ground state mainly contribute for both Rayleigh and Stokes scattering. Figure 2.2 shows that the intensity of the anti-Stokes transition remains lower than Stokes transition because at ambient temperature, the majority of the atoms/molecules are located in their lowest vibrational level.

Compared to the Rayleigh signal, the intensity of both Stokes and anti-Stokes lines tends to be relatively weak and special measures should be taken to improve these signals on the Raman spectrum. Instruments such as Notch filters and laser stops apertures are typically used to filter the inelastic scattering signals.

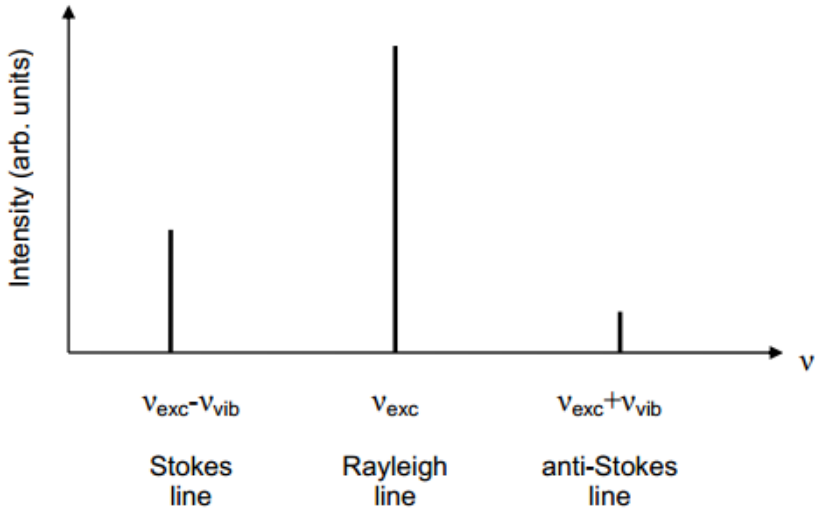

Figure 2.2: Difference in the relative intensities of the elastic and inelastic scattering at room temperature

2.3 Raman scattering in solids

In a crystal, atoms vibrate rapidly about their lattice positions and independently to each other since they are involved in chemical bonding. When an atom moves from its equilibrium position, it exerts a force on its neighboring atom causing it to move. This movement produces vibrational waves in the solid. The vibration mode in which atoms in a lattice oscillates uniformly at a single frequency can be imagined as a type of quasi particle known as phonon which defines a special wave of lattice distortion that propagates through the solid.

For a solid to experience the Raman peaks, the absorption of photons should be accompanied with a change in the polarisability of the crystal lattice. In a simple 1D crystal lattice system, the vibration of the atoms can be defined by a wavenumber denoted by *v* and the phonon travels in the solid as a longitudinal wave. In a solid containing a number of random particles, the propagating longitudinal wave is characterized by the movement of these particles in the direction of the propagation wave, with the longitudinal wavelength being the distance of two consecutive rarefactions or compressions.

In a 3D lattice of atoms, the wave vector is replaced by a 3D vector which moves in the direction of propagation. This vector is denoted as k and has unit of cm^{-1} which defines the vector in a reciprocal space. In contrast to 1D lattice, the vibration is not restricted only to the direction of the wave propagation but it can also take place in atomic planes perpendicular to the wave in 3D systems. Hence in these systems, phonons can be described either as longitudinal or transverse wave depending on the direction. When a solid consists of a minimum of two different types of atoms in a smallest unit cell structure, phonons can be categorized as either Acoustic phonons or Optical phonons.

2.3.1 Types of phonons

2.3.1.1 Acoustic phonons

Acoustic phonons occur when neighboring atoms move in the same direction out of their equilibrium lattice positions. In case where the atomic displacement is in the direction of the propagation, the atoms tend to be closer to each other during a half period and then to move away, this is analogous to a sound wave in air.

Acoustic phonons tend to exhibit a linear relationship between frequency and phonon wave vector when the wave numbers are small, i.e. for long wavelength and the frequency converges to zero when for infinite wavelength. Acoustic phonons vary depending on whether they are longitudinal (LA) or transverse (TA). An illustration of both cases is presented in Figure 2.3.

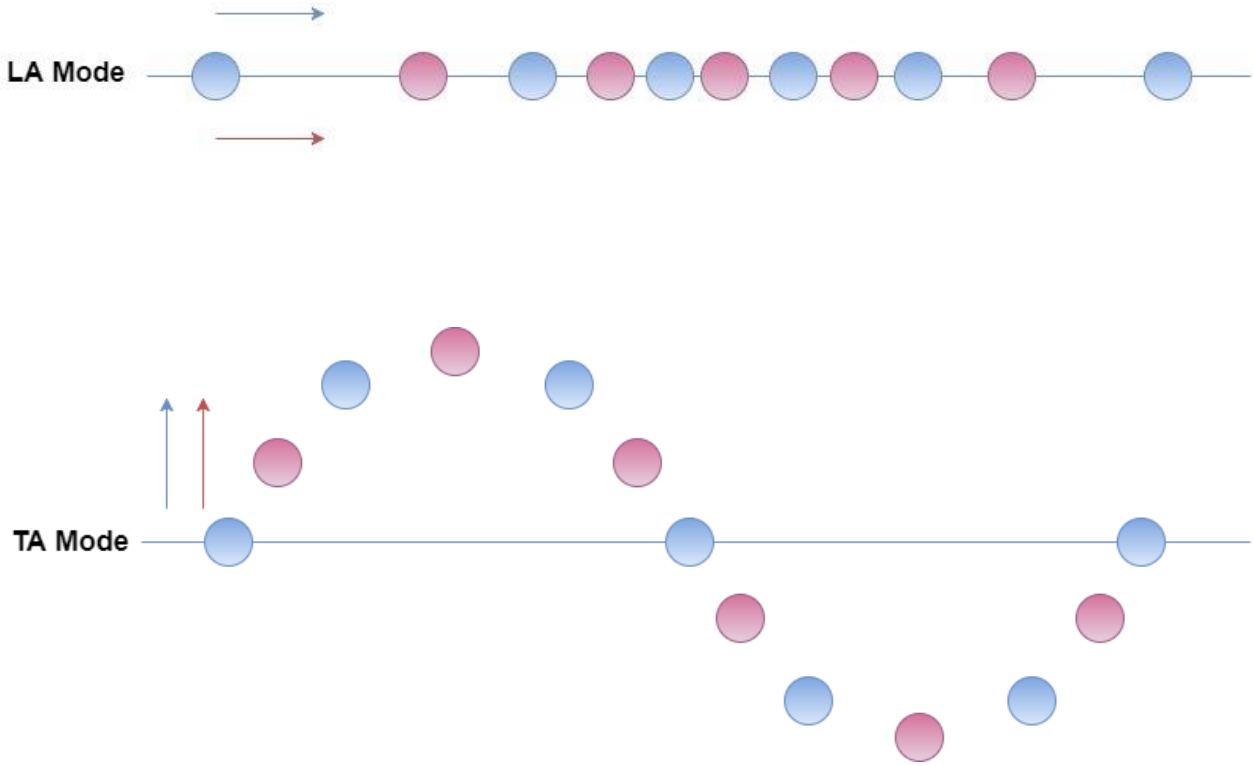

Figure 2.3: Longitudinal and Transverse modes of acoustic phonon

2.3.1.2 Optical phonons

Optical phonon is due to the out-of-phase movement of the atoms in the lattice when one atom moves in a particular direction and its neighboring atom moves in the opposite direction. Lattice that contains atoms of different charge and mass experience this type of phonons.

In crystals, optical phonons are excited by electromagnetic radiation. The electric field of the light guides the positive cations to the direction of the field, and the negative anions to the opposite direction. The movement of these ions causes the crystal to vibrate and hence creates time-dependent electrical dipole moment. This type of vibration is defined as optical phonons and can exist as either transverse mode (TO), in which the vibrations do not produce any polarization effects, or longitudinal mode (LO), where long range electric fields due to polarization is produced as illustrated in Figure 2.4.

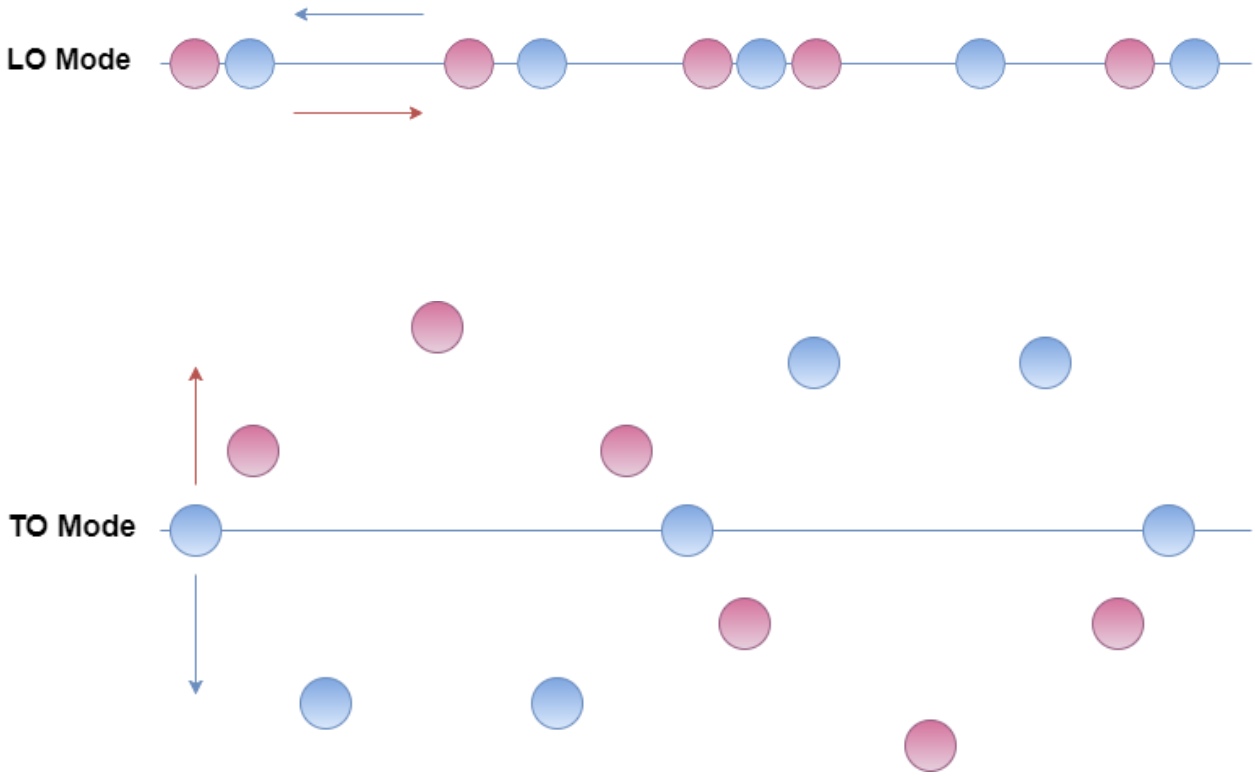

Figure 2.4: Longitudinal and Transverse mode of optical phonons

2.4 Raman spectroscopy of UO_2

According to Yun *et al.* [94] & Livneh *et al.* [95], UO_2 has only one Raman-active mode which occurs at 13.8 THz on its phonon dispersion curve as indicated by the red arrow in Figure 2.5. The latter corresponds to 445 cm^{-1} as shown on its Raman spectra. This peak is referred as the symmetry Raman-allowed phonon scattering of UO_2 and is the signature of compounds sharing the Fm3m space group.

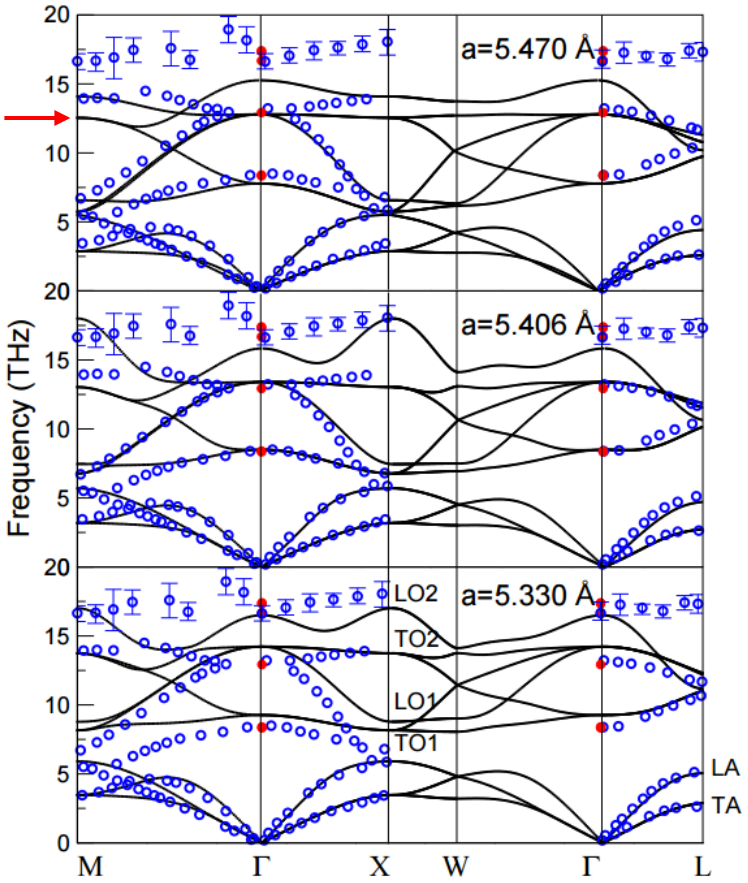

Figure 2.5: Calculated (Color line) and measured phonon dispersion curves (Open symbols) of UO_2 along the high-symmetry directions in the face cubic centered FCC Brillouin zone for different lattice constant values. The notation of the points is M: (1,1,0), Γ: (0,0,0), X: (1,0,0), W: (1,½,0) and L: (½,½,½) [94]

Figure 2.6 shows a typical low frequency Raman spectrum for an acquisition between 300 cm^{-1} to 700 cm^{-1} for a non-irradiated UO_2 (heat treated at 1700°C under 5% Ar/H_2 atmosphere during 4 hours) using a 633 nm red laser. The 300-700 cm^{-1} spectral range was selected because most of the irradiation-induced changes occur in this region.

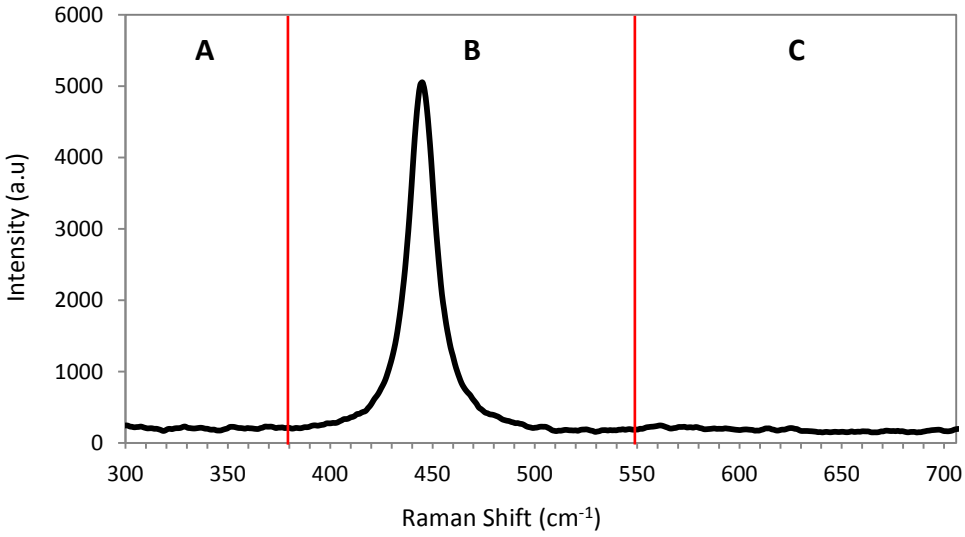

Figure 2.6: Raman spectrum of a fresh stoichiometric UO_2 pellet

The figure shows that the UO_2 spectrum can be divided into three main regions; namely zone A (300-380 cm^{-1}), zone B (380-560 cm^{-1}) and zone C (560-700 cm^{-1}). No major apparent peaks appear in zones A and C. The peak with the highest intensity is observed at 445 cm^{-1} in zone B. As explained earlier, it is the only Raman active mode which is allowed in oxides exhibiting the fluorite structure and is referred as the symmetric T_{2g} vibration mode [[96]- [97]]

However over a larger spectral range, other peaks can also be observed. For instance, Figure 2.7 shows the difference in the Raman spectra when the same unirradiated pellet was characterized by a 532 nm green laser and 633 nm red laser. It can be seen that the green laser induces a peak with a high intensity at 575 cm^{-1}. Livneh *et al.* [95] reported that the peak could be due to a resonant Raman phenomenon on the T_{1u} LO UO_2 mode. Thus to avoid this resonant effect, the 633 nm red laser will be employed for all Raman characterizations of the nuclear fuels in this study. In addition, it is also important to note that the red laser allows a higher probing depth compared to the 532 nm green laser.

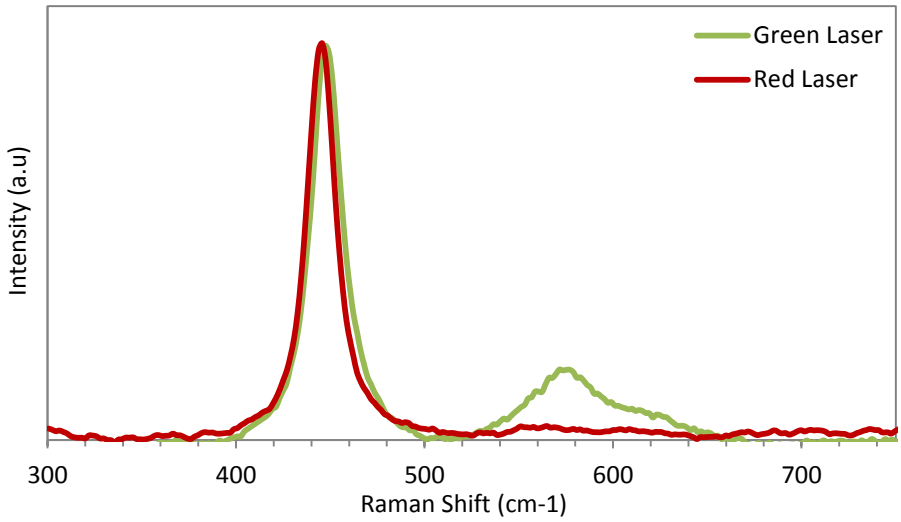

Figure 2.7: Raman spectra of a virgin UO_2 pellet obtained from a green laser (532 nm) and red laser (633 nm)

Furthermore, Table 2.1 provides an overview of the different bands observed in the literature when a virgin UO_2 was analyzed with different excitation sources.

Table 2.1: Reported values of the observed bands in UO_2

Excitation Wavelength (nm)	**Raman Shift (cm^{-1})**	**Reference**
488	450, 585, 1595	Senanayake *et al.* [98]
488	445, 585, 920, 1150	Senanayake *et al.* [98]
514	448, 630, 1104, 1152	Graves [99]
514	445	Allen [100]
514	232, 445, 1151	Manara *et al.* [101]
785	445, 583, 640, 1160, 1360	Senanayake *et al.* [98]

Livney *et al*. [95] proposed an attribution of most of the peaks mainly to the weak unauthorized modes or mixed modes.

2.5 Raman measurements of irradiated UO_2

The damage that occurs during irradiation modifies the crystalline structure of a solid, causing a change in the lattice vibrations of the crystal. Raman spectroscopy determines the lattice vibrational mode and any changes of the Raman modes parameters, such as wavenumbers, polarization, widths, band shape and their intensities directly; reveal any structural modifications in the crystalline structure.

In a perfect crystal, the phonons lifetimes are theoretically infinite, thus vibrations are defined as harmonic functions. However, defects (irradiation defects, low angle grain boundaries and cracks, amorphous regions etc.) act as anharmonic perturbations and lead to a finite phonon lifetime. They manifest themselves as additional peaks on the spectra and may also cause a broadening of the first-order Raman peaks described by its full-width at half maximum (FWHM) [102]. The following section is solely devoted to understand how the Raman spectra are modified in the presence of irradiation defects.

Figure 2.8 shows the Raman spectrum obtained when UO_2 pellets were irradiated with 25 MeV alpha ions at room temperature. Compared to Figure 2.6, it can be observed that the implantation results in a decrease in the T_{2g} peak intensity which is accompanied by an increase in its FWHM. These observations are consistent with the local disorder and changes in bond lengths (atomic effects) that take place during ionic implantation [102].

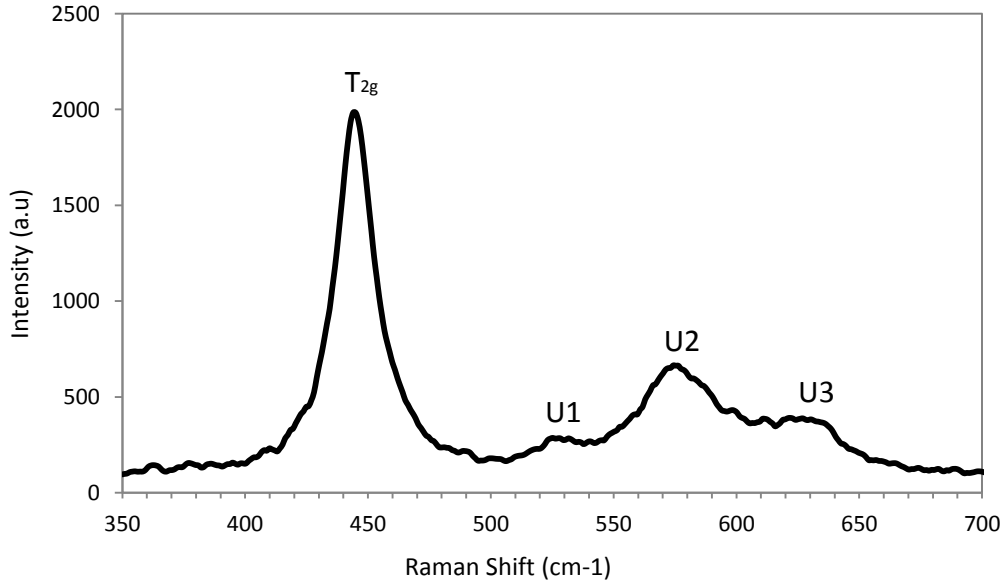

Figure 2.8: Modified Raman spectrum of UO_2 when implanted with alpha ions. The T_{2g} peak and the formation of the triplet defect peaks due to irradiation can be observed (characterized by the 633 nm red laser)

Another striking observation is the apparition of three additional peaks in the 500-700 cm^{-1} spectral range and are denoted as U1 (~527 cm^{-1}), U2 (~575 cm^{-1}) & U3 (~635 cm^{-1}). According to Guimbretière *et al.* [103], these peaks are referred as the Raman triplet defect bands and are characteristics to irradiation damages. It is worthy to note that the defect bands appear for any given irradiation conditions as illustrated in the figure below.

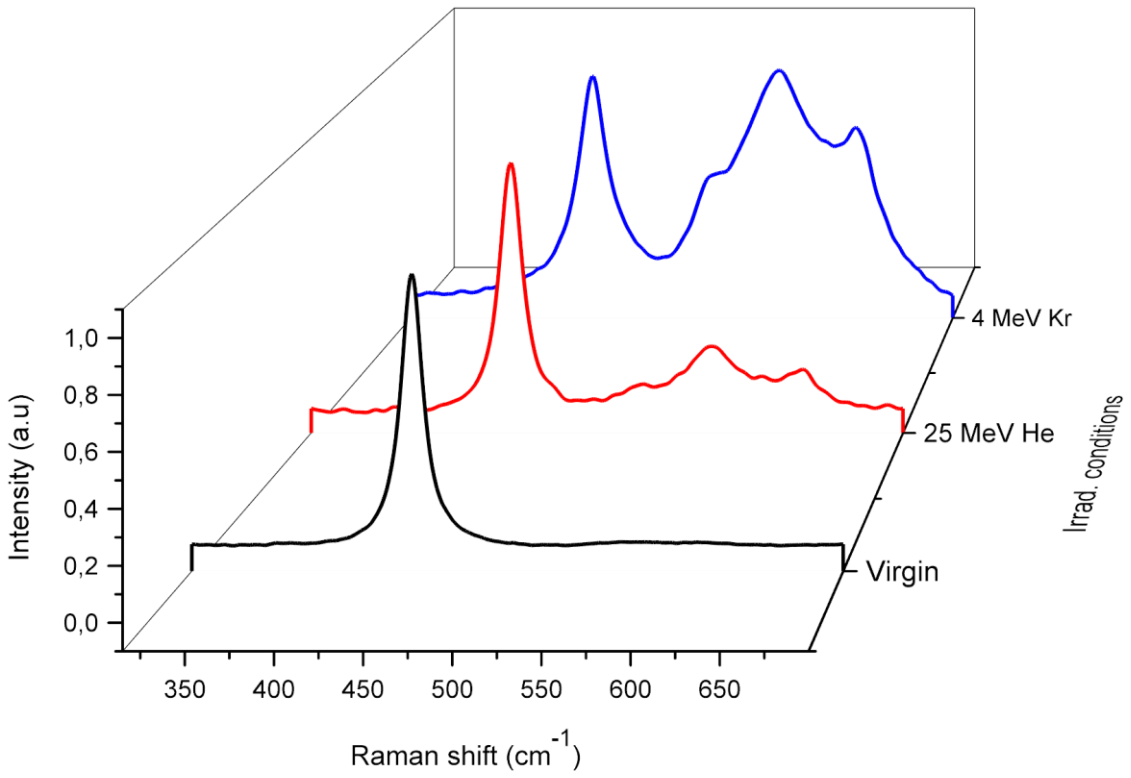

Figure 2.9: Comparison of the Raman spectra of UO_2 subjected to different irradiation conditions

Guimbretière *et al.* [103] provided an interpretation of the nature of the Raman defect bands. The authors attributed the U1 (~527 cm^{-1}) peak to a Raman signature associated with sub-stoichiometry UO_{2-x}. The U2 (~575 cm^{-1}) appeared at the same position as the Raman forbidden T_{1u} LO phonon as observed in a virgin UO_2. The presence of irradiation defects induces a breakdown in the selection rules which allows the T_{1u} LO mode to become Raman active. The U3 (~635 cm^{-1}) was assigned to a structural defect related to the cuboctahedra symmetry of the U_4O_9 crystalline structure. Figure 2.10 shows that the Raman peak of the U_4O_9 phase appears at the same position as the U3 band.

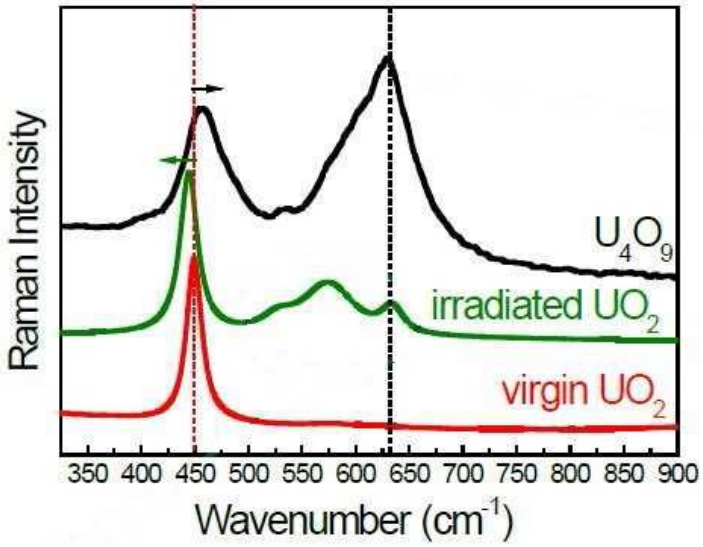

Figure 2.10: Comparison of the Raman Spectra of a virgin UO_2, irradiated UO_2 with 25 MeV alpha ions and U_4O_9

The Raman triplet defect bands have also been evidenced in irradiated PuO_2 as illustrated in Figure 2.11. It was observed that the positions of the defect bands do not change when different excitation sources were used for the Raman measurements.

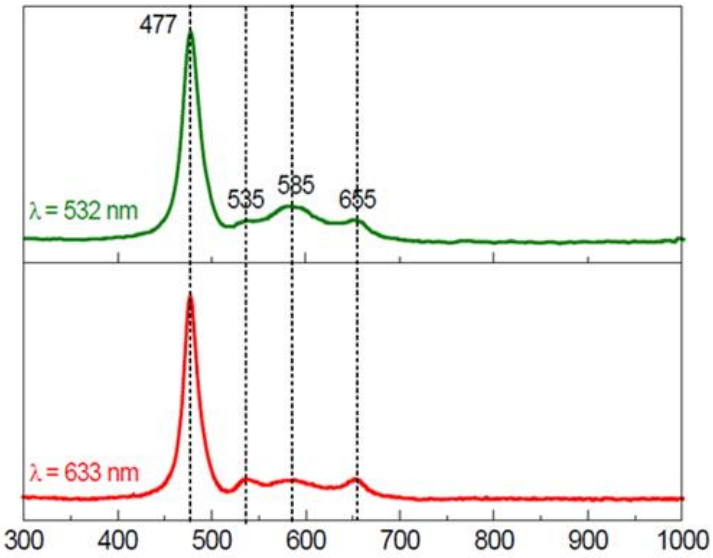

Figure 2.11: Raman spectra of PuO_2 characterized with the 633 nm (red laser) and 532 nm (green laser) respectively [104]

Referring to Figure 2.6 and Figure 2.8, it can be seen that the accumulation of irradiation defects decreases the T_{2g} intensity but increases the T_{2g} width. Recently, Guimbretière *et al.* [105] carried out a study to investigate the temperature effect on the T_{2g} position (ν_{2g}) and T_{2g} width (σ_{2g}) of a UO_2 disk.

From Figure 2.12, it can be seen that the T_{2g} line tends to move to shorter wavenumbers while the width shows a continuous increase at higher temperatures. The figure also indicates the increase in the T_{2g} width observed during the 25 MeV alpha irradiation of a UO_2 disk (illustrated as the grey horizontal lines). Thus by comparing the irradiation and the temperature influences, the T_{2g} width is more sensitive to a change in temperature. Finally, the authors showed that the temperature effect on both parameters (position and width) can be expressed as a second and third order polynomial function, such that:

$$\Delta\nu_{2g}(T) = 0.27 - 0.01T + (2.27 \text{ x } 10^{-5})\, T^2 - (2.4 \text{ x } 10^{-9})\, T^3 \tag{2.8}$$

$$\sigma_{2g}(T) = 16.2 + (3.1 \text{ x } 10^{-2})\, T + (1.1 \text{ x } 10^{-5})\, T^2 \tag{2.9}$$

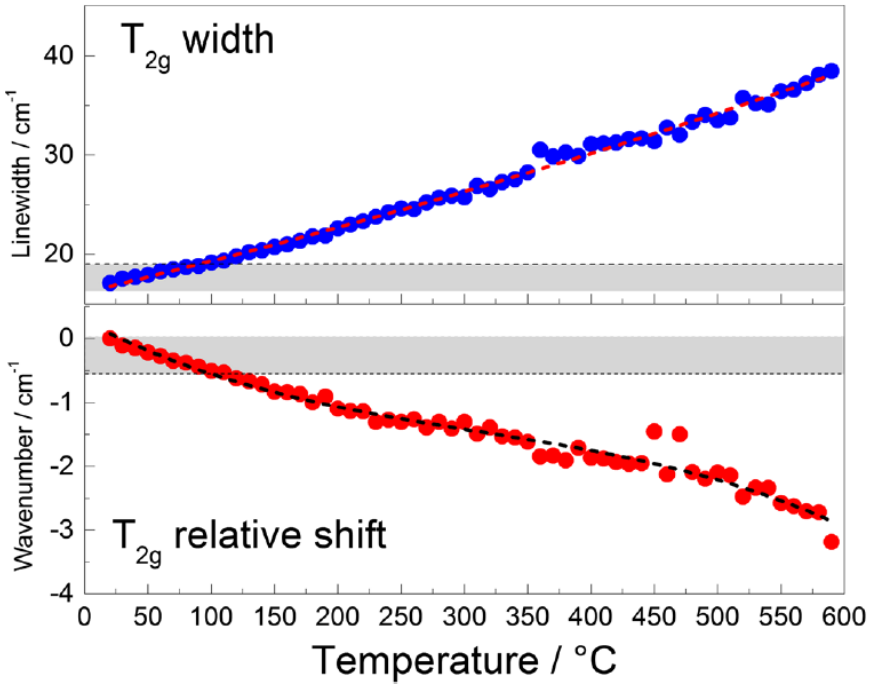

Figure 2.12: Temperature dependency of the T_{2g} peak, in terms of its width and position shift

2.5.1 Formation kinetics of Raman triplet defect bands

In another study, Guimbretière *et al.* [106] investigated the formation kinetics of the triplet defect peaks. The authors irradiated a UO_2 disk with 45 MeV alpha ions and 50nA ion current in an Ar/H_2 environment. The irradiation was carried out at different sequential time intervals. The thickness of the UO_2 was chosen such that the helium ions leave the disk at 5 MeV, which represents the natural radioactive decay of an alpha emitter. The alpha ions pass through the UO_2 disk and are attenuated in the argon gaseous medium. The interaction of the alpha ions with the argon gas generates an Ar-plasma ray as shown in Figure 2.13.

A Raman probe was placed at the back of the irradiation cell to characterize the sample during irradiation. The thickness of the argon contact gas was largely sufficient to attenuate all the alpha ions and protect the Raman probe-head from the ion-beam irradiation.

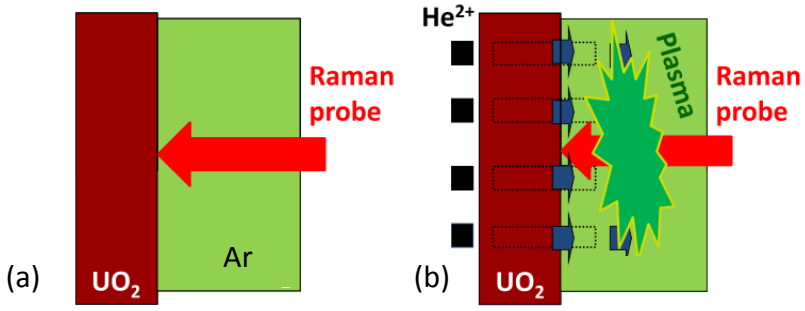

Figure 2.13: Raman characterization of UO_2 in contact with argon gas *(a)* without irradiation *(b)* under ionic irradiation and generation of Ar-plasma

The authors demonstrated that the kinetics of the triplet defect peaks can be modelled using a simple Direct Impact (DI) model which relates the concentration of defects (ρD) and the alpha dose (Dα). Weber *et al.* [107] proposed a similar interpretation of the DI model which can be used to study the kinetics of irradiation defects in UO_2 under alpha irradiation. The proposed model can be described as:

$$d\rho_D/dD_\alpha = R_\alpha - B\rho_D \quad (2.10)$$

Where:

R_α = number of irradiation defects (I.D) produced per unit path length travelled by alpha particle (I.D/cm.α)

$B\rho_D$= annihilation term describing the recombination of the irradiation defect.

The parameter B defines the annealing/elimination constant in (cm^2/α) while ρ_D is in I.D/cm^3 and is obtained by:

$$\rho_D = \rho_D(\infty)\, x\, (1 - e^{-BD_\alpha}) \tag{2.11}$$

$\rho_D(\infty)$ is the measured value of ρ_D at the saturation phase.

Figure 2.14 shows the experimental results obtained (black dots) during irradiation and fitted with the DI model (red line). The annealing constant (B) from the fit was determined to be $10^{-16} \pm 10^{-17}$ cm^2/α and is consistent with the 0.85 x 10^{-16} cm^2/α value reported by Weber *et al.* [107].

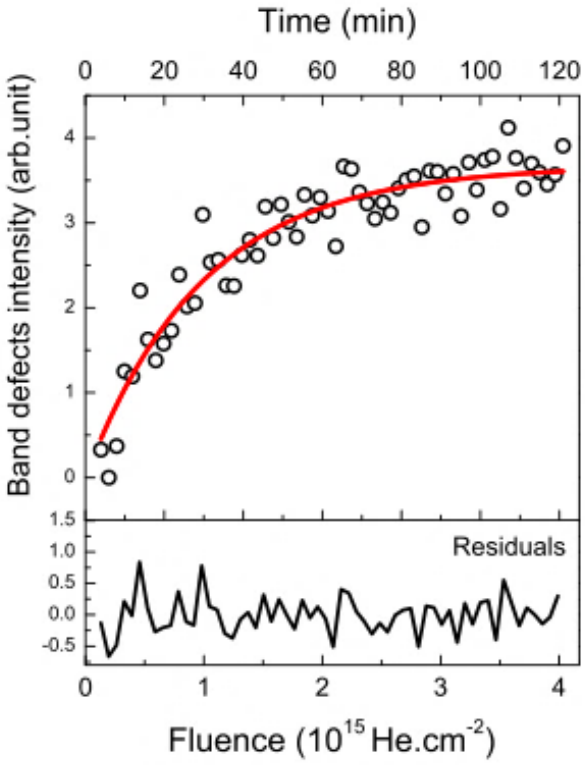

Figure 2.14: Kinetic rates of the defects bands. Black circles show the experimental results and the fit of the DI model is illustrated by the red line

2.5.2 Annealing of Raman triplet defect bands

Desgranges *et al.* [108] studied the annealing behavior of the irradiation-induced peaks under high temperature conditions. A UO_2 pellet was firstly irradiated with 25 MeV He^{2+} ion beam under vacuum during 2 hours to reveal the triplet peaks on its Raman spectrum. Post-irradiation, the irradiated sample was heated at higher temperature and then cooled to room temperature before a Raman acquisition was carried out.

Figure 2.15 (a) shows the evolution of the triplet defect peaks under the influence of temperature. It can be seen that the irradiation-induced signal was reset to zero after the irradiated UO_2 was heat treated at 525°C. Hence, Raman spectroscopy shows that the annealing temperature of the defects lies between 375 and 525°C. This observation is however different to the data reported by Labrim *et al.* [109] and Weber [110] in alpha irradiated UO_2, CeO_2 and PuO_2 disks.

The effect of high temperature irradiation of UO_2 was also investigated (Figure 2.15 (b)). In this study, it was observed that the annealing temperature was altered in the 575°C- 675°C range. The Direct Impact model (Equation 2.10) was used to explain this dissimilarity in the annealing temperature. In the absence of alpha beam, the irradiation defect production rate is non-existent ($R\alpha = 0$) and the annealing rate constant (B) depends on the annealing temperature of the defects. Consequently, all the pre-existing defects are annealed between 375 and 525°C.

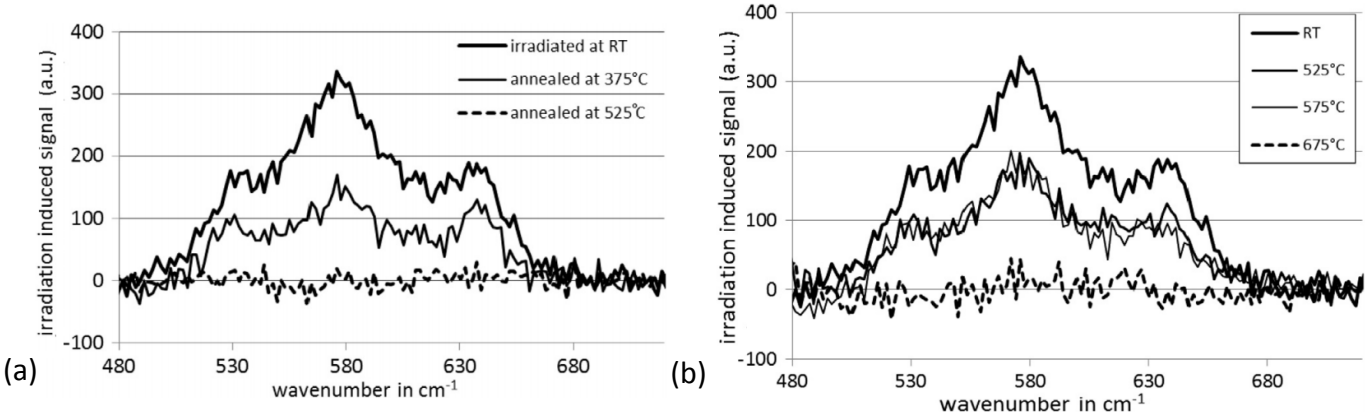

Figure 2.15: *(a)* Evolution of irradiation induced signal as a function of the annealing temperature. *(b)* Behavior of the irradiation induced signal for different irradiation temperatures

Under the effect of irradiation, the defect creation rate is much higher than that in the absence of irradiation, i.e. $R\alpha \neq 0$. Thus, higher temperature and annealing rate constant (B) values are required to completely anneal the defect concentration. Based the information provided in the above sections, Raman spectroscopy can be viewed as a new characterization method for acquiring important information regarding irradiation defects in nuclear fuels.

2.6 Raman measurements of secondary altered phases

The previous sections were devoted to describe the application of Raman spectroscopy for the analysis of irradiation defects in nuclear fuels. On the other hand, Raman spectroscopy can also be used to identify the secondary altered phases that are formed during a nuclear fuel matrix-water interaction.

Amme *et al.* [89] developed a complete Raman database for a number of alteration products that are more likely to be formed during both interim and final storage of SNF. The characteristics of the secondary phases considered by the authors are summarized in Table 2.2. The compounds analyzed were obtained either in their natural form or fabricated from uranyl nitrate ($UO_2 (NO_3)_2$) under different conditions.

Table 2.2: UO_2 alteration products considered by Amme e*t al.* [89]

Product	Formula	Color
Uranium dioxide	UO_2	Black
Coffinite	$USiO_4$	Black
Becquerelite	$Ca ((UO_2)6O_4(OH)_6)$	Yellow
Schoepite	$(UO_2)(OH)_2.xH_2O$	Yellow
Uranophane	$Ca(UO_2)SiO_3(OH)_2.5H_2O$	Yellow
Na-Botlwoodite	$(H_2O)Na(UO_2)(SiO_4)$	Yellow
Soddyite	$(UO_2)2SiO_4.2H_2O$	Yellow
Studtite	$UO_4.xH_2O$	Yellow

Most of the samples were characterized with NIR Raman (Near-infrared laser: 785 nm or 1084 nm). The U(VI) compounds (yellow in color) yield a good spectral resolution. On the other hand, the darkly colored samples were analyzed using an Argon laser (514 nm) because they tend to absorb NIR light resulting in Raman spectra of poor quality.

Figure 2.16 indicates that the yellow colored compounds show a strong signal at the vicinity of 800 cm^{-1}. The latter can be attributed to the symmetrical axial stretching of the uranyl ions $(UO_2)^{2+}$.

According to Weidlein [111], the position of the uranyl ions in the Raman spectra vary according to the type of bonding in which they are involved. In addition, minor peaks corresponding to the U-O bending mode and equatorial U-O stretching vibrations can also be distinguished in the 300-500 cm^{-1} spectral range.

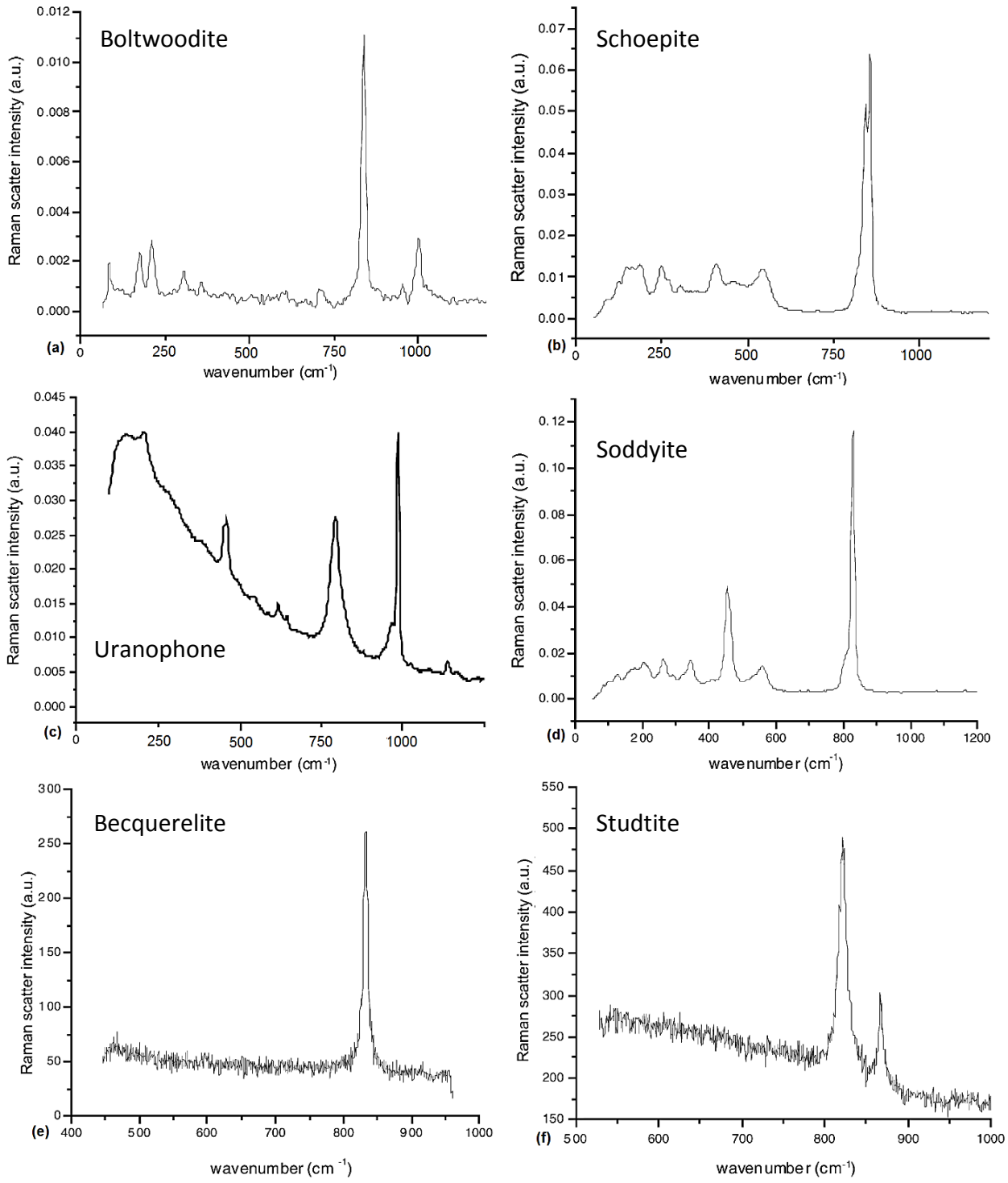

Figure 2.16: Raman spectra of yellow colored compounds. *(a)* Synthetic Boltwoodite, *(b)* Synthetic Schoepite, *(c)* naturally occurring Uranophane, *(d)* Synthetic Soddyite, *(e)* Synthetic Becquerelite and *(f)* natural Studtite. All the measurements were carried out using a 1064 nm laser source.

During the interim storage of SNF, only schoepite and studtite are expected to occur. Figure 2.16 (b) shows that schoepite is characterized by the presence of a double peak which is due to the presence of uranyl ions at two non-equivalent sites. The studtite spectrum also indicates the presence of two different peaks, occurring around 819 cm^{-1} and 865 cm^{-1}. They can be attributed to the axial stretching of the uranyl ions (UO_2^{2+}) and peroxide ion (O_2^{2-}) in the studtite phase.

In regards to the darkly colored samples, the Raman spectrum of pure UO_2 powders is shown in Figure 2.17 (a). The T_{2g} peak, related to the U-O stretching mode, appears at 445 cm^{-1} and the small band occurring near 400 cm^{-1} can be due residual compounds contained in the UO_2 powders after the fabrication process. Figure 2.17 (b) shows that the coffinite spectrum has a strong Raman signal at 1150 cm^{-1}. The latter corresponds to the silicate vibrational mode and is analogous to zircon ($ZrSiO_4$). Thus in this study, the Raman database reported by Amme *et al.* [89] can be taken as reference for the identification of secondary U(VI) phases during leaching experiment as it will be further discussed in Chapter 5.

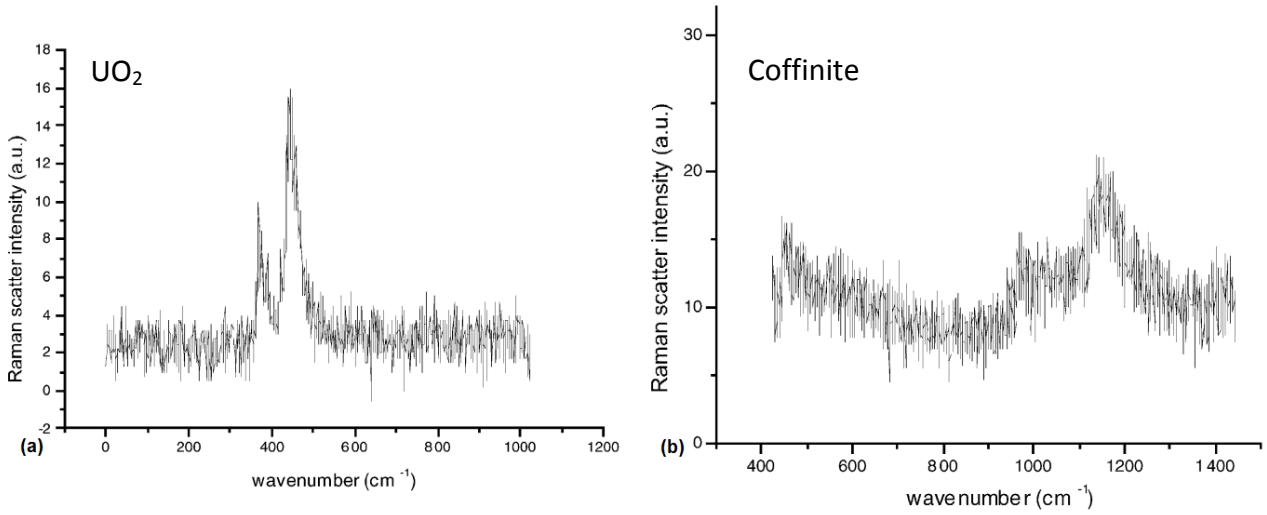

Figure 2.17: Raman spectra of dark compounds. *(a)* Synthetic UO_2, *(b)* Synthetic coffinite. Characterizations were carried out using 514 nm VIS laser

2.7 Motivation of the thesis

This study is an integral part of the Research Program on the Long Term Behavior of Spent Nuclear Fuel (abbreviated and referred as PRECCI in French). The aim of the program is to study all types of scenarios relevant to the back-end nuclear fuel management. As part of the project, it is necessary to evaluate the possibility of storing the unprocessed irradiated spent nuclear fuels in pools for an extended period with the general objective to be recycled for the next generation fast reactors.

In this study, an incidental scenario of a damaged fuel rod stored in water pool after in-reactor operation is considered. The physical cladding failure creates a pathway through which water is allowed to enter and interact with the irradiated fuel matrix as illustrated in Figure 2.18. Considering the water chemistry in pools (acidic aerated water (pH: 5-5.5), slightly high temperature (60-90°C) and the irradiation dose from the adjacent fuel assemblies), one can expect the alteration of the irradiated fuel matrix at the defect point through oxidizing dissolution and precipitation of oxidized secondary phases on the altered surface.

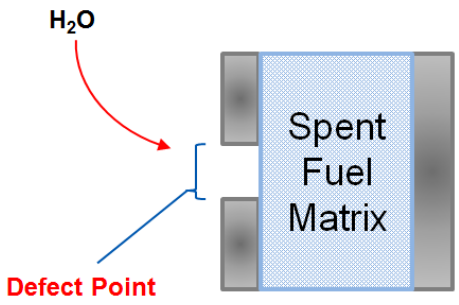

Figure 2.18: Schematic representation of a defective fuel rod and the defect point where the *"Fuel Matrix-Water interaction"* takes place

A thorough literature review has provided a clear overview regarding the UO_2 leaching behavior and the mechanisms of formation of secondary U(VI) phases in the conditions expected during both interim storage (aerated environment) and final disposal environment (anoxic). However, relevant data regarding MOX fuels needs to be further gathered. Furthermore, till now there have been no previous studies devoted to understand the irradiation defects during a potential interaction between the fuel matrix and water.

Amongst the different characterization techniques, Raman spectroscopy has recently put into evidence the existence of a specific signature, referred as "triplet defect bands" which is characteristic to irradiation defects in UO_2. Although several studies have been focused towards

the understanding of the triplet defect bands, addition information are still required to provide a more conclusive interpretation regarding the exact origin of the Raman defect bands.

The aim of this thesis is to carry an in-depth analysis of the triplet defect bands in order to investigate how this Raman signature can be used to characterize actual spent nuclear fuels stored in pools. In this context, three main fields of study were defined, namely to;

1. **Identify the type of irradiation defects responsible for the apparition of the Raman triplet defect bands**

An electron irradiation experiment of sintered UO_2 disks was necessary in order to investigate the origin of the triplet defect bands. The goal of this study is to correlate the triplet defect bands either to the electronic or ballistic interactions of the incident ions with the target UO_2 atoms. An attempt is then made to identify the irradiation-induced defects that are signatures of the triplet defect bands. Chapter 4 is devoted to the electron irradiation experiment.

2. **Investigate the behavior of the Raman triplet defect bands during UO_2 leaching under oxidizing conditions**

The formation kinetics of irradiation defects in UO_2 under alpha irradiation was then studied using a unique *in situ* Raman experimental set-up. This experiment is devoted to quantify the role of irradiation defects in UO_2 when exposed to different interfaces, especially in the presence of aerated water to simulate a possible "*Fuel Matrix-Water interaction*". Furthermore, the study was extended to characterize the alteration mechanisms of the UO_2 matrix. The UO_2 leaching under alpha irradiation is detailed in Chapter 5**.**

3. **Study the effect of chemical doping and microstructure on the Raman triplet defect bands**

In regards to actual MOX fuels, it was necessary to understand the effect of chemical doping and microstructure on the apparition of the triplet defects bands. The motivation of this study is driven by the complex microstructure of MOX fuels. However, due to radiological constraints, heterogeneous (U, Ce)O_2 and homogeneous (U, Th)O_2 samples will be used to simulate the characteristics of MOX fuels under laboratory conditions. This is dealt with in Chapter 6.

The fuel samples and experimental installations that were employed to meet the targeted objectives are presented in the following chapter.

Chapter 3

Fuel samples and experimental installations

3.1 Introduction

This chapter reviews the principles of the experimental techniques used for the need of this study. The objectives of the current project are focused on the Raman triplet defect bands, characteristics of irradiation damages in nuclear fuels. As previously described in Chapter 2, three main areas of study were identified, namely;

1. To conduct an in-depth analysis of the Raman triplet defect bands
2. To compare the kinetic formation of the Raman defect bands in the presence of a chemically inert and reactive environment
3. To investigate the effect of microstructure on the apparition of the Raman defect bands

A series of experiments were carefully designed to meet the targeted objectives. To identify the type of irradiation defects responsible for the apparition of the Raman triplet defect bands, an electron irradiation of several UO_2 disks was conducted. The experiment aimed to correlate the Rama defect bands either to the electronic or nuclear stopping power.

The kinetic formation of the Raman triplet defect bands was then investigated using an external alpha irradiation source to simulate the alpha decay of SNF. The irradiation experiment was carried out under different experimental set-ups; UO_2 in contact with (a) aerated water and (b) a chemically inert medium (argon). The study was intended to determine whether the formation kinetics of the irradiation-induced Raman bands vary according to the irradiation conditions.

The field of study was also extended to investigate the Raman triplet defect bands in MOX fuels, driven by their highly complex heterogeneous microstructure. However due to the glove box requirements for the handling of plutonium-containing materials, MOX fuels could not be used

in the experimental set-up developed for the need for this study. Thus to replicate MOX fuels under laboratory conditions, UO_2 doped with compounds, such as cerium and thorium, were used as surrogate nuclear fuels.

Although Raman spectroscopy was used as the main characterization tool, complementary techniques such as X-ray diffraction and Positron Annihilation Spectroscopy were also used to provide relevant information regarding the irradiation-induced damages/or changes in the nuclear fuel samples.

This chapter aims to provide a complete description of the different ion implantation installations and characterization techniques that were used for in this study. However, it is important to note that each irradiation campaign consisted of its unique experimental set-up and irradiation conditions. More specific information regarding the experimental procedures and their associated parameters are provided in the subsequent chapters.

3.2 Sample preparations

The following section is intended to present the methodologies involved during the fuel fabrication process. Sintered UO_2 ceramics were manufactured at the Laboratoire des Combustibles Uranium (LCU) at CEA-Cadarache and were intended for the electron irradiation experiment and leaching study under alpha irradiation. In addition, to simulate MOX fuels, several (U, Th)O_2 and (U, Ce)O_2 solid solutions were manufactured at the Institut de Chimie Séparative de Marcoule (UMR 5257 CEA, CNRS, ENSCM, Univ. Montpellier), in the Laboratory of Evolving Interfaces in Materials.

3.2.1 Preparations of UO_2 samples

Sintered UO_2 disks were fabricated using UO_2 pellets (0.2 at.% U-235) at CEA-Cadarache. The pellets used were initially sintered using UO_2 powders at 1700°C during 24 hours under 95%Ar-5%H_2 environment and were 13 mm long with a diameter of 8 mm. A wire saw was used to cut the pellets into several disks. The disks were then glued using hot wax onto studs for the different polishing steps.

The first polishing step was carried out using a silicon carbide adhesive back disk sheet of different grain sizes (22 µm and 15 µm) which considerably reduces the thickness of the disks. After the first polishing step, the disks were then washed with distilled water in an ultrasonic bath and subjected to another polishing using a diamond abrasive (1 µm) cloth. This final polishing step delivers a mirror-polished surface which is important for characterization purposes. The disks were then peeled off from the studs and washed with acetone in the ultrasonic tank.

For the electron irradiation, the polishing steps were again repeated on the other side of the disks, i.e., both surfaces were mirror-polished. The thickness of the disks was reduced to ~500 ± 10 µm. On the other hand, UO_2 with only one mirror-polished surface and a thickness close to ~300 ± 2 µm were used for the leaching experiment under alpha irradiation.

A final annealing of the UO_2 disks was then carried out at 1400°C during 4 hours under reducing environment in order to maintain stoichiometry. This step also removes any surface damages and stresses induced during the different polishing steps. These annealing parameters were chosen because Guimbretière *et al.* [103] previously observed a grain boundary signal for UO_2 annealed at 1700°C. The signal appears at 555 cm^{-1} on its Raman spectrum. Thus, it was important to avoid the grain boundary signal because it lies in the range where the triplet defect bands are expected to occur during irradiation.

It is to be noted that the density of the UO_2 disks used in this study remained close to 98% of the theoretical density, i.e., approximately 10.63 g/cm^3.

3.2.2 Preparations of mixed fuel oxides

In reference to the French scenario and also in regards to the defective fuel rod as defined in Chapter 1 and Chapter 2, the field of study was extended to investigate the Raman triplet defect bands in MOX fuels. The objective was to determine the effect of microstructure on the apparition of the Raman defect bands.

MOX fuel is more radioactive than used UO_2, mainly attributed to the presence of plutonium. Their specific radioactivity should agree with confinement requirements and be handled under glove box environment. In order to develop an understanding regarding irradiation defects in $(U, Pu)O_2$ fuels, the contained alpha emitters such as Pu-238 and Pu-239 act as intrinsic sources to initiate irradiation damages. However, sufficient time is required for the alpha emitters to reach a targeted irradiation dose and defect concentration.

An external irradiation beam provides an alternative option to study the effect of irradiation defects in nuclear fuels. However, the application of an external irradiation source to MOX fuels is complicated considering their radiological constraints. Thus, UO_2-doped with compounds such as thorium and cerium were used in this study to simulate MOX fuels under laboratory conditions.

ThO_2 and CeO_2 were used as dopants because they form oxides with the same crystallographic structure and share comparable physico-chemical properties with UO_2 and PuO_2, as displayed in Table 3.1.

Table 3.1: Comparison of the physico-chemical properties of ThO_2, CeO_2 with that of UO_2 and PuO_2

Properties	**ThO_2**	**CeO_2**	**UO_2**	**PuO_2**
Space Group	Fm3m [112]	Fm3m	Fm3m	Fm3m
Lattice parameter (Å)	5.597	5.412 [113]	5.4707 [114]	5.386 [115]
Density (g/cm^3)	10	7,65	10,97	11,46 [116]
Melting point (C)	3200 [117]	2470 [118]	2875 [117]	2840 [119]
Thermal conductivity (at 700K)	4.78 [120]	2.85 [121]	3.85 [121]	7.30 [122]
Physical appearance	White solid	Pale chamois	Black solid	Yellow-brown

As part of this study, Chapter 6 will be devoted to determine whether irradiation induces the apparition of the Raman triplet defect bands in ThO_2 and CeO_2 such as to be in good agreement with irradiated UO_2 and PuO_2.

3.2.2.1 Preparation of (U, Ce)O_2 samples

In order to mimic the fabrication of MOX fuels, (U, Ce)O_2 samples were prepared at ICSM/LIME (Marcoule) by powder metallurgy. UO_2 and CeO_2 (initially obtained by oxalic precipitation then firing at 700°C under argon atmosphere) were then used as parent compounds. The two powders were weighed in order to reach final molar ratio of 10 mol.% in CeO_2 and mixed together by mechanical milling (30 Hz, 30 min.). The resulting compound was then shaped as 10mm-diameter cylindrical pellets by uniaxial pressing (P = 200 MPa). Finally, green pellets were turned into dense bodies by sintering under reducing atmosphere (Ar-2%H_2) at 1600°C for 8 hours.

The green pellets (10 cm long and a diameter of 8 mm) were then transported to the LCU lab at CEA-Cadarache. The (U, Ce)O_2 pellets were sectioned into several disks using the wire saw and then mirror-polished only on one surface for subsequent characterization purposes. For the need of this experiment, the final thickness of the (U, Ce)O_2 disks was reduced to 320 ± 5 µm with a sintered density close to 10.52 g/cm^3. The choice for such (U, Ce)O_2 dimensions will be further discussed in Chapter 6**.**

3.2.2.2 Preparation of (U, Th)O_2 samples

The (U, Th)O_2 solid solutions with different thorium doping content, ranging from 20% to 80% at a 20% interval level, were prepared at ICSM/LIME (Marcoule) using the wet chemistry method. This fabrication technique offers the advantage of having a sample with a homogeneous microstructure. The preparation is based on the formation of an initial oxalate precipitate when an aqueous hydrochloric solution containing the required amount of uranium and thorium was constantly stirred in a 1M oxalic acid solution. The oxalate solid solution precipitated with a known *x%* of Th as defined by the equation below:

$$(1-\mathrm{x})\mathrm{U}^{4+}{}_{(aq)} + \mathrm{x}\,\mathrm{Th}^{4+}{}_{(aq)} + 2\mathrm{H_2C_2O_4}{}_{(aq)} + \mathrm{yH_2O} \rightarrow \boldsymbol{U_{1-x}\,Th_x\,(C_2O_4)_2.y(H_2O)_{(s)}} + 4\,\mathrm{H^+}{}_{(aq)} \quad (3.1)$$

The reaction products were then washed with deionized water and ethanol, filtered and dried at 90°C. The precipitates were heat treated at 700°C during 8 hours in an alumina crucible under reducing Ar-2%H_2 conditions to deliver a solid solution with a high quality and purity powders, as indicated by Equation 3.2:

$$U_{1-x}\,Th_x\,(\mathrm{C_2O_4})_2.y(\mathrm{H_2O})_{(s)} \rightarrow \boldsymbol{U_{1-x}\,Th_x\,O_{2\,(s)}} + 2\mathrm{CO_{2\,(g)}} + y(\mathrm{H_2O})_{(g)} \quad (3.2)$$

The powders were then compacted by uniaxial pressing at 500 MPa using a hand press and the green pellets were then subjected to a final heat treatment at 1550°C during 8 hours in Ar-2%H_2 environment to increase the theoretical density up to 95%.

The characteristics of the solid solutions prepared at Marcoule are presented in the table below.

Table 3.2: Characteristics of (U, Th)O_2 solid solutions

Sample	Gross Mass (g)	Mass Th (g)	Mass U (g)	Activity (Bq)
$(U_{0.2}Th_{0.8})O_2$	3.14	0.64	0.17	6810
$(U_{0.4}Th_{0.6})O_2$	3.16	0.49	0.34	10460
$(U_{0.6}Th_{0.4})O_2$	3.11	0.31	0.47	12990
$(U_{0.8}Th_{0.2})O_2$	3.27	0.18	0.74	19220

In this work, the prepared disks were sectioned into two-half disks along their cylindrical axis as shown in Figure 3.1. This method enables to correlate the penetration profile of the ions along the depth of the samples with simulated data. A final polishing of the half-disks was necessary to ensure that they share the same characteristics as the initial bulk sample.

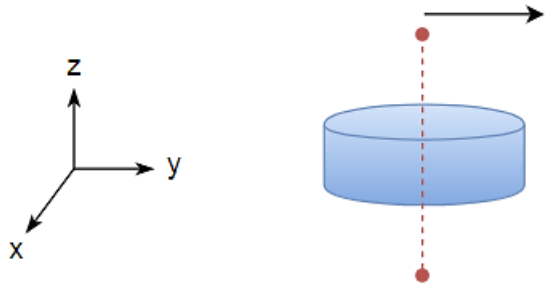

Figure 3.1: Shape of a typical sintered pellet before sectioning

3.3 Ionic implantation techniques

External irradiation is an alternative way through which the damages induced in nuclear fuels by fission products during nuclear operations and also the particles resulting from the radioactive decay of spent nuclear fuel can be investigated.

For the need of this study, several UO_2 samples were firstly irradiated with an electron beam. The experiment aimed to provide additional information regarding the Raman triplet defect bands, i.e., to correlate the defect bands either to the electronic or nuclear stopping power during the interaction of an incident ions with the target atoms. The ESTAR, Stopping Powers and Ranges for Electrons, database [123] were used to select the appropriate electron irradiation parameters.

On the other hand, an external alpha irradiation source was also used to simulate the alpha decay of irradiated nuclear fuels. The appropriate irradiation parameters were determined by the SRIM, Stopping and Range of Ions in Matter, simulation software [25]. Depending on the types of ionic implantation and corresponding energy, the code provides relevant information regarding the energy loss during the electronic and nuclear interactions of the implanted ions with target atoms. Additional information such as the Bragg's peak and maximum penetration depth of the ions can also be obtained.

The irradiation fluence is however essential because it defines the concentration of ions implanted in the target material and the resulting atomistic defects. Indeed with the SRIM software, it is possible to determine the concentration of cationic and anionic vacancies generated by the incident atoms. These data are then used to calculate the total displacements

per atom (dpa), which represent the number of times that the atoms in the target material are displaced in the damaged zone.

The dpa can be obtained by the following equation:

$$n_{\varphi}(dpa) = (n_{TRIM}\ x\ \varphi)\ \ x\ \left(\frac{A}{\rho\ x\ N}\right)\ x\ 10^{8} \tag{3.3}$$

Where:

n_{φ} = number of dpa

n_{TRIM} = displacement. $Ion^{-1}.A^{-1}$

φ = irradiation fluence (ions. cm^{-2})

ρ = density of the target material (g/cm^3)

N = Avogadro's number ($6.022\times10^{23}\ mol^{-1}$)

A = Atomic mass

SRIM software can also be used to simulate the trajectory of a projectile in a target material in which the atoms are arranged in a random manner. Based on the input parameters such as the ion type and energy (in the range 10 eV – 2 GeV) and the target material of one or several target layers, the code is allowed to generate stopping-power tables which can be used to determine the electronic and nuclear energy deposited in the target material. In addition, the code can also be used to provide an estimation for the atomic displacements, in terms of dpa, resulting due to ballistic collisions of the projectile with the target atoms.

As an example, during the alpha decay of nuclear spent fuels, alpha particles with kinetic energy of 5-6 MeV are emitted. A simulation of the 5 MeV alpha particles in a UO_2 target material shows that the incident ions lose most of their energy via inelastic interactions. The electronic stopping power (average loss of electronic energy of the particle per distance traveled) then decreases as the energy of the alpha particle is further decreased. Finally, the nuclear stopping power component becomes important at low energies as illustrated in Figure 3.2.

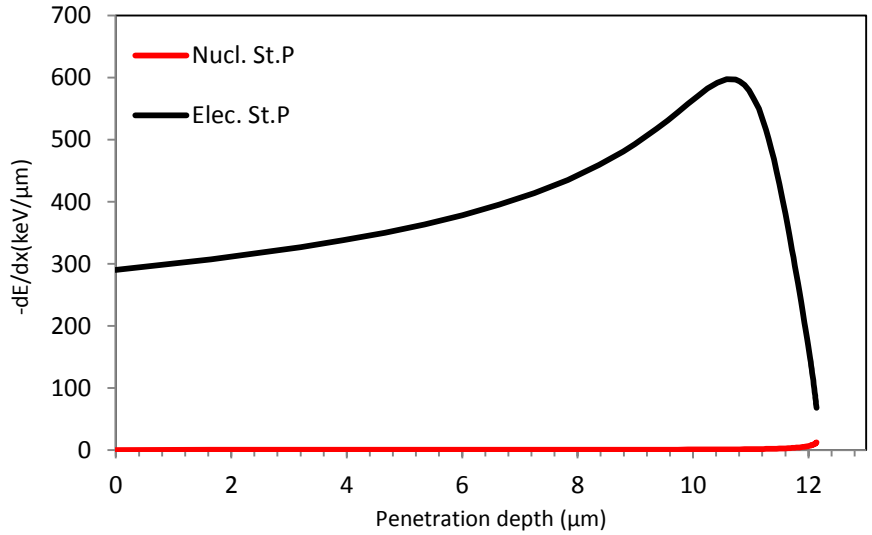

Figure 3.2: Electronic and nuclear stopping energy profile during the implantation of 5 MeV alpha particles in UO_2 obtained from SRIM software

Figure 3.3 shows the calculated implanted incident ions and induced atomic displacements profiles along the depth of the UO_2 target.

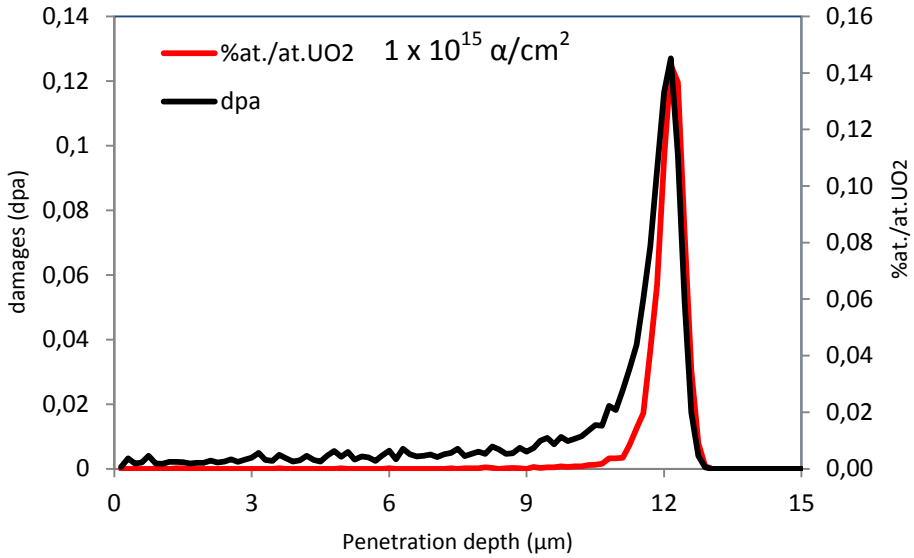

Figure 3.3: Incident ion implantation and damage profile during the implantation of 5 MeV alpha particles (fluence: 1 x 10^5 α/cm^2) in UO_2 obtained from SRIM software

All these information are very important especially in regards to the UO_2 leaching under alpha irradiation experiment. This is because the energy of the incident beam and the thickness of the UO_2 disk, both had to be dimensioned in such a way that the alpha ions are firstly allowed to irradiate the disk and also pass through the UO_2 to be attenuated in the aqueous solution to initiate the water radiolysis mechanisms.

The following sections aim to provide a description of the two accelerators that were used as the external irradiation sources to induce damages in the different pellets.

3.3.1 Electron irradiation source

The electron irradiation of UO_2 disks was performed at the Laboratoire des Solides Irradiés (LSI-Ecole Polytechnique/CEA/CNRS, Palaiseau) using the Pelletron SIRIUS Van de Graaff electron accelerator. The facility is able to function on a 24 hour basis without interruption and can hence attain sufficiently high electron charges. The accelerator allows irradiation to be carried out at different temperatures, ranging from -250°C to 100°C and under controlled atmosphere. The pressure in the irradiation chamber is kept relatively higher than 0.5 bars in order to avoid overheating of the sample during irradiation. In addition, the sample holder is designed such that several disks can be accommodated and irradiated at once.

In regards to UO_2, Soullard [124] reported the displacement threshold energy for both oxygen atoms (20 eV) and uranium atoms (40 eV). To attribute the Raman triplet defect bands to either the electronic or nuclear stopping power, the irradiation conditions were chosen such that to induce damages in both sub-lattices. In the present study, several UO_2 disks were irradiated at different energies in the range of 1.6-2.5 MeV. The irradiation campaigns were carried out at room temperature. The methodology for the data analysis to attribute the Raman triplet defect bands to the electronic or nuclear stopping power will be further discussed in Chapter 4.

Figure 3.4 and Figure 3.5 show a schematic diagram of the Pelletron SIRIUS Van de Graaff accelerator and the sample holder employed for the electron irradiation experiment.

Figure 3.4: Illustration of the Pelletron SIRIUS Van de Graaff electron accelerator

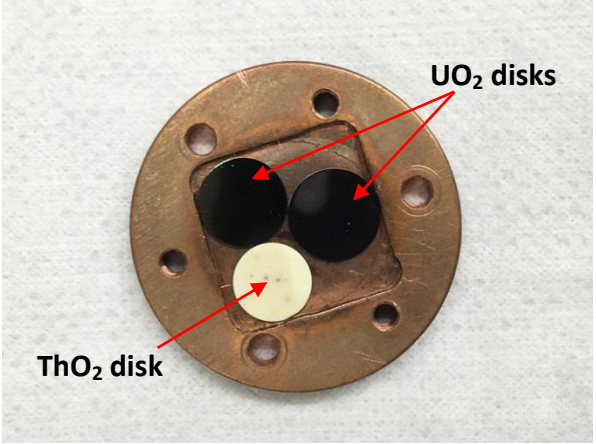

Figure 3.5: Sample holder capable of holding 3 disks (2 UO_2 + 1 ThO_2) during the electron irradiation

3.3.2 Alpha irradiation source

The alpha irradiation was carried out at the Conditions Extrêmes et Matériaux: Haute Température et Irradiation (CEMHTI, CNRS) on the Cyclotron facility. The facility only deals with the implantation of light ions such as deuterons, protons, helions, alpha particles and neutrons. The alpha irradiation of the different nuclear fuels was carried out using an isochronous cyclotron instrument.

The cyclotron facility is divided into the casemate cyclotron and the irradiation cell. The initial irradiation beam is produced in the casemate section which contains the cyclotron device along with a centered integrated ionization chamber that acts as the primary ion source.

The ions are accelerated by hollow electrodes called Dees as they follow a flight spiral path from the center towards the edges and the speed of the ions is increased as they move from one dee to another. The ions are then extracted out of the accelerator and projected on the target at a very high intensity. The configuration of the cyclotron accelerating device is presented in Figure 3.6. The CNRS uses a Cyclotron Model 680 that has a rated magnetic field of 1.53 T and is capable of delivering an alpha ion beam with a maximum energy up to 50 MeV at an intensity of 15uA on target.

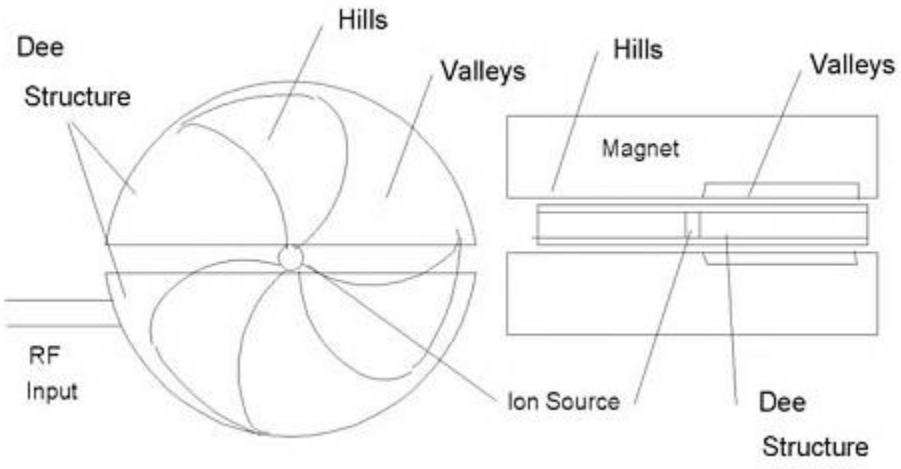

Figure 3.6: Configuration of the Cyclotron accelerating system

Depending on the purpose of the experiment, the accelerated beam can be diverted towards four main gates in the irradiation cell as illustrated in Figure 3.7. Gate 1 is devoted to all irradiation on target samples which are then followed by quick *ex situ* characterizations. Gate 2 is mainly used for sample analysis (both *in situ* and *ex situ*) during transmission experiments, while Gate 3 is used for the generation of radioactive isotopes for imaging. Gate 4 was previously used for medical purposes but is not operational at the present time.

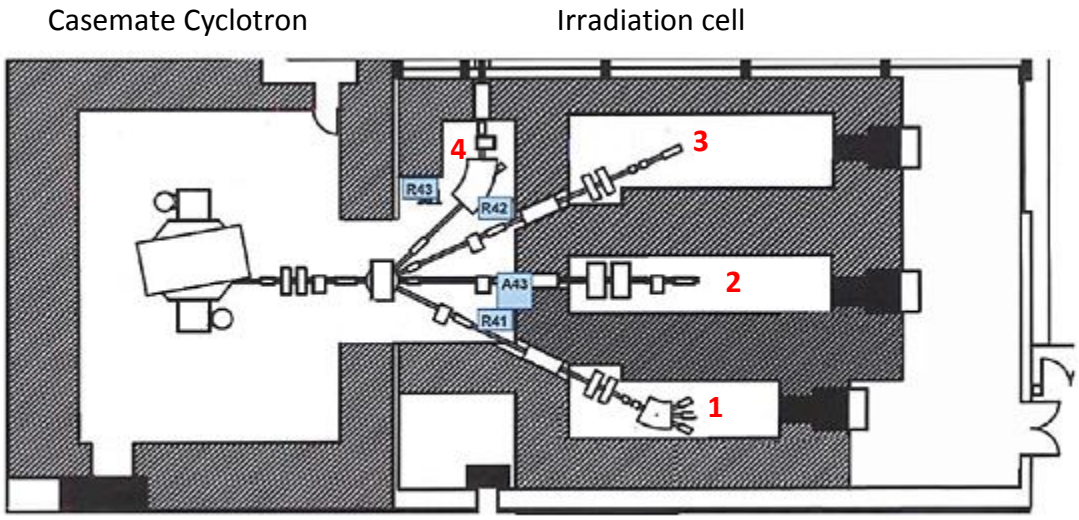

Figure 3.7: Schematic of the Cyclotron building at CEMHTI-CNRS showing the Casemate cyclotron and the four irradiation cells

As previously mentioned at the beginning of this chapter, different alpha irradiation conditions and experimental set-ups were employed over the course of the present study. For instance, Gate 1 was essentially used for the alpha irradiation and *ex situ* characterization of (U, Th)O_2 mixed oxides using the Dispositif d'Irradiation Appliqué aux MAtériaux du Nucléaire en Température (DIAMANT) installation. The latter will be further discussed in Chapter 6. On the other hand, the irradiation behaviour of UO_2 and (U, Ce)O_2 samples under both chemically reactive and inert environment was investigated through a use of a newly developed *in situ* Raman experimental set-up installed in Gate 2 (more information in Chapter 5).

3.4 Experimental characterization techniques

Raman spectroscopy, XRD and Positron Annihilation Spectroscopy (PAS) methods were used to analyze the as-prepared (virgin) and irradiated samples. It is to be considered that UO_2, being a highly absorbent material, restricts the probing depth of these characterization techniques to only few micrometers below the disk surface. Thus, Raman, XRD and PAS analyses can provide relevant information regarding the irradiation-induced damages/or changes arising near the UO_2 surface.

The Raman analysis of the samples was performed at CEMHTI-CNRS, Orléans. The Raman spectrometer uses a 632.8 nm He-Ne red laser and a 1800 grooves/mm holographic grating. These configurations were sufficient to allow a 2-3 cm^{-1} spectral resolution. As Raman spectroscopy was principally used in the present work, the following sections are devoted to present a complete description regarding the functioning of the Raman apparatus.

3.4.1 Raman spectroscopy

The Raman measurements were conducted through the use of two types of Renishaw Raman spectrometers; the portable RA-100 device and the microscope Invia Reflex spectrometer. The luminous RA-100 Raman spectrometer was used for all *in situ* analysis. A complete description of the *in situ* Raman experimental set-up will be provided in Chapter 5. The following paragraphs will mainly focus on the Renishaw Invia Reflex spectrometer, which is suited for *ex situ* measurements. A schematic of the Renishaw Invia Reflex spectrometer is shown in Figure 3.8.

Figure 3.8: Raman Renishaw Invia Spectrometer located at CEHMTI-CNRS, Orléans

As previously discussed in Chapter 2, Raman signals are relatively weak compared to the Rayleigh signals and there exists a small frequency variation with respect to frequency of the excitation source. Hence, an intense and monochromatic light source is required for an improved Raman acquisition. Therefore in Raman spectroscopy, a laser is today always used as the excitation source in order to increase the photon density.

Figure 3.9 illustrates the principle of the Renishaw Invia Reflex apparatus. The photons from the laser source are initially focused on the sample. The photons are absorbed and interact either elastically or inelastically. The re-emitted photons are collected and analyzed in order to extract the relevant information.

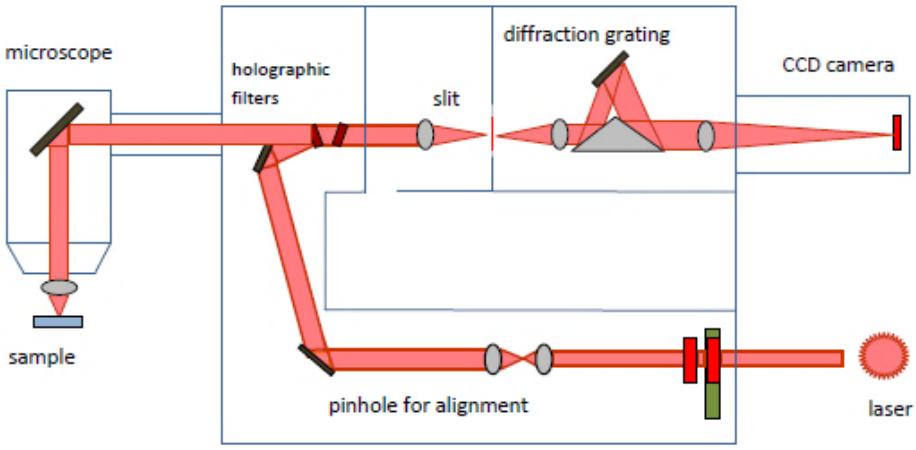

Figure 3.9: Detail illustration of the light pathway during the functioning of the Raman spectrometer

A brief description of the different components that form part of the spectrometer is provided below.

3.4.1.1 Laser source

The Invia spectrometer is able to operate on a wide range of laser types depending on the sample to be analyzed, with automatic software switching of excitation wavelength near the visible and infrared region. The lasers can be categorized as follows:

- Visible regions: 457 and 514 nm (violet and Green: laser diodes accorded at the well-known wavelength of Ar+ laser) and 633 nm (Red: He-Ne).
- Infrared Region: 785 nm (laser diode)

Figure 3.10 shows a general view of the different laser types installed near the Renishaw Invia spectrometer at CNRS-CEMHTI. A neutral density filter located just after the laser source is responsible to attenuate the parasitic plasma signal, hence supplying a clean laser beam to the system.

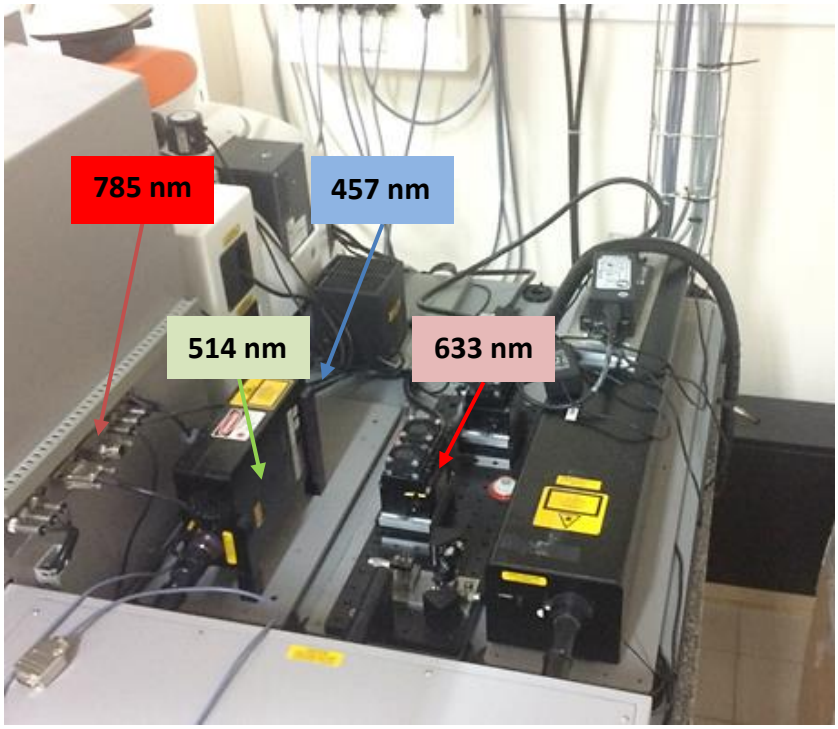

Figure 3.10: Laser excitation source available at CEHMTI-CNRS, Orléans

3.4.1.2 Microscope

The spectrometer uses a high-quality Leica DM2500 light microscope with four possible objectives (x5, x20, x50 & x100). The microscope has two main functions: *(a)* focusing the excitation laser beam on the surface of the sample and *(b)* re-directing the resulting scattered photons towards the spectrometer. The Leica microscope has a high optical efficiency along with an excellent mechanical stability.

3.4.1.3 Holographic filters

The efficient detection of the Raman Stokes and anti-Stokes modes is only possible when there is a significant attenuation of the intense Rayleigh line and other stray lights. The latter is ensured by the Edge filters. The filters also enable a sharp spectral cutoff's with an acquisition starting as close as 100 $cm^{-1.}$ (Rayleigh signal usually occurs at 0 cm^{-1}).

3.4.1.4 Diffraction grating

The scattered photons are then directed with a suitable angle towards the diffraction grating system. The latter contains grooves blazed into the surface which improve the stray light performance of the spectrometer and optimize the response at the chosen diffraction order. In order to obtain a better spectral resolution, the number of lines per unit length in the system

should be higher because it helps to broaden the dispersion angle. The Invia Raman spectrometry can support different grating system such as the 600 grooves/mm, 1200 gr/mm, 1800 gr/mm and 2400 gr/mm. The choice of the suitable grating number depends on the incidence wavelength and final desired resolution.

3.4.1.5 Charged Couple Device (CDD camera)

The photons are then focused onto the long axis of the CCD detector. The latter is a multi-channel detector, extremely sensitive to light, and also allows the whole spectrum of a sample to be obtained in only one acquisition. The resulting spectrum is displayed as x (representing the wavelength in units of cm^{-1}) vs y (peak intensity) plot.

3.4.2 X-ray diffraction

The principle of X-ray diffraction is based on the interaction of monochromatic X-rays and a crystalline material. A tube composed of a cathode and an anode, guided by a high voltage filament, is used to generate X-rays (characteristics X-rays). The resulting X-ray beam is filtered by a crystal monochromator and then directed onto the target sample.

The interaction of the incident rays with the sample produces constructive interferences and gives rise to wave emission in all directions. In case if the diffusion occurs without any loss of energy, i.e. elastic scattering, the X-rays are diffused by each atom of the crystal and interfere with each other. This is referred as diffraction and is represented in Figure 3.11. Diffraction depends on the atomic structure of the material. The direction of the diffracted beam is defined by the Bragg's law. The latter relates the wavelength of electromagnetic radiation to the diffraction angle and the lattice spacing in a crystalline sample.

Bragg's law is given by the following equation:

$$n\lambda = 2d\ x\ sin\theta \tag{3.4}$$

Where;

n: order of reflection and is the path difference, in terms of number of wavelengths, between waves scattered by adjacent planes of atoms

λ: wavelength of the diffracted X-ray beam

d: crystal plane separation

θ: angle between the reflected beam and the crystal plane

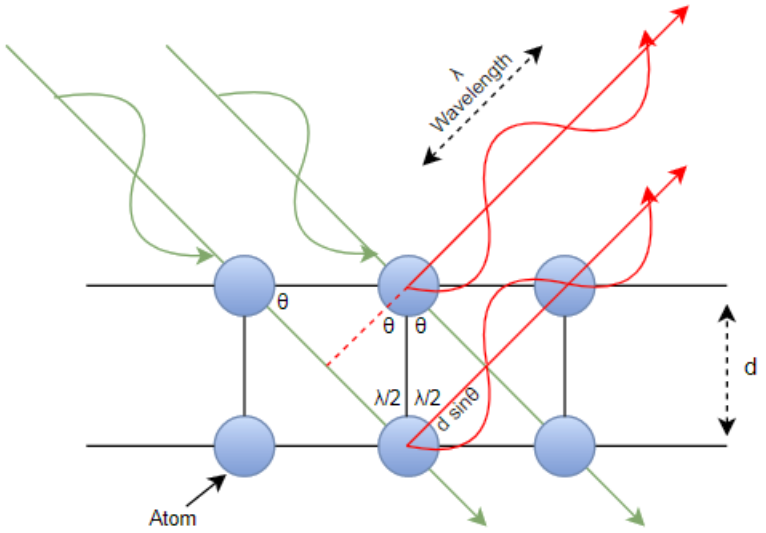

Figure 3.11: Diffraction of X-ray by a crystal lattice

The Bragg's law is important in indexing X-ray patterns and determining the crystal structure of a material. The X-ray patterns and structures of most cubic materials are well documented. Thus, the lattice can be determined from the Miller indices {hkl} of each diffraction peak by using Equation 3.5, which relates the diffraction spacing, d, and the lattice parameter, a.

$$\mathbf{d} = \frac{a}{\sqrt{h^2 + k^2 + l^2}} \tag{3.5}$$

3.4.2.1 Configuration of the Bragg-Brentano diffractometer in the θ- θ configuration

The XRD measurements of the virgin and irradiated disks were performed by a D8 Bruker diffractometer (45kV, 40 mA) mounted on a Bragg-Brentano design with copper radiation from a conventional tube source ($K_{\alpha1}$+ $K_{\alpha2}$ radiation, λ=1.5406Å and 1.5444Å). The intensity ratio of $K_{\alpha1}$ to $K_{\alpha2}$ is approximately 0.51 [126]. The Bragg Brentano uses a parafocusing geometry to increase the intensity and angular resolution. The incident X-rays are guided by divergence slits onto the sample. The latter rotates uniformly around its plane (goniometric circle), thus making it possible to increase the number of possible orientations of the reticular planes.

The diffractometer uses a graphite monochromator and a NaI scintillation detector to measure the intensity of the diffracted X-rays in certain directions. The geometry of the diffractometer is such that the sample rotates in the path of the collimated X-ray beam at an angle θ, while the detector rotates at an angle of 2θ, i.e., the speed of the detector is twice to that of the sample. In the Bragg Brentano θ-θ configuration, the principle is the same except that the sample remains stationary while the X-ray source and the detector move symmetrically around it. Figure 3.12 illustrates the mode Bragg Brentano θ-θ configuration of the diffractometer.

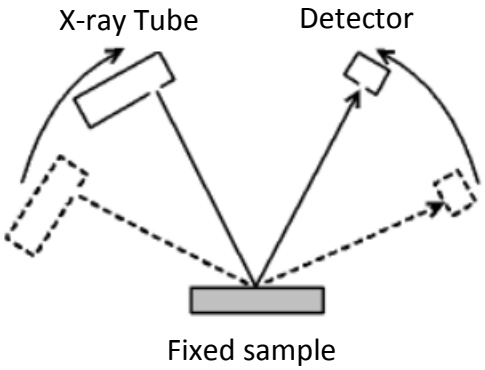

Figure 3.12: Schematic of the Bragg-Brentano design with a θ-θ configuration

In this study, all XRD measurements of the nuclear samples were performed at the LCU lab at CEA-Cadarache. The X-ray diffractograms were recorded for a scan in the 20°- 140° (2θ) range using a 0.01° step with a counting step of 5s. The analysis was performed at room temperature and the total measuring time was 16 hours. The lattice parameter was determined by Rietveld analysis of the X-ray patterns using the Topas 4.2 software [125].

3.4.3 Positron annihilation spectroscopy

Positron, the anti-particle of an electron, can be used to probe lattice defects such as vacancies, concentration of vacancies and dislocation in materials. The principle of the Positron Annihilation Spectroscopy (PAS) is based on the photons emerging from the annihilation of positrons with electrons in a sample as it will be further explained in the following sections.

3.4.3.1 Principle of PAS

PAS is based on the special properties of positron-electron annihilation process. Similar to electron, positron has an electric charge of $+1.6 \times 10^{-19}$ C, spin of ½ and a mass of about 0.511 MeV/c^2. Positrons are obtained from the β^+ decay of radioisotopes (^{64}Cu, ^{58}Co, ^{19}Ne, ^{22}Na…). In most of the positron annihilation experimental studies, positrons directly emitted from a ^{22}Na source are commonly used. The decay scheme of ^{22}Na radioisotope is illustrated in Figure 3.13.

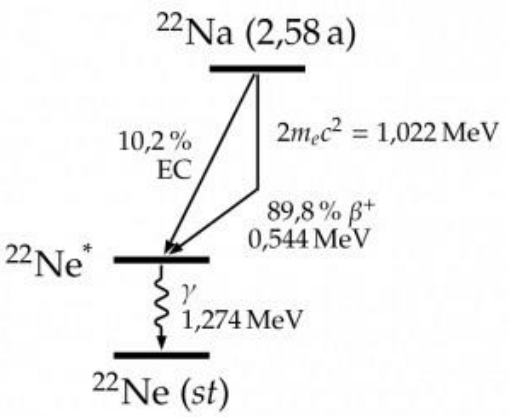

Figure 3.13: Positive beta decay scheme of ^{22}Na radioisotope

The main advantages of using ^{22}Na isotope lie on its corresponding long half-life (~2.6 years) and the effective β^+ (≥ 90%) emission within few picoseconds. The positrons are then implanted into the material to be analyzed. The particles undergo several processes that influence the state to which a positron annihilates with an electron.

The initial kinetic of a positron is reduced as a result of electronic interactions as it penetrates the material. This is referred as thermalization and corresponds to the stage where the kinetic energy of the positron has been reduced to the thermal energy level of the lattice, i.e. about 25 meV. It is worth to note that the probability of positron annihilation during this step is very low.

After reaching thermal equilibrium with the medium, the thermalized positron develops free diffusion process over the area occupied by the host atoms. The positron interacts with its surrounding and finally annihilates during its encounter with an electron within 200-500 picoseconds. The annihilation process results in two gamma-rays photons as indicated by the equation below:

$$e^+ + e^- = \gamma_1 + \gamma_2 \tag{3.6}$$

3.4.3.2 Doppler Effect

In the center-of-mass frame of the e^+-e^- pair, the two emitted annihilation photons must have energies of approximately $E_o = mc^2$ = 0.511 MeV and their quanta must be emitted in the exactly opposite direction as shown in Figure 3.14 (a). However in the laboratory frame, in which positron is considered to be at rest, a certain deviation from collinearity is expected as illustrated in Figure 3.14 (b).

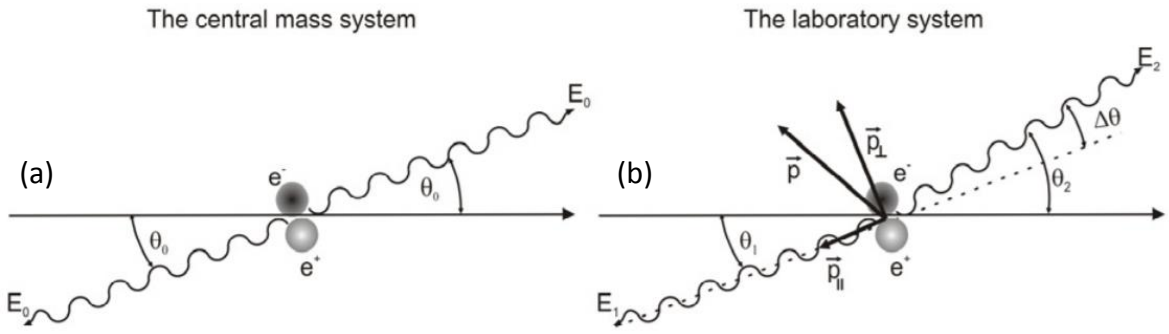

Figure 3.14: Representation of the positron-electron annihilation in center-of-mass and laboratory frame

The deviation from the collinearity can be expressed as:

$$\Delta\theta = \frac{p_{\perp}}{mc} \tag{3.7}$$

Where;

m: mass of electron

c: speed of light

$p_{\perp}$: perpendicular component of the momentum of the annihilation pair

Due to the finite momentum of the electron-positron pair, the quantum manifests itself in gamma quanta energies, which are changed as a result of Doppler Effect. These shifts in photon energy are called the Doppler broadening.

$$\mathrm{E}_{\gamma} \cong mc^2 + E_B \pm \frac{p_{\parallel} c}{2} \tag{3.8}$$

Where;

E_B: energy of the positron-electron pair coupling

$p_{\parallel}$: parallel component of the pair's momentum

3.4.3.3 Doppler broadening of the annihilation line

Doppler broadening of the annihilation line consists of measuring the energy of the gamma rays emitted during the annihilation process. The 511 keV peak is more Doppler broadened by the longitudinal momentum of the annihilating pairs at defects sites than it would occur in the case of the annihilation with the nucleus. Thus, the broadening will be more important in a highly defective sample compared to a less defective sample.

The analysis of the annihilation line can provide relevant information about the defects contained in a sample. The broadened Doppler spectrum can be interpreted in terms of the *line shape (S)* and *wings (W)* parameters as illustrated in Figure 3.15.

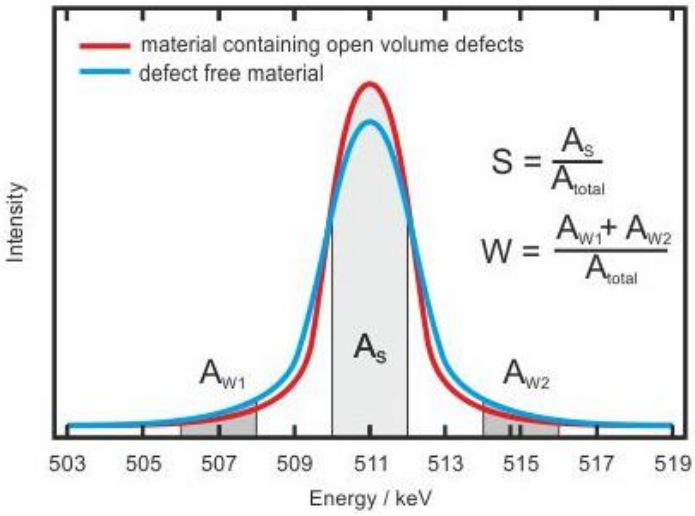

Figure 3.15: Doppler broadening of the of the positron annihilation radiation line

The line shape parameter, also referred as the S parameter, corresponds to the annihilation of positrons with low-momentum electrons at 511 keV. It is the parameter that is related to the defects in a material. The S parameter can be defined as the ratio of the area over the central part of the 511 keV line to the total area. A high S-parameter value indicates a high defect concentration.

The wings parameter, referred as W-parameter, is expressed as the ratio of the contribution of the peak tails to the total peak area and is more sensitive to the annihilation of positrons with high momentum electrons. It gives information about the chemical environment of the defects.

As illustrated in the above figure, it can be seen that a single energy range around the center of the 511 keV peak [$-E_s$, E_s] is needed to calculate the S-parameter. On the other hand, two energy ranges are required for the W-parameter [$-E_{W1}$, $-E_{W2}$] and [E_{W1}, E_{W2}]. S and W parameters are defined based on the number of events in their intervals (N) and the total number of events (N_{Total}) in the annihilation peak.

$$S = \frac{N(-E_s\,;E_s)}{N_{Total}} \tag{3.9}$$

$$W = W_1 + W_2 = \frac{N(-E_{W1}\,;E_{W2}) + N(-E_{W2}\,;E_{W2})}{N_{Total}} \tag{3.10}$$

3.4.3.4 PAS experimental set-up

In this study, all the PAS measurements were performed using the positron accelerator beam coupled with a Doppler broadening spectrometer at CEMHTI-CNRS, Orléans. The experimental installation uses a slow positron beam energy which enables to characterize the first few microns below the specimen surface. A schematic of the experimental set-up is provided in Figure 3.16.

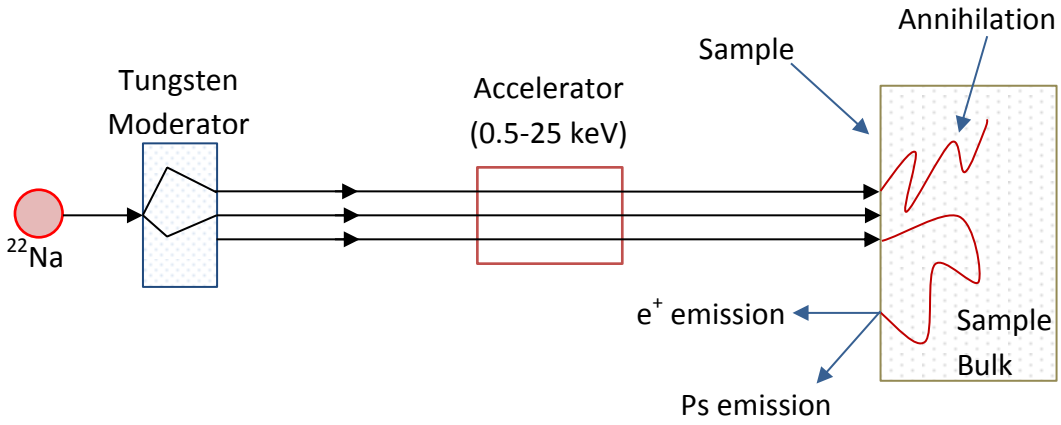

Figure 3.16: Schematic representation of the positron accelerator available at CEMHTI-CNRS, Orléans

A tungsten moderator is initially used to thermalize a fraction of the positrons emitted from the radioactive ^{22}Na source. The thermalized positrons are spontaneously re-emitted into a vacuum with a relatively low energy close to 3 eV due to the negative positron work function of tungsten. It is important to note that the tungsten moderator limits the positron beam intensity to 10^5-10^6 e^+/s.

The low-energy positrons are extracted from the positron production target by electric field and transported through an energy filter to separate the monoenergetic positrons from any remaining high-energy positrons and electrons. Thus, the clean slow-positron energy beam is guided towards the target sample. The apparatus uses a slow positron beam energy (0.2-2.5 keV) which enables to characterize the first few microns below the specimen surface.

3.4.3.5 Interpretation of PAS experimental data

The annihilation of positrons in vacancy defects sites, where the electron density is smaller compared to the defect's environment, is marked by decrease in the high momentum annihilation of e^+-e^- pair (W parameter) and an increase in the low momentum annihilation of e^+-e^- pair (S parameter). The characteristics of the annihilation in the bulk lattice network and defect sites are referred as (S_L, W_L) and (S_V, W_V) respectively.

Barthe *et al.* [127] carried out a series of positron annihilation measurements to investigate the evolution of the S and W parameters as a function of positrons energy of a UO_2 disk before and after it was irradiated with electrons at different fluences. The low (S) and high (W) annihilation fractions were normalized by a reference sample referred as Ga16, which is a virgin UO_2 disk with the S= 0.3713 and W= 0.07856 values respectively. The results obtained are shown in Figure 3.17.

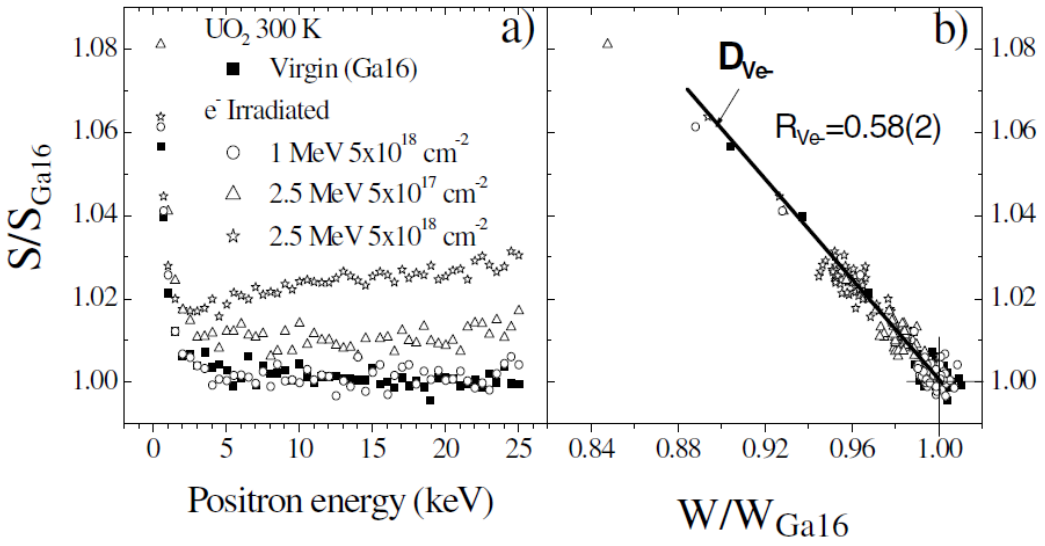

Figure 3.17: Relative low momentum fraction S/Sref (a) as a function of positron energy and (b) as a function of relative high momentum fraction W/Wref for the unirradiated and irradiated UO_2 at different electron fluence [127]

From the above Figure 3.17 (a), it can be observed that for the unirradiated UO_2, the S parameter shows a rapid decrease as a function of positron energy from 0.5 to 2 keV. The decrease is much slower up to 5 keV, after which the S parameter reaches a plateau till 25 keV. In regards to the irradiated UO_2 disks, the low momentum S parameter tends to increase as a function of increasing electron fluence, which corresponds to the presence of vacancy-type defects resulting due to the electron implantation.

Figure 3.17 (b) represents the S parameter as a function of the W parameter and shows that all (S, W) points lie on the same straight whatever is the positron energy and the electron fluence.

The straight line is referred as the defect line (De-line) and is characteristics to the positron annihilation in a defect resulting from the displacement of a uranium atom, i.e. the annihilation of positron in a uranium vacancy site. Recent studies by Wiktor *et al.* [128] on the positron lifetime measurements of UO_2 showed that the PAS defect line is characteristic to a complex defect made of one uranium and two oxygen vacancies which is inappropriately referred as Schottky defects. These observations are important and will be used for the interpretation of experimental results in Chapter 4.

3.5 Conclusions

This chapter provided an overview of the different samples and experimental installations that were used in order to meet the objectives defined for this thesis. The experimental methodology was based on the fabrication of several fuel samples followed by their ionic implantation using external irradiation sources. The irradiated fuel samples were then analyzed by several characterization techniques.

An in-depth analysis of the Raman triplet defects was firstly conducted by irradiating several UO_2 disks with electrons using the Pelletron SIRIUS Van de Graaff accelerator. In addition, a cyclotron device was used to generate defects structures in the different nuclear oxides in order to simulate the alpha decay of actual irradiated nuclear fuels.

Finally, to study the effect of microstructure on the Raman triplet defect bands, UO_2-doped oxides having different microstructures were fabricated and subjected to alpha irradiation. For this study, CeO_2 and ThO_2 were used as dopants because they share the same physico-chemical properties as both PuO_2 and UO_2. Thus, (U, Ce)O_2 heterogeneous mixed oxides were used to simulate MOX fuels under laboratory conditions. On the other hand, (U, Th)O_2 homogeneous samples were used to study the effect of doping on the Raman defect bands.

Raman spectroscopy and XRD methods were used as characterization tools for the measurements of irradiation-induced defects in the fuel materials. Both characterization methods are suited for surface measurements, thus any change occurring on the sample surfaces during irradiation can be revealed. In addition, PAS method was also employed to characterize lattice damages, mainly vacancy-type defects, which are generated during electron irradiation.

Chapter 4

Identification of irradiation defects responsible for the Raman triplet defect bands

4.1 Introduction

The behavior of nuclear fuels under irradiation is rather well experimentally understood [[129], [130], [104], [131], [132]- [133]] and simulated by numerical models [[134], [135], [136], [137]- [138]]; but the physical mechanisms that occur during irradiation of UO_2 nuclear fuels are still subject of intense research. One major hurdle is the low number of experimental results relevant for the validation of point defect modelling, from which UO_2 behavior could be deduced. As previously discussed in Chapter 2, Raman spectroscopy offers an alternative approach for the characterization of irradiation defects. The occurrence of the Raman triplet defect bands in doped or irradiated UO_2 appears as a promising path for the understanding of irradiation effects in UO_2.

Irradiation effects in solids are by convention assigned to either electronic or nuclear stopping power. Guimbretière et *al.* [103] showed that the maximum intensity of the Raman defect bands occurs principally in areas where the maximum energy of the incident ions is deposited. But no definitive conclusion can be derived from these results because in all ion irradiation experiments, both electronic and ballistic stopping coexist. Moreover, it is difficult to study the Raman bands intensity as a function of stopping power because Maslova [139] recently showed that the intensity of the Raman allowed lines in UO_2 strongly depends on the crystallographic orientation. Most of the published Raman data presented in Chapter 2 were obtained on polycrystalline samples, thus no quantification of the Raman data is therefore possible until a well suited method is developed that takes into account the grain orientation effects.

To support the identification of the irradiation defects responsible for the apparition of the Raman triplet defect bands, an electron irradiation experiment of several UO_2 disks was performed to differentiate between the electronic and nuclear stopping power. In this chapter, the experimental results obtained are initially presented. A detailed analysis of the data will then be conducted so as to provide a better interpretation regarding the Raman defect bands.

4.2 Initial characterization of virgin UO_2 disks

4.2.1 Raman measurements

The surface of the as-prepared UO_2 disks was initially analyzed by the Renishaw Invia Reflex spectrometer. The apparatus was equipped with a 633 nm excitation laser and an 1800 grooves/mm diffraction grating system for a spectral acquisition between 350 and 700 cm^{-1}. The spot size of the red laser is about 1 µm. Thus in regards to UO_2, Raman spectroscopy characterizes one grain at a time (average grain size of UO2: ~8-10 µm).

Figure 4.1 shows the Raman spectra of two virgin UO_2 disks. Each spectrum was obtained with an acquisition time of 120s after 5 accumulations. For both samples, the expected T_{2g} peak can be distinguished at 445 cm^{-1}. The latter is characteristics to the only Raman active mode allowed in oxides sharing the Fm3m space group. The low intensity of the LO-mode occurring at 568 cm^{-1} indicates the presence of a small concentration of intrinsic defects in the virgin samples. Finally, no peaks related to oxidation [96] can be observed from Figure 4.1.

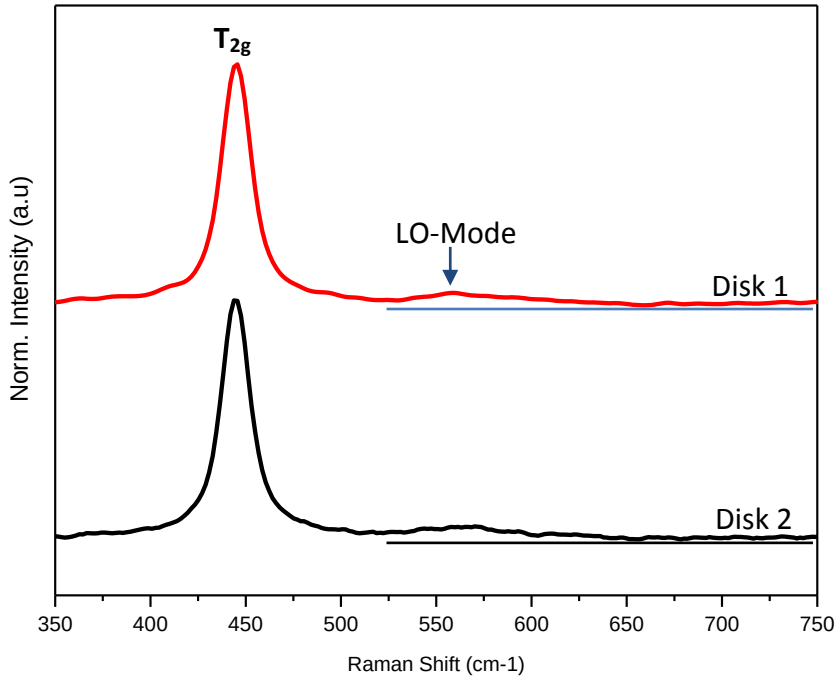

Figure 4.1: Raman analysis of two virgin UO_2 disks annealed at 1400°C during 4 hours

4.2.2 XRD measurement

The diffractogram obtained for the virgin UO_2 disk is illustrated in Figure 4.2 below. The lattice parameter was determined by a Rietveld analysis of the X-ray patterns using the Topas software and a value of 5.4693 Å was obtained for the virgin UO_2 samples. This result is in good agreement with reported values in the literature [[140], [141]& [142]].

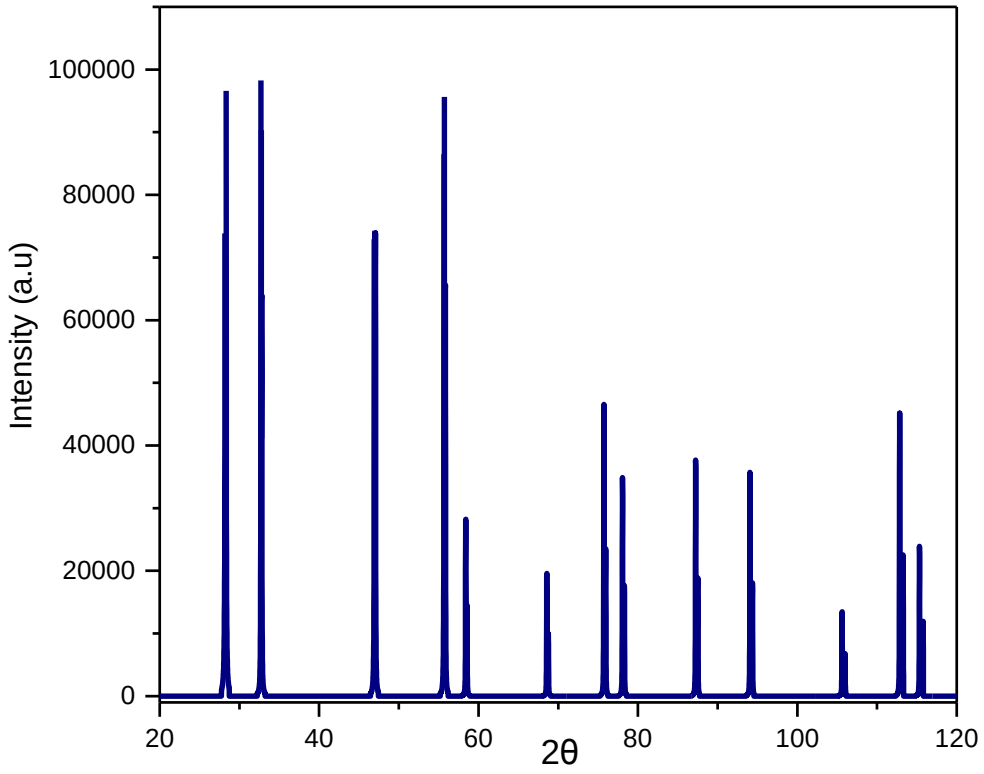

Figure 4.2: X-ray patterns for the virgin UO_2 disk annealed at 1400°C during 4 hours

4.3 Electron irradiation

4.3.1 Generalities

The electron irradiation was been performed using the Van de Graaff accelerator at the Irradiated Solids Laboratory (LSI) at École Polytechnique, France. The objective of this study was to correlate the irradiation-induced Raman bands (U1, U2 & U3) either to the inelastic or elastic collisions of the electrons with the UO_2 atoms.

The energy loss for the different electron beam energy resulting from the inelastic collisions of the electrons can easily be computed by the program ESTAR code provided by the National Institute of Standard and Technology (NIST) Physical measurement Laboratory [123]. For the calculations, the displacement energy (Ed) of oxygen and uranium in UO_2 were taken to be 20 eV and 40 eV respectively [124].

Figure 4.3 shows the variation of the electronic energy loss for the electron beam in the 1 MeV to 3 MeV energy range.

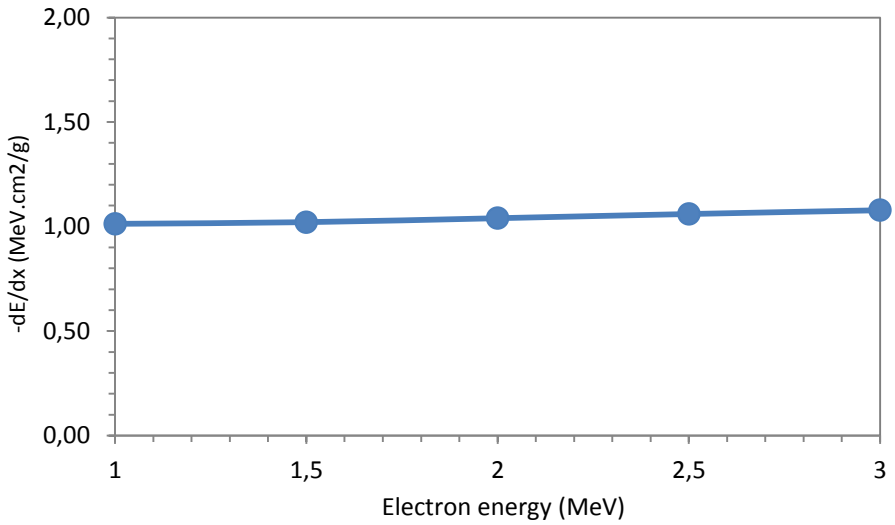

Figure 4.3: Electron stopping power in UO_2 calculated using the ESTAR program code

On the other hand, the values of the nuclear stopping power at the different electron energies were estimated by the Non Ionizing Energy Loss (NIEL) calculator program developed by the Istituto Nazionale di Fisica Nucleare (INFN) Milano-Bicocca group [143]. The calculated values for the nuclear stopping power for the electron energy ranging from 1 MeV to 3 MeV are shown in Figure 4.4 below.

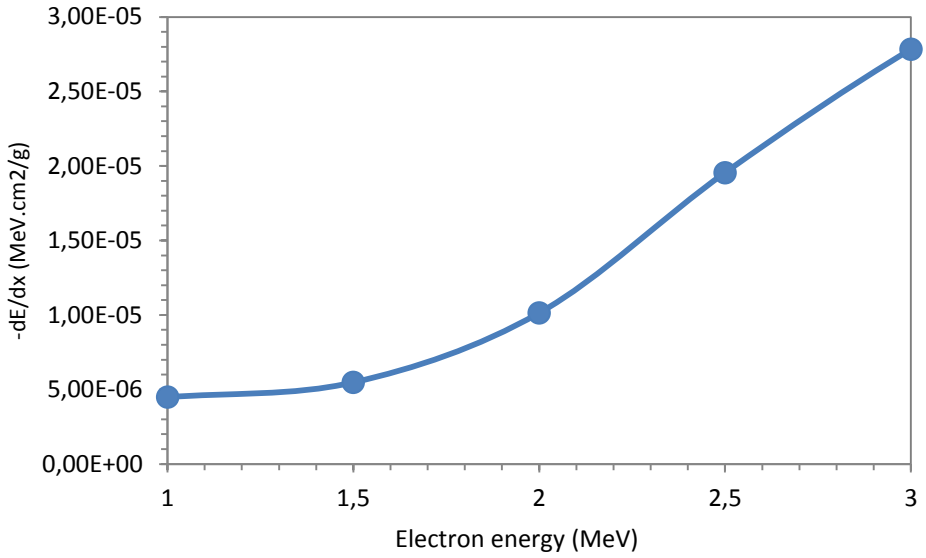

Figure 4.4: Nuclear stopping power in UO_2 obtained by Non Ionizing Energy Loss (NIEL) calculator program

From the above figures, it can be seen that the nuclear stopping power increases significantly in the 1.6-2.5 MeV electron energy range. On the contrary, the electronic energy loss remains almost constant in the same energy range. Therefore to differentiate between nuclear and electronic stopping power, several sintered UO_2 disks were irradiated with electrons at different energies in the 1.6-2.5 MeV range.

Thus, the origin of the Raman triplet defect bands can be determined by comparing the change in their relative intensity to that of Figure 4.3 and Figure 4.4. For instance, if the irradiation-induced Raman peaks were due to the formation of electronic defects, the intensity of the U1, U2 and U3 should then follow the same trend as observed in Figure 4.3, i.e. no major evolution of the defect bands intensity should be witnessed with increasing electron energy. However, if intensity of the defect bands increases gradually and follows the same tendency as in Figure 4.4, the defect bands can then be attributed to atomistic defects resulting from the elastic collisions of the electrons with UO_2 target atoms.

In addition, the above figures show that the total electron energy loss (electronic + nuclear) for the different electron energies between 1.6 MeV and 2.5 MeV lies close to 1.04-1.08 keV/µm. The corresponding thickness of the UO_2 disks used in this experiment is in the order of 500 µm. The irradiation was carried out such that the electrons are initially allowed to irradiate the entire front UO_2 surface and are then transmitted out through the back surface. Hence, the electrons lose ~500 keV during their interactions with the UO_2 atoms. For example, electrons with an initial 2.2 MeV will reach the rear surface with energy of ~1.7 keV.

4.3.2 Irradiation and characterization campaigns

For the different electron beam energies used in this study, a 1.8 Coulomb electron charge was targeted. This corresponds to 18 hours of irradiation. However due to technical issues related to the functioning of the accelerator, it was not possible to replicate the targeted 1.8 C charge during all the irradiation campaigns that were performed.

Three irradiation campaigns were required to irradiate the UO_2 disks in the 1.6-2.5 MeV range. It is to be noted that a higher electron charge was used for the 1.9 MeV beam energy to investigate the effect of electron charge on the concentration of irradiation defects.

A summary of the different irradiation conditions that could be achieved on the sintered UO_2 samples are presented in Table 4.1. In addition, the different characterization tools that were employed for each irradiated disk are also indicated.

Table 4.1: Summary of the irradiation conditions and characterization tools that were used for the UO_2 disks in this study

Electron Energy (MeV)	**Irradiation Campaign Accumulated electron Charge (Target charge: 1.8 Coulombs)**			**Characterization**		
	1st (2015)	2nd (2016)	3rd (end of 2016)	Raman	PAS	XRD
1.6	0.94	-	-	✓	✓	✓
1.9	-	5.59	-	-	✓	-
2.0	1.8	-	-	✓	-	✓
2.1	1.686	-	-	✓	✓	✓
2.2	-	1.8	-	✓	✓	-
2.3	1.8	-	-	✓	-	✓
2.4	-	0.24	-	✓	✓	-
2.4		1.43	-	✓	✓	-
2.5	0.311	-	-	✓	-	-
2.5	0.615	-	-	✓	✓	-
2.5	-	-	1.8	✓	-	✓

4.4 Experimental results

4.4.1 Raman measurement

This section presents the experimental results acquired during the Raman analysis of the irradiated UO_2 disks. The obtained results are compared with a reference unirradiated UO_2 sample to evidence the formation of the Raman triplet defect bands and also to investigate their evolution as a function of increasing electron beam energy.

Two different data processing techniques were adopted to study the irradiation-induced Raman lines; namely *(a)* surface characterization of the irradiated UO_2 samples and *(b)* Raman mapping across the cross section of an irradiated UO_2 disk.

4.4.1.1 Method A: Surface characterization

As initiated in Table 4.1, the UO_2 disks were irradiated at different electron energies but it was not possible to replicate the targeted electron charge (1.8 C). Thus for a better comparison, only the UO_2 samples subjected to an electron charge close to 1.8 C were selected to express the intensity of the Raman triplet defect bands as a function of electron energy. Hence, a Raman measurement was conducted on the surface of the disks irradiated at 2.0 MeV (1.8 C), 2.1 MeV (1.686 C), 2.2 MeV (1.8 C), 2.3 MeV (1.8 C), 2.4 MeV (1.43 C) and 2.5 MeV (1.8 C).

The electrons lose about 500 keV when they reach the UO_2 back surface. Thus, the irradiated back surfaces of the 2.0 MeV, 2.1 MeV, 2.2 MeV, 2.3 MeV and 2.4 MeV disks were also characterized in order to obtain the Raman spectra corresponding to 1.5 MeV (1.8 C), 1.6 MeV (1.686 C), 1.7 MeV (1.8 C), 1.8 MeV (1.8 C) and 1.9 MeV (1.43 C) respectively.

As the intensity of the Raman allowed lines in UO_2 depends on the crystallographic orientation, a Raman mapping was performed over irradiated surface so as to select the UO_2 grains which delivers the maximum T_{2g} intensity. Figure 4.5 represents the Raman spectra obtained following the surface analysis of an unirradiated UO_2 and the irradiated disks.

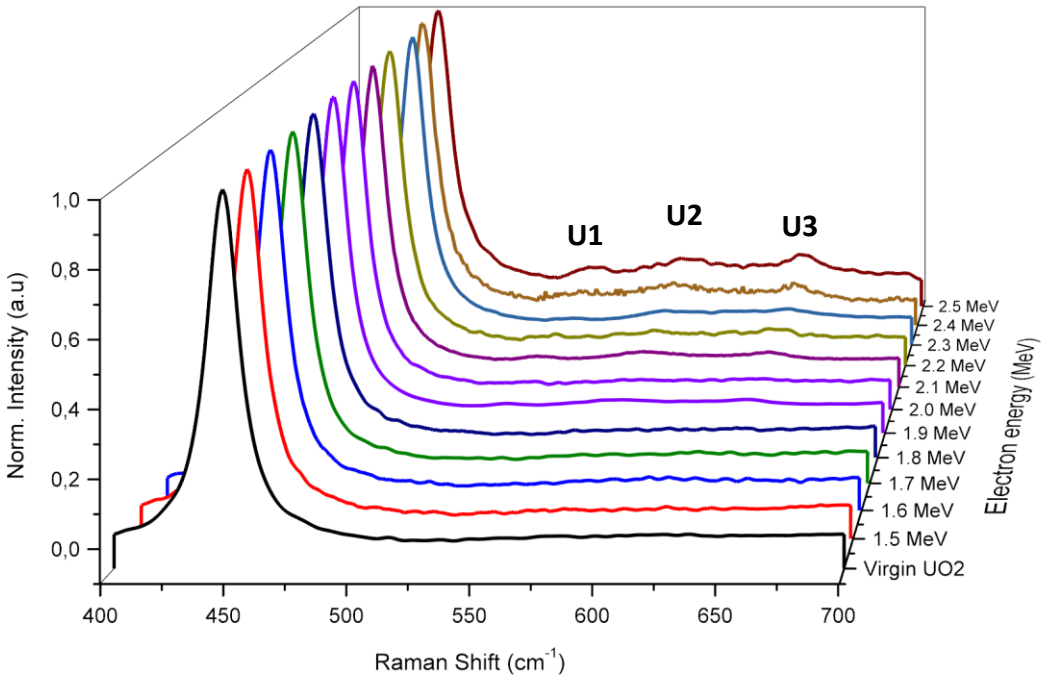

Figure 4.5: Raman spectra of a virgin UO_2 and the disks irradiated at different electron energies at equivalent electron charge (1.8 C). The Raman spectra were normalized by the T_{2g} peak intensity to bring all the spectra at the same scale

The above figure shows that the intensity of the Raman triplet defect bands (U1, U2 & U3) increases as a function of electron energy. The intensity increase observed in this experiment is relatively smaller compared to data reported during alpha and heavy ion irradiations [[106], [104]- [129]]. The Raman defect bands appear clearly for the 2.5 MeV irradiated sample, but it is difficult to estimate the energy threshold for the apparition of the defect peaks from the above figure. Therefore, it was necessary to develop a data analysis strategy in order to extract the relative intensities of U1, U2 and U3 as a function of electron energy.

4.4.1.2 Evolution of the Raman triplet defect peaks *vs.* electron energy

Desgranges *et al.* [108] developed a numerical methodology to estimate the annealing temperature of irradiation defects when a UO_2 was irradiated with 25 MeV alpha ions. The method consisted of fitting the 480-720 cm^{-1} range of the Raman spectrum of an unirradiated UO_2 in the form of a hyperbolic curve to define the background, right foot of the T_{2g} and the small hump corresponding to the forbidden LO-mode. The hyperbolic curve, considered as a reference baseline for virgin UO_2, was then superimposed on the Raman spectra of irradiated UO_2. The Raman signals occurring solely due to the effect of irradiation were derived by subtracting the experimental spectrum with that of the reference curve.

The same procedures were initially chosen to analyze the Raman spectra but several difficulties were encountered. The methodology proposed by Desgranges *et al.* [108] was efficient mainly because the Raman measurements were performed on the same sample. Thus, the background noises associated to that particular sample could be determined and considered during the data analysis.

However in this study, measurements were carried out on different samples which were associated with different level of background noises. The small increase in the defect bands intensity makes it difficult to differentiate the Raman defect peaks from the background noises. In addition, an increase in the FWHM of the T_{2g} peak was evidenced for the 2.3 MeV and 2.5 MeV electron-irradiated samples. The latter restricts the correct superimposition of the reference curve onto the experimental spectrum of irradiated samples and the peaks relevant to irradiation damages could not be properly extracted.

A different approach was therefore required. After the experimental acquisitions, an initial baseline subtraction of the raw Raman data was performed to eliminate residual fluorescence signals and background noises. The value of the T_{2g} peak intensity was then recorded (T_{2gMAX}) after the baseline subtraction. The 510-720 cm^{-1} spectral range was selected and normalized by the T_{2gMAX} value. The same steps were repeated for all spectra. Finally, the spectra of the irradiated samples were subtracted with the unirradiated UO_2 spectrum in order to extract the variation of the defect bands intensity as a function of election energy. The obtained results are represented in Figure 4.6.

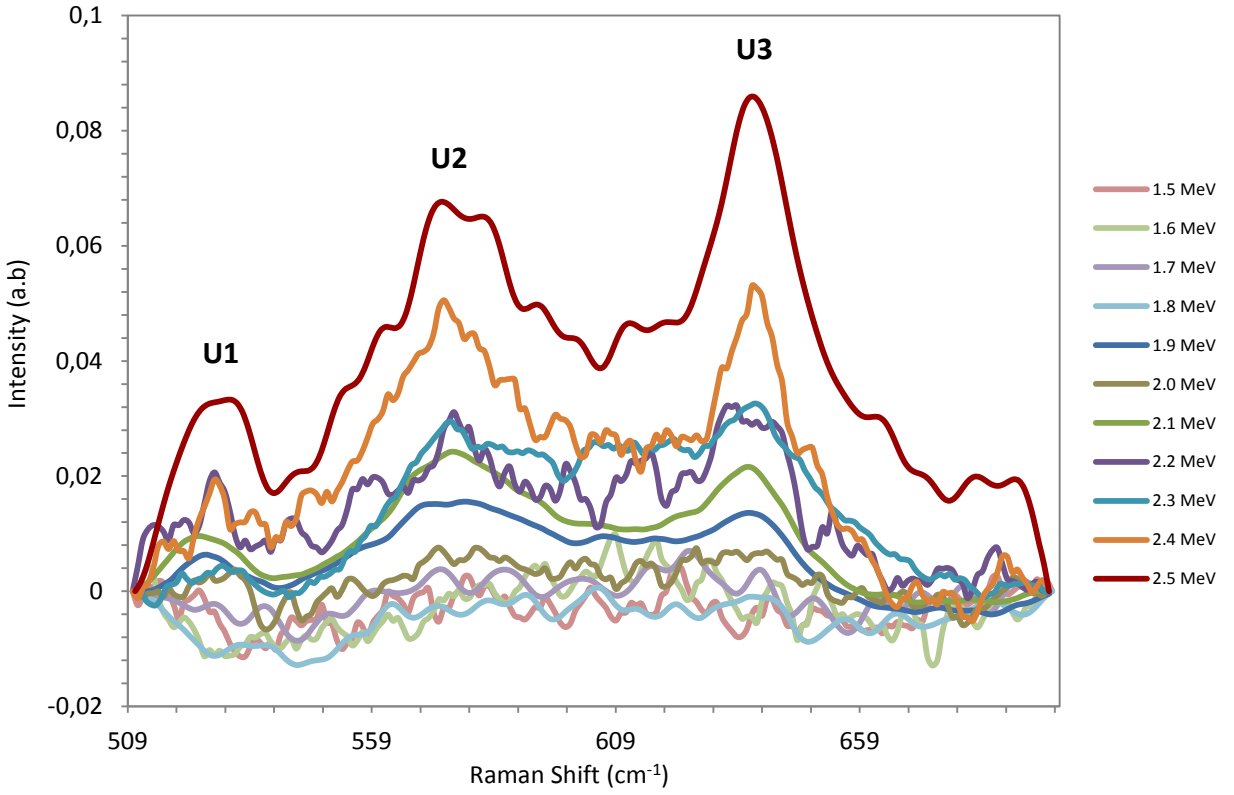

Figure 4.6: Evolution of the irradiation-induced Raman signals as a function of electron energies obtained after subtraction with a reference unirradiated UO_2 spectrum

The difficulty to separate the Raman defect bands (U1, U2 & U3) from the background at lower energies is clearly evidenced from the above figure. The triplet defect peaks become more visible as the electron energy is further increased and were seen to occur at 532 cm^{-1}, 574 cm^{-1} and 636 cm^{-1} respectively. A deconvolution of the Raman spectra was performed by fixing the positions of the triplet defect bands. The intensities of U1, U2 and U3 at different electron energies were then extracted and are presented separately in the figures below.

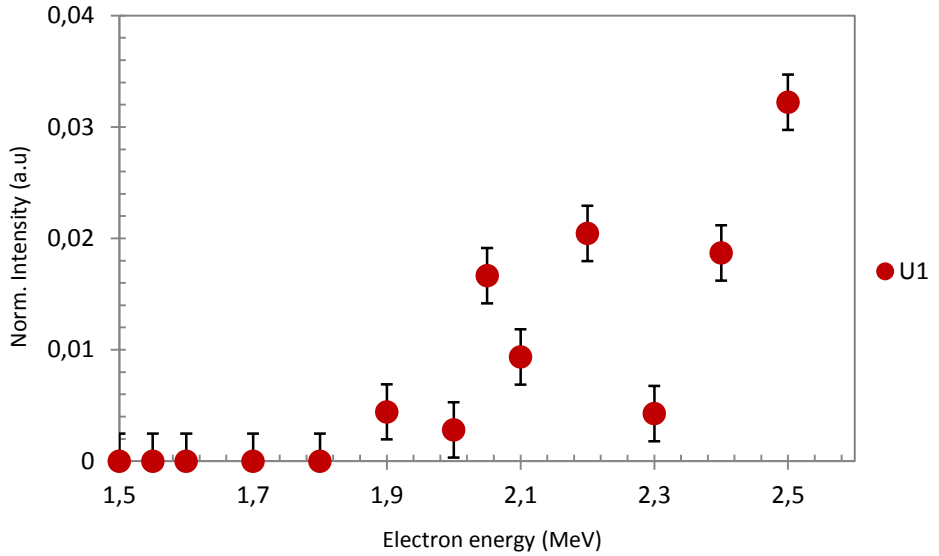

Figure 4.7: Evolution of U1 (532 cm^{-1}) as a function of electron energy

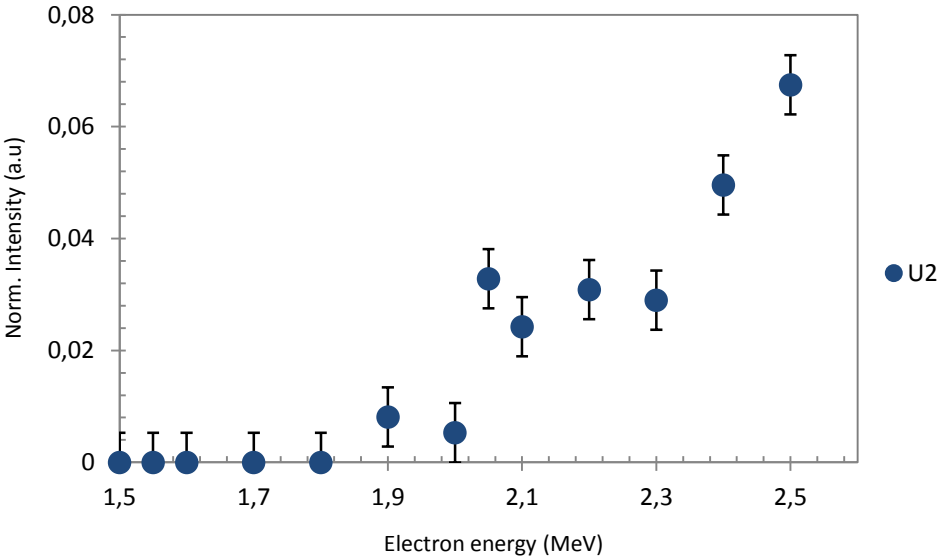

Figure 4.8: Evolution of U2 (574 cm^{-1}) as a function of electron energy

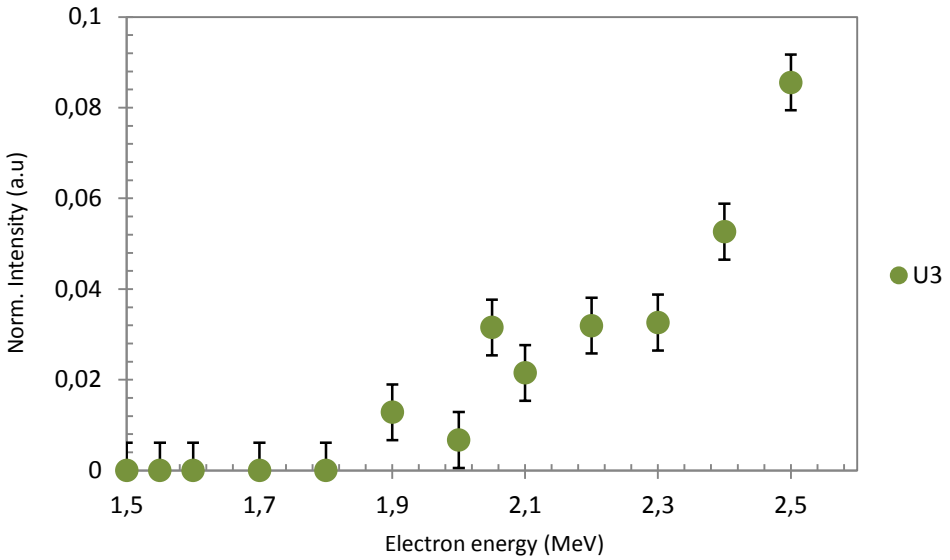

Figure 4.9: Evolution of U3 (636 cm^{-1}) as a function of electron energy

The figures clearly indicate that the U1, U2 & U3 bands follow the similar behavior under irradiation. They are inexistent below 1.8 MeV but then show a gradual increase as the electron energy is increased. As a first approximation, the energy threshold for the apparition of the Raman defect bands can be estimated to lie between 1.8 MeV and 2.0 MeV.

4.4.1.3 Method B: Cross section of the irradiated sample parallel to the irradiation beam

The change in the Raman triplet defect bands intensity as a function of electron energy can also be investigated by taking into consideration the electron energy loss across the UO_2 disks. As previously stated, i.e. the electron energy is reduced by 1 keV for every 1 µm travelled in the disk. The thickness of the UO_2 disks used were 500 µm, hence the electrons lose approximately 500 keV as they travel across the samples.

An alternative method to measure the Raman defect bands intensity at different electron energies involves the Raman measurements at different points along the depth of the irradiated disks. However according to Maslova [139], the profiling depth of the Raman spectroscopy is restricted only to 3-4 µm on the UO_2 surface and is therefore insufficient to characterize the entire depth of the irradiated disk. Thus, it was necessary to section an irradiated UO_2 into two half-disks using a wire saw apparatus so as to be able to analyze the entire depth of the irradiated sample which was parallel to the electron beam direction.

Due to the small dimensions of the half-disk, it was important to immobilize the half-disk into a resin support solution for further manipulations. After the sectioning, one of the half-disk was held vertically in a small beaker with the help of a stainless-steel support. A resin solution was

then poured into the beaker but care was taken so as not to completely overflow top cross section of the irradiated sample. The resin solution was left still to solidify during 24 hours. The top cross section of the half-disk was then mirror polished for subsequent characterization purposes. The different steps involved during the sample preparation are illustrated in Figure 4.10.

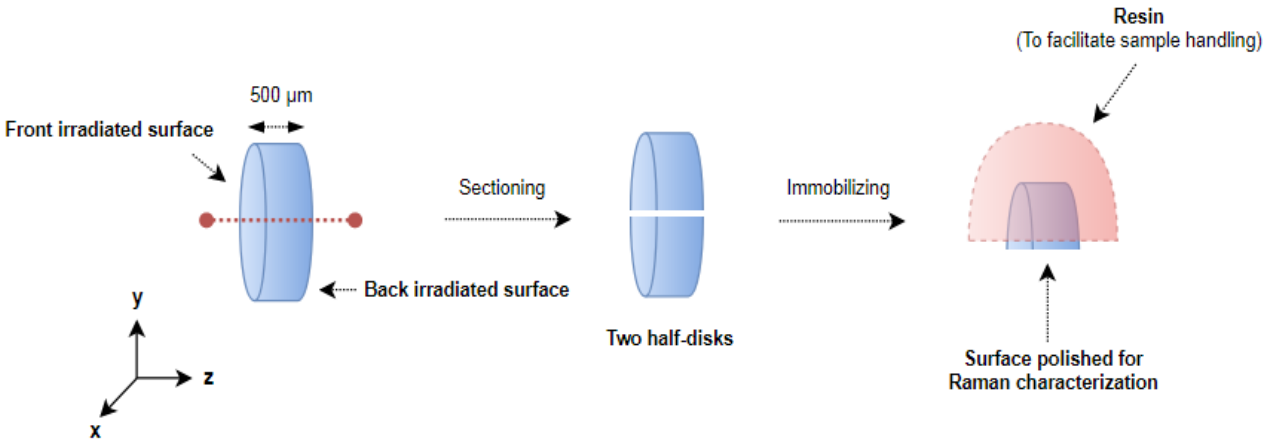

Figure 4.10: Sectioning of the irradiated disk followed by the application of the resin solution to facilitate the handling of the half-disk

From Section 4.4.1.2, it was concluded that the electron energy threshold for the apparition of the Raman triplet defect bands lies between 1.8 MeV and 2.0 MeV. For the need of this study, the 2.3 MeV irradiated UO_2 was chosen because it gives relevant information in the 1.8-2.3 MeV range. Hence, a further investigation to determine the electron energy threshold for apparition of the Raman defect bands can be carried out.

A Raman spectral mapping was performed over a selected area on its cross section starting from the irradiated surface extending to the back surface, i.e., parallel to the electron beam direction. The dimensions of the chosen area were 500 x 200 μm^2 on the z and x axis respectively, with a moving step of 1 µm in the snake mapping mode.

The microscope image illustrating the Raman defect bands intensity profile along the selected area is shown in Figure 4.11. The red zone indicates the area where the intensity of the defect bands is the maximum and can be referred as the maximum damaged zone. This was obtained through a multivariate analysis, with providing to the software (Renishaw Wire 3.4, DCLS analysis) two reference spectra: virgin UO_2 and a spectrum with intense triplet defect. The intensity of the defect bands decreases as the energy of the electrons is reduced (green area). The green signals near the irradiated front surface can be attributed to the porosity contained in the disk.

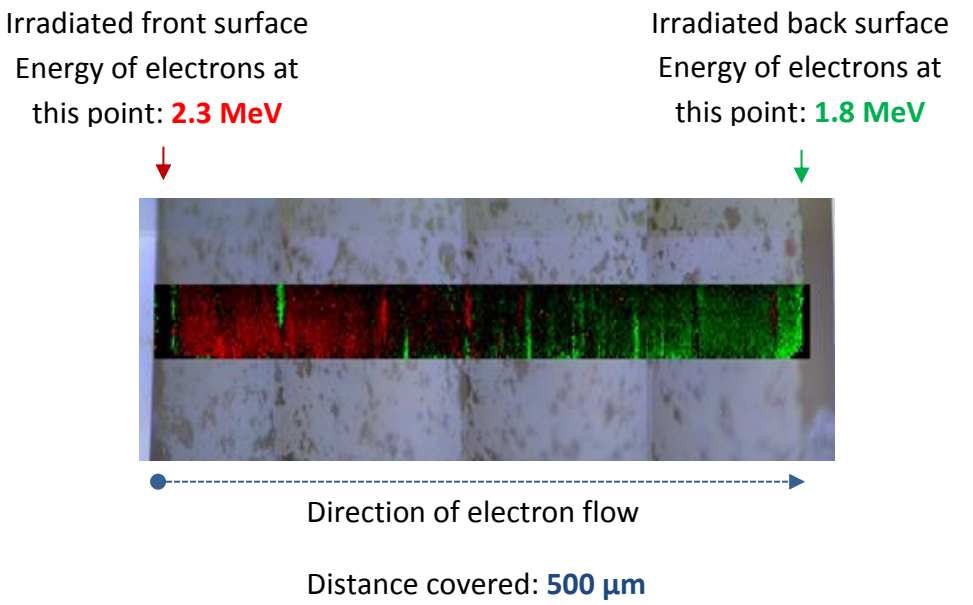

Figure 4.11: Microscope image of the two-dimensional area on the cross section of the 2.3 MeV half disk indicating the pathway and distance travelled by the electrons during irradiation. Red area indicates the maximum damage zone and green area shows the region where the intensity of the defect bands is low

The difference in the Raman spectrum corresponding to irradiated front surface (red area) and the irradiated back surface (green area) is illustrated in Figure 4.12. The Raman defect bands can clearly be distinguished from the red spectrum but are practically inexistent in the green spectrum which is consistent with the lower electron energy near the back surface.

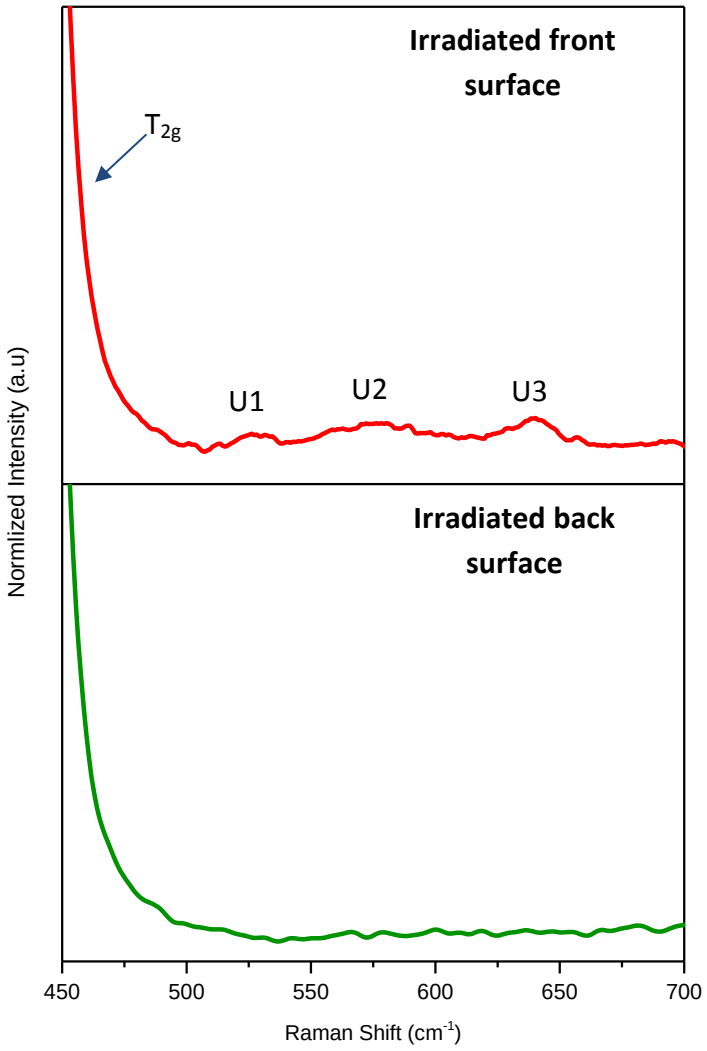

Figure 4.12: Raman spectra of the irradiated front surface (red spectrum) and irradiated back surface (green spectrum)

4.4.1.4 Evolution of the Raman triplet defect peaks *vs.* electron energy

The Raman map was analyzed and the spectrum corresponding to every 100 keV decrease in the electron energy was chosen by moving from the front to the back surface by a step of 100 µm. The Raman spectra were acquired from the UO_2 grains which gives the maximum T_{2g} peak intensity. Thus, the spectra relevant to the 1.8 MeV, 1.9 MeV, 2 MeV, 2.1 MeV, 2.2 MeV and 2.3 MeV electron energies were collected. Figure 4.13 illustrates the Raman spectra as a function of electron energy obtained from the mapping of the cross section of the 2.3 MeV irradiated disk. A zoom in the 462-700 cm^{-1} spectral range was required to highlight the evolution of the Raman triplet defect bands.

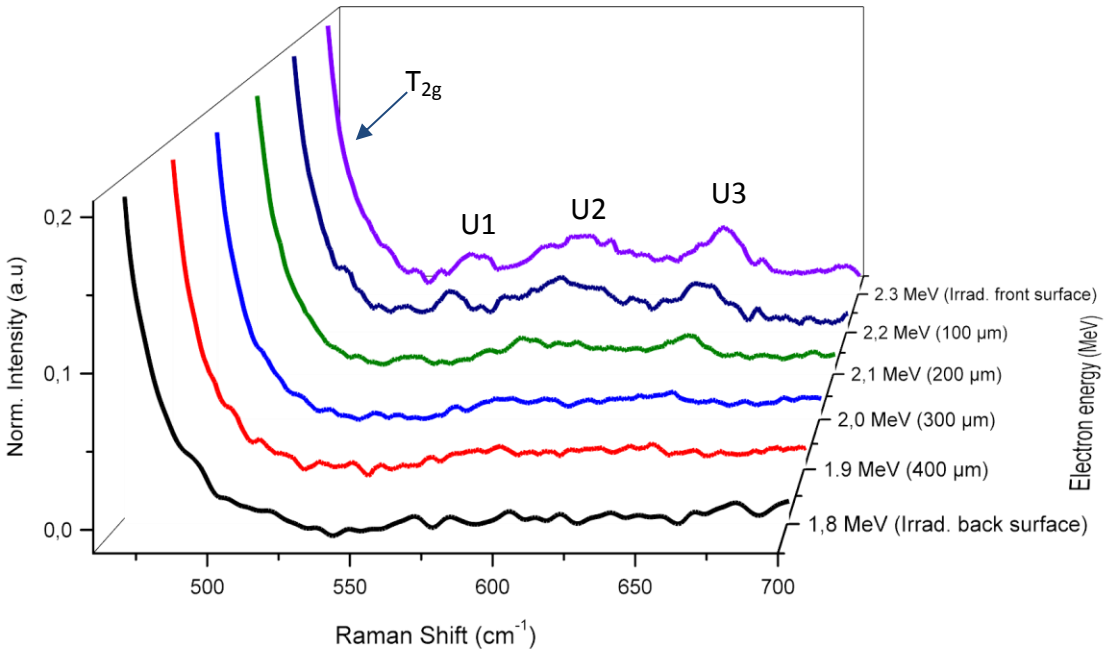

Figure 4.13: Raman spectra representing different electron energy obtained at a 100 µm interval level along the cross section of the 2.3 MeV irradiated sample

The above figure shows very close similarities to the previous findings obtained during Raman measurements of the irradiated sample surfaces as reported in Figure 4.5. The high intensity of the defect bands can clearly be evidenced near the irradiated front surface and then it shows a gradual decrease along the depth of the disk which is mainly attributed to a decrease in the electron energy.

The same methodology previously defined in Section 4.4.1.2 was adopted to determine the variation of the defect band intensity in the 1.8-2.3 MeV. The findings are presented in the figures below.

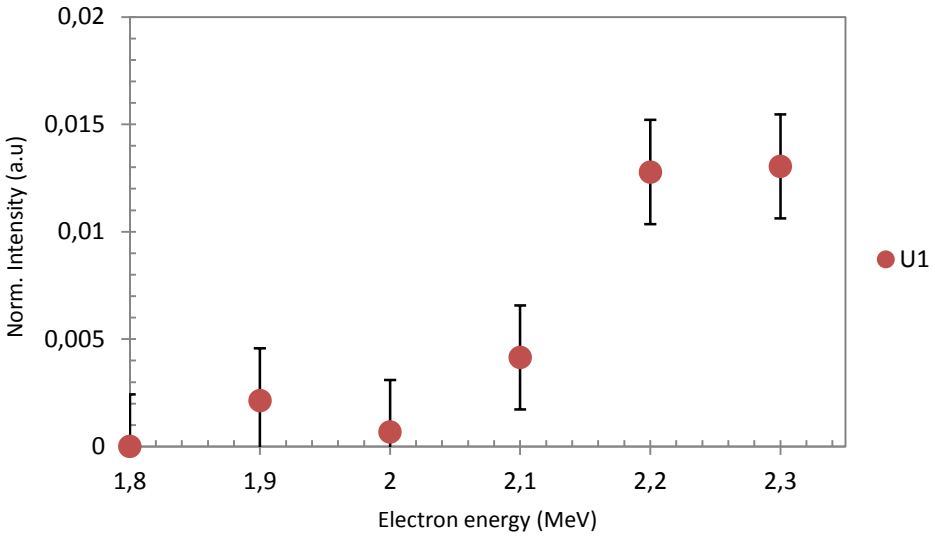

Figure 4.14: Variation of the U1 (532 cm^{-1}) intensity with different electron energy

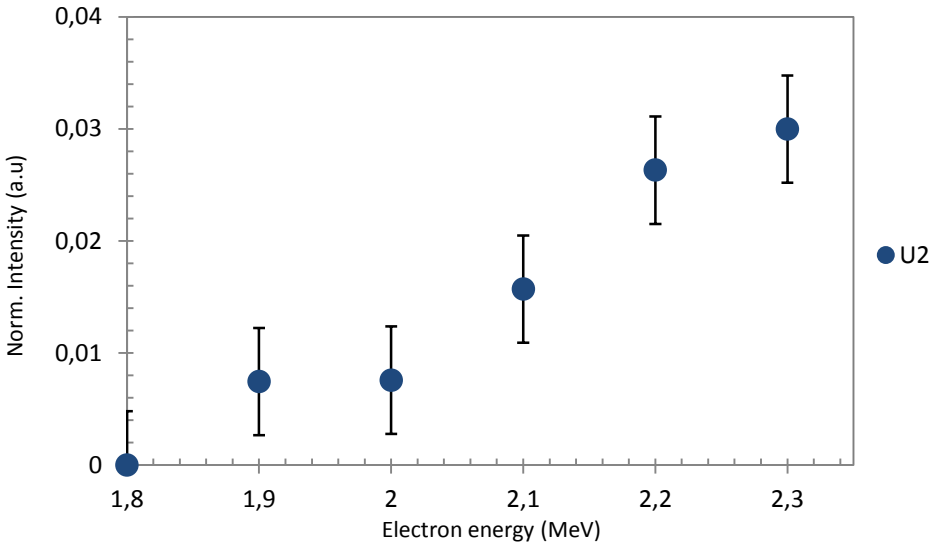

Figure 4.15: Variation of the U2 (574 cm^{-1}) intensity with different electron energy

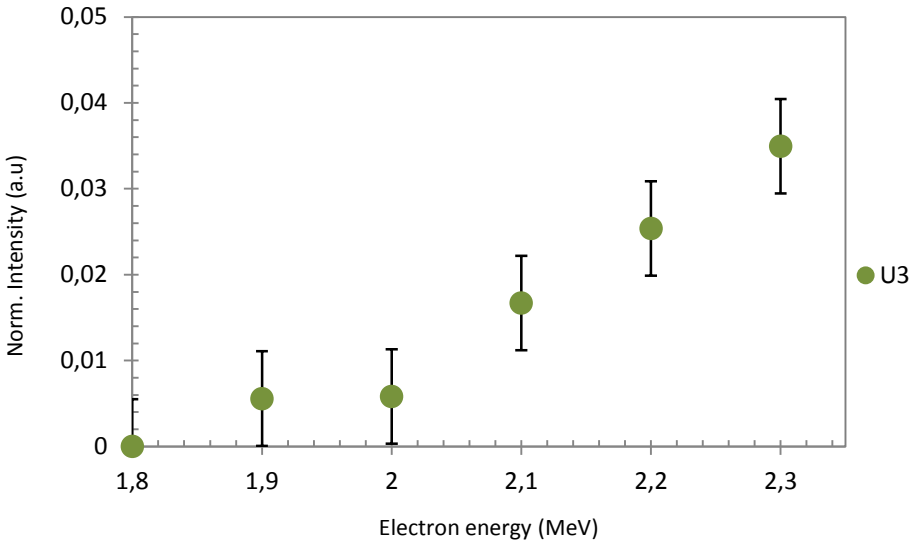

Figure 4.16: Variation of the U3 (636 cm^{-1}) intensity with different electron energy

The above figures show that the intensity of the U1, U2 and U3 bands increases as a function of increasing the electron energy. In addition, the graphs also indicate that the electron energy threshold for the apparition of the Raman triplet defect bands lies below 1.9 MeV. Additional irradiation campaigns need to be done in the 1.8-1.9 MeV electron energy range so as to determine the exact threshold energy.

The method of analysis discussed in this section offers an alternative method for to express the intensity of the Raman defect band in terms of different electron energy. It also gives the advantage to extract all the relevant information from a single irradiated UO_2 disk which enables to define a reference baseline regarding the background noises for all spectra. For example, it was possible to study the Raman defects bands in the 1.8-2.3 MeV range from the single 2.3 MeV irradiated UO_2 disk. On the other hand, six independent irradiation campaigns were required to obtain the same information using Raman analysis of the irradiated samples surfaces method (Section 4.4.1.1).

4.4.2 PAS measurement

The PAS analysis was firstly conducted on the virgin UO_2 samples which were annealed at 1400°C during 24 hours under Ar/H_2 reducing environment. In Chapter 3, it was mentioned that these annealing conditions were chosen such as to avoid the UO_2 grain boundary signal. The latter occurs at 555 cm^{-1}, thus in the same spectral range as the Raman triplet defect bands.

It is to be noted that for the PAS measurements at CEMHTI-CNRS, a UO_2 annealed at 1700°C is taken as reference for an unirradiated disk and considered as a "defect-free" UO_2 lattice (referred as "lattice UO_2 ref A"). Hence, the PAS measurements obtained for the virgin UO_2 used in this study were initially compared with the reference UO_2 to account for the effect of annealing temperature on the intrinsic defect concentration. Post-irradiation, the irradiated UO_2 front surface and back surface were both analyzed. The positron-electron momentum distribution was measured by recording the Doppler broadening of the 511 keV annihilation radiations.

In the following section, the results obtained during the characterization of the irradiated surface will be firstly presented followed by the analysis of the rear surface.

4.4.2.1 Evolution of S(E) and W(E) parameters: Measurements on irradiated front surfaces

The S and W parameters were measured over the first few µm below the surface of the pellets as a function of positron energy. The results for a reference UO_2 lattice (lattice UO_2 ref A), virgin UO_2 disk used in this study (virgin UO_2 B) and the different UO_2 irradiated in the 1.6-2.5 MeV energy range with varying electron charge are shown in Figure 4.17.

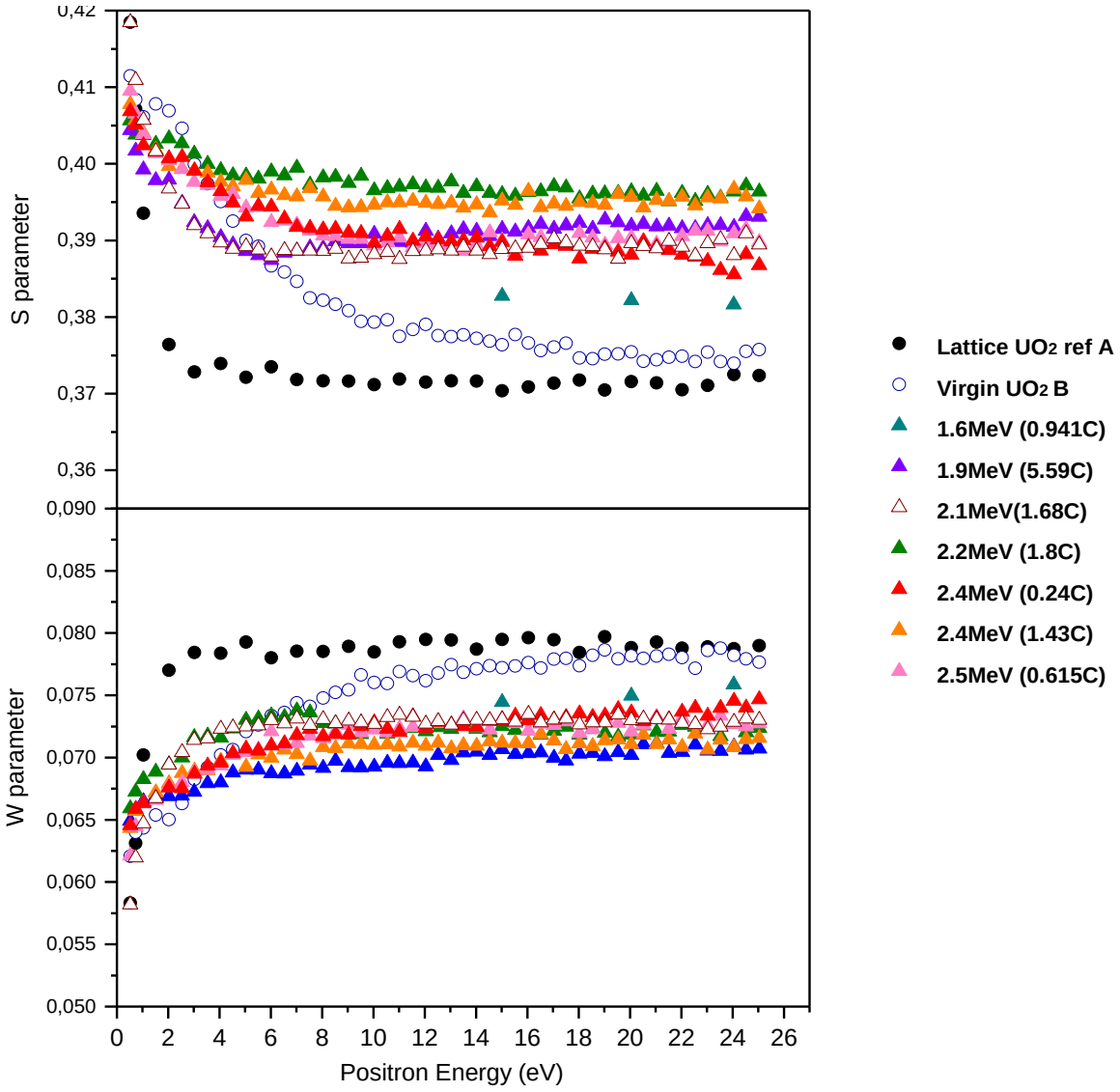

Figure 4.17: Relative low momentum (S) and high momentum (W) as a function of positron energy for the irradiated UO_2 surface

From the above figure, it can be observed that the S and W parameters for the unirradiated UO_2 disk (virgin UO_2 B) decreases and increases respectively as a function of increasing positron energy before reaching stabilization. The measured values of S and W at 25 keV are (S_B, W_B) = (0.371 ± 0,001, 0.077 ± 0,002). The figure shows that the plateau is reached in the positron energy range of 18 keV and 25 keV compared to the reference UO_2 lattice (lattice UO_2 ref A) whereby the S(E) and W(E) values remain constant between 2.5 keV to 25 keV. The difference indicates the presence of intrinsic defects in the virgin UO_2 used in this experiment and can be due to the difference in the annealing conditions. However, the concentration of intrinsic defects can be taken to be small as the plateau of the unirradiated UO_2 (virgin UO_2 B) and lattice reference UO_2 lattice (lattice UO_2 ref A) lie close to each other at 25 keV.

Figure 4.17 also shows that the evolution of the S(E) and W(E) parameters can be separated into two regimes. The first regime lies in the positron energy range between 0.5 keV and 2.5 keV, which is characterized by a decrease in S(E) accompanied by an increase in W(E). The second regime occurs from 2.5 keV to 25 keV and is defined by a slight decrease of S(E) and an increase of W(E) as a function of positron energy. The values eventually reach a plateau.

In regards to the irradiated UO_2 samples, it can be observed that the values of S(E) (resp., W(E)) becomes higher (resp., lower) than the virgin UO_2 B. The evolution of the S and W parameter can however be seen to depend on both electron beam energy and electron charge.

4.4.2.2 Evolution of S-parameter as a function of the W-parameter: Measurements on irradiated front surfaces

Figure 4.18 shows the evolution of the (S *vs* W) values obtained from the plateau in Figure 4.17, i.e. in the positron energy range from 2.5 keV to 25 keV.

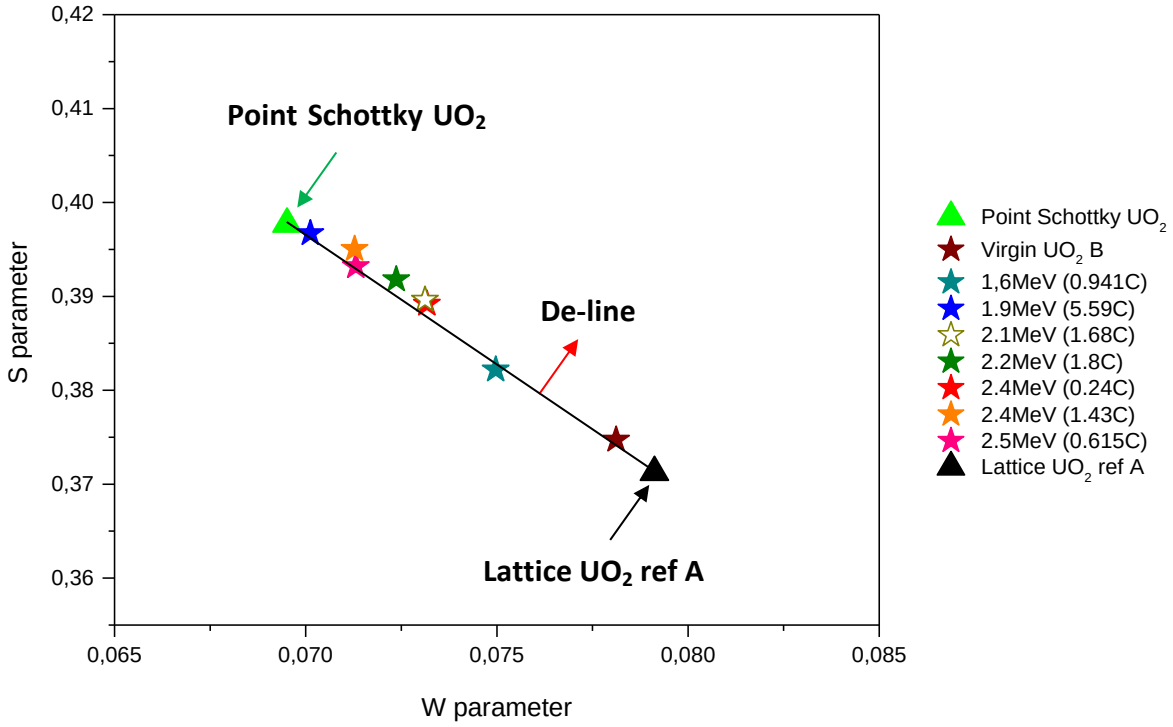

Figure 4.18: Relative low momentum (S) as a function of high momentum (W) for the irradiated UO_2 surface

The values obtained from the measurements of the unirradiated and irradiated samples can be observed to follow a straight line characterized by the reference sample (lattice UO_2 ref A) and the saturation point of Schottky defects in UO_2 (Point Schottky UO_2). As defined in Chapter 3, the straight line is denoted as the defect line (De-line) and corresponds to the positron annihilation in a uranium vacant defect sites.

The results show that most of the points lie below the saturation of the positron trapped in Schottky defects. The figure indicates the presence of a small amount of Schottky defects in the virgin UO_2 as the associated S(W) point is located on the De-line and lie close to the reference UO_2 point.

In regards to the irradiated samples, the S(E) and W(E) values are higher (lower) than the virgin UO_2 and lie on the Schottky line away from the S(W) reference UO_2 point. This observation suggests that Schottky-type defects are created under all irradiation conditions but their concentrations vary depending on the electron energy beam and electron charge.

For instance, the S(W) point states that a low defect concentration is generated when the UO_2 was irradiated at 1.6 MeV with an electron charge of 0.94C. The effect of electron fluence can be determined by considering the UO_2 irradiated at 2.4 MeV with a low (0.24 C) and high (1.430 C) charge. Comparing the positions of the S(W) points for these two charges on the De-line relative to the reference UO_2 (lattice UO_2 ref A) point, it can be evidenced that the concentration of Schottky defects depends on the electron charge. This observation explains the S(W) point for the sample irradiated at 1.9 MeV with a high electron charge (5.59C) which lie close to the saturation point of Schottky defects in UO_2.

4.4.2.3 Evolution of S(E) and W(E) parameters: Measurements on irradiated back surfaces

In this section, the results obtained during the PAS analysis of the irradiated back surfaces are presented. For this study, the samples initially irradiated at 1.6 MeV (0.941C), 1.9 MeV (5.59C), 2.1 MeV (1.686C), 2.2 MeV (1.8C), 2.4 MeV (1.43C) and 2.5 MeV (0.615C) were analyzed. Taking into account the 500 keV electron energy loss, the selected UO_2 sample provide relevant information for energies at 1.1 MeV, 1.4 MeV, 1.6 MeV, 1.7 MeV, 1.9 MeV and 2.0 MeV respectively. Hence, the measurements of the irradiated back surfaces enable to investigate the S and W parameters for energies lower than 1.6 MeV.

The evolution of the S and W parameters for the irradiated back surfaces as a function of positron energy is plotted in Figure 4.19.

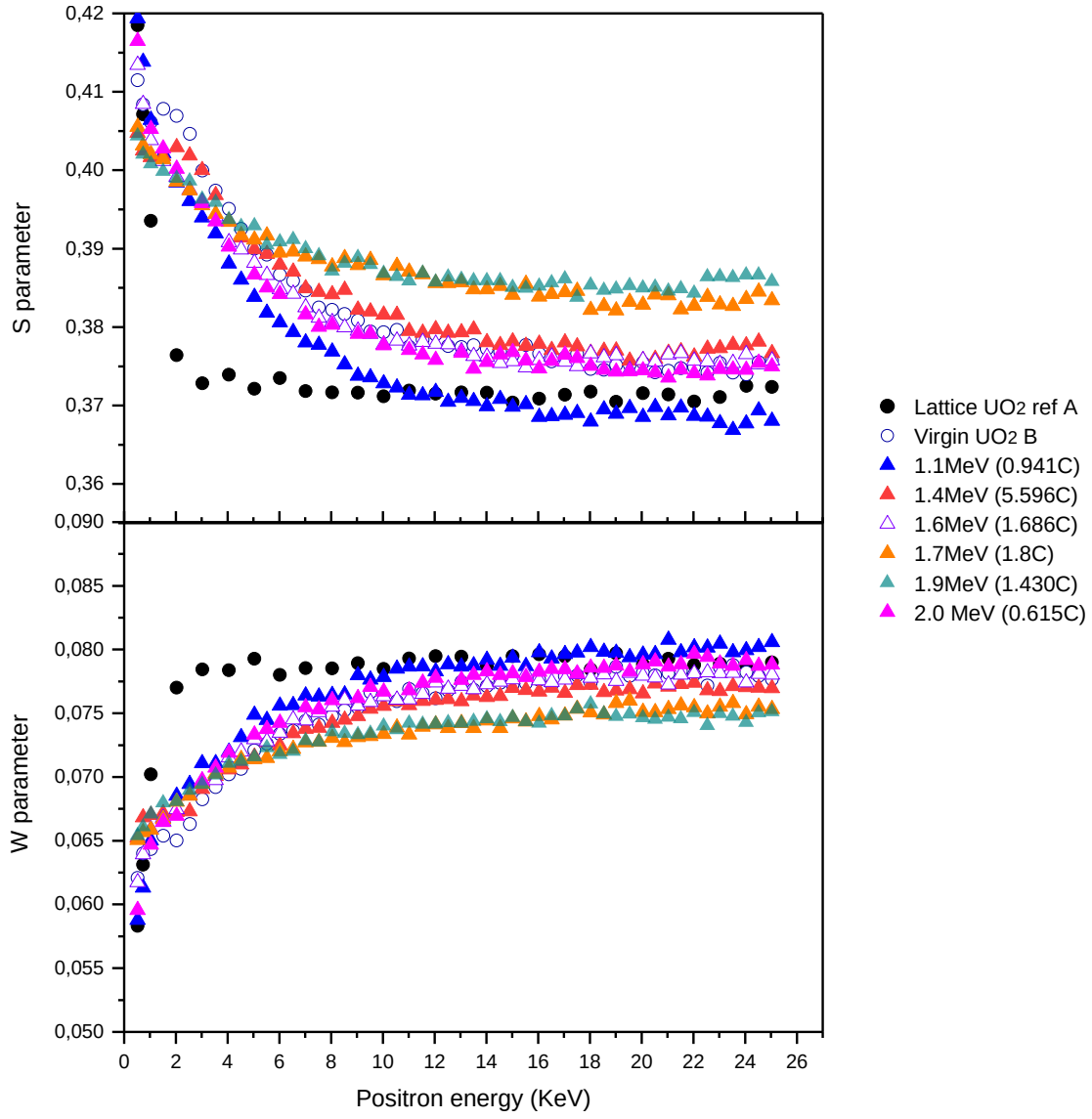

Figure 4.19: Relative low momentum (S) and high momentum (W) as a function of positron energy for the rear UO_2 surface

The above figure is in good agreement with previous results obtained during the irradiated front surface analysis. The S(E) and W(E) curves decreases and increases respectively as a function of positron energy and can also be characterized by a decrease (increase) of S(E) (W(E)) before reaching a stable phase.

The S(E) and W(E) curves for the irradiation at 1.4 MeV and 1.6 MeV lie close to the virgin UO_2 B, thus indicating that the concentration of irradiation defects generated under these conditions is very small. In contrast, the results show defect concentrations become more important for surfaces which were subjected to electron irradiation above 1.6 MeV. This is consistent with the higher S(E) values for the 1.7 MeV and 1.9 MeV.

4.4.2.4 Evolution of S(E) and W(E) parameters: Measurements on irradiated back surfaces

Figure 4.20 shows that the (S *vs* W) points for the irradiated back surfaces are also positioned on the De-line. This indicates the presence of Schottky defects in the irradiated UO_2 and is in good agreement with the findings obtained for the irradiated front surfaces. It is however to be noted that the S(E) (W(E)) curves for the 1.1 MeV and 2.0 MeV become lower (higher) than that of the virgin UO_2 B. No reasonable explanation could be determined for these unexpected findings.

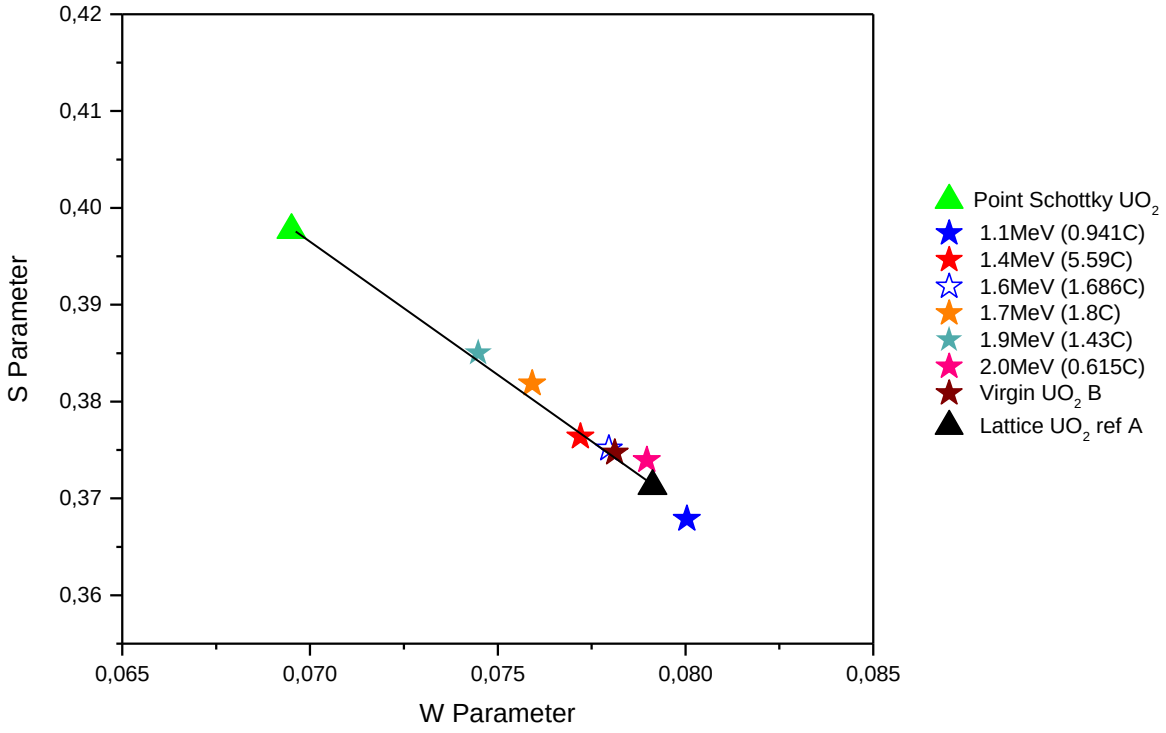

Figure 4.20: Relative low momentum (S) as a function of high momentum (W) for the rear UO_2 surface

4.4.2.5 Evolution of the S-parameter as a function of electron beam energy

The previous results have shown that the concentration of Schottky defects in UO_2 depends on electron energy. Hence by expressing the S parameter as a function of electron beam energy, it is possible to deduce the threshold energy for displacements in the uranium sublattice.

In order to be representative in terms of electron charge, only the S parameters for which both front and back irradiated surfaces that were subjected to a high irradiation charge were considered, i.e. in the range of 1.43-1.8 C. The variation of the S parameter as a function of electron energy is illustrated in Figure 4.21.

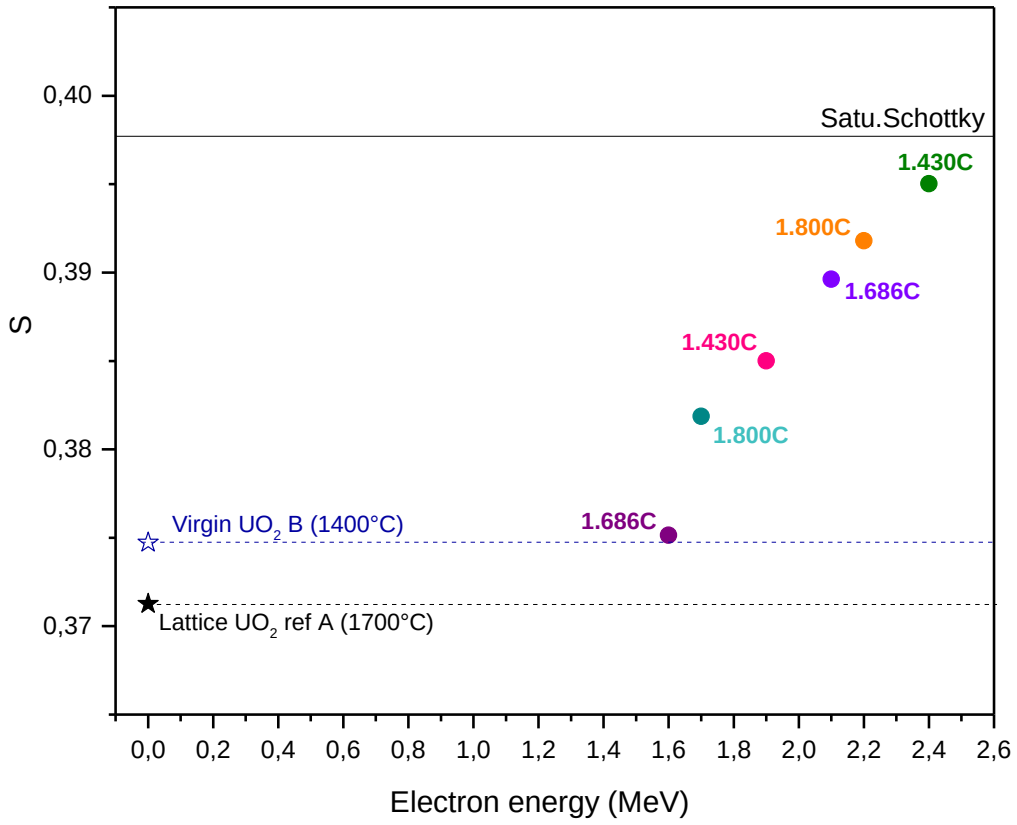

Figure 4.21: S parameter plotted as a function of electron energy and different irradiation charges in the range of 1.43C-1.8C

The figure show that the S values increase linearly with electron energy. It can be observed that the S parameter for the irradiation at 1.6 MeV lies close to the line corresponding to the virgin UO_2 used in this experiment (Virgin UO_2 B). This indicates that the minimum electron energy required to displace uranium atoms in Virgin UO_2 B samples lies below 1.6 MeV.

4.4.3 XRD measurement of irradiated UO_2 disks

The lattice parameter of the different irradiated UO_2 disks was determined and is presented in Figure 4.22. The latter clearly shows a slight lattice expansion as a function of increasing electron energy.

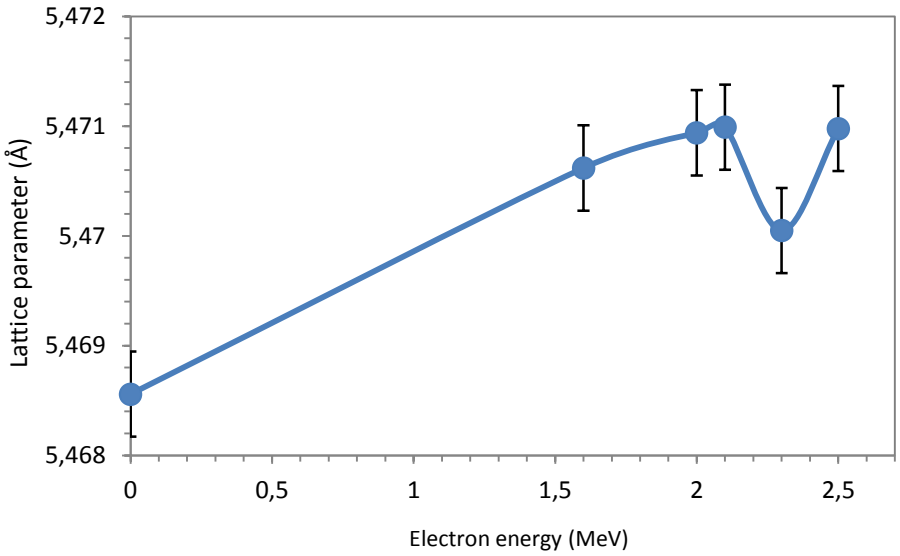

Figure 4.22: Variation of the UO_2 lattice parameter for the irradiated UO_2 disks as a function of electron energy

A particular attention can be drawn to the 2.3 MeV irradiated disk as its lattice parameter does not follow the increasing trend as observed for the other irradiated disks. This observation can be attributed to an ageing effect.

Indeed, the 2.3 MeV irradiation campaign was performed 12 months earlier compared to the other disks presented (refer to Table 4.1). The 2.3 MeV irradiated disk was left exposed in open ambient air conditions until all the irradiation campaigns were completed so that the XRD measurements of all the irradiated disks could be performed at once. Hence, the lattice parameter of the 2.3 MeV irradiated UO_2 was determined almost one year following its irradiation.

A deeper analysis and understanding regarding the behavior of the 2.3 MeV irradiated sample under continuous air exposure will be provided in Section 4.5.2.

4.5 Data interpretation and discussion

The experimental results presented in the above sections were important to provide a detailed interpretation of the Raman triplet defect bands observed during the measurements of irradiated UO_2. In this study, it was mentioned that the targeted 1.8 C electron charge could not be achieved for all the irradiated disks. The latter was due to experimental equipment constraints.

The experimental results have shown that the intensity of the Raman triplet defect bands depends on the electron charge. To study the evolution of the Raman defect bands intensity at different energies, it was necessary to normalize the defect bands intensity to a constant electron charge. Thus, it was important to determine the relationship between the Raman triplet defect bands intensity and the electron charge. From Table 4.1, it can be seen that three UO_2 disks were associated with 2.5 MeV electron energy but different electron charge values (0.311 C, 0.615 C and 1.8 C). On the contrary, the other UO_2 disks were restricted to only two electron charges for a given beam energy.

Therefore, the overall intensity of the Raman triplet defect bands (U1+U2 +U3) for the three samples irradiated with the 2.5 MeV electron beam were determined and plotted as a function of electron charge, as shown in Figure 4.23.

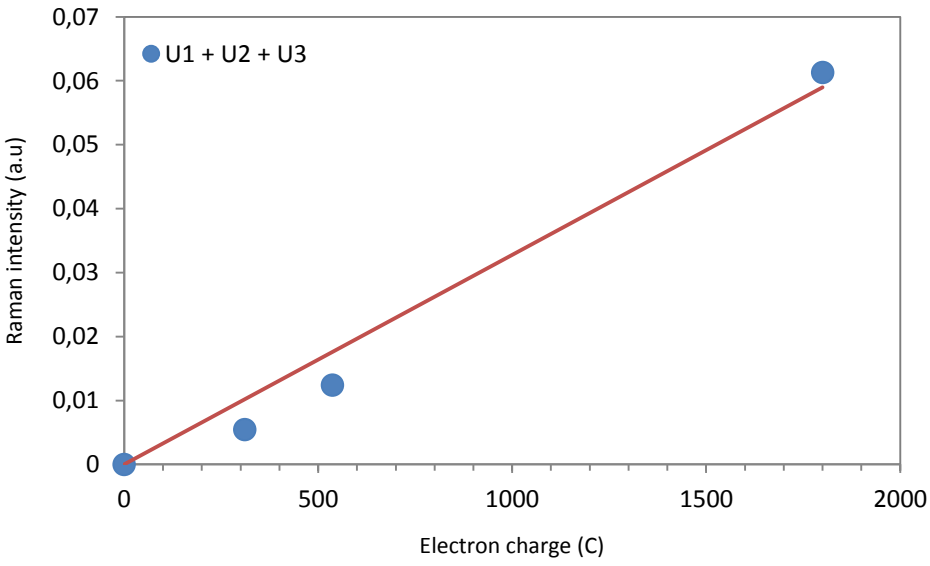

Figure 4.23: Variation of the Raman triplet defect bands intensity as a function of electron charge for the 2.5 MeV beam energy

From the above figure, the intensity of the Raman triplet defect bands can be seen to vary almost linearly along with the electron charge for the 2.5 MeV irradiation beam. Hence for a better comparison of the experimental data, a linear interpolation of the obtained Raman results was conducted to normalize all electron charge values to a constant 1.8 C value.

The discussion section is devoted to relate the Raman triplet defect bands to the type of interaction of the incident electrons with UO_2 atoms, i.e. to differentiate between elastic and inelastic collisions. An in-depth analysis is then carried out in order to attribute the Raman defect bands either to electronic or ballistic defects.

4.5.1 Raman triplet defect bands: electronic *vs*. nuclear stopping power

In this study, the evolution of the Raman defect bands (U1, U2 & U3) as a function of electron energy was determined by two data analysis techniques; Raman analysis of the irradiated UO_2 surfaces (Section 4.4.1.1) and Raman measurements along the depth of a truncated irradiated UO_2 disk (Section 4.4.1.3). Both methods show good consistency to extract relevant information regarding the Raman defect bands.

To facilitate the interpretation and discussion, the overall change in the Raman defect intensity at different electron energy obtained from the two data analysis techniques were considered which were followed by a linear normalization at constant 1.8 C electron charge. The obtained findings are presented in Figure 4.24.

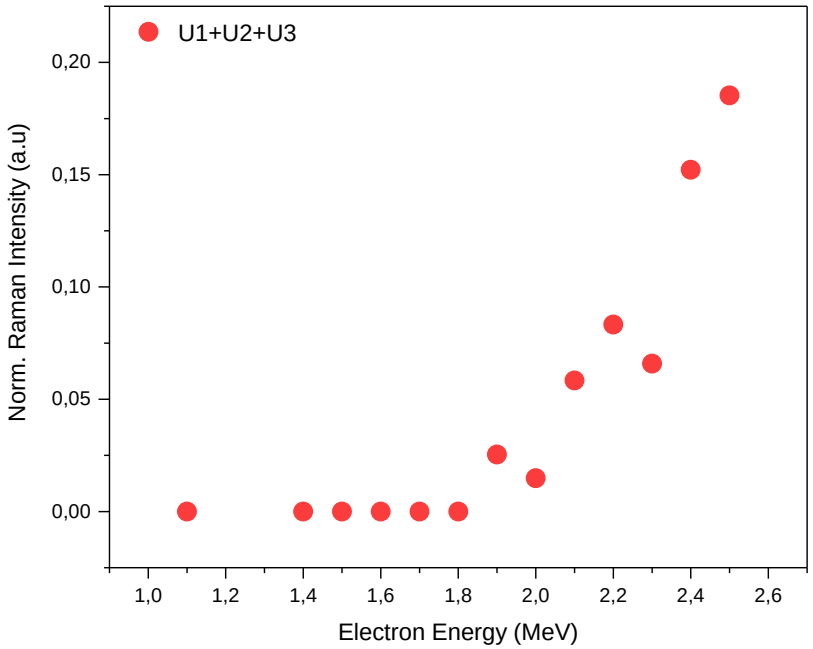

Figure 4.24: Evolution of the Raman triplet band intensity along with increasing electron irradiation energies normalized to constant electron charge at 1.8C

The intensity of the Raman defect bands is almost negligible when the energy of the electrons is lower than 1.8 MeV but then increases linearly when the energy is increased up to 2.5 MeV. In addition, Figure 4.24 shows that the electron energy threshold for the apparition of the defect bands can be estimated to be between 1.8-1.9 MeV.

The calculated electronic and nuclear stopping power values during electron irradiation were required in order to determine the origin of the Raman defect bands. A comparison of the stopping power in the 1.0-2.5 MeV range is illustrated in Figure 4.25.

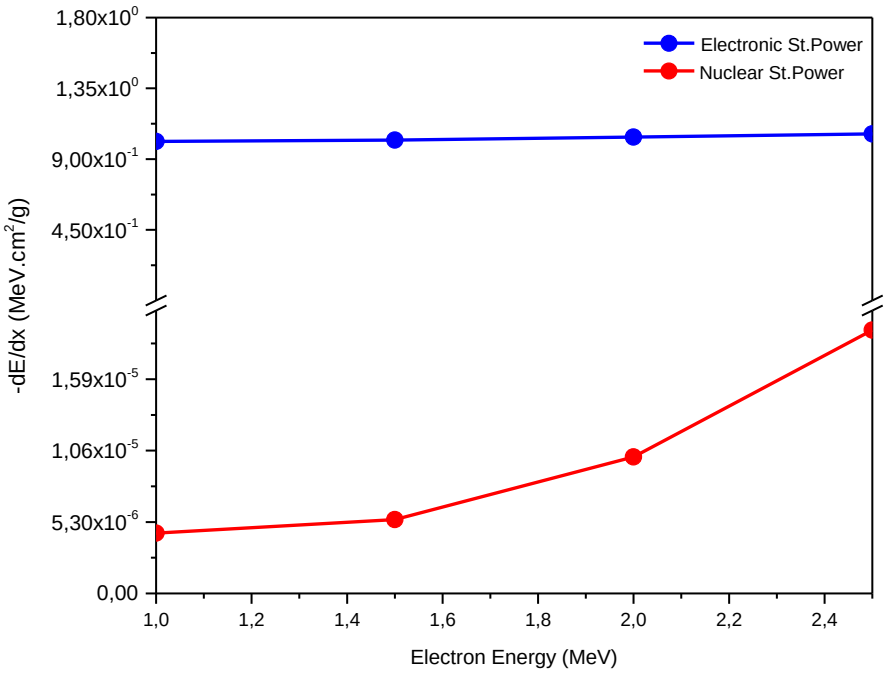

Figure 4.25: Comparison of the electronic and nuclear stopping power in the 1.0-2.5 MeV electron energy range

From Figure 4.24 and Figure 4.25, it can be observed that the intensity of the Raman defect bands follows the same trend as that of the nuclear stopping power; both are characterized by a continuous increase between 1.8 MeV and 2.5 MeV. On the other hand, the electronic stopping power remains almost constant in the same energy range. Thus, this observation provides sufficient evidences to suggest that the irradiation-induced bands observed on Raman spectrum of irradiated nuclear fuels take their origin from the elastic collisions of electrons with UO_2 atoms, i.e. due to the formation of atomistic defects.

In the following sections, an attempt is made to identify the type of atomic defects responsible for the apparition of the Raman defects bands.

4.5.1.1 Attribution of the Raman triplet defect bands to the type of defects resulting from the elastic collisions

Electron irradiation has the possibility to induce defects given that their energies are sufficient enough to displace the UO_2 atoms off their normal positions. As reported in Section 4.3.2, the PAS analysis clearly pointed out the existence of point defects in the irradiated disks. It was also indicated that the concentration of the displaced atoms depends on both electron energy and irradiation charge. In regards to Raman spectroscopy, the increase in the defect bands intensity in the ballistic regime indicates that they are due to the presence of atomistic defects. This

study was extended to determine the type of defects which are consistent with the Raman triplet defect bands, i.e. to differentiate between uranium and oxygen defects.

The concentration of defects produced due to elastic collisions for the different electron energies can be determined by:

$$N = \phi N_o \sigma_t (E) \quad (4.1)$$

Where:

Φ: electron irradiation dose

N_o: atomic density of UO_2

σ_t (E) is the effective cross section for the production of defects by electrons with an energy E. The effective cross section is given by:

$$\sigma_t (E) = \int_{E_d}^{T_m} P(T)\ \nu (T) \frac{d\sigma}{dT} \mathrm{dT} \quad (4.2)$$

Where:

P(T): probability of displacing an atom receiving an energy T higher than its E_d

v(T): number of atoms displaced by an energy T.

T_m: maximum transferred to an atom of atomic mass A by an electron. The latter is expressed in eV and can be estimated using:

$$T_m = \frac{2147.6\ E\ (E + 1.022)}{A} \quad (4.3)$$

E is expressed in MeV.

For diatomic materials, the calculation can be extended by considering the fact that the atoms displaced from one sub-lattice can induce additional secondary displacements. For instance in UO_2, an oxygen atom displaced by an electron can in its turn displace another uranium atom provided that the energy of the oxygen atom is greater than the E_d for uranium atoms. Soullard [124] showed that the cross section for the defect production during secondary collisions is 10^4 times smaller than the mechanisms involving direct collisions. Hence for the need of this study, only displacements resulting solely from direct interactions between the electrons and UO_2 atoms, i.e. only e – O and e –U collisions, were considered for the calculations.

Soullard [124] also reported the differential cross sections for the displacement in the uranium and oxygen sub-lattice resulting from direct collisions. The calculated values for different minimum displacement energies were obtained using the McKinley-Feshbach equation [144] and are illustrated in the figures below.

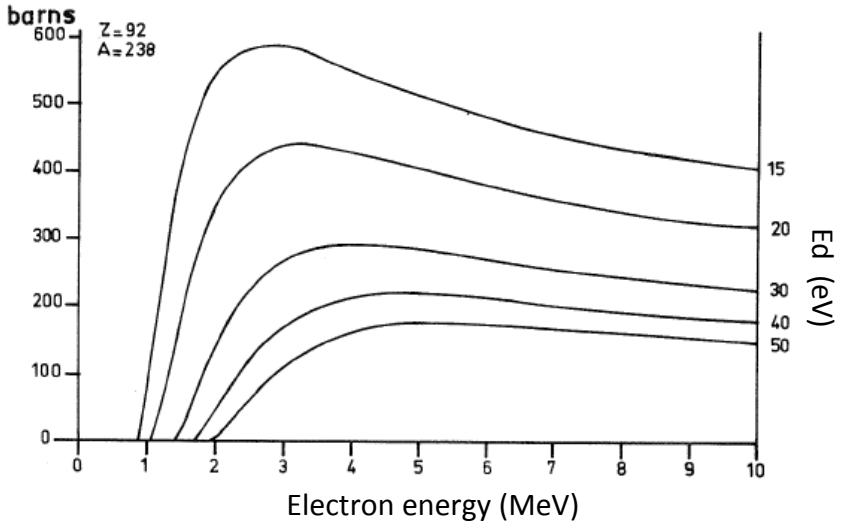

Figure 4.26: Effective cross section for the displacement in the uranium sub-lattice for different Ed values as a function of electron energy

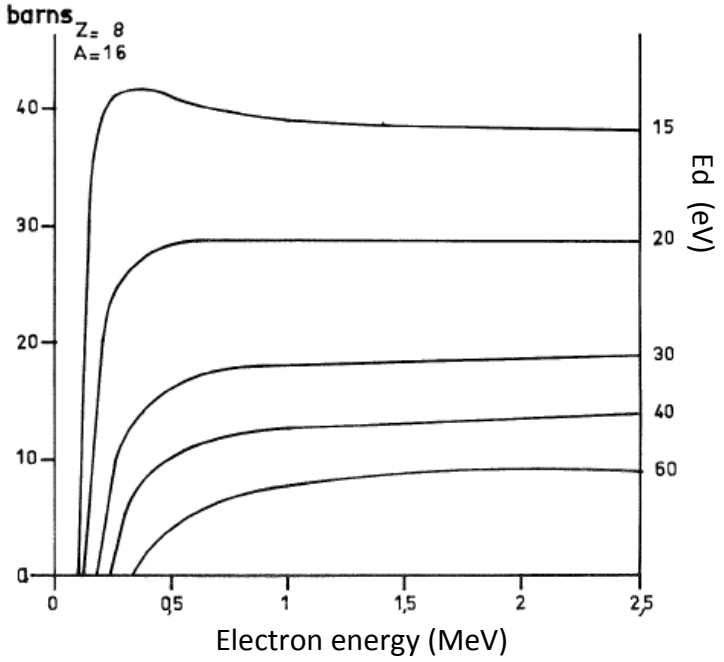

Figure 4.27: Effective cross section for the displacement in the oxygen sub-lattice for different Ed values as a function of electron energy

For the need of the calculations, only the effective cross section curves corresponding to the Ed for oxygen and uranium at 20 eV and 40 eV were considered. Equation 4.1 indicates that the concentration of defects is directly proportional to the effective cross section for the defect production.

Figure 4.26 shows that an electron energy greater than 1.6 MeV is required to induce displacements in the uranium sub-lattice and it can also be observed that the concentration of uranium defects shows a continuous increase in the 1.6-2.5 MeV electron energy range. In regards to the oxygen sub-lattice, electron energies as low as 0.5 MeV are sufficient to displace oxygen atoms but their concentration varies slightly between 1 MeV and 2.5 MeV as shown in Figure 4.27.

The calculated uranium and oxygen defect concentration are tabulated in Table 4.2 and schematically represented as a function of electron energy in Figure 4.28.

Table 4.2: Calculated uranium and oxygen defect concentration in the 1.6-2.5 MeV energy range

Electron Energy (MeV)	**ϕ (é/cm^2)**	**N (U defect production)**	**N (O defect production)**
1.6	1.76E+19	-	2.13E-26
1.9	1.76E+19	2.30E-23	2.13E-26
2	1.76E+19	3.80E-23	2.13E-26
2.05	1.76E+19	3.90E-23	2.13E-26
2.1	1.76E+19	5.40E-23	2.13E-26
2.2	1.76E+19	6.90E-23	2.13E-26
2.3	1.76E+19	8.50E-23	2.13E-26
2.4	1.76E+19	1.08E-22	2.13E-26
2.5	1.76E+19	1.23E-22	2.13E-26

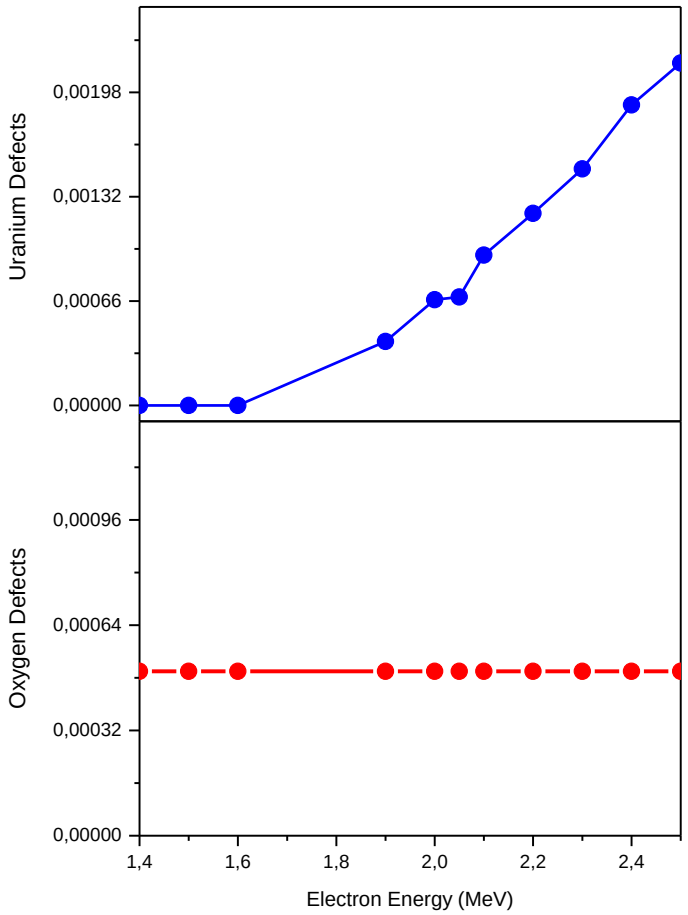

Figure 4.28: Comparison of the oxygen and uranium defect production rate in the 1.6-2.5 MeV electron energy range

The increase in the uranium defect concentration observed between 1.8 MeV and 2.5 MeV follows the same trend as the intensity of the Raman triplet defect bands in the same energy range, as it can be observed in Figure 4.29. This observation suggests that the Raman triplet defect bands might be linked to uranium-type point defects.

In addition, PAS analysis confirmed the presence of point defects involving uranium vacancies, i.e. Schottky defects, in the irradiated UO_2 samples. From Figure 4.29, the Raman defect bands are seen to follow a similar behavior as the PAS S-parameter under increasing electron energy. Thus, this provides addition information to suggest that the Raman triplet defect bands are related to point defects that take their origin from displacements occurring in the uranium sub-lattice.

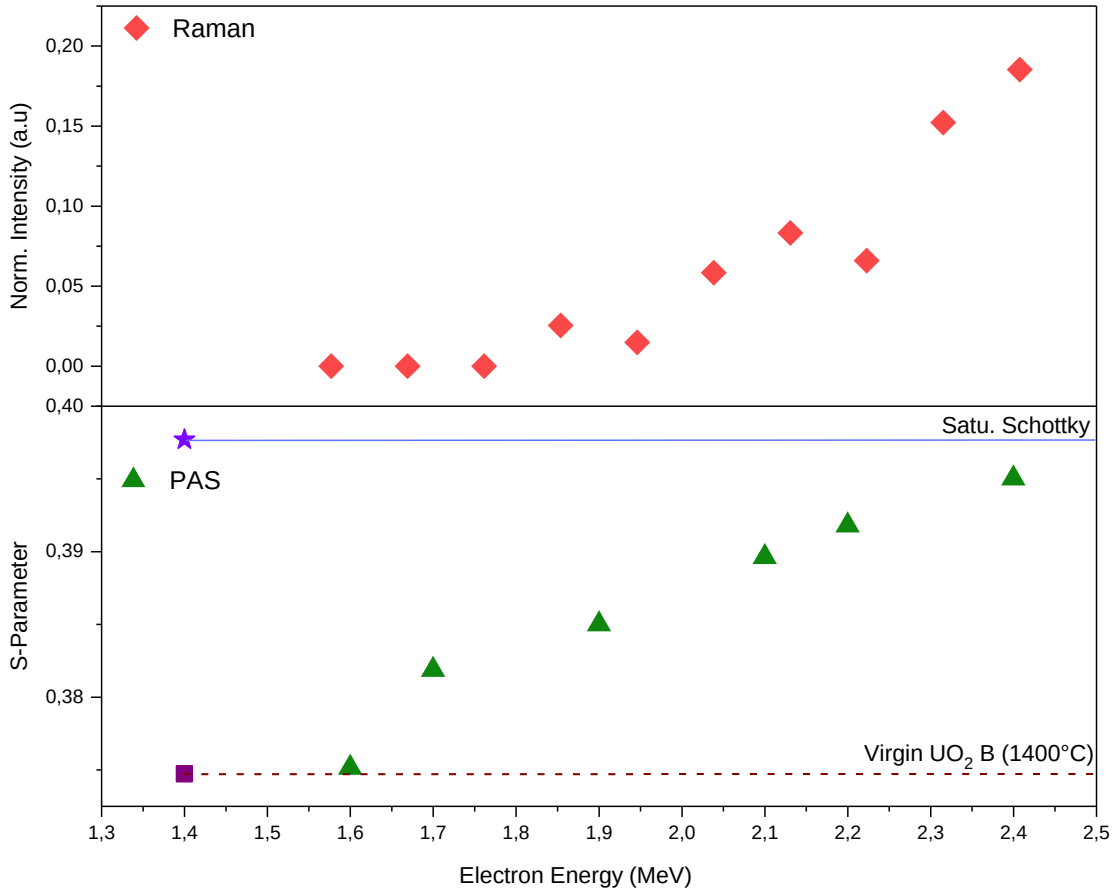

Figure 4.29: Comparison between Raman and PAS results in the 1.6-2.5 MeV electron energy range

It is to be noted that not all the irradiated samples were analyzed by PAS method. Due to the lack of experimental results, it was not possible to normalize all the PAS results to 1.8 C constant electron charge. Hence, the evolution of the S-parameters shown in Figure 4.29 is the same as that previously presented in Section 4.4.2.5.

Figure 4.29 also indicates a difference in the electron threshold energy in regards to the Raman defect bands and PAS S(E) parameter. The minimum electron energy required to induce the apparition of the Raman triplet bands lies between 1.8 MeV and 1.9 MeV. On the other hand, PAS method is capable to characterize point defects that are generated by electrons with energy close to 1.6 MeV. Therefore, PAS technique shows a much higher sensitivity to probe irradiation defects compared to Raman spectroscopy.

4.5.1.2 Raman triplet defect bands: Uranium interstitials *vs*. Uranium vacancies

The electron irradiation experiment carried out in this study allowed to assign the Raman defect bands to irradiation damages involving uranium-type point defects. However, additional information is still required in order to differentiate between uranium interstitials and uranium vacancies. In this section, an attempt is made to determine the exact origin of the Raman defect bands by comparing the Raman and PAS data that are reported in the literature.

Desgranges et *al.* [108] used the Raman spectroscopy to show that the irradiation defects induced in a UO_2 sample irradiated with a 25 MeV alpha beam are completely annealed at a temperature between 375°C and 525°C. On the other hand, Labrim *et al.* [109] investigated the thermal evolutions of the S(E) and W(E) parameters of a 25 MeV irradiated UO_2 disk. The authors reported that the uranium vacancies are annealed at a temperature between 800°C and 1300°C. These data are consistent with those reported by Garcia *et al.* [145], Nakae *et al.* [146] and Weber [147].

The difference in the annealing temperature states that the uranium-type defect observed by Raman is not the same as that characterized by PAS method. As PAS technique is predominantly sensitive to vacancy-type defects, it can be said that uranium interstitials are involved in the mechanisms which are responsible for the apparition of the Raman triplet defect bands.

However, Raman spectroscopy is not sensitive to point defects and first-principles electronic structure calculations showed that the formation energy of U-interstitial (7.33 eV) is relatively higher than O-vacancy (6.54 eV) and O-interstitial (-0.15 eV) but is approximately half the formation energy of U-vacancy defect (10.67 eV) [148]. In another study, Dorado *et al.* [149] reported that the U-interstitial mechanism in UO_2 is very unlikely due to its high activation energies compared to oxygen-type defects.

Therefore considering their high formation energy, it can be hypothesized that U-interstitial defects produced during irradiation are instantaneously re-arranged in such a way that they invoke symmetry-breaking spectroscopic features. The latter is visible by Raman spectroscopy and appears as the Raman defects bands.

4.5.2 Ageing of UO_2 irradiated disks

In this section, the effect of irradiation defects during UO_2 ageing will be discussed. For this study, the 2.3 MeV irradiated UO_2 was stored in ambient-air for a duration of 15 months. Raman spectroscopy was used to characterize the surface evolution of the disk at different time intervals. Measurements were also performed on an unirradiated UO_2 which was used as reference for this study. XRD method was used as an additional tool to support Raman results.

The virgin and 2.3 MeV irradiated UO_2 disks were both initially characterized (t = 0) and the changes occurring in 465-700 cm^{-1} spectral range measured at different time intervals are presented in Figure 4.30.

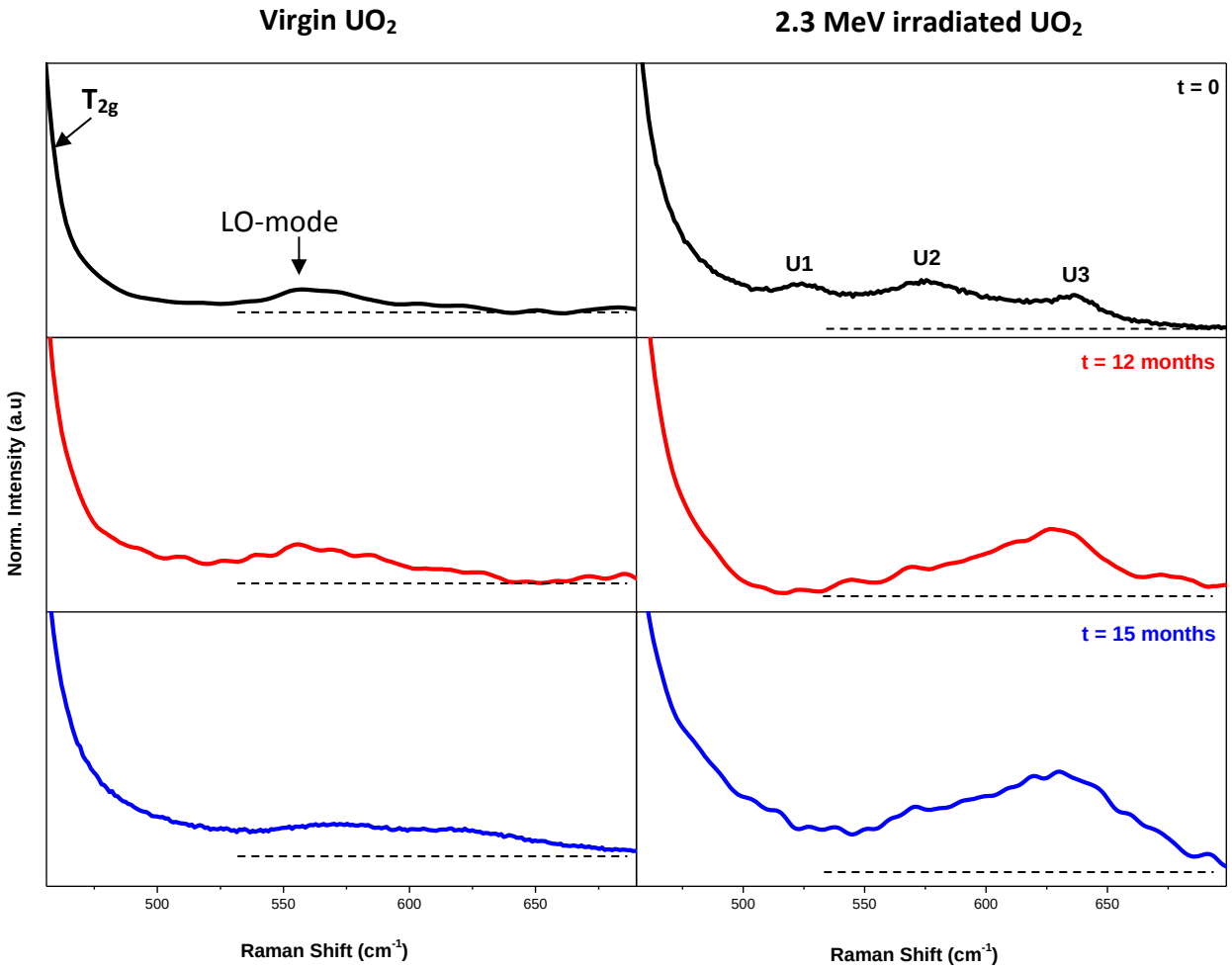

Figure 4.30: Raman spectra evolution of the virgin and 2.3 MeV irradiated UO_2 during continuous air exposure under ambient conditions

The initial Raman analysis of the virgin UO_2 sample shows the presence of the forbidden LO-mode at 568 cm^{-1}. Figure 4.30 shows no major evolution of the Raman spectra of the virgin UO_2 except a relatively small band at 630 cm^{-1} that appeared after 15 months of air exposure. This band has previously been reported by Desgranges *et al.* [96] & He *et al.* [150] and was attributed to the formation of a UO_{2+x} layer.

On the other hand, the irradiation defects induced by the 2.3 MeV electron beam can clearly be evidenced by the presence of the triplet defect bands (U1, U2 & U3) on the Raman spectra of the irradiated UO_2 (t = 0). The continuous air exposure of the irradiated sample causes a significant increase in the 630 cm^{-1} band intensity. It can be seen that the Raman triplet defect bands are completely overshadowed by the 630 cm^{-1} peak after 15 months. Thus comparing the Raman spectra of the virgin and irradiated UO_2, the obtained results indicate that irradiation defects enhance the UO_2 surface oxidation mechanisms.

At the end of the study, i.e. after 15 months of air exposure, both samples were analyzed by XRD method to measure the degree of UO_2 oxidation. In addition, the measurement was also conducted on the 2.5 MeV (1.8 C) irradiated UO_2, which left in ambient-air for three weeks after its irradiation. The study of the 2.5 MeV irradiated sample aims to investigate whether the oxidation mechanism is initiated immediately after the irradiation campaign.

Figure 4.31 illustrates the X-ray patterns at the (111) and (200) selected reflections for the three UO_2 disks at low diffractions angles.

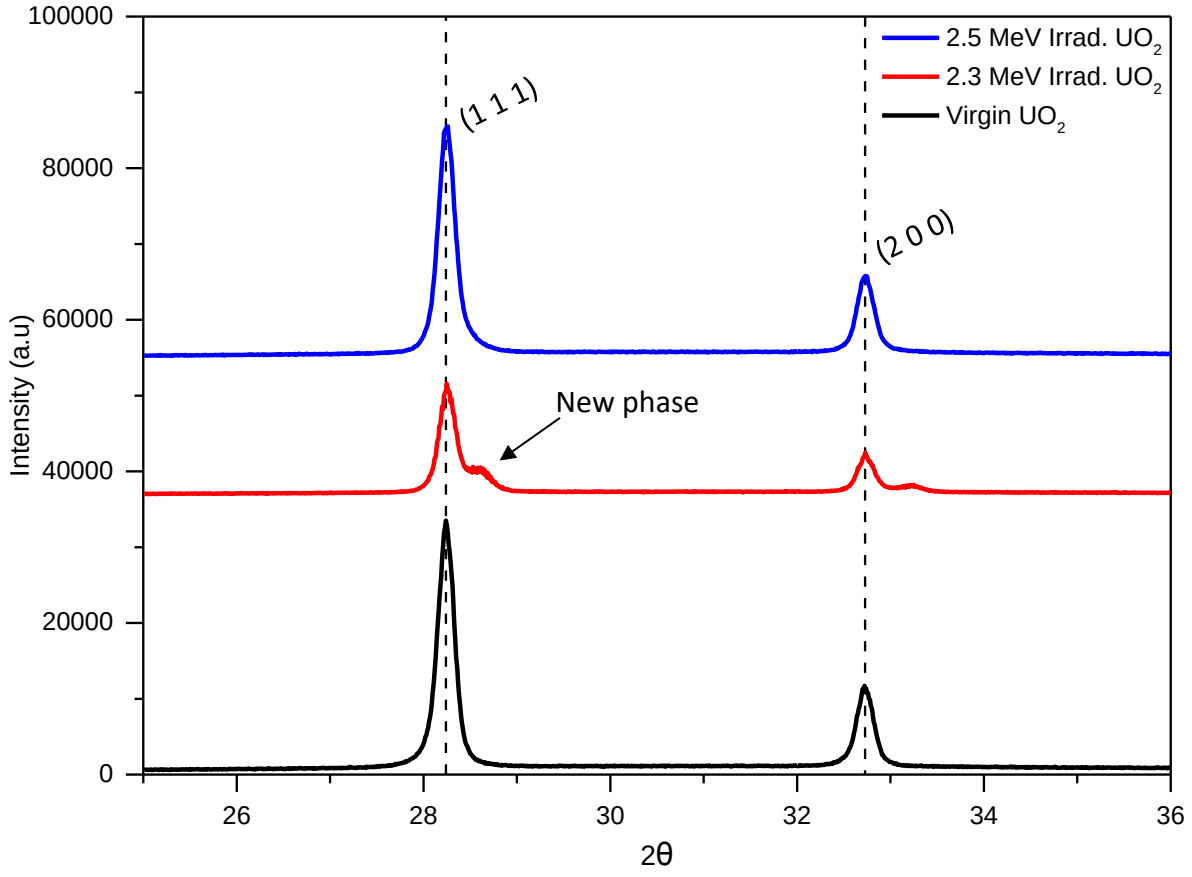

Figure 4.31: Low angles X-ray diffraction patterns for the virgin and 2.3 MeV irradiated UO_2 (both analyzed 15 months after exposed to air) and the 2.5 MeV irradiated UO_2 (analyzed few weeks after its irradiation)

Figure 4.31 does not show major differences in the X-ray patterns for the virgin and 2.5 MeV irradiated UO_2. Their peaks on the diffraction patterns do not deviate from the (111) and (200) reflections of a stoichiometric UO_2 cell (illustrated by the black dotted line).

In regards to the 2.3 MeV irradiated UO_2, the presence of additional peaks occurring next to the UO_2 peaks can be observed. According to Tempest *et al.* [151] and Taylor *et al.* [152], these peaks are due to the formation of cuboctahedral oxygen clusters and thus, correspond to the presence of a UO_{2+x} superlattice. A similar observation was reported by Elorrieta *et al.* [153] where the intensity of the additional peaks was seen to increase with higher degree of stoichiometry in UO_2.

These observations are consistent with Raman data and hence confirm the surface oxidation of the 2.3 MeV irradiated UO_2. The lattice constant of the oxidized phase was determined by Rietveld analysis and measured to be 5.4033Å. The latter corresponds to an intermediate phase between U_3O_7 (5.38 Å) [154] and U_4O_9 (5.4431 Å) [155].

4.5.2.1 Discussion

The surface oxidation of unirradiated UO_2 under ambient conditions has been reported by several authors [[16], [156], [157] & [158]]. In addition, Kim *et al.* [159] evidenced a significant difference in the oxidation behavior of virgin and irradiated UO_2 fuels at elevated temperatures. A similar observation was recorded in this study but the experiments were conducted under ambient temperature conditions.

According to McEachern [160], oxygen diffusion can be regarded as the rate-determining step for UO_2 oxidation. In addition, the authors reported that the rapid oxidation of the irradiated disk under ambient conditions can be due to a supersaturation of the oxygen vacancy concentration. Thus, it can be said that the UO_2 oxidation mechanism is driven by the mobility of oxygen vacancy defects. In UO_2, oxygen vacancies show a favorable diffusivity and are highly mobile compared to oxygen interstitials as indicated by their migration energy values in Table 4.3.

Table 4.3: Migration energy for oxygen interstitials (Io) and vacancies (Vo) in UO_2 (eV)

Defect type	**Dorado *et al.*** [161]	**Gupta *et al.*** [162]	**Kuskin *et al.*** [163]	**Norman *et al.*** [164]
I_O	3.6	2.14	0.68	0.8-1.3
V_O	1.2	1.01	0.32	0.5-0.6

Due to their low migration energy values, oxygen vacancies are more likely to diffuse through the lattice and move towards the UO_2 sample surface. A study carried out by Corkhill *et al.* [165] showed that the presence of oxygen vacancies near the fuel surface give rise to energetically reactive sites which enhance the fuel surface reactivity.

In this study, the irradiated UO_2 disks were stored in ambient-air conditions. The migration of oxygen vacancies near to the UO_2 surfaces creates a difference in the oxygen concentration gradient near the UO_2-air interface. To restore thermodynamic equilibrium, oxygen atoms are allowed to diffuse in the UO_2 to occupy the oxygen vacant sites. Thus, the high oxygen mobility near the UO_2 interface decreases the oxygen vacancy concentration and can also be regarded as the initiating step towards the UO_2 oxidation mechanisms.

A schematic representation of the proposed UO_2 oxidation mechanisms driven by the diffusion of oxygen near the UO_2-air interface is illustrated in Figure 4.32.

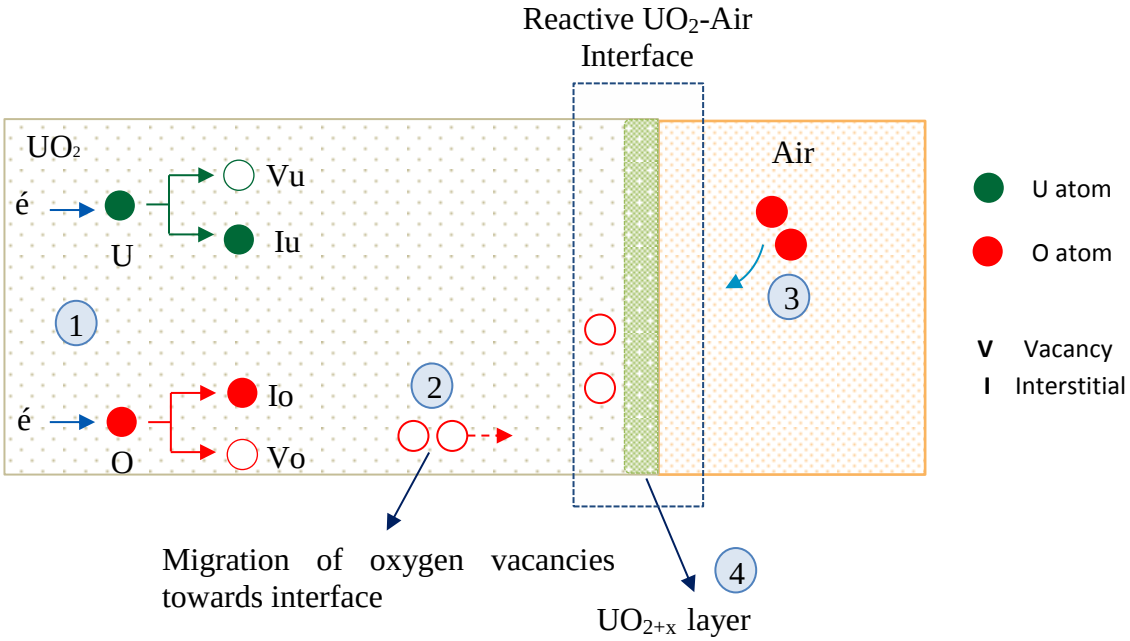

Figure 4.32: Different steps involved during the oxidation mechanisms of irradiated UO_2 stored under ambient-air conditions. *1:* Production of uranium and oxygen point defects, *2:* Migration of oxygen vacancies towards the fuel interface, resulting in the formation of energetic reactive surface sites, *3:* Diffusion of oxygen atoms from air towards the reactive surface sites, *4:* Formation of the oxidized UO_2 layer due to the enhanced oxygen mobility.

The proposed mechanism is in good agreement with the oxidation of the 2.3 MeV irradiated UO_2 disk. The absence of traces of oxidation on the 2.5 MeV irradiated disk shows that the oxidation mechanism is not initiated immediately after irradiation, but sufficient time is required to allow the migration of oxygen vacancies near the UO_2 surfaces.

In regards to the virgin UO_2 disk, such energetically reactive sites near the UO_2 boundary do not hold much importance mainly due to the absence of irradiation defects. Hence compared to the irradiated UO_2, the increase in the surface reactivity and enhance oxygen diffusion are not expected to occur, which therefore explains its lower degree of oxidation.

4.6 Conclusions

This work was intended to provide detailed information regarding the irradiation-induced triplet bands which appear on the Raman spectra of irradiated nuclear fuels. In this study, an electron irradiation experiment was conducted using different sintered UO_2 disks. During irradiation, electrons lose most of their energy via inelastic collisions but they can also interact elastically to displace UO_2 atoms off their lattice positions. The aim of this study was to identify the types of irradiation defects that are responsible for the apparition of the Raman triplet defect bands.

Several UO_2 samples were irradiated at SIRIUS irradiation facility (LSI, École Polytechnique), in the 1.6-2.5 MeV electron energy range. The irradiation conditions were justified by the fact in the selected energy range; the electronic stopping power remains almost constant while the nuclear stopping power increases gradually as a function of electron energy.

The evolution of the Raman triplet defect bands intensity as a function of electron energy was investigated by two different approaches; namely *(a)* characterization of irradiated surfaces and *(b)* Raman mapping along the depth of a sectioned irradiated disk. It was shown that the electron energy threshold for the apparition of the triplet defect bands lies between 1.8 MeV and 1.9 MeV. The intensity of the defect bands was seen to increase as a function of electron energy up to 2.5 MeV. This observation is consistent with the evolution of the nuclear stopping power in the same energy range. Thus, the obtained findings indicated that the Raman defect bands take their origin from the ballistic collisions of the incident electrons with the UO_2 atoms and are due to the formation of atomistic defects.

The presence of point defects in the irradiated UO_2 disks was confirmed by PAS and XRD measurements. The correlation between the Raman triplet defect bands and the types of point defects was then determined. The concentration of uranium and oxygen point defects was calculated using numerical methods. It is observed that the energy threshold for the apparition of the Raman defect bands lies close to the minimum electron energy required to induce displacements in the uranium sub-lattice (1.6 MeV) compared to the oxygen sub-lattice (0.5 MeV). The calculated uranium concentration was also seen to follow the same tendency as the Raman triplet defect bands intensity in the 1.6-2.5 MeV range. These observations indicated that the irradiation-induced bands on the Raman spectrum are related to displacements in the uranium sub-lattice.

Finally, the ageing of virgin and irradiated UO_2 disks when stored under ambient air conditions was investigated. It was observed that the presence of irradiation defects accelerates the UO_2 oxidation. A suitable oxidation mechanism model, based on chemical reactions occurring near the UO_2 surface-air interface due to the migration of oxygen vacancies towards the UO_2 surface boundary, was then proposed. It was also reported that the oxidation mechanism is not initiated immediately after irradiation, but occurs gradually along with increasing air exposure.

Chapter 5

Behavior of Raman triplet defect bands during UO_2 leaching study

5.1 Introduction

In the previous chapter, it was evidenced that the migration of oxygen defects near the surfaces of UO_2 disks enhances the fuel surface reactivity, which initiates a chemical reaction mechanism between the UO_2 disk and ambient air. In regards to the interim wet storage of irradiated nuclear fuels, it is interesting to quantify the role of these reactive boundary surfaces. This chapter is devoted to investigate the interplay of alpha irradiation-induced defects when the irradiated UO_2 is in contact with aerated water.

The first part of this chapter will be devoted to detail a unique *in situ* Raman experimental set-up that was used to measure the formation kinetics of irradiation defects during the alpha irradiation of a UO_2/H_2O system. The obtained results were then compared with a reference UO_2/Argon system, i.e. a UO_2 sample was irradiated under a chemically non-reactive inert environment. The comparison between the UO_2/H_2O and UO_2/Argon systems aims to investigate whether the irradiation conditions impact the formation kinetics of irradiation defects.

The study was further extended to investigate the effect of alpha irradiation on the UO_2 oxidative dissolution mechanisms. It has been speculated that irradiation-induced damages involving the accumulation of point defects in the crystalline structure of nuclear fuels impact their dissolution behavior [[166]- [167]]. For instance, research focused on the leaching study of PuO_2-surrogate compounds, such as CeO_2, showed that the cationic release rate is higher for both hypo-stoichiometric and ion-implanted CeO_2 compared to stoichiometric CeO_2 [[168]-[169]]. However in regards to UO_2, the latter is difficult to quantify because several factors impact its normal dissolution such as the rapid oxidation of U(IV) into U(VI) which is highly water

soluble, amongst others. Hence in this study, an alternative approach was adopted to correlate the irradiation-induced point defects and uranium release in the aqueous solution.

5.2 Experimental installation

5.2.1 *In situ* Raman experimental set-up

In situ Raman experiments specify that Raman measurements are performed in an irradiation chamber during and without irradiation, where no human access is allowed when the irradiation beam is turned on. Irradiation can cause significant damages to equipment and it is more advisable to limit the exposure of the main components of the Raman spectrometer to irradiation. Hence taking into consideration all these limiting factors, a unique *in situ* Raman experimental installation was designed at CEHMTI-CNRS, Orléans and used in this study. The latter consisted of two different set-ups: first one was placed in the irradiation chamber and the second one was located in another chamber, referred as the safety room. A schematic simplified representation of the experimental installation is shown in Figure 5.1.

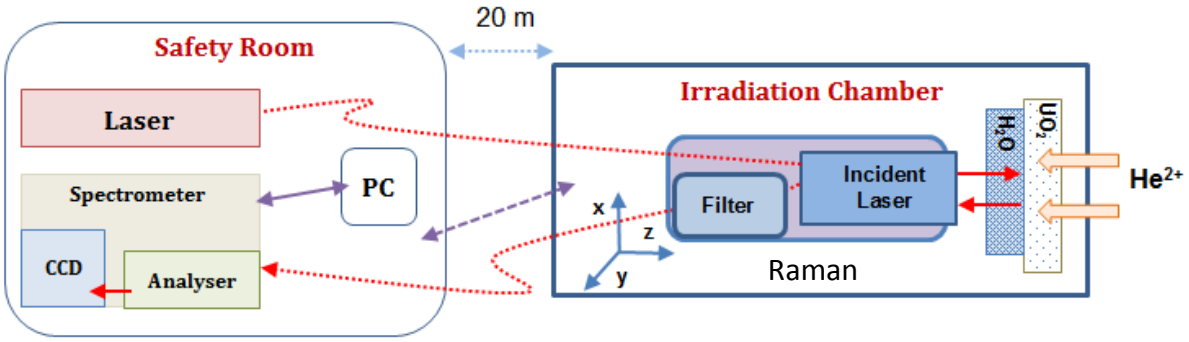

Figure 5.1: Diagram showing the *in situ* experimental set-up contained in the irradiation chamber and the safety room

An irradiation cell, containing the UO_2 disk and a contact medium (aerated water in the scenario shown in Figure 5.1), was accommodated in the irradiation chamber Gate 2 of the cyclotron facility. During irradiation, the non-polished UO_2 surface is held in the direction of the incoming alpha beam, while the polished surface remains in contact with the water slab, i.e. representing the UO_2/H_2O interface. The irradiation conditions were chosen such that the alpha ions are allowed to irradiate the UO_2 disk and then pass through the sample to be attenuated in the aqueous medium.

For the *in situ* measurements, a Raman probe head positioned on a three-dimensional XYZ motion-control system (Newport MFA and ILS 250 stages) was installed behind the irradiation cell, i.e. facing the irradiation beam. The probe head uses an ultra large working distance (30

mm) 20x microscope objective and is controlled by an eight-axes Newport XPS driver system located in the safety room. A visualization system integrated in the Raman head allows to calibrate both the position and focalization of the Raman incident laser beam onto the UO_2 surface (spot size of the laser on the sample: ~1 µm) as illustrated in Figure 5.2.

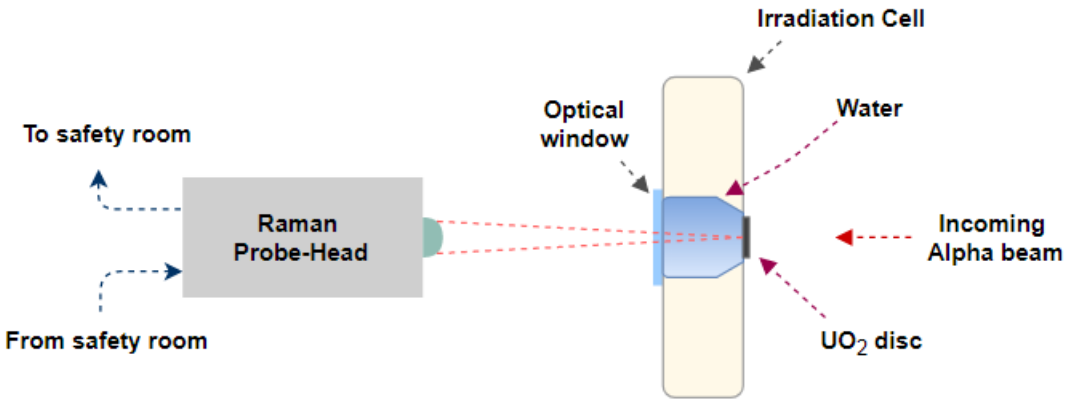

Figure 5.2: Schematic diagram of part of the *in situ* Raman installation placed in the irradiation chamber

Figure 5.3 shows a general representation of the *in situ* Raman set-up installed in the irradiation chamber of the cyclotron facility at Orléans.

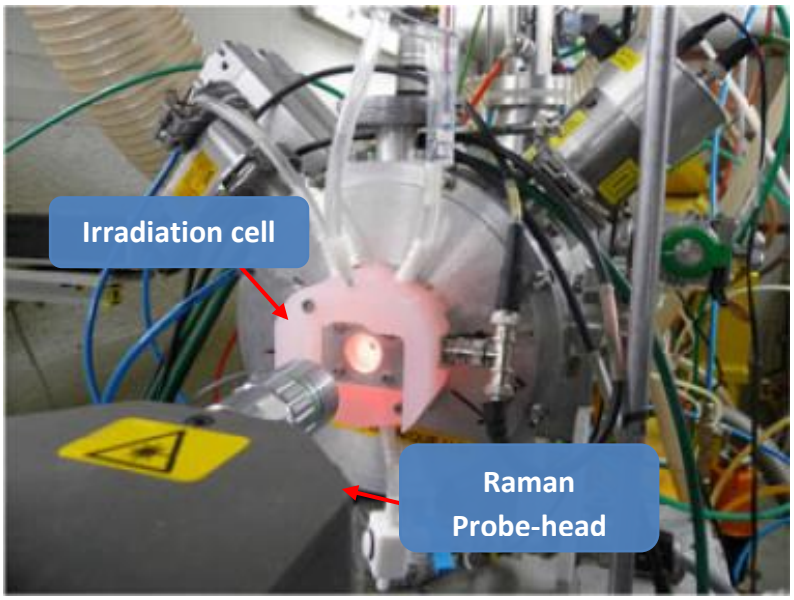

Figure 5.3: Overview of the *in situ* Raman installation used during the UO_2 leaching study. The irradiation cell, containing the UO_2 disk and water, is loaded onto the beamline (alpha beam arrives from the rear side of the view). The Raman probe-head and microscope objective can also be distinguished

To avoid radiation damage, all the essential components that form part of the luminous Renishaw RA100 spectrometer were placed in the safety room which is located 20 m away from the irradiation chamber. The connection between the irradiation chamber and the safety room was ensured through the use of optic fibers and electrical cables.

5.2.2 Alpha irradiation conditions

The radioactive alpha decay of spent nuclear fuels produces an alpha particle of ~5 MeV and a recoil atom of ~100 keV [170]. SRIM software was used to replicate the alpha decay of actinides under laboratory conditions. For the need of this experiment, a 45 MeV alpha beam was used to irradiate a UO_2 disk having a thickness of 300 ± 5 µm and a diameter of 8 mm.

Under these conditions, the alpha ions are firstly allowed to irradiate the UO_2 disk and then reach the back surface at 5 MeV as illustrated in the figure below.

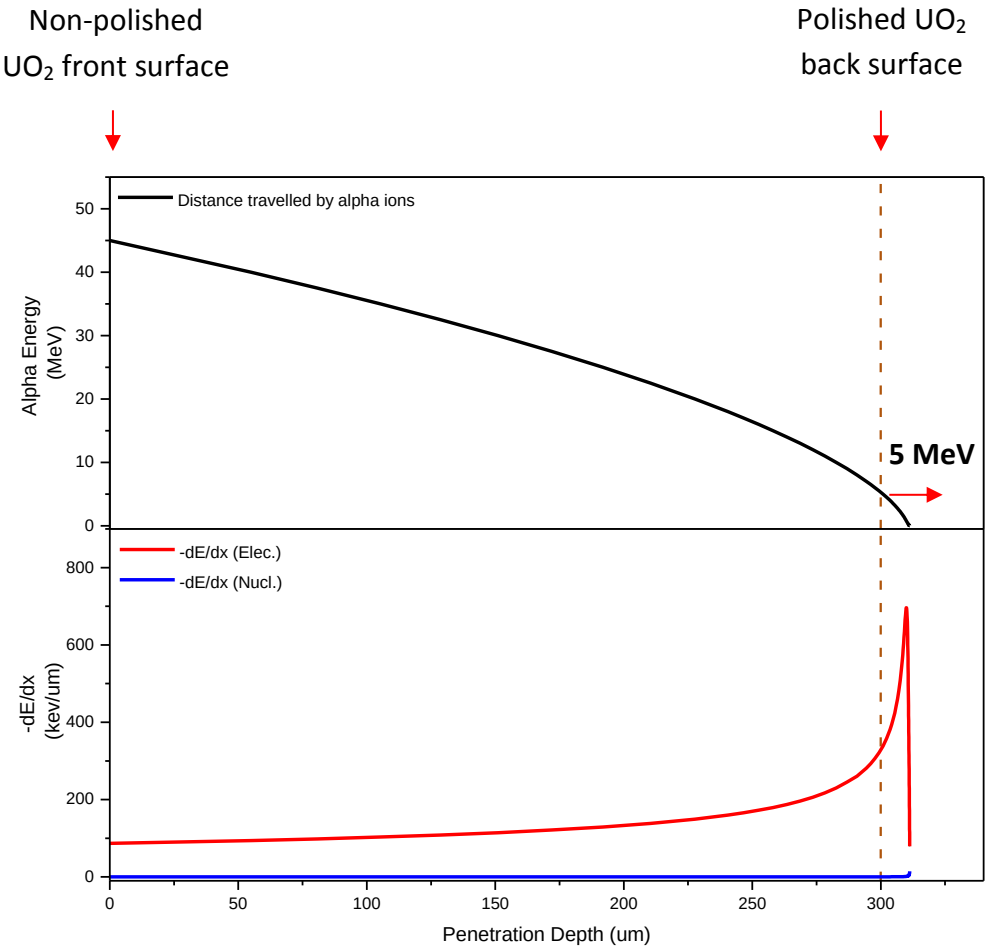

Figure 5.4: Distance travelled by the alpha ions and the stopping powers (Nuclear and Electronic) of UO_2 during the implantation of 45 MeV alpha ions

In this study, the UO_2 were irradiated under two different settings; *(a)* in contact with reactive medium (aerated water) and *(b)* in contact with an inert gaseous medium (argon gas). The following sections are devoted to present a detailed description of the two different *in situ* experiments.

5.2.3 Alpha irradiation of UO_2 in contact with aerated water

A new irradiation cell capable of holding a UO_2 disk tightly in contact with water during the irradiation process was designed and manufactured for the leaching experiment. A schematic representation of the irradiation cell is shown in Figure 5.5.

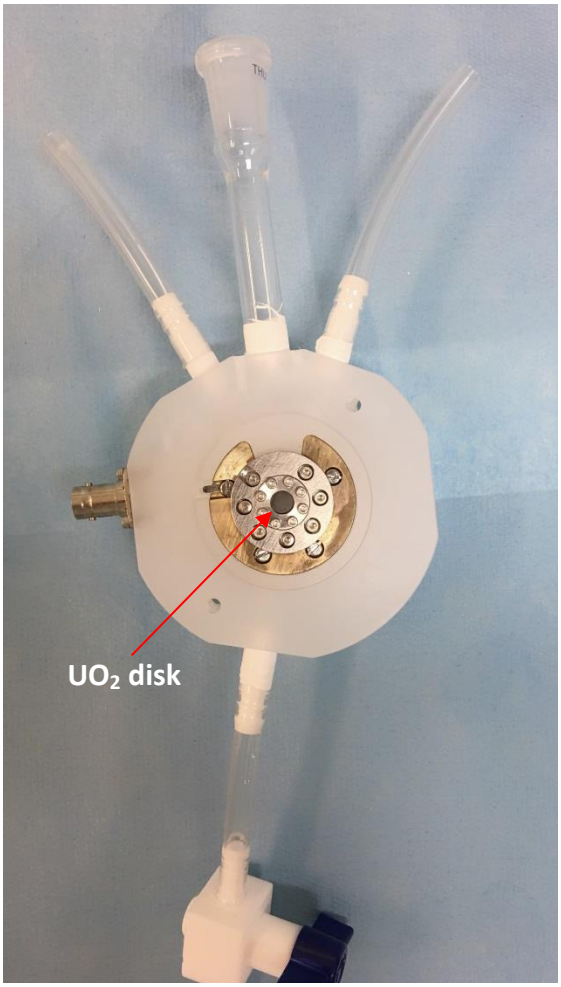

Figure 5.5: Illustration of the irradiation cell used for the leaching experiment showing the UO_2 surface which is exposed to the incoming alpha beam

The irradiation cell was constructed using a poly (chloro-tri-fluoro-ethylene) [(PCTFE: $(CF_2CClF)n$] material. The PCTFE material was chosen because it shows a good resistance against both ionization radiation and radiolytic species. It also exhibits low absorption characteristics towards uranium in solution and good mechanical properties insuring minimal deformation during machining and operating conditions.

The UO_2 disk was mounted in the irradiation cell such that the non-polished surface was positioned in the direction of the incoming irradiation beam while the polished surface was placed to the inside in order to be in contact with the aqueous medium. The volume of the water solution that can be accommodated in the sample holder varies from 10 to 20 mL which is equivalent to a 2 cm thick water slab. Precautions were taken to prevent any leakage so as to limit the escape of the aqueous solution containing the dissolved uranium, which may also lead to radiological contamination.

In addition, due to the supports required to hold the disk during irradiation, the surface of the sample exposed to the alpha beam has a diameter of 4 mm. The cyclotron device was used to deliver a 45 MeV alpha beam and 50 nA ionic flow to reach a final fluence of 7.06×10^{15} α/cm^2. According to SRIM simulations, the chosen irradiation conditions produce a total defect concentration of 3.62×10^{-2} per α ion in the UO_2 bulk.

The initial energy of the alpha ions is reduced as a result of their collisions with UO_2 atoms. The incident ions emerge from the UO_2 at 5 MeV and are then attenuated over a distance of 37 µm in the water solution [25]. The 2 cm thick water slab is therefore largely sufficient to stop all the alpha ions to prevent their escape from the irradiation cell. The attenuation initiates a water radiolysis mechanism which results in the production of several radiolytic species such as radicals, hydrated electrons and hydrogen peroxide.

It is important to note that during water alpha radiolysis, the density of the radicals increases in the ionization tracks and the probability for a recombination of short-lived radicals to form H_2O_2 and H_2 is higher than their diffusion from the spurs in which they are formed [[35]- [37]]. These species, in particular H_2O_2, are more likely to accelerate the alteration of the irradiated UO_2 back surface through oxidizing dissolution and the precipitation of secondary U(VI) phases on the altered layer.

An illustration of the accumulation of irradiation defects and formation of secondary U(VI) altered phases during the alpha irradiation of the UO_2/H_2O system is shown in Figure 5.6.

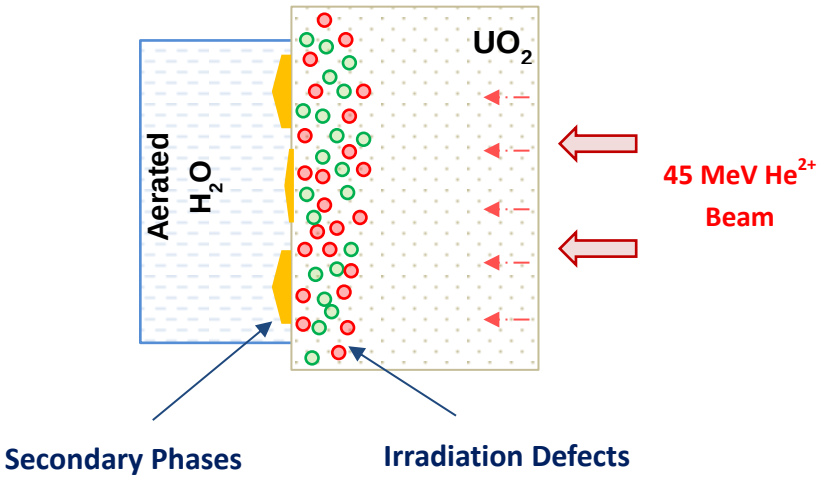

Figure 5.6: Alpha Irradiation of the UO_2/H_2O system indicating the formation of irradiation defects and secondary U(VI) phases

5.2.4 Alpha irradiation of UO_2 under inert gaseous conditions

The UO_2 ceramic was placed in a similar configuration in the irradiation cell as previously described for the UO_2 dissolution study, except that the aerated water solution was replaced by a chemically inert gaseous medium. Argon gas was chosen for this experiment because it provides an inert UO_2 boundary interface to which the mechanisms occurring near the UO_2-H_2O interface can be compared.

The irradiation parameters chosen for this study were similar to those employed for the UO_2 leaching experiment so as to be representative both in terms of irradiation fluence and accumulated irradiation defects in the sample. However, the attenuation of the 5 MeV alpha ions in the inert gaseous medium generates an Ar-plasma. The latter can be distinguished on the Raman spectra because it appears as an intense and narrow peak at 825 cm^{-1} with the red (633 nm) excitation laser. Contrary to Raman lines, the position of this plasma line is defined by an absolute wavenumber, not a relative one on the Raman shift scale.

Figure 5.7 shows the mechanism that occurs during the alpha irradiation of the UO_2/Ar system.

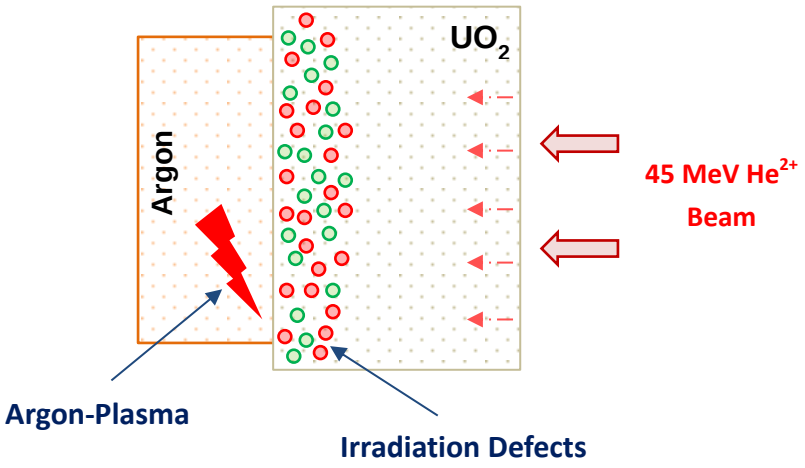

Figure 5.7: Alpha Irradiation of the UO_2/Ar system indicating the formation of irradiation defects and argon-plasma

5.3 Experimental protocol

In regards to the alpha irradiation of the UO_2/H_2O system, a special experimental protocol had to be adopted mainly due to the presence of a reactive contact medium. The individual steps involved will be described in this section.

The different experimental protocols applied to the UO_2 disk, after it was mounted in the irradiation cell, can be summarized as follows:

1. Normalization of the UO_2 polished surface with the aqueous solution before irradiation
2. *In situ* Raman measurements of the UO_2/H_2O interface during irradiation
3. *In situ-post irradiation* measurements of the UO_2/H_2O interface

The objectives of the different protocols were mainly to determine the evolution of the UO_2-H_2O interface under and without the influence of alpha irradiation through the use of Raman spectroscopy and also to quantify the concentration of uranium dissolved in the solution during the different stages of the experimental procedures. A complete description of the different sequential stages is presented in the following paragraphs.

5.3.1 Normalization of the UO_2 polished surface with the aqueous solution before irradiation

A sequential pre-leaching with carbonated water and pure aerated demineralized water was conducted on the UO_2 polished surface before starting the irradiation campaign. Carbonated water (10^{-3} M) was initially filled and left for 1 hour in the irradiation cell in order to remove any traces of oxidized layer from the UO_2 surface. Two such pre-leaching steps were carried out (2 x 1 hour).

Following the removal of the oxidized UO_2 layer, the irradiation cell was then positioned on the cyclotron beam line. Two other sequential pre-leaching steps using pure aerated demineralized water were then conducted (2 x 1 hour). This procedure enables to quantify the uranium concentration released from an unirradiated disk when exposed to aerated water solution. The concentration of the dissolved uranium was taken as reference to which the uranium release under the effect of irradiation can be compared. In addition, a Raman acquisition was carried out during the pre-leaching with aerated demineralized water. In doing so, it was possible to stabilize and enhance the Raman signals for a better measurement of the UO_2/H_2O interface under irradiation.

5.3.2 *In situ* Raman measurements of the UO_2/H_2O interface during irradiation

After the pre-leaching step, the irradiation cell was filled with 15 mL of aerated deionized water. The pH of the aqueous solution was kept in equilibrium with air, i.e. close to ~5.5. The irradiation beam was then turned on and an *in situ* Raman measurement of the UO_2/H_2O interface was carried out.

The objective of this study was to investigate the formation kinetics of the Raman triplet defect bands. Hence, a continuous Raman measurement was carried out on the UO_2/H_2O without any interruptions during the irradiation process.

5.3.3 *In situ-post irradiation* Raman measurements of the UO_2/H_2O interface

At the end of irradiation, the UO_2 disk and irradiated water solution were left in the sample holder for additional 10 hours. The Raman acquisition was extended to investigate whether a change in the kinetics of the Raman triplet defect bands is observed when the alpha beam is turned off.

After the *in situ-post irradiation* Raman measurements, the irradiated aqueous solution was recovered and transferred into suitable flasks for further detailed chemical analysis. The latter aimed to determine the concentration of radiolytic H_2O_2 and dissolved uranium in the solution. Molecular H_2O_2 dissociates rapidly into hydroxyl radicals under exposure to UV light. Thus, the flasks were enrolled with aluminium foils and stored at low temperature (in fridge ~4°C). On the other hand, the irradiated UO_2 disk was dismantled from the irradiation cell and stored for subsequent surface characterizations.

Figure 5.8 shows a representation of the different experimental steps that were involved during the UO_2 leaching study.

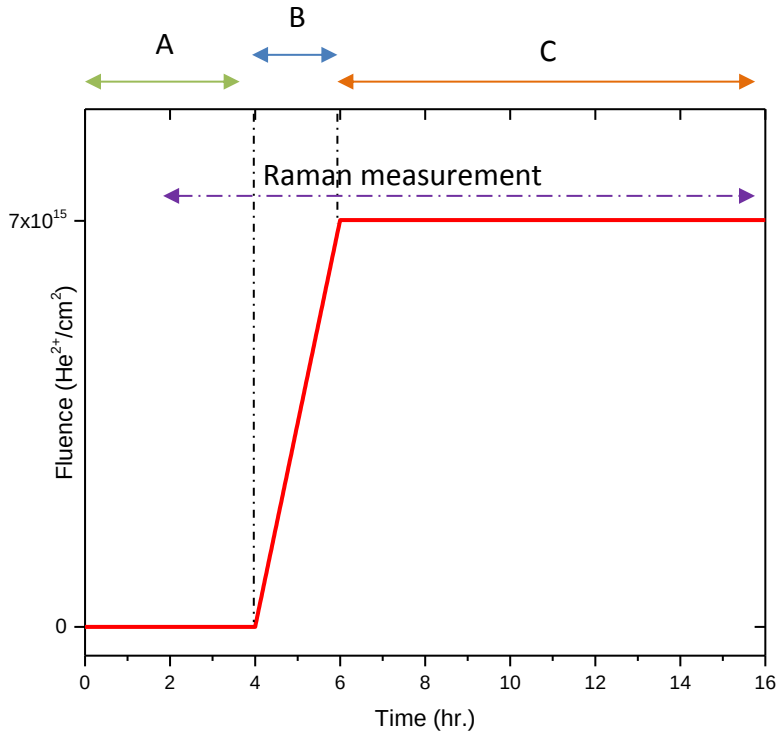

Figure 5.8: Schematic representation of the experimental protocol applied during the UO_2 leaching experiment. ***A:*** Pre-leaching with carbonated water (2 x 1 hour) followed by surfaced stabilization with aerated water (2 x 1 hour), ***B:*** Irradiation and *in situ* Raman analysis of the UO_2/H_2O system during irradiation, ***C:*** *In situ-post irradiation* Raman measurements of the UO_2/H_2O interface when the alpha beam was turned off

5.4 Results: Alpha irradiation of UO_2/H_2O system

5.4.1 Raman measurements

The Raman spectra of the UO_2/H_2O interface acquired at the end of each experimental protocol used in this study, i.e. pre-leaching with aerated water, alpha irradiation and *in situ-post irradiation* Raman measurements, are presented in Figure 5.9.

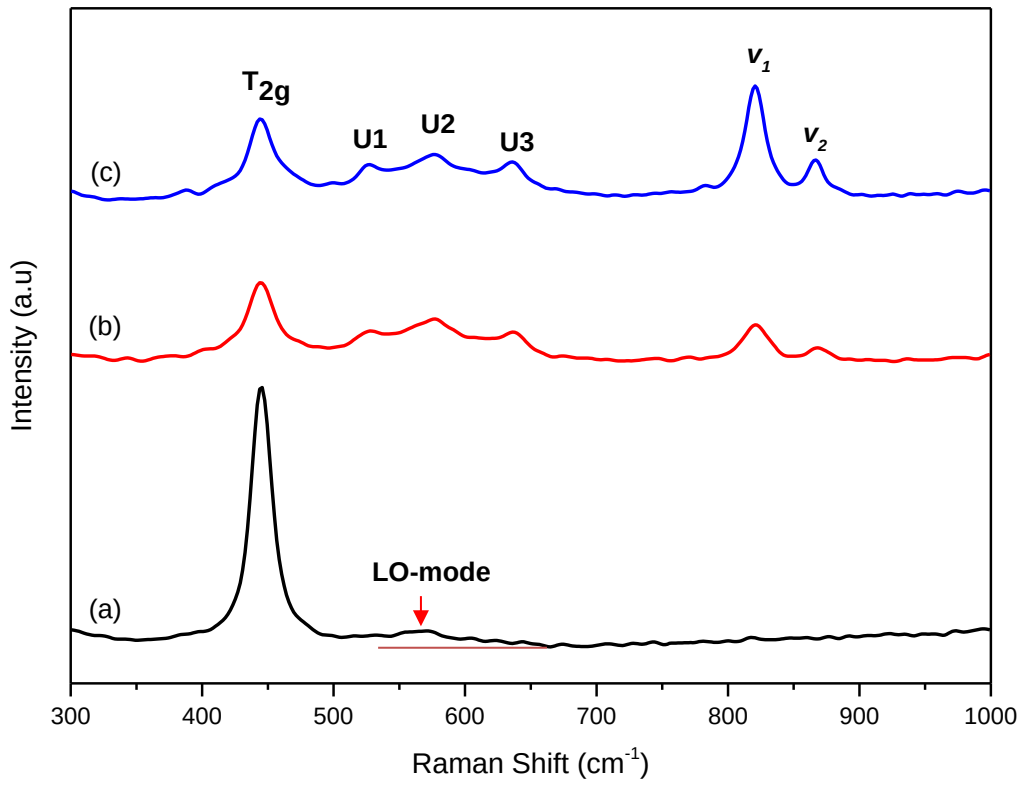

Figure 5.9: Raman spectra of the UO_2/H_2O interface collected at the end of the *(a)* 2 hours pre-leaching with aerated water before the ionic implantation, *(b)* 2 hours alpha irradiation & *(c)* 10 hours extended post-irradiation measurement

Before irradiation, the Raman spectrum of the virgin UO_2 indicates the presence of the only Raman active T_{2g} mode at 445 cm^{-1} and the forbidden LO-mode occurring at 568 cm^{-1}. The absence of other noticeable peaks suggests that the UO_2 disk was close to stoichiometry before the alpha irradiation.

During irradiation, alpha ions induce significant damages in the UO_2 disk. It can be observed that the ionic implantation affects the T_{2g} peak (decrease in the intensity accompanied by a peak broadening). Similar observations have previously been reported by Guimbretière *et al.* [171] during the alpha irradiation of UO_2 ceramics.

The Raman triplet defect bands (U1: 527 cm^{-1}, U2: 575 cm^{-1} & U3: 635 cm^{-1}) can also be observed in the 500-660 cm^{-1} spectral range. The intensity of the defect bands grows continuously under increasing irradiation fluence and is consistent with the increase in the defect concentration during irradiation.

During the leaching study, the radiolytic species formed due to the attenuation of the alpha ions in the aqueous medium enhance the UO_2 oxidation and the uranium dissolution rate in the form of uranyl ions. These ions precipitate as secondary phases once the solution has reached the solubility limit towards the precipitation of U(VI) phases. The two distinct peaks occurring at 820 cm^{-1} and 865 cm^{-1} on the spectra are signatures of the studtite phase ($UO_2.(O_2).4H_2O$). According to Amme *et al*. [89], the 820 cm^{-1} peak corresponds to the symmetrical axial stretching mode of uranyl ion (UO_2^{2+}) (v_1) while the 865 cm^{-1} is attributed to the peroxide ion (O_2^{2-}) (v_2) in the studtite phase.

5.4.2 *In situ* Raman measurements during alpha irradiation

As previously discussed in Section 5.2, the experimental set-up designed for this study enables to conduct an online monitoring of the UO_2/H_2O interface under alpha irradiation during which significant modifications of the Raman spectra were observed.

The *in situ* Raman spectra were collected with an excellent signal-to-noise ratio. This offers the main advantage of a precise analytical data treatment to determine the kinetic evolution of the different peaks occurring on the Raman spectra.

The *in situ* evolution of the Raman spectra during alpha irradiation as a function of irradiation fluence is illustrated in Figure 5.10.

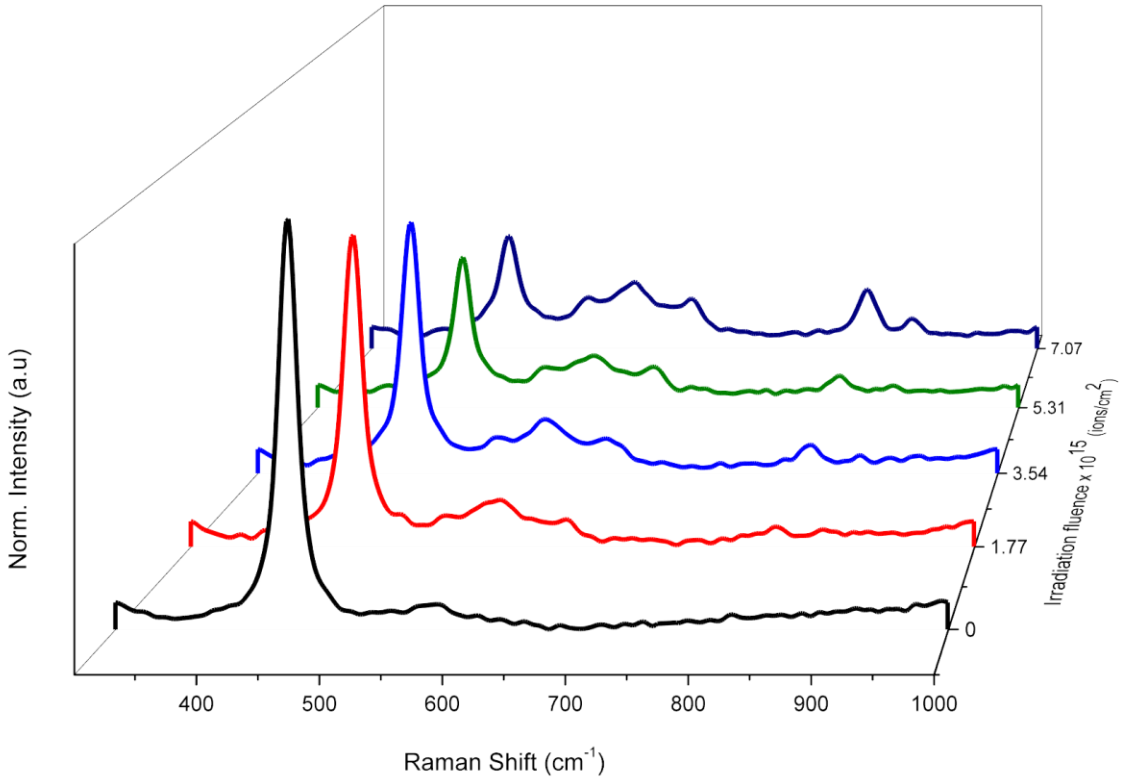

Figure 5.10: *In situ* Raman acquisition under increasing irradiation fluence for the UO_2/H_2O system under alpha irradiation

The figure shows the growing intensity of the triplet defect bands and the characteristic double peaks of the studtite phase under increasing irradiation fluence. The WIRE (Window-based Raman Environment) Renishaw software [172] was used to remove any fluorescence signals and background noises from the Raman spectra. A classical deconvolution of the different peaks occurring on the spectra was then carried out using the ORIGIN-Lab mathematical tool [173] which provided relevant information regarding their positions, widths and relative intensities. Thus, it was possible to determine their kinetic evolution during the different stages involved this study.

Relevant information regarding the kinetics of the T_{2g} mode and Raman triplet defects peaks will be presented in the following sections. On the other hand, the formation kinetics of the studtite phase will be discussed in the second part of this chapter.

5.4.3 Kinetic evolution of the T_{2g} band

A sequential Raman acquisition was carried out during the different stages involved in this study to determine kinetic evolution of the T_{2g} mode. The obtained findings are presented in Figure 5.11.

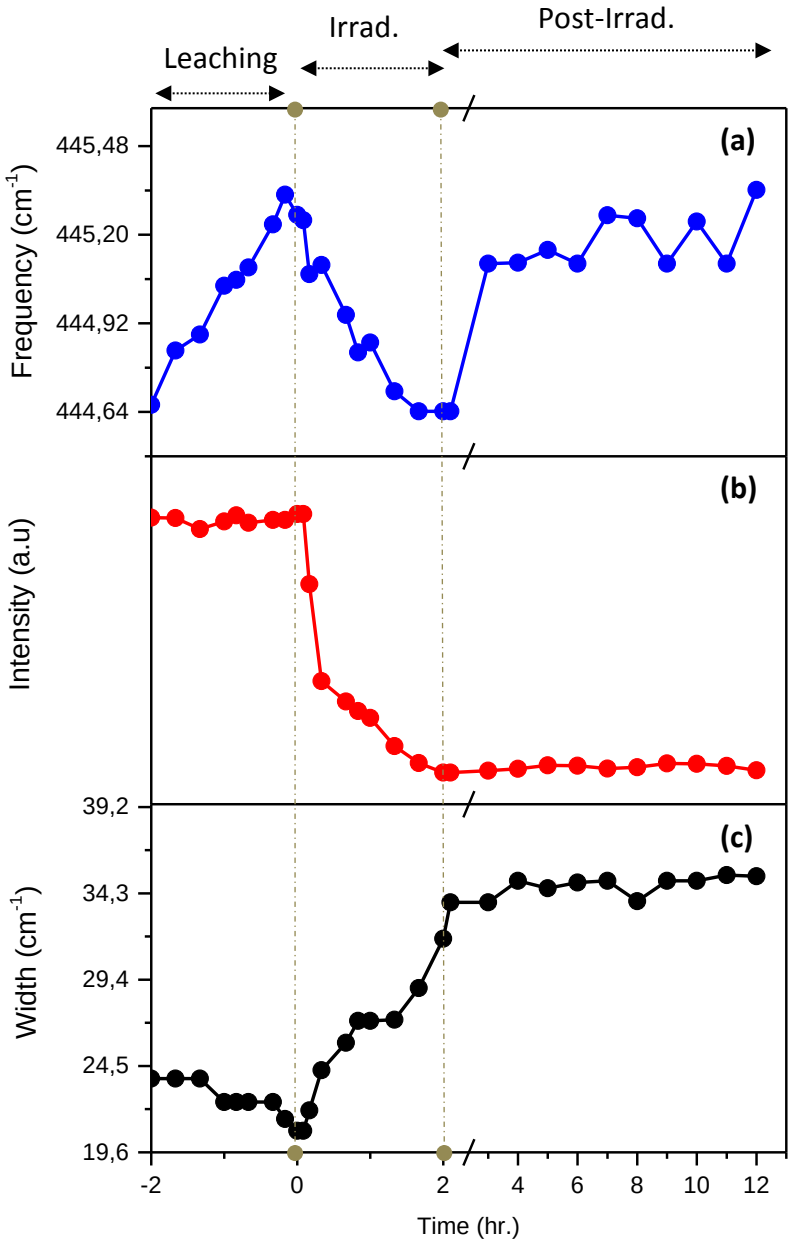

Figure 5.11: Sequential Raman measurement showing the kinetic evolution of the T_{2g} *(a)* frequency, *(b)* intensity and *(c)* width during the pre-leaching, under alpha irradiation and *in situ-post irradiation* acquisitions

During the pre-leaching stage, the figure shows that the frequency of the T_{2g} mode increases slightly but the intensity and FWHM remain relatively stable. The influence of irradiation on the T_{2g} mode can clearly be observed. The latter causes a significant decrease in the frequency and intensity and induces an important broadening of the peak. After irradiation, T_{2g} frequency can be seen to recover gradually and tends to increase discontinuously. On the other hand, the intensity and FWHM of the T_{2g} band seem to become stable in the absence of the alpha beam.

Baddour *et al.* [174] reported that the decrease in the intensity and broadening of the T_{2g} band observed during irradiation is consistent with the local disorder in the irradiated UO_2 ceramic. On the other hand, Guimbretière *et al.* [106] conducted a more detailed analysis to differentiate between the irradiation and temperature effect on the T_{2g} peak. Indeed, a rise in the temperature of the UO_2 pellet is expected during irradiation which is due to the heat generated due to the inelastic interactions of the alpha ions with UO_2 atoms.

Considering that irradiation-induced damage is a non-reversible effect whereas temperature-induced changes are reversible, Guimbretière *et al.* [106] reported that the change in the T_{2g} frequency observed during alpha irradiation can be attributed to a heating effect. This argument was based on the fact that the T_{2g} frequency returned to its original starting value when the irradiation was stopped. On the other hand, the increase in the T_{2g} width can be attributed to the presence of mechanical or chemical strain due to the altered layer at the surface of UO_2 that continues growing after irradiation.

5.4.4 Kinetic evolution of the Raman triplet defect bands

Figure 5.12 illustrates the formation kinetics of the Raman triplet defect bands during irradiation and their respective evolution during the extended acquisition when the irradiation beam was turned off.

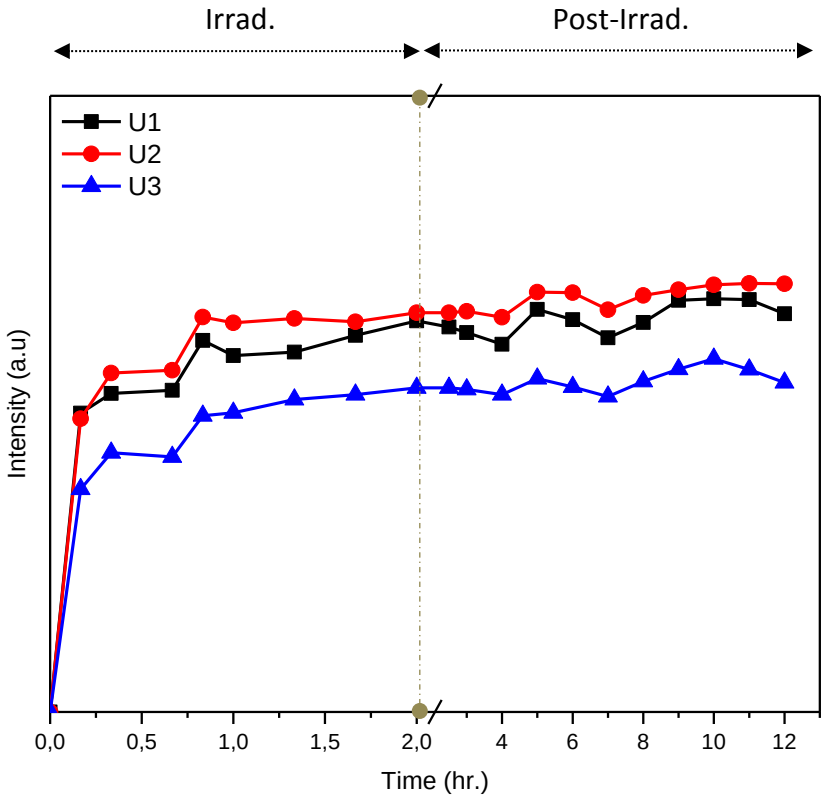

Figure 5.12: Kinetic of the defect peaks intensity of the UO_2/H_2O system under and after the alpha irradiation

From the above figure, it can be seen that the formation kinetics of U1, U2 & U3 during irradiation (0-2 hours) can be divided into two distinct regimes. They show a rapid increase during the initial stages of irradiation, but tend towards a saturation phase till the end of irradiation.

Several models defining the irradiation damage accumulation kinetics have been proposed by Jagielski *et al.* [175]. A comparison with the available data show that the defect kinetics observed in Figure 5.12 follow a Direct-Impact (DI) model. The DI states that each ion implanted creates a given amount of disorder in the volume and the damage accumulation is proportional to the probability that the ions hit the target material [175]. Thus, the initial increase in the defect bands intensity is consistent with the creation of irradiation defects. On the other hand, the damage measured at the saturation describes the stage where an annealing/elimination of defects is initiated to counter the growing concentration of irradiation defects.

The figure also shows that the intensity of the defect bands tends to remain stable during the extended Raman acquisition when the alpha beam was turned off.

5.5 Results: Alpha irradiation of UO_2/Ar system

5.5.1 *In situ* Raman measurements during irradiation

The *in situ* Raman spectra acquired during the alpha irradiation of the UO_2 disk when exposed to a chemically inert medium, i.e. argon environment, are presented in Figure 5.13.

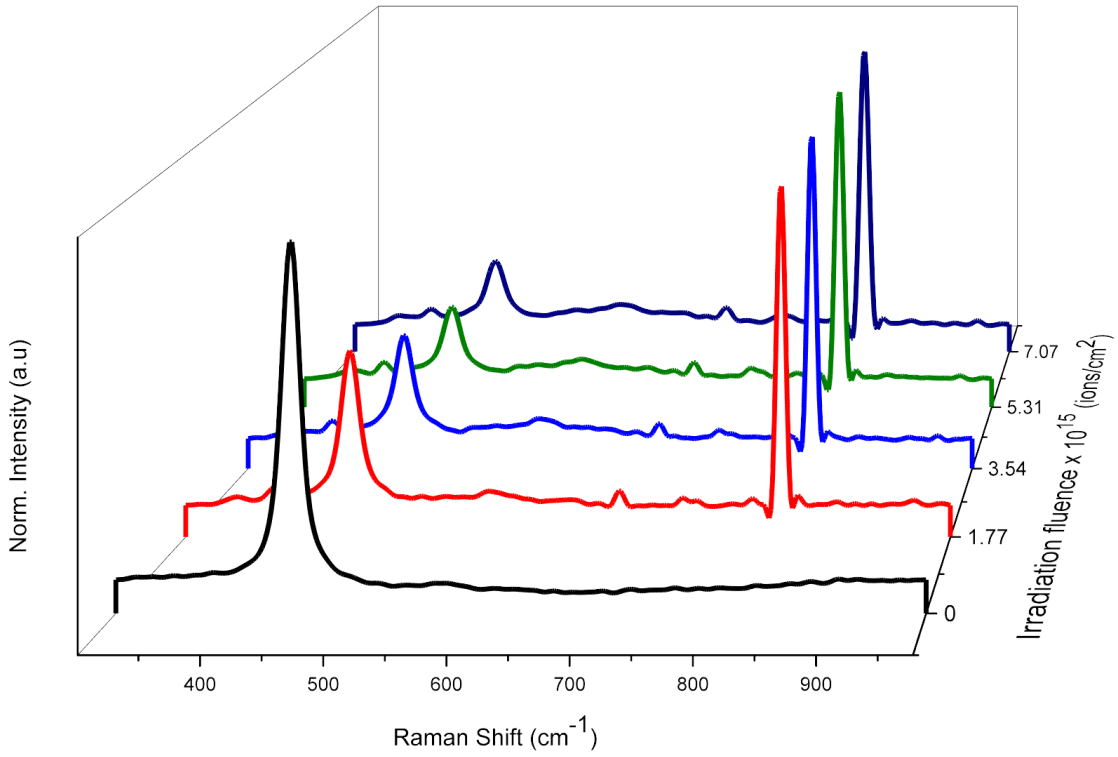

Figure 5.13: *In situ* Raman acquisition at different time intervals for the UO_2/Ar system under alpha irradiation

The above figure shows a significant decrease of the T_{2g} intensity during the initial stages of irradiation. The broadening of the T_{2g} band as a function of irradiation fluence can also be evidenced.

The argon plasma formed due to the attenuation of the helium ions energy in the gaseous medium appears as a relatively intense peak at 825 cm^{-1} (relative to 633 nm reference, *i.e.* 667.9 nm as wavelength) on the spectra. The high intensity of the plasma rays tends to mask the Raman triplet defect bands and needs to be corrected in order to study the kinetic evolution of the T_{2g} and triplet defect bands. Another plasma line of lower intensity is visible near 700 cm^{-1}.

It is worthy to note that the *in situ* Raman spectra collected for the UO_2/Ar system are of lower signal-to-noise ratio compared to the UO_2/H_2O experiment. This explains the presence of several parasitic peaks in Figure 5.13, especially in the 650-900 cm^{-1} spectral range.

5.5.2 Kinetic evolution of the T_{2g} band

A curve fit was conducted on the spectra obtained during the *in situ* acquisition in order to determine the kinetic behavior of the T_{2g} peak during irradiation. The findings are presented in Figure 5.14.

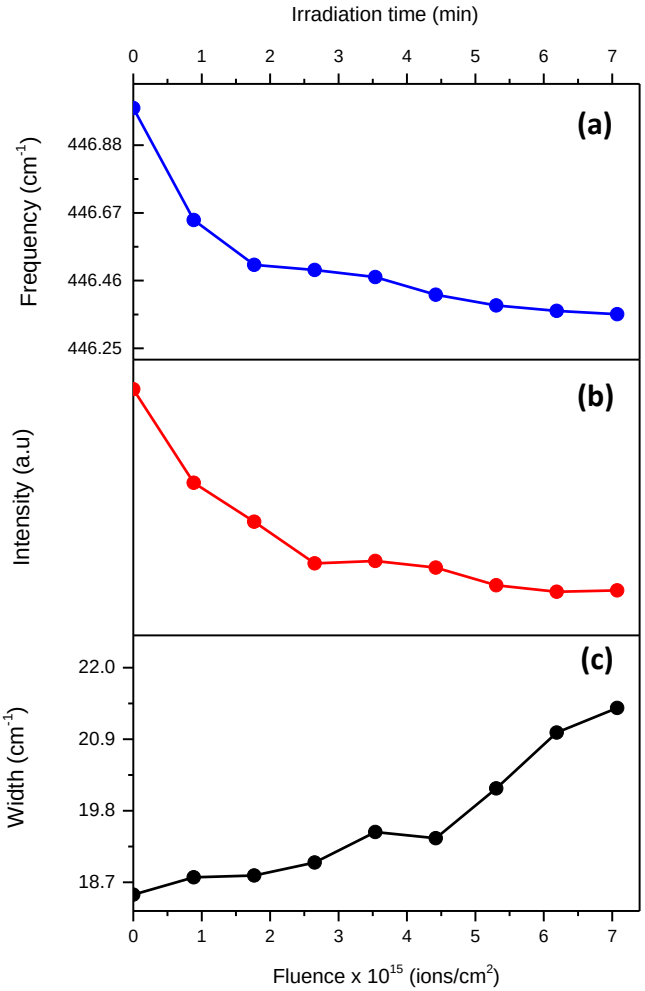

Figure 5.14: *In situ* kinetic evolution of the T_{2g} *(a)* frequency, *(b)* intensity and *(c)* width during the ionic implantation

The *in situ* T_{2g} kinetics observed in Figure 5.14 is consistent with the findings previously obtained during the alpha irradiation of the UO_2/H_2O system. A similar observation was also observed by Guimbretière *et al.* [171] during the alpha irradiation of a UO_2 disk in the presence of an argon

gas. The authors showed that shift of the T_{2g} frequency and T_{2g} width recorded during the *in situ* measurements are related to a temperature effect because both are restored to their starting values when the irradiation beam was turned off.

In this study, no post-irradiation *ex situ* Raman measurements of the UO_2/Ar interface were carried. Thus, it was not possible to confirm the results reported by Guimbretière *et al.* [171].

5.5.3 Kinetic evolution of the Raman triplet defect bands

As previously reported in Section 5.5.1, the intense plasma peak tends to overshadow the growing intensity of the Raman triplet defect band. For a better illustration, Figure 5.15 focusses on the 475-680 cm^{-1} spectral range where the increase of the U1, U2 and U3 peaks as a function of irradiation fluence can clearly be observed.

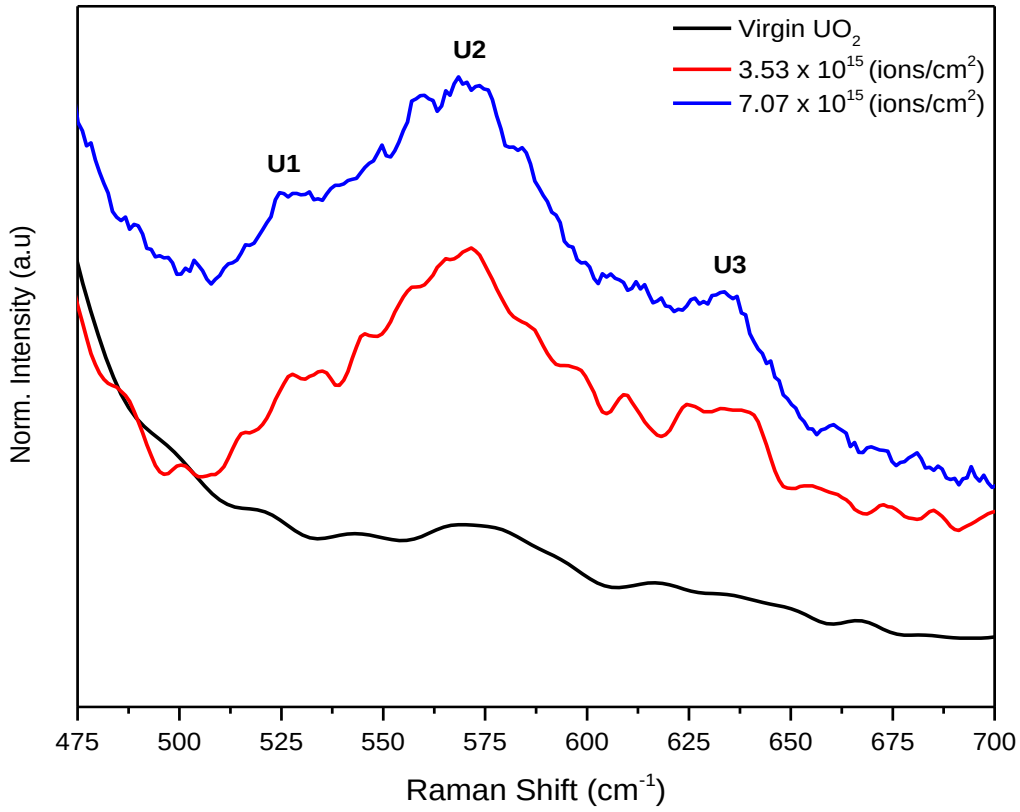

Figure 5.15: Evolution of the Raman triplet defects peaks in the 475-680 cm^{-1} spectral range during alpha irradiation of the UO_2/Ar system

The kinetics of the Raman triplet defect bands obtained after the curve fitting are presented in Figure 5.16.

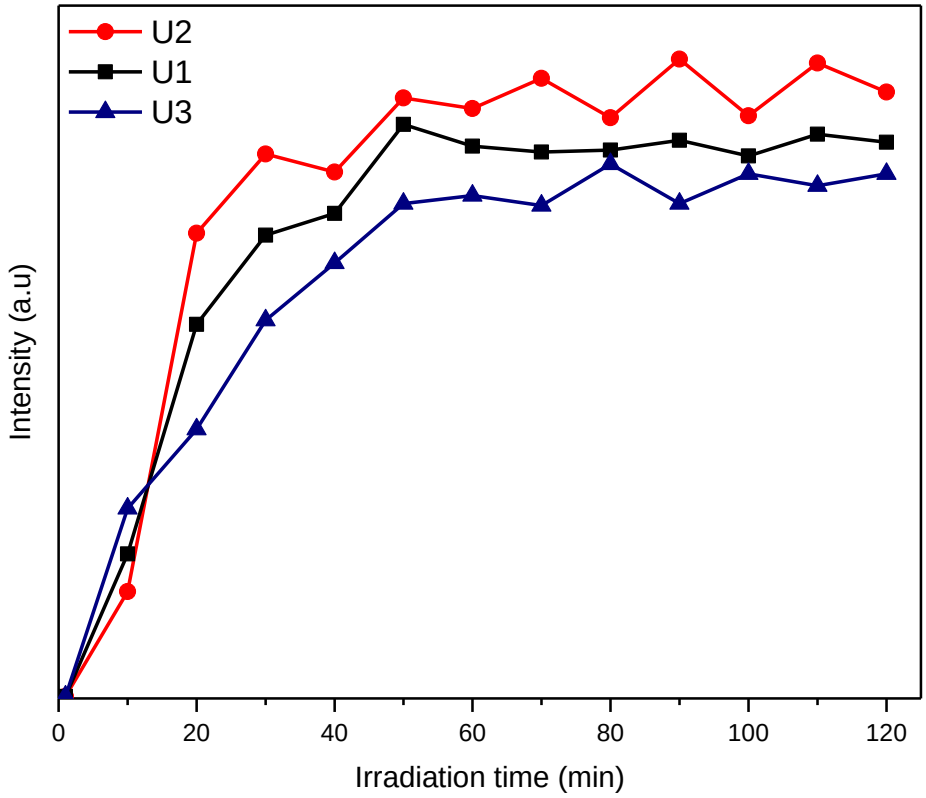

Figure 5.16 : Kinetic of the defect peaks intensity of the UO_2/Ar system under alpha irradiation

The kinetics of the defect bands are highlighted by the fact that they follow the same trend as the findings obtained during the UO_2 leaching experiment. The intensity of the defect bands increases gradually during the initial stages of irradiation and then reaches saturation.

Thus, the *in situ* Raman set-up designed for the need of this study has successfully enabled to determine the formation kinetics of irradiation defects induced by alpha ions in the UO_2 disks. Although a similar behavior of the defect kinetics was observed when the disk was exposed to a reactive environment (aerated water) and an inert medium (argon gas), a deeper analysis of the preliminary results will be performed in the following section. The aim was to investigate whether the formation kinetics of irradiation defects is modified by the different experimental conditions that were used during the alpha irradiation.

5.6 Discussion

5.6.1 *In situ* kinetics of irradiation defects during alpha irradiation

As shown in Section 5.4.4 and Section 5.5.3, the Raman triplet defect bands during the alpha irradiation of the UO_2/H_2O and UO_2/Ar systems follow a unique kinetics, characterized by a rapid increase during the initial stages of irradiation before reaching saturation. The initial increase in the defect bands intensity corresponds to the production of irradiation defects while the saturation phase indicates the elimination/annihilation of defects respectively. It was also mentioned that the two-staged defect kinetics follow a Direct Impact (DI) model. According to Guimbretière *et al.* [106], the two-staged defect kinetics can be interpreted by relating the defect concentration (ρ_D) and alpha dose (Dα) in the form of:

$$d\rho_D/dD_\alpha = R_\alpha - B\rho_D \quad (5.1)$$

Rα is the number of irradiation defects (I.D.) produced per unit of path length travelled by alpha particles (I.D/cm.α). (B x ρD) corresponds to the annihilation terms describing the irradiation defects recombination. The B-parameter defines the annealing rate constant in (cm^2/α) and ρD is in I.D/cm^3. Equation 5.1 can also be expressed as:

$$\rho_D = \rho_D(\infty)\, x\, (1 - e^{-BD_\alpha}) \quad (5.2)$$

Where ρD(∞) is the defect concentration at saturation.

In order to set the numerical values for the ρD(∞) and B-parameter for the UO_2/H_2O and UO_2/Ar scenarios, the integrated Raman intensity of the triplet defect bands (U1+ U2+ U3) was considered and a theoretical fit in the form of Equation 5.2 was conducted using ORIGIN software to define their evolution versus irradiation time as shown in Figure 5.17 and Figure 5.18.

It is to be noted that the intensities of the defect bands in both cases were normalized with respect to their corresponding maximum intensities, i.e. to rescale the y-axis to the same limits, in order to facilitate the data comparison and interpretation.

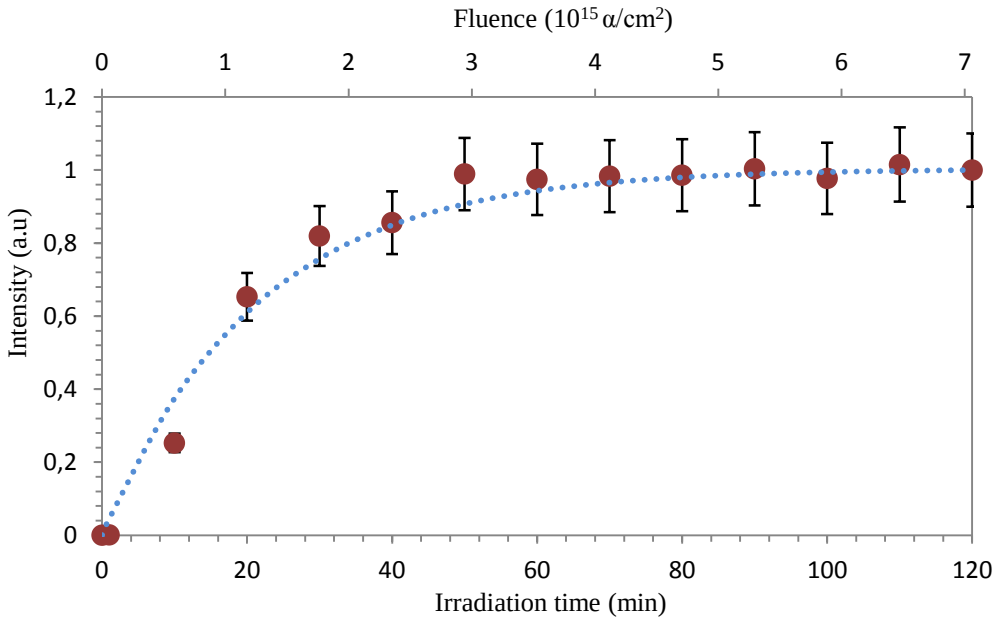

Figure 5.17: Kinetics of Raman defect peak intensity (Red dots) fitted with the Direct Impact model (Blue dotted line) for the UO_2/H_2O system under the 45 MeV alpha beam

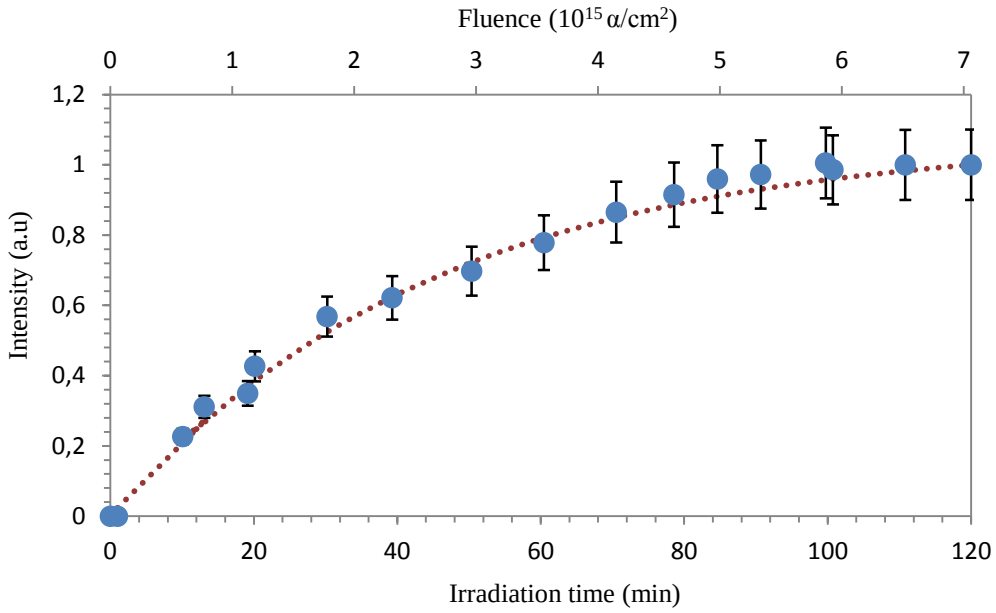

Figure 5.18: Kinetics of Raman defect peak intensity (Blue dots) fitted with the Direct Impact model (Green dotted line) for the UO_2/Ar system under the 45 MeV alpha beam

The numerical values of ρD(∞) and B-parameter obtained after DI model fitting are presented in Table 5.1.

Table 5.1: Comparison of the defect concentrations at saturation (ρD(∞)) and the defect annealing parameter (B) for the UO_2/H_2O and UO_2/Ar system

Scenario studied	**$\rho_{D(\infty)}$**	**Annealing Parameter (B) + Uncertainties**
UO_2/H_2O	1.02 ± 0.022	$7.95 \times 10^{-16} \pm 7.29 \times 10^{-17}$
UO_2/Ar	1.10 ± 0.023	$3.75 \times 10^{-16} \pm 1.93 \times 10^{-17}$

Table 5.1 shows that the defect kinetics for the UO_2/Ar can be modelled with an annealing rate constant of $3.75 \times 10^{-16} \pm 1.93 \times 10^{-17}$ cm^2. These observations are in good agreement with the values reported by Guimbretière *et al.* [106] ($10^{-16} \pm 10^{-17}$ cm^2) and Weber [107] (0.85×10^{-16} cm^2). The slight variance could be attributed to different UO_2 density used in those mentioned studies. The fit for the UO_2/H_2O gives a B-parameter of $7.95 \times 10^{-16} \pm 7.29 \times 10^{-17}$ cm^2, i.e. twice the value obtained for the reference UO_2/Ar system. This observation suggests that the elimination of defects is much faster when the irradiation is carried out under a chemically reactive environment (aerated H_2O).

In the previous chapter, it was shown that the Raman triplet defect bands are related to uranium interstitials. The enhanced annealing of defects observed in the presence of aerated water can be interpreted as a faster recombination of uranium interstitials. Thus, the evolution of uranium interstitials during irradiation can be defined as:

$$\mathrm{d}I_U/dD_\alpha = R_\alpha - BI_U \tag{5.3}$$

The increase in the annealing rate of uranium interstitials during the leaching study explains why the saturation stage is reached much quicker compared to the inert argon environment as illustrated in Figure 5.19.

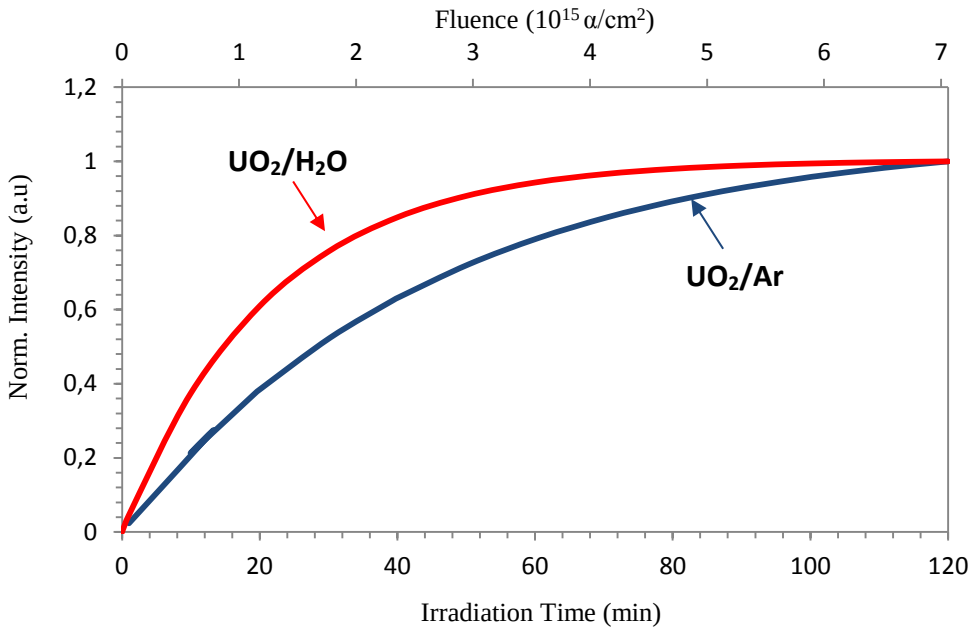

Figure 5.19: Comparison of the *in situ* kinetic defect peak intensity of the UO_2/Ar (dark blue line) with the obtained kinetic for the UO_2/H_2O (Red line)

The difference in kinetics observed from Figure 5.19 can be interpreted by considering the specific role of oxygen vacancy defects near the UO_2 surface boundary. In Chapter 4, the rapid oxidation of the irradiated UO_2 disk was attributed to the chemical reactions occurring near the UO_2 surface-air interface. The latter was initiated by the migration of oxygen vacancies towards the UO_2 surface boundary. Based on this observation, the following paragraph is intended to identify the suitable irradiation defect mechanisms occurring during the alpha irradiation of UO_2 in the presence of a chemically reactive (aerated water) and inert (argon) environment.

For the reference UO_2/Ar system, the concentration of irradiation defects increases during the initial stages of irradiation and at a given point, an elimination/annihilation of defects will be initiated by a simple vacancy-interstitial (Io + Vo $\longrightarrow$null) + (Iu + Vu $\longrightarrow$ null) recombination mechanism as illustrated in Figure 5.20. In contrary to what was observed during the oxidation of electron-irradiated UO_2 disk, the irradiation defects do not chemically interact with the contact medium. This is mainly attributed to the inert characteristic of the argon gas.

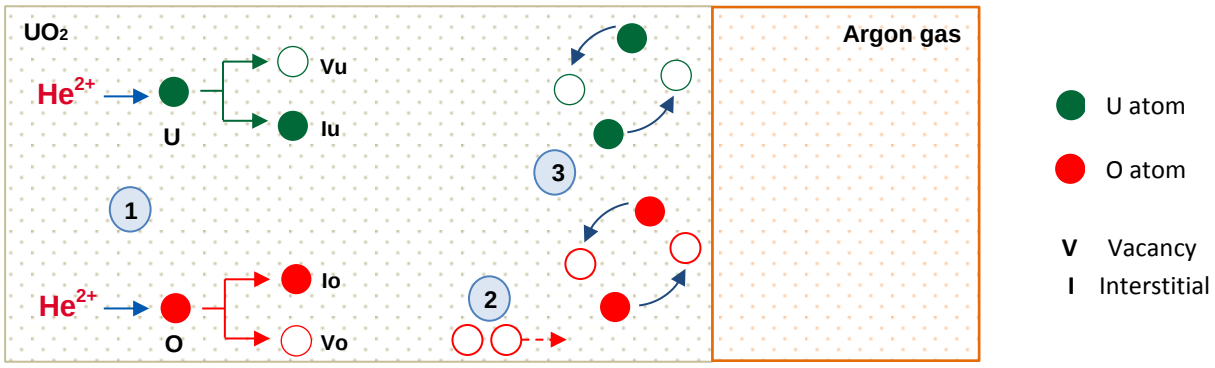

Figure 5.20: Stepwise illustration of the irradiation defect kinetics during the alpha irradiation of the UO_2/Ar system. ***1:*** Production of uranium and oxygen point defects, ***2:*** Migration of oxygen vacancies towards the fuel interface, ***3:*** Simple vacancy-interstitial recombination of oxygen and uranium point defects

In regards to the UO_2 leaching experiment, the presence of the chemically reactive medium needs to be considered. The migration and presence of oxygen vacancies near the UO_2 surface-H_2O interface creates a difference in the oxygen concentration gradient which enhances the oxygen mobility to anneal the vacancy sites as previously discussed in Chapter 4. Assuming that oxygen point defects are initially at equilibrium, the decrease in the oxygen vacancy concentration leaves an excess of oxygen interstitials in the UO_2 bulk.

The elimination of uranium point defects is initiated by a vacancy-interstitial recombination mechanism. However, the excess oxygen interstitials might also show an affinity for neighboring uranium interstitials. The oxygen interstitials can interact with uranium interstitials to form anti-Schottky defects ($I_U + 2I_O \rightarrow I_{UO2}$). This mechanism involving oxygen interstitials causes a rapid decrease in the concentration of uranium interstitials to what would have been expected if the elimination of uranium interstitials was solely dependent on uranium vacancies. An illustration of such defect kinetics during the UO_2 leaching study is presented in Figure 5.22.

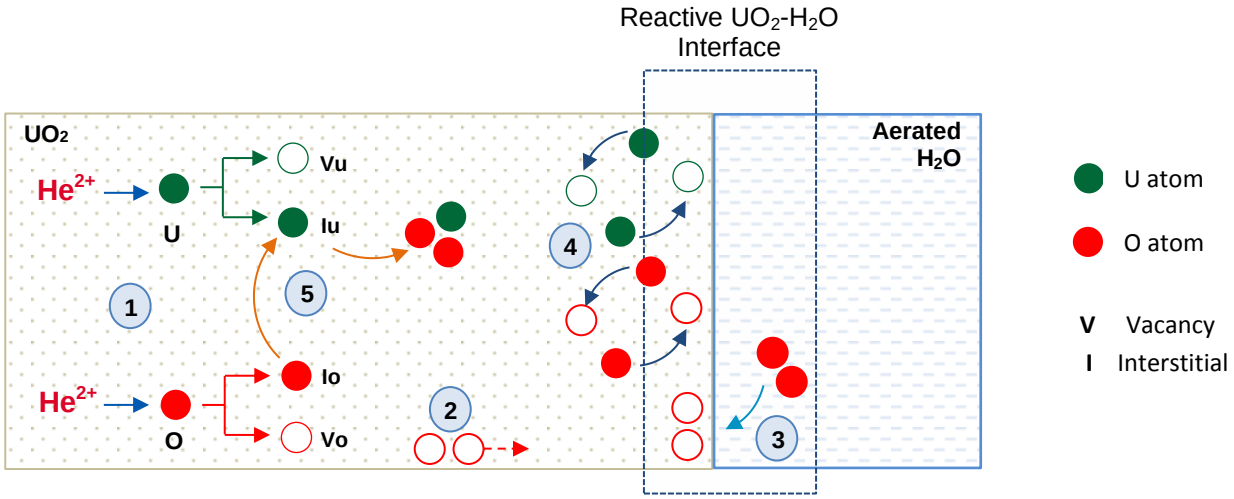

Figure 5.21: Stepwise illustration of the irradiation defect kinetics during the UO_2 oxidative leaching experiment.***1:*** Production of uranium and oxygen point defects, ***2:*** Migration of oxygen vacancies towards the fuel interface, ***3:*** Annealing of oxygen vacancies near the UO_2-H_2O interface due to the enhanced oxygen diffusion from the aerated contact medium, ***4:*** Simple vacancy-interstitial recombination of oxygen and uranium point defects, ***5:*** Recombination of excess oxygen interstitials with uranium interstitials resulting in the formation of anti-Schottky defects

From the proposed interpretation, it is very important to investigate whether the chemical reactions occurring near the UO_2-H_2O interface has an impact on the UO_2 dissolution mechanism. Tocino *et al.* [176] highlighted the importance of oxygen vacancies during the dissolution of uranium mixed oxides. The authors showed that the presence of crystal defects, such as oxygen vacancies, reduces the chemical durability of the nuclear materials which leads to an increase in their dissolution in aqueous solutions.

The second part of this chapter will be devoted to further investigate the UO_2 oxidative dissolution mechanisms and the formation kinetics of secondary U(VI) phases.

5.7 Formation kinetics of studtite secondary phases

The *in situ* Raman experimental set-up was also used to measure the kinetics of the secondary phases. It was therefore possible to quantify the initial formation kinetics of the studtite phase during the alpha irradiation. As the irradiated UO_2 disk was left in contact with the irradiated water solution for an additional time of 10 hours when the irradiation beam was turned off, an *in situ-post irradiation* Raman measurement was also carried out to follow the evolution of the altered phases.

5.7.1 *In situ* Raman measurements of the studtite phase

Figure 5.22 below focusses on the 750-1000 cm^{-1} spectral range of the Raman spectra collected during the alpha irradiation. The figure shows the increase in the intensity of the double peaks (v_1 & v_2) characteristics to the studtite phase under increasing irradiation fluence.

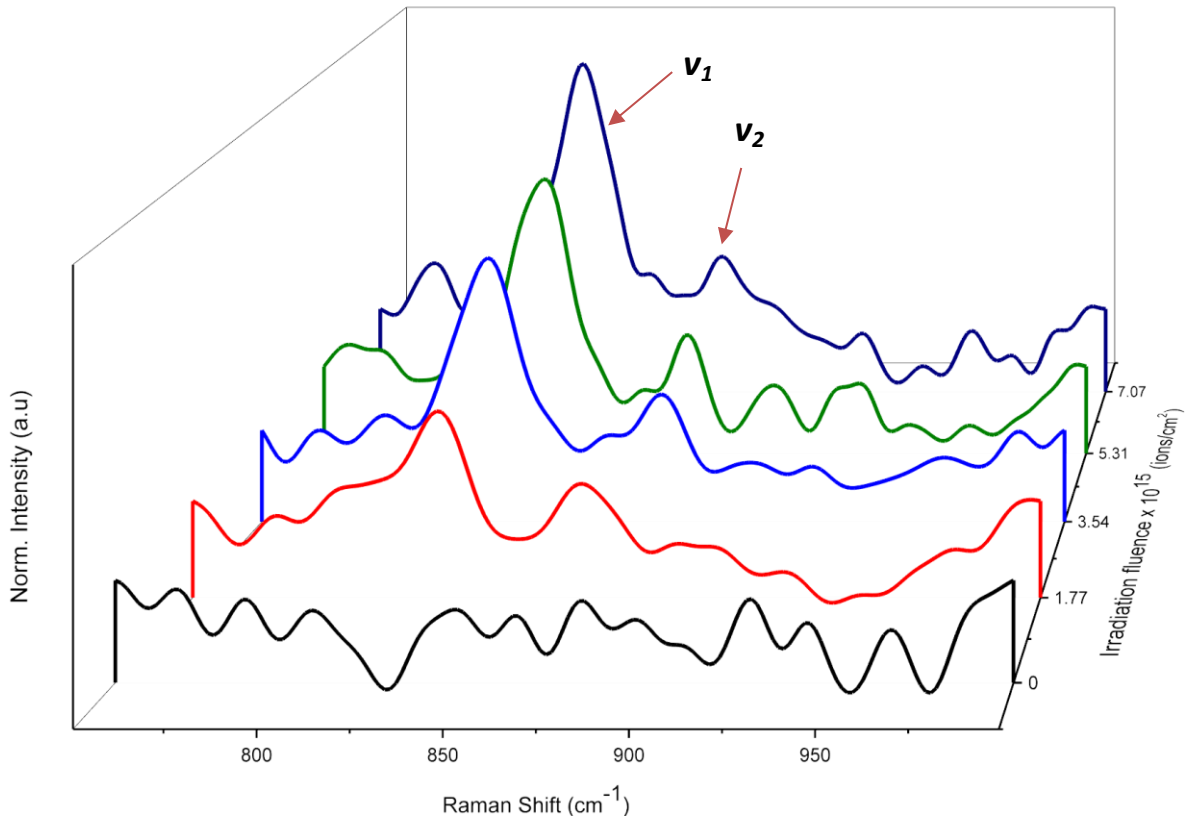

Figure 5.22: Evolution of the characteristic double peaks corresponding to the studtite phase against irradiation fluence

Due to the low signal-to-noise ratio of the Raman spectra as it can be seen in Figure 5.22, it was not possible to apply the same methodology that was previously used to determine the kinetic evolution of the Raman triplet defect bands. Thus, the formation kinetics of the secondary phases was derived by applying a simple signal-to-background integrated intensity in the 815-870 cm^{-1} range using the WIRE software.

5.7.2 *In situ* formation kinetics of the studtite phase

The *in situ* formation kinetics of the studtite phase during and after alpha irradiation is presented in Figure 5.23.

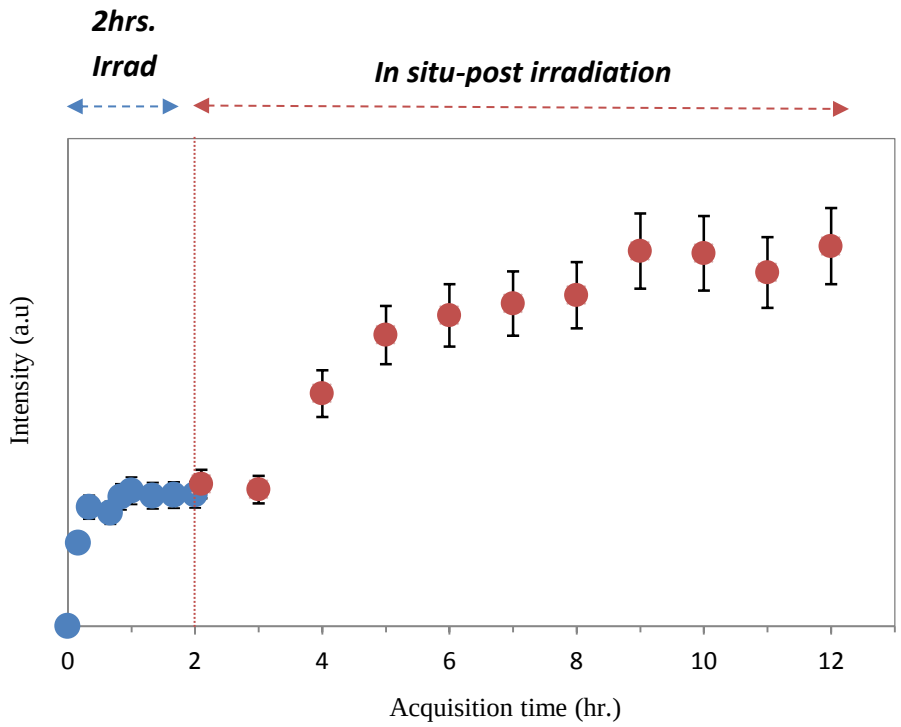

Figure 5.23: *In situ* Raman acquisition for the secondary phases (800-900 cm^{-1}) during the 2 hours irradiation (blue dots) followed by the extended *in situ-post irradiation* Raman measurement to monitor the formation kinetics of secondary phases in the absence of alpha beam (red dots)

From the Figure 5.23, it can be observed that the formation of the studtite phase is enhanced during the initial stages of irradiation but then quickly tends towards a saturation phase, where the formation kinetics does not show significant evolution. Although UO_2 alteration under alpha irradiation is mainly governed by the activity of radiolytic H_2O_2, the rapid increase of the studtite intensity during the initial irradiation stages indicates that the contribution of short-lived oxidizing species, such as $^{\cdot}OH$ radicals, also needs to be considered.

On the other hand, the *in situ-post irradiation* acquisition showed an increase in the kinetic evolution of the secondary phases in the absence of the irradiation beam. At this stage of study, it is difficult to propose a clear mechanisms to explain the physical chemistry of the UO_2 alteration growth kinetics observed during the *in situ-post irradiation*. As an extension of the current study, the use of principal components analysis methods as proposed by Guimbretière et *al.* [177] might prove useful to provide additional information.

5.8 Characterization of leached UO_2 surface

At the end of the extended *in situ-post-irradiation* Raman measurement, the irradiated UO_2 sample was dismantled from the irradiation cell, dried, and subjected to a number of surface characterizations in order to analyze the change in the microstructure resulting from the leaching study (SEM analysis) and also to confirm the presence of studtite on the altered layer (Raman mapping).

5.8.1 SEM analysis of virgin UO_2 surface

Prior to irradiation, the mirror-polished surface of the UO_2 disk was analyzed by the SEM method. The UO_2 grains and grain boundaries can clearly be distinguished from Figure 5.24. The high surface porosity can also be evidenced on the virgin disk.

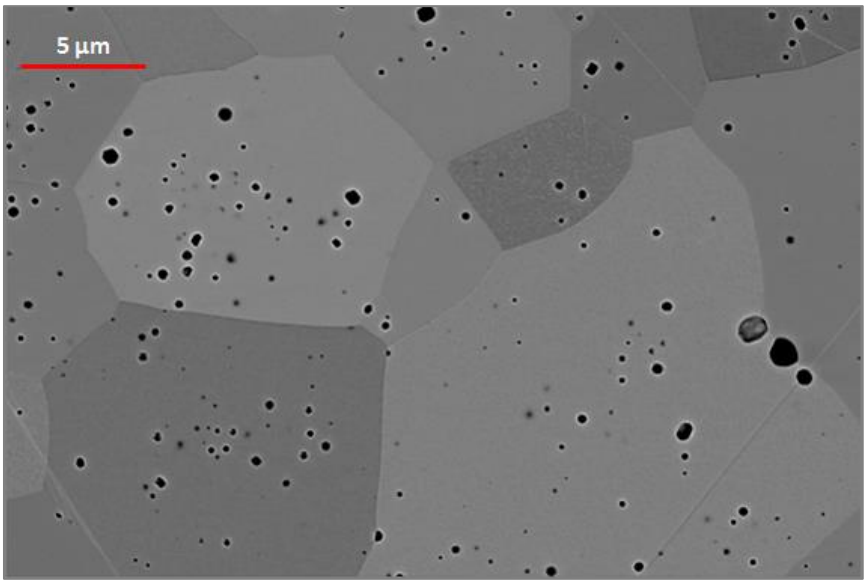

Figure 5.24: Scanning electron microscopy image of the UO_2 mirror-polished surface before the leaching study *(x 12000)*

5.8.2 SEM analysis of leached UO_2 surface

The leached UO_2 surface was analyzed so as to visually assess the microstructural changes induced by the radiolytic species. Figure 5.25 shows the post leaching analysis of the irradiated UO_2 disk. Compared to the microstructure of the virgin UO_2 sample, it can be seen that the radiolytic attack brings out significant microstructural changes. The figure shows the formation of a thick altered studtite layer displaying microcracks, which is homogeneously distributed over the entire UO_2 leached surface.

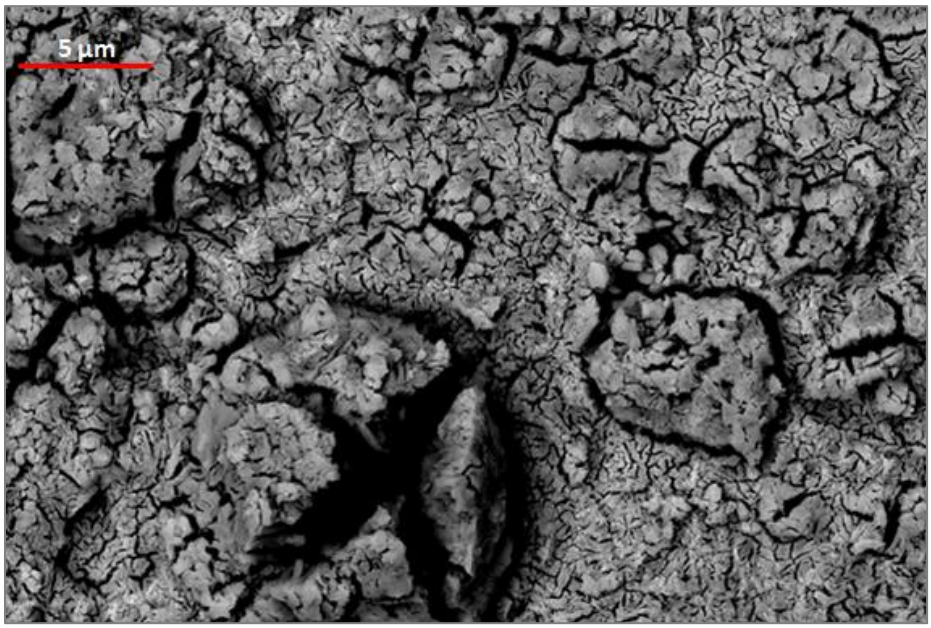

Figure 5.25: Scanning electron microscopy image showing the formation of the secondary altered studtite layer over the UO_2 surface after the leaching experiment (*x 12000*)

Additional SEM analysis was conducted by inclining the irradiated UO_2 disk to 35° to the direction of the electron beam during the SEM measurements. This step enables to distinguish between the UO_2 surface and secondary altered phases. Thus, the thickness of the studtite phase can be estimated. Figure 5.26 and Figure 5.27 show that the studtite phase appears as very compact fibers with parallel orientation which grow in the perpendicular direction of the UO_2 surface. The thickness of the altered layer was estimated to be in the 1-2.5 µm range.

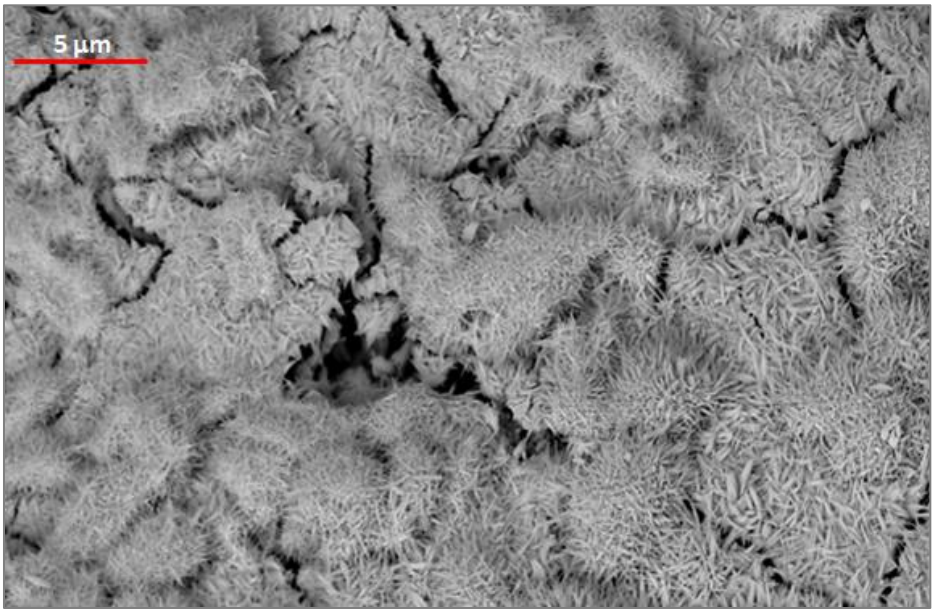

Figure 5.26: Scanning electron microscopy image of the inclined UO_2 leached surface showing the studtite in the form of compact fibers *(x 12000)*

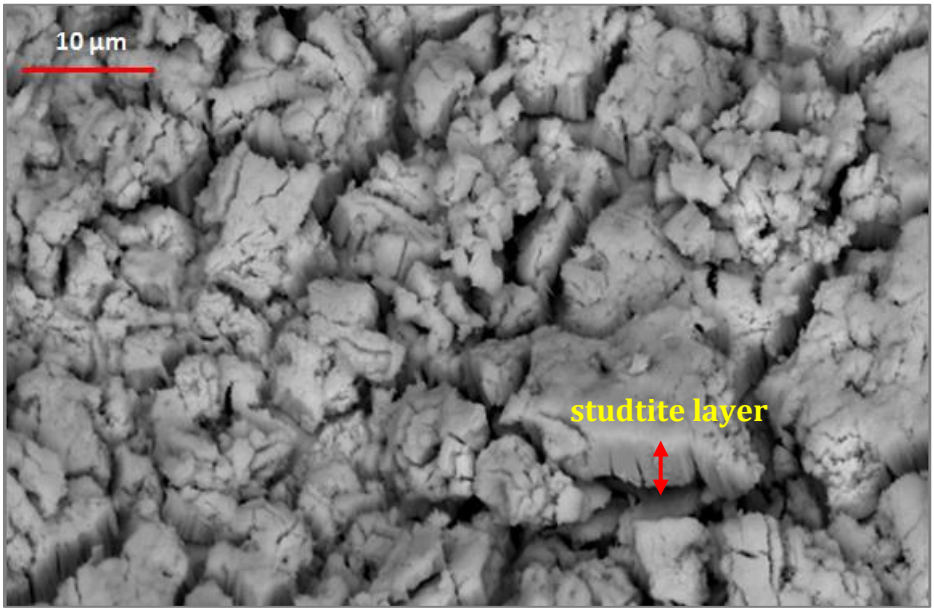

Figure 5.27: Scanning electron image of the inclined UO_2 leached enables to differentiate between the UO_2 surface and the secondary thick layer *(x 12000)*

5.8.3 *Ex situ* Raman surface mapping

An *ex situ* analysis of the irradiated/leached UO_2 sample was carried out using the Renishaw Invia Reflex spectrometer. The UO_2 grains and grain boundaries attacks were analyzed by performing a Raman spectral mapping over a selected area of the sample after the leaching experiment. This method gives the detailed composition of the area analyzed by the spectrometer. The dimensions of the chosen area were 55 x 25 μm^2 on the x and y axis respectively, with a moving step of 1 µm in the snake mapping mode.

Figure 5.28 shows the microscope image of the selected UO_2 area for the characterization. The bright green color on the map indicates the highly oxidized region while the blue color corresponds to the low oxidized zones. The mapping shows that the UO_2 grain boundary regions endured the highest radiolytic attack which is represented by the high intensity of the studtite precipitates compared to the UO_2 grains.

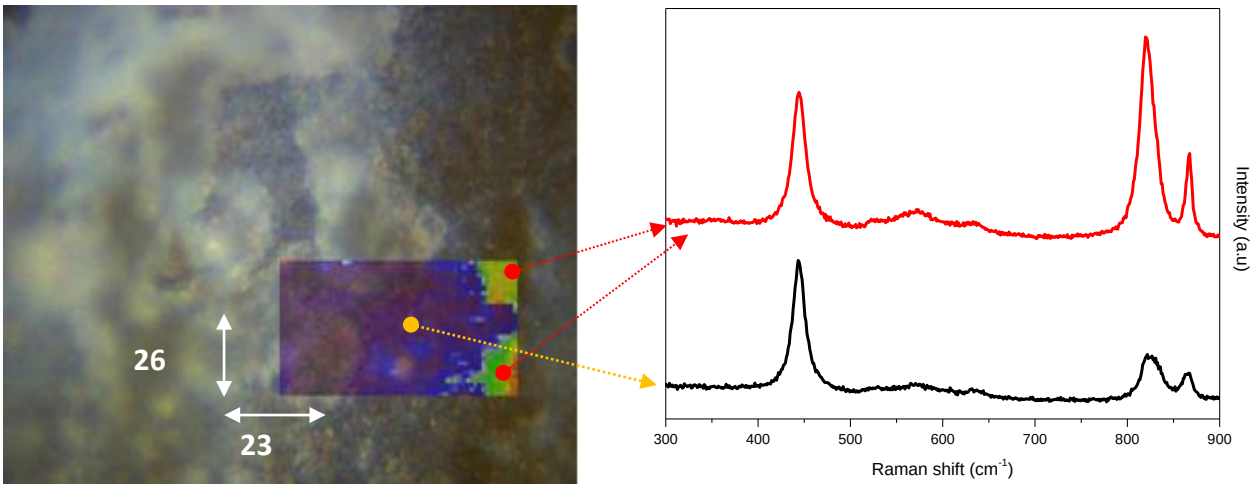

Figure 5.28: Space-resolved Raman spectral mapping of the irradiated UO_2 surface showing the grain boundaries (Green color) and the grains (Blue color)

5.8.4 Studtite phase: *in situ vs. ex situ* measurements

The formation of the studtite phase during the UO_2 leaching study was evidenced and confirmed by Raman spectroscopy. Figure 5.29 compares the intensity of the characteristic double peaks (820 cm^{-1} & 865 cm^{-1}) relevant to the studtite phase at different stages involved in this study, namely *(a) in situ* under irradiation, (b) *in situ-post* irradiation and *(c) ex situ* Raman mapping.

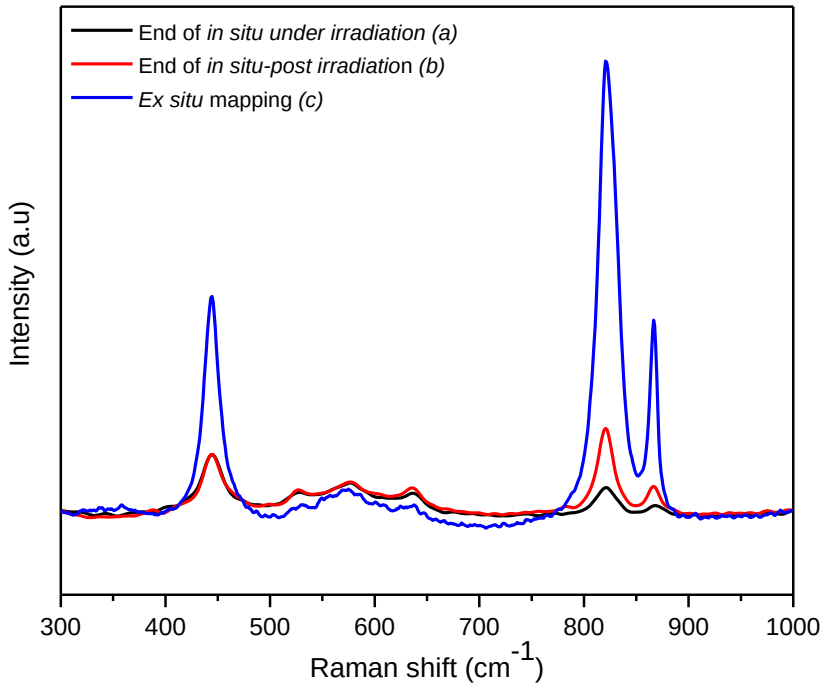

Figure 5.29: Raman spectra of the irradiated UO_2 acquired *(a)* at the end of *in situ-under alpha* irradiation, *(b)* at the end of *in situ-post irradiation* and *(c)* during the *ex situ* analysis

From the above figure, the relative intensity of the characteristic double peaks can be seen to increase gradually during the *in situ* acquisitions. However, the intensity of the studtite phase can be seen to be much higher during the *ex situ* measurements. Based on the intensity difference, this observation suggests that the studtite observed during the *in situ* acquisitions of the UO_2/H_2O interface is not exactly the same as that seen during the *ex situ* mapping (dried sample).

It can be postulated that a weathered thin layer which is supersaturated in the studtite phase ($UO_2.(O_2).xH_2O$ where x > 4) is formed by the alpha-induced water radiolysis and starts to organize itself near the UO_2-H_2O interface. The characteristics of the weathered thin layer are such that it can be considered as a homogeneous and transparent layer because it enables to characterize the UO_2 disks during *in situ* measurements (presence of T_{2g} mode). In addition, a quick visual analysis of the altered UO_2 surface before the water was removed from the irradiation cell did not show major modifications of the leached UO_2 surface.

During the *ex situ* measurements, even if the modification of optical conditions (focalization, numerical aperture) can have some effect, the high studtite intensity indicates that the sample drying causes the weathered thin layer to rapidly crystallize itself to form a thick studtite layer on the UO_2 bulk. This is consistent with the intense studtite bands that largely surpass the T_{2g} intensity. The studtite phase was seen to appear as white heterogeneous precipitates on the leached surface at this stage of analysis (refer to Figure 5.28).

5.9 Irradiated water solution analysis

At the end of the leaching experiment and after the *ex situ* Raman analysis, the irradiated aqueous solution was purged out from the irradiation cell and recovered. The irradiated water solution was analyzed to determine the concentration of radiolytic H_2O_2 and dissolved uranium.

The spectrophotometric Ghormley method [178] was used to determine the concentration of H_2O_2 in the solution bulk ranging from 4 x 10^{-6} M to 2 x 10^{-4} M. The dissolved uranium in the solution was measured by a laser-induced Kinetic Phosphorescence Analyzer (KPA) with a quantitative limit of 0.1 µg/L.

In this section, the results obtained during the chemical analysis are discussed in order to propose a suitable uranium dissolution mechanism based on the different species contained in the irradiated solution.

5.9.1 Concentration of radiolytic H_2O_2

The concentration of radiolytic H_2O_2 contained in the aqueous solution at the end of the leaching study was measured to be 5.4 x 10^{-3} ± 1.1 x 10^{-3} mol L^{-1}. According to Shoesmith *et al.* [57], under such regime the dissolution of UO_2 increases with a first order dependency on the H_2O_2 concentration.

5.9.2 Concentration of dissolved uranium

This study also enables to investigate the effect of irradiation on the uranium dissolution rate. The quantity of uranium released before irradiation was measured from the carbonated and aqueous water solutions used for the UO_2 pre-leaching steps. The uranium release following the sequential pre-leaching with carbonated water was measured to be 2.56 ± 0.30 µg L^{-1}. For the following two sequential (2 x 1 hour) pre-leaching with deionized water, it was observed that the uranium release decreases from 1.93 ± 0.20 µg L^{-1} to 0.121 ± 0.012 µg L^{-1}.

After irradiation, the concentration of dissolved uranium contained in the irradiated water solution was measured to be 207 ± 21 µg L^{-1}. However, the chemical analysis also revealed a high concentration of fluoride ions (890 ± 180 µg L^{-1}) in the water solution. These ions originate from the poly(chlorotrifluoroethylene) polymer material used for the fabrication of the irradiation cell because the presence of chloride ions (570 ± 110 µgL^{-1}) was also revealed in the solution. The complexing and corrosive characteristics of fluoride ions are more likely to affect the normal UO_2 dissolution mechanisms.

5.10 Discussion: UO_2 dissolution mechanisms

The findings obtained during the detailed chemical analysis of the irradiated water solution were analyzed in order to propose a suitable UO_2 oxidative dissolution mechanism applicable to this study.

The measured H_2O_2 concentration in the irradiated water solution was found to be of the same order as those previously reported by Corbel *et al.* [81] and Sattonnay *et al.* [74]. The Saturation Index (SI) of the irradiated water solution towards the studtite precipitation was then determined. The SI value is derived from the equilibrium reaction between ${UO_2}^{2+}$ ions and H_2O_2 (Equation 5.4).

$$H_2O_{2(aq)} + {UO_2}^{2+}_{(aq)} + 4H_2O_{(aq)} \leftrightarrow UO_2(O_2).4H_2O_{(s)} + 2H^+_{(aq)} \quad (5.4)$$

The SI with respect to the precipitation of the studtite phase is obtained by using Equation 5.5.

$$SI_{(studtite)} = log \frac{\left[{UO_2}^{2+}\right].[H_2O_2]}{[H^+]^2} / Ks_{studtite} \quad (5.5)$$

Where log $Ks_{Studtite}$ = -2.86 and represents the solubility constant for studtite [179].

The conditions for studtite precipitation are as follows:

SI < 0: Under-saturated. No precipitation is expected to occur.
SI ≥ 0: Solubility limit for the formation of studtite.

The irradiated water solution was largely oversaturated with uranium ions (calculated SI: 3.53). Therefore, the formation of studtite was inevitable and shows good consistency with Raman, SEM and XRD analysis. According to Equation 5.4, the precipitation of the secondary phase increases the acidity of the solution. The measured solution pH was 4.5 and according to Torrero *et al.* [180], the oxidative UO_2 dissolution proceeds with little surface oxidation under acidic conditions. Besides, the high concentration of fluoride ions should also be taken into account due to their highly corrosive and excellent complexing ability with respect to uranium ions. They tend to form strong $UO_2F^+_{(aq)}$ ligands with free uranyl ions in the solution and hence complex the fuel surface. In doing so, the fuel oxidation and formation of U_3O_7 or U_4O_9 layer on the UO_2 outer surface is restricted. The absence of fuel oxidation was also confirmed by the Raman data because no peaks characteristic to hyper-stoichiometric UO_2 as previously reported in Chapter 4.

A schematic representation of the UO_2 oxidative dissolution based on the findings obtained in this study is illustrated in Figure 5.30.

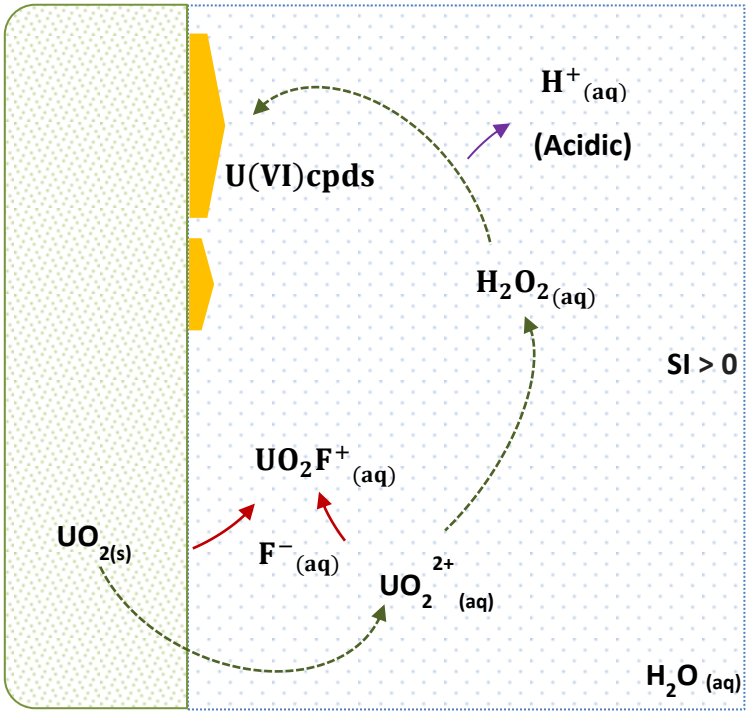

Figure 5.30: Illustration showing the different steps involved during the UO_2 oxidative dissolution mechanism.*(a)* Green arrows indicate the dissolution of the UO_2 disk into uranyl ions followed by their reaction with H_2O_2 to form secondary phases (U(VI) compounds). *(b)* Red arrows show the formation of complex ligands resulting from the complexation of free uranyl ions and the fuel surface by fluoride ions.

5.11 Conclusions

In this study, a newly designed *in situ* Raman installation was designed and used to characterize the behavior of a UO_2 disk in contact with deionized aerated water under the influence of a 45 MeV alpha beam. The main objective of this study was to measure the formation kinetics of irradiation defects and the acquired data were then compared to a reference UO_2/Ar system. In addition, the formation kinetic of secondary phases formed on the UO_2 surface during leaching experiment was also investigated.

The irradiation defects in both cases followed a two-staged kinetics that is characteristic of a simple direct model, but the kinetics was seen to depend on the experimental conditions. During the leaching study, the acquired data showed that irradiation defects are involved in chemical reactions occurring near the UO_2-H_2O interface which contributes to the dissolution mechanisms. Hence, the UO_2 surface boundary acts as sink to accelerate the elimination of defects. However, no such mechanism exists for the UO_2/Ar system due to the chemically inert characteristics of the gaseous medium. The defect annealing thus depends on a simple interstitial-vacancy/recombination process.

Finally, the irradiated solution was analyzed to determine the UO_2 oxidative dissolution mechanisms. It was observed that the concentration of radiolytic H_2O_2 and dissolved uranium were largely sufficient to precipitate secondary U(VI) phases in the form of the studtite phase. In addition, it was also reported that the dissolution process proceeds without the formation of an outer UO_2 oxidized layer due to the combined effect of complexing fluoride ions and the acidic characteristics of the irradiated aqueous solution.

Chapter 6

Effect of doping and microstructure on the Raman triplet defect bands

6.1 Introduction

Chapter 4 was devoted to provide an in-depth analysis of the irradiation-induced Raman defects bands in UO_2 pure samples. In addition, the alpha irradiation of UO_2 disks when exposed to different contact mediums showed that the formation kinetics of the Raman defect bands depends on the irradiation environment (Chapter 5). The previously studies were solely restricted to pure UO_2 compounds. In accordance to the French scenario, it is of outmost importance to acquire sufficient experimental data in regards to MOX fuels.

The field of study was hence extended to investigate the Raman triplet defect bands in MOX fuels, driven by their complex heterogeneous microstructure. However due to glove box requirements for the handling of plutonium-containing materials, MOX fuels could not be used in the *in situ* Raman experimental set-up developed for the need for this study. Thus several UO_2 doped compounds were used as surrogate nuclear fuels to replicate MOX fuels under laboratory conditions.

The objective of this study is to determine the influence of irradiation on UO_2-mixed samples, namely UO_2-CeO_2 and UO_2-ThO_2 solid solutions. A series of experiments were conducted to investigate the effect of microstructure on the formation of the Raman triplet defect peaks under alpha irradiation. The content of this chapter can be divided into two folds. The first part is focused on heterogeneous (U, Ce)O_2 compounds. It compares the irradiation response of (U, Ce)O_2 solid solutions under chemically inert (Ar) and reactive (H_2O) atmosphere. On the other hand, the findings obtained for the study of the irradiation effects in homogeneous (U, Th)O_2 systems are then presented in the second part of this chapter.

6.2 Heterogeneous microstructure: UO_2 doped with Cerium

In order to replicate the heterogeneous microstructure of MOX fuels, UO_2 doped with CeO_2 mixed oxides having a heterogeneous microstructure were fabricated.

Cerium dioxide (also referred as ceria) has a fluorite structure consisting of each cerium cation octahedrally coordinated by eight equivalent nearest-neighbor oxygen anions at the corner of a cube, while each oxygen anion is tetrahedrally coordinated with four cerium cations. The electronic configuration of cerium ([Xe] $4f^1 5d^1 6s^2$) suggests that it can exhibit +3 and +4 oxidation states. The varying oxidation states show that ceria has a high tendency to form and rapidly diffuse oxygen vacancies within the materials [181] and experiments carried out by Courtel *et al.* [182] gave indication that a range of solid solutions exist from Ce_2O_3 to CeO_2. The final stoichiometry eventually depends on the conditions employed during heat treatment after the fabrication process.

According to Bevan *et al.* [183], CeO_2 experiences large deviation from stoichiometry at elevated temperature and under oxygen-deficient environment. In sub-stoichiometric ceria, oxygen ions are moved from the CeO_2 lattice to form anionic vacant sites. To maintain charge neutrality, Ce^{4+} is converted to Ce^{3+} for each oxygen vacancy formed according to the equation below:

$$4\mathrm{Ce}^{4+} + \mathrm{O}^{2-} \rightarrow 4\mathrm{Ce}^{4+} + \frac{2\acute{e}}{\mathrm{V\ddot{o}}} + 0.5\ \mathrm{O}_2 \rightarrow 2\mathrm{Ce}^{4+} + \mathbf{2Ce^{3+}} + \mathrm{V\ddot{o}} + 0.5\mathrm{O}_2 \qquad (6.1)$$

The oxygen vacant site is represented by $\mathrm{V\ddot{o}}$ and the charge balance is ensured through the reduction of Ce^{4+} to Ce^{3+}. The ability of ceria to maintain its fluorite structure even with relatively high concentration of atomistic defect needs to be highlighted. It has been speculated that the crystal structure is not affected even after accommodating 14% oxygen vacancies [184].

6.2.1 Irradiation response of CeO_2

Several studies have been carried out to understand the irradiation-induced defects in CeO_2. According to Tyaki *et al.* [185] and Kim *et al.* [186], CeO_2 can be used to simulate irradiation effects in PuO_2 because of their pre-existing similarities in terms of physico-chemical properties. In addition, CeO_2 offers the possibility to be easily manipulated mainly attributed to its non-existing radiological characteristics.

The irradiation stability of CeO_2 under both light and swift heavy ions has been reported in the literature. For instance, Yasunaga *et al.* [187] highlighted the formation of defect clusters during the irradiation of CeO_2 with energetic electrons in the 200-1000 KeV range at temperatures between 293 and 373K. The defect clusters were attributed to oxygen interstitials formed by the selective displacements in the oxygen sub-lattice. In another study, Yasunaga *et al.* [188] extended their research to understand the properties of the dislocation loops by using an electron beam in the range of 200-3000 KeV. The authors concluded that oxygen interstitial-type non-stoichiometric dislocation loops are formed in the range of 200-1250 KeV due to the insertion of an extra oxygen layer on the (111) plane. However, electron irradiations above 1250 KeV produce perfect oxygen interstitial-type dislocation loops.

Irradiation studies with swift heavy ions were conducted with high energy Xe ions and led to the formation of ion tracks whose average diameter was seen to depend on the electronic stopping power [189]**.** Furthermore, other studies have concluded that the crystalline structure and lattice positions are both maintained even if the ion tracks cover the whole CeO_2 surface [190]**.** In addition, these tracks are not significantly affected at a temperature as high as 800°C [191]. Atomic defects during the swift heavy ion irradiation were evidenced by Ohhara *et al.* [192]**,** Shizumi *et al.* [193] & Iwase *et al.* [194]*.* The authors reported attributed the increase in the lattice parameter in irradiated CeO_2 to the formation of Ce^{3+} and oxygen vacancies ions.

Similar observations were recorded by Grover *et al.* [195] by means of Raman spectroscopy during the characterization of CeO_2 nanopowders, initially obtained under different sintering conditions, after their irradiation with 100 MeV silver ions. The authors put into evidence the formation of the Raman triplet defect bands on the spectrum of the irradiated CeO_2 sample as illustrated in Figure 6.1.

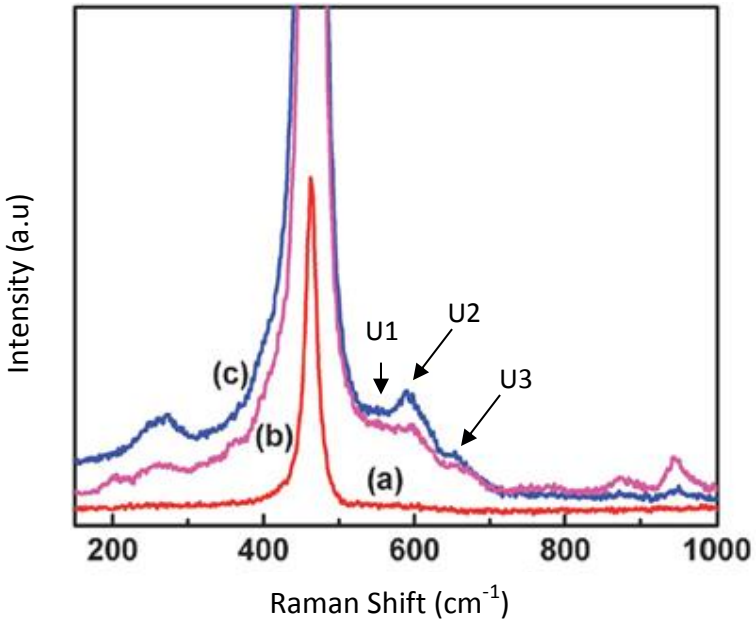

Figure 6.1: Raman spectra of irradiated CeO_2 powders, sintered at (a) 800°C, (b) 1300°C & (c) 1000°C [195]

6.2.2 Irradiation and characterization of (U, Ce)O_2 disks

In this study, the formation kinetics of irradiation defects in heterogeneous (U, Ce)O_2 mixed oxides will be compared with the findings obtained for the alpha irradiation of pure UO_2 samples. This experiment will enable to investigate the microstructure effect on the apparition of the Raman triplet defect bands.

Hence for a better comparison with UO_2 samples, the (U, Ce)O_2 mixed oxides were irradiated under the same irradiation conditions using the *in situ* Raman experimental set-up that were previously described in Chapter 5. Thus, an alpha ion beam was diverted towards the irradiation cell containing the (U, Ce)O_2 disk of which one of its surface was exposed to a contact medium (inert argon gaseous medium and reactive water environment were again considered in this study). The experimental conditions were again chosen such that the alpha ions pass through the sample and are attenuated in the contact medium.

The irradiation was carried out using a 45 MeV and 50 nA ionic flow during 4 hours in order to reach to a final fluence of 7.06 x 10^{15} alpha/cm^2. Unlike UO_2 samples, SRIM software specifies that a 320 µm thick (U, Ce)O_2 sample should be used during the 45 MeV alpha irradiation so that the ions are allowed to pass through the disk at 5 MeV. The latter can be attributed to the difference in the density of UO_2 and (U, Ce)O_2 samples.

The *in situ* Raman installation was again used to monitor the behavior of the disk during irradiation. In regards to the (U, Ce)O_2 oxidative dissolution experiment, an extended *in situ-post irradiation* Raman measurement was conducted to determine the kinetic evolution of the secondary phases after irradiation. Each spectrum was obtained with an acquisition of 120s after 5 accumulations over a spectral range of 300-900 cm^{-1}. The Renishaw Invia Reflex Raman spectrometer was then used for the (U, Ce)O_2 irradiated surface mapping.

6.2.3 Results: Initial surface characterization

The experimental results obtained during the initial characterization of the as-prepared (U, Ce)O_2 disks are presented in this section. SEM and Raman measurements were carried out to highlight the heterogeneous microstructure of the samples.

6.2.3.1 SEM images of virgin (U, Ce)O_2 disks

The microstructures of the virgin pellets are illustrated in Figure 6.2 and Figure 6.3 respectively. The SEM images show the (U, Ce)O_2 pellets are representative to the standard MIMAS MOX fuels, in the sense that they are defined by a complex heterogeneous microstructure which can be characterized by three distinct phases, namely; an uranium-rich agglomerate (~0.3 at.% Ce), cerium clusters (~31 at.% Ce) and a (U, Ce)O_2 solid solution phase.

The prepared samples were also seen to contain very little surface porosity. SEM-EDX was used to determine the elemental distribution of the elements in each of the phases. The obtained data are reported in Table 6.1.

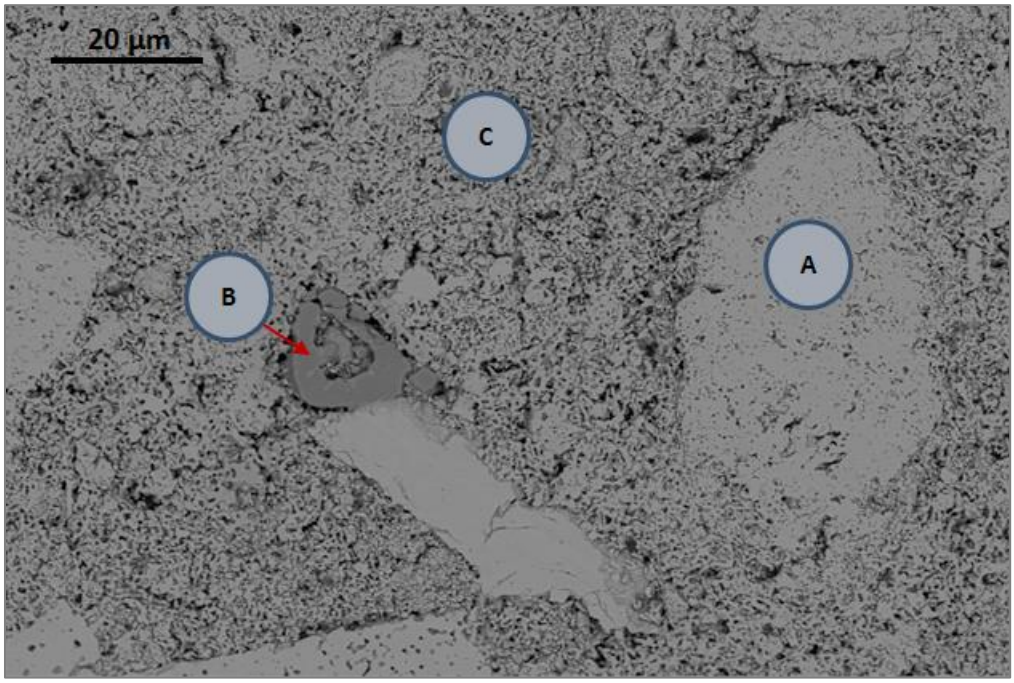

Figure 6.2: Heterogeneous microstructure of sintered (U, Ce)O_2 disk *(x3000)*

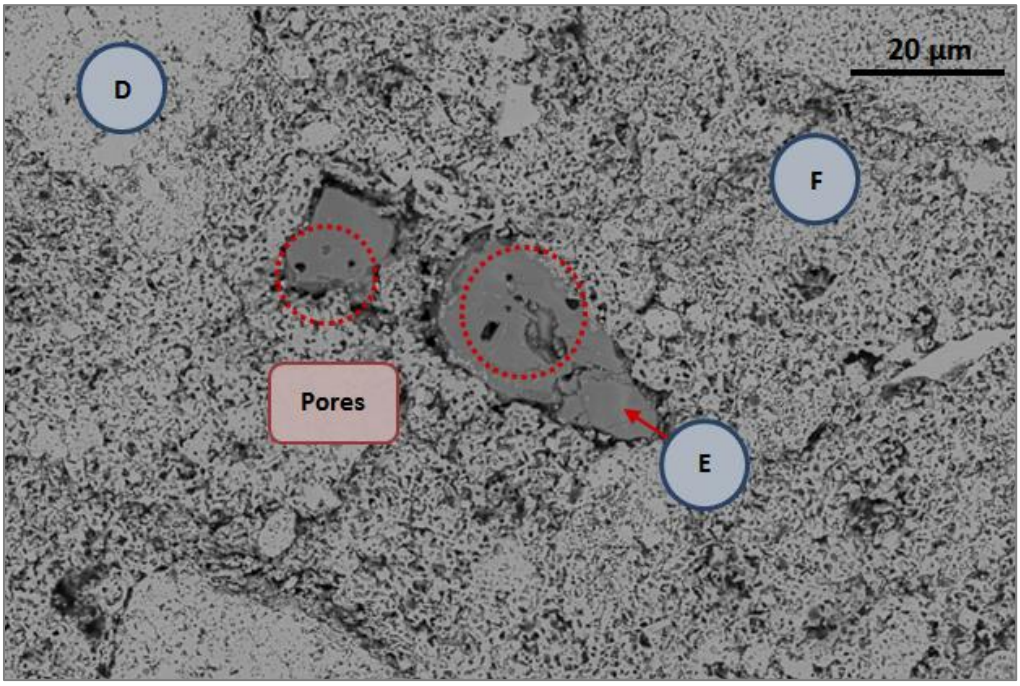

Figure 6.3: Heterogeneous microstructure of sintered (U, Ce)O_2 showing some open porosity *(x3000)*

Table 6.1: Atomic composition of the three distinct phases in Figure 6.2 and Figure 6.3 obtained by SEM-EDX

Region	Phase	U (at. %)	Ce (at. %)	O (at. %)
A	U-rich	32.98	0.23	66.79
B	Ce-rich	1.72	31.05	67.24
C	(U, Ce)O_2	31.16	5.63	63.21
D	U-rich	33.64	0.29	66.07
E	Ce-rich	1.05	51.8	47.15
F	(U, Ce)O_2	39.35	4.22	56.43

6.2.3.2 Raman measurements of virgin (U, Ce)O_2 disks

An initial Raman characterization was carried out on the three distinct phases in the (U, Ce)O_2 sample and the obtained results are illustrated in Figure 6.4.

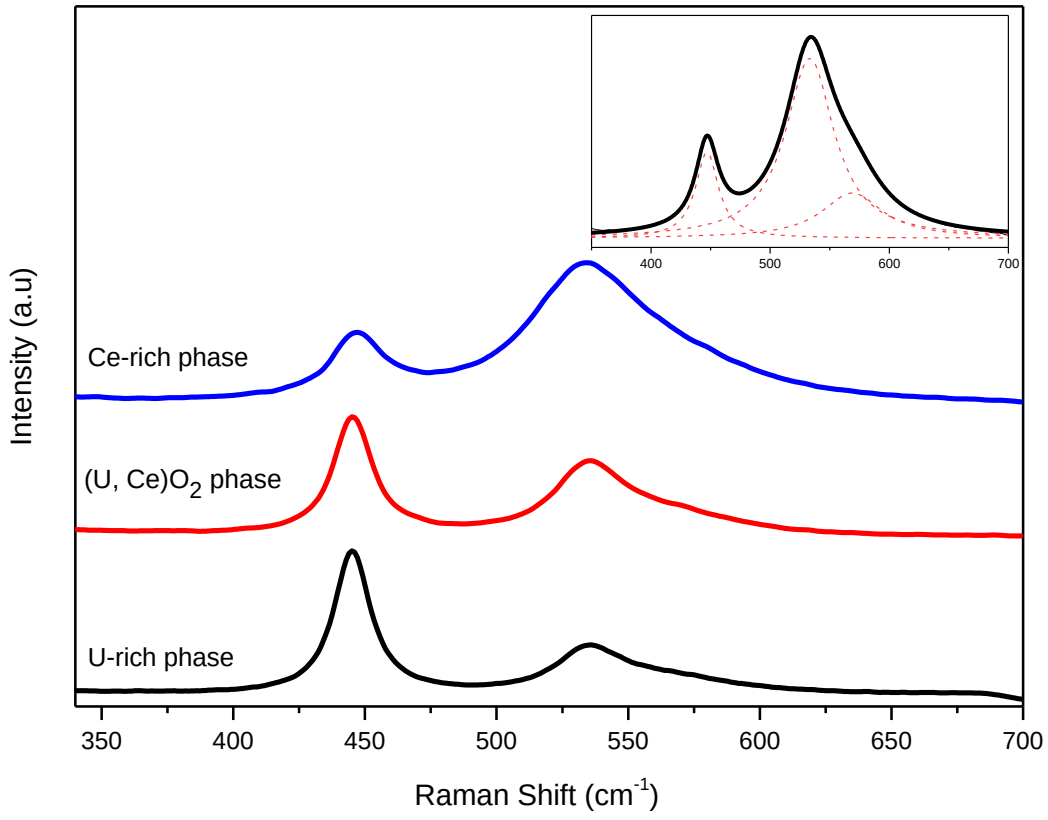

Figure 6.4: Initial Raman acquisition of the different phases present in the (U, Ce)O_2 pellet. The inset corresponds to the deconvolution of the Ce-rich spectrum

The presence of the Raman-active T_{2g} mode in all the three phases indicates that the heterogeneous sample retains a fluorite-type crystallographic structure. The Raman T_{2g} band for the uranium-rich phase occurs at 445 cm^{-1} but it tends to shift to higher wavelength with increasing cerium content. A deconvolution of the peaks show that T_{2g} band evolves to 446 cm^{-1} and 447 cm^{-1} for the (U, Ce)O_2 coating phase and cerium-rich region respectively.

In addition to the T_{2g} peak, two other bands at 537 cm^{-1} and 566 cm^{-1} can be observed. The presence of these two bands is in agreement with available data for cerium-doped pellets [[196], [197] & [198]]. Guo *et al.* [196] assigned the two peaks to the presence of intrinsic oxygen vacancies related to hypo-stoichiometric cerium contained in the virgin sample.

However with increasing cerium content, the two peaks merge into a broad band at 537 cm^{-1} and might correspond to the defect-induced LO peak previously as previously reported for virgin UO_2 disks. The intensity ratio of the LO mode/T_{2g} peak (I_D/I_{T2g}) from Figure 6.4 indicates that the degree of defect sites is proportional to the cerium content in each phases.

6.2.4 Results: Alpha irradiation of (U, Ce)O_2/Ar system

6.2.4.1 *In situ* Raman measurement

During the *in situ* Raman measurement, it was observed that the high intensity of the plasma band at 825 cm^{-1}, arising due to interaction of the alpha ions with the argon gas, completely overshadows both the T_{2g} and the defect bands. In order to improve the spectrum resolution in regards to the main peaks of interest, it was viewed as more feasible to proceed with a sequential irradiation campaign. The helium beam was turned off at different time intervals so as to avoid the plasma. A Raman measurement was immediately conducted after which the beam was turned on again. This procedure was repeated until the beam delivers a final fluence of 7.07 x 10^{15} α/cm^2. The collected Raman spectra corresponding to their respective irradiation fluence are presented in Figure 6.5.

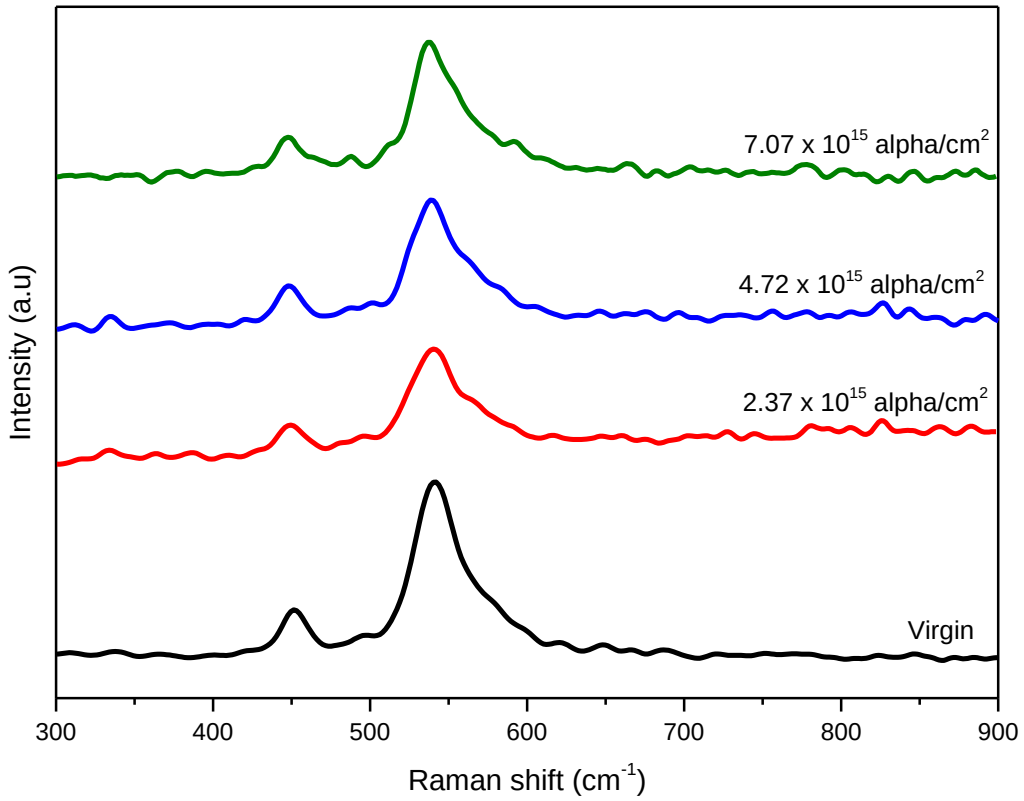

Figure 6.5: *In situ* Raman spectra recorded at different time interval during the alpha irradiation of (U, Ce)O_2 when exposed to argon gas

6.2.4.2 Kinetic evolution of the T_{2g} band

The kinetic behavior of the T_{2g} band under alpha irradiation was also analyzed through the use of the *in situ* Raman set-up. As previously defined in Chapter 5, the acquired Raman spectra were initially analyzed by the Renishaw WIRE software in order to remove any parasitic signals. A deconvolution of the T_{2g} band was then carried out using the ORIGIN software. The kinetic evolution of the T_{2g} intensity and width as a function of irradiation time is shown in Figure 6.6 and Figure 6.7 respectively.

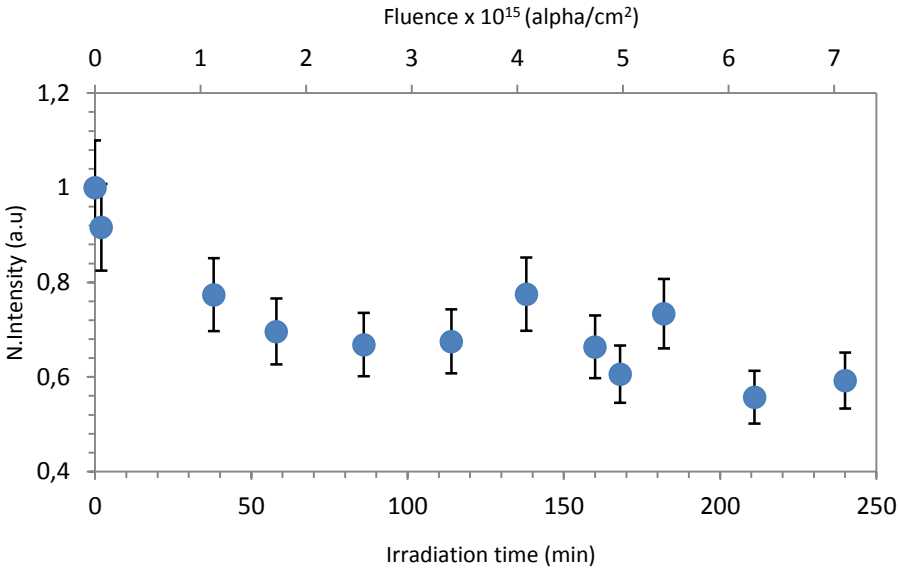

Figure 6.6: Kinetic evolution of the T_{2g} intensity during the alpha irradiation of (U, Ce)O_2 under inert argon environment

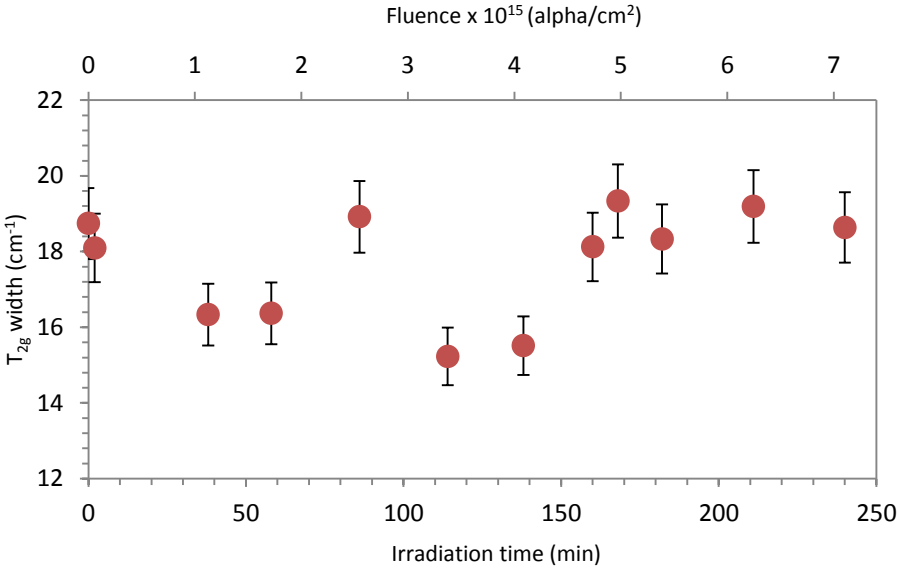

Figure 6.7: Kinetic evolution of the T_{2g} width during the alpha irradiation of (U, Ce)O_2 under inert argon environment

Figure 6.6 is in good agreement with the T_{2g} behavior acquired during the alpha irradiation of the UO_2/Ar system as previously reported in Chapter 5. However as no *in situ-post irradiation* Raman measurement was carried out, it was not possible to determine whether the T_{2g} intensity was restored to its starting value when the alpha beam was turned off. Thus based on the study of Guimbretière et *al.* [105], it is difficult to assign the T_{2g} intensity decrease either to a temperature effect or an irradiation-induced effect.

It is to be noted that prior to irradiation, the width of the T_{2g} band provides an indication regarding the local damages (U/Ce) in the virgin sample. Figure 6.7 shows no broadening of the T_{2g} peak under alpha irradiation. This might initiate that the damages resulting from the irradiation beam are not sufficiently high enough compared to the initial intrinsic defect concentration in order to modify the width of the T_{2g} band. To further support this argument, it is important to study the kinetic evolution of the defect-induced LO peak occurring at 537 $cm^{-1.}$

6.2.4.3 Kinetic evolution of the defect-induced LO peak

In regards to the (U, Ce)O_2 mixed oxides, it was observed that the alpha irradiation does not induce the apparition of the Raman triplet defect bands. In fact, the initial defect-induced LO-mode occurring at 537 cm^{-1} remained on the spectra even at the end of the alpha irradiation. As mentioned earlier, intensity ratio of the LO mode/T_{2g} peak (I_D/I_{T2g}) corresponds to the degree of defect sites related to hypo-stoichiometric cerium content. Thus, to investigate whether the alpha irradiation affects the initial defect sites, an *in situ* Raman analysis of the LO mode/T_{2g} peak (I_D/I_{T2g}) intensity ratio was conducted and the findings are shown in Figure 6.8.

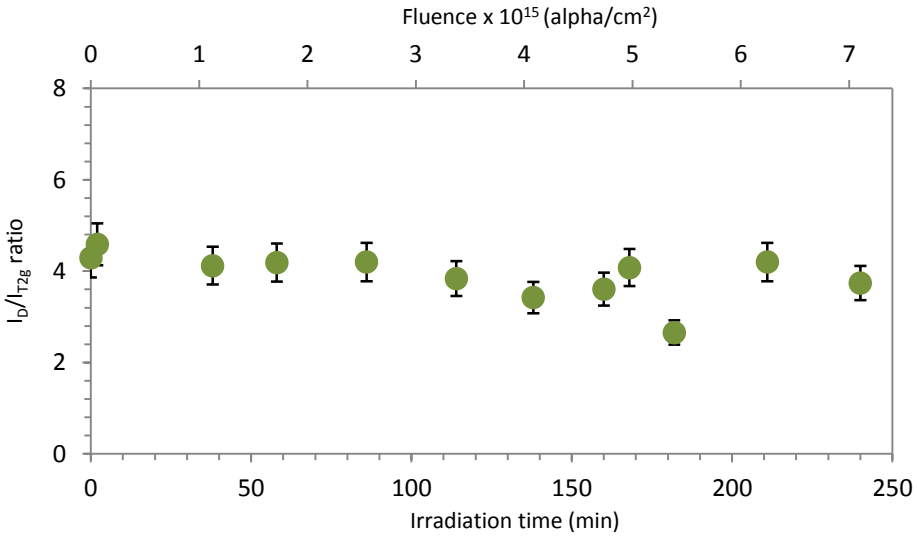

Figure 6.8: Kinetic evolution of the I_D/IT_{2g} intensity ratio during the alpha irradiation of (U, Ce)O_2 under inert argon environment

The initial high I_D/I_{T2g} intensity ratio before irradiation indicates an important concentration of oxygen vacancies related to the high surface cerium (Ce^{3+}) content. From the above figure, it can be seen that the initial defect band is not influenced by the alpha ions as it shows an almost constant evolution under increasing irradiation fluence. This observation provides further evidence to suggest that the concentration of irradiation defects induced by the alpha ions is inferior to the initial intrinsic defect concentration.

6.2.5 Results: Alpha irradiation of (U, Ce)O_2/H_2O system

6.2.5.1 *In situ* Raman measurement

In the previous chapter, it was shown that the formation kinetics of irradiation defects in UO_2 depends on the irradiation environment. A similar study was carried out to determine whether alpha irradiation induces the apparition of the Raman triplet defect bands in the (U, Ce)O_2 sample when the latter was exposed in a chemically reactive environment, i.e., aerated water.

However for this study, it was again difficult to carry out a continuous monitoring of the fuel surface during irradiation. It was noted that the gaseous radiolytic products formed during the irradiation-induced water radiolysis cause a significant accumulation of water bubbles in the irradiation cell. The bubbles failed to escape from the sample holder and were trapped on the polished fuel surface onto which the laser of the Raman head was focused. In doing so, the laser focalization on the fuel surface was reduced and the *in situ* Raman spectra were collected with a high background noises to signal ratio as it can be seen in Figure 6.9.

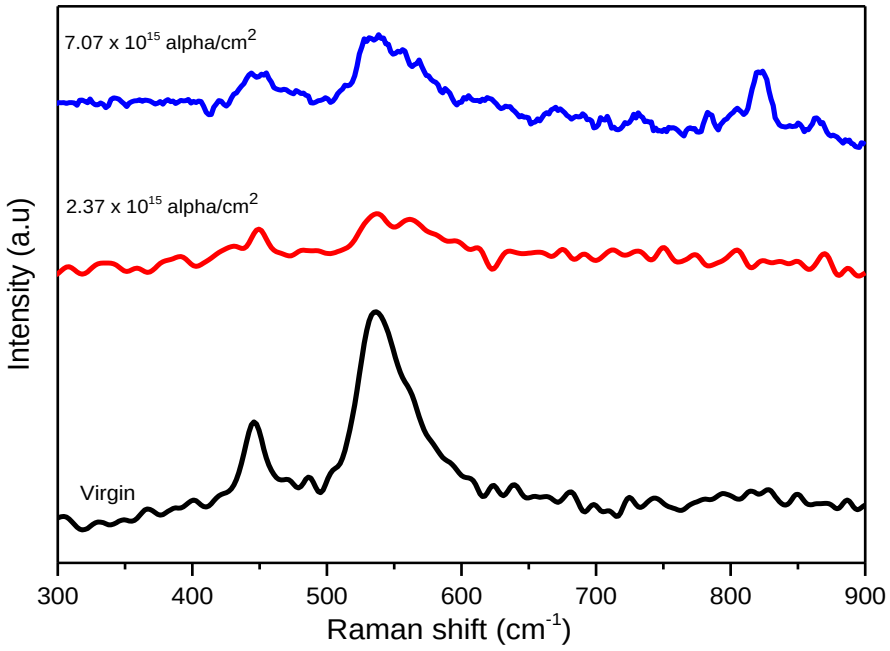

Figure 6.9: *In situ* Raman spectra collected during the alpha irradiation of (U, Ce)O_2/H_2O system

Before irradiation, the T_{2g} peak and the defect-induced LO-mode can both be clearly distinguished on the spectrum of virgin (U, Ce)O_2 in Figure 6.9. To enhance the laser focalization during the *in situ* measurements and to avoid the water bubbles, the laser focus point was changed to different positions on the fuel surface by moving the Raman probe head. Even though, it can be seen from Figure 6.9 that the *in situ* Raman spectra were acquired with a relatively poor spectral resolution.

As a first approximation, the Raman spectra collected at the end of irradiation indicates that the alpha irradiation did not induce the apparition of the Raman triplet defect bands on the irradiated (U, Ce)O_2. These observations are consistent with the findings obtained during the irradiation of the (U, Ce)O_2 under inert gaseous environment. On the other hand, a deconvolution of the Raman spectra showed the double peaks in the 800-900 cm^{-1} range which can be attributed to the correspond to the axial stretching mode of uranyl ion (819 cm^{-1}) and peroxide ion (865 cm^{-1}) of the studtite structure. However as discussed in Section 5.8.4, the small intensity of the peaks indicates that the studtite phase occurs in the form of a weathered thin layer which has not yet fully crystallized on the fuel leached surface.

6.2.5.2 *In situ* post irradiation Raman measurement

Post irradiation, the sample holder was manually manipulated to purge out the water bubbles through the top openings of the irradiation cell, but without removing the (U, Ce)O_2 disk and the irradiated water solution. The (U, Ce)O_2 disk was then left in contact with the irradiated water solution for an additional 10 hours.

An extended *in situ-post irradiation* Raman acquisition was carried out to investigate the kinetic evolution of the secondary phases. The removal of the water bubbles from the irradiation cell largely enhanced the quality of the Raman spectra as illustrated in Figure 6.10.

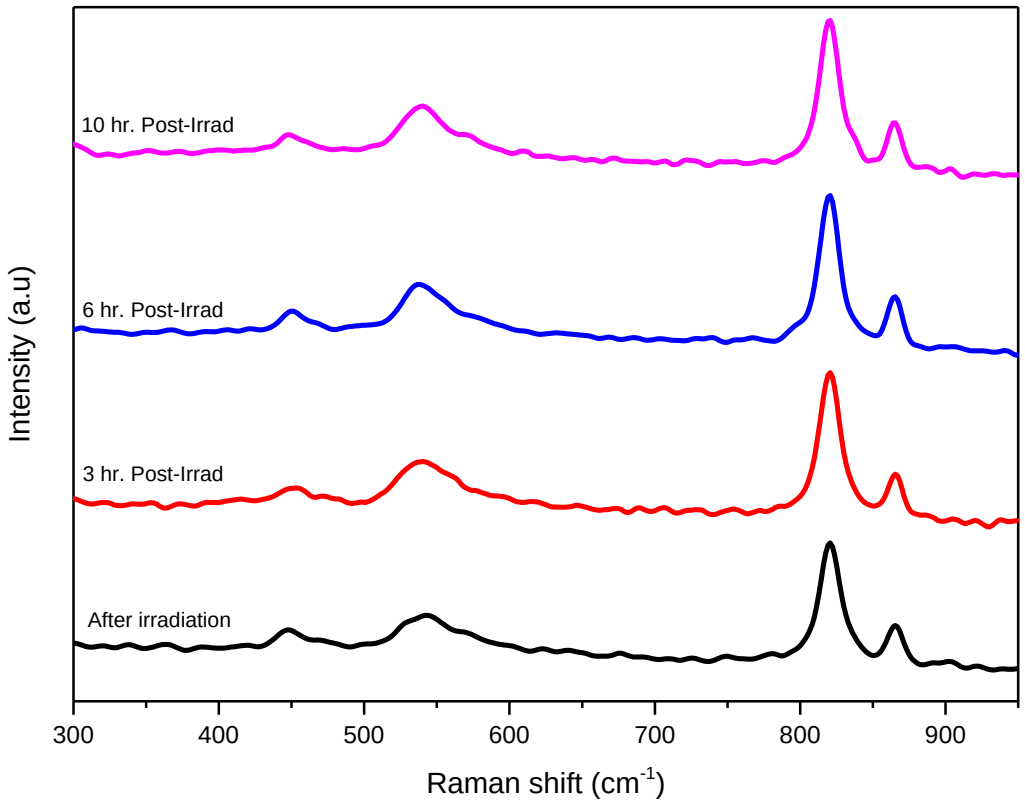

Figure 6.10: Extended *in situ-post irradiation* Raman measurement of the (U, Ce)O_2/H_2O interface after alpha irradiation

Similar to the methodology adopted during the UO_2 leaching experiment, the kinetic evolution of the secondary phases was determined through the use of the WIRE software by a simple signal to background integrated intensity in the 815-870 cm^{-1}. The obtained kinetics is presented in Figure 6.11.

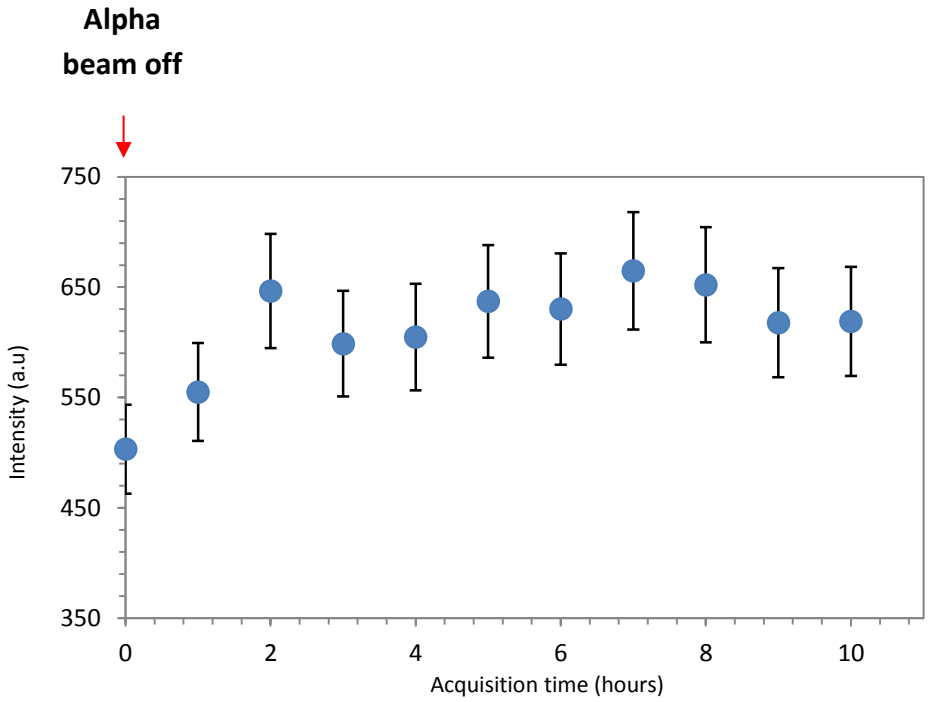

Figure 6.11: Kinetic evolution of the studtite secondary phase during the extended *in situ-post irradiation* Raman measurement

The presence of the studtite phase on the fuel surface at the end of irradiation suggests that the irradiated water solution contained sufficient radiolytic H_2O_2 and dissolved uranium to initiate the formation of the altered U(VI) phases. In addition the kinetics acquired in Figure 6.11 shows that the studtite precipitation continues to increase in the absence of the alpha irradiation beam. This observation is consistent with the *in situ-post irradiation* kinetic of the studtite phase obtained during the UO_2 leaching under alpha irradiation (Chapter 5).

6.2.5.3 SEM characterization of leached (U, Ce)O_2 surface

After the extended *in situ-post irradiation* Raman measurement, the irradiated water solution was recovered and the (U, Ce)O_2 disk was dismantled from the irradiation cell for subsequent surface analysis.

The microscopic evolution of the leached (U, Ce)O_2 surface was analyzed by SEM method. The radiolytic-induced surface alteration of the leached surface is illustrated in Figure 6.12 and Figure 6.13 respectively. The formation of a thick altered layer displaying microcracks which completely cover the sample surface can clearly be observed. In addition, the SEM analysis reveals that the secondary altered phases appear as compact fiber-like structures dispersed over the sample surface which can be distinguished at higher magnification.

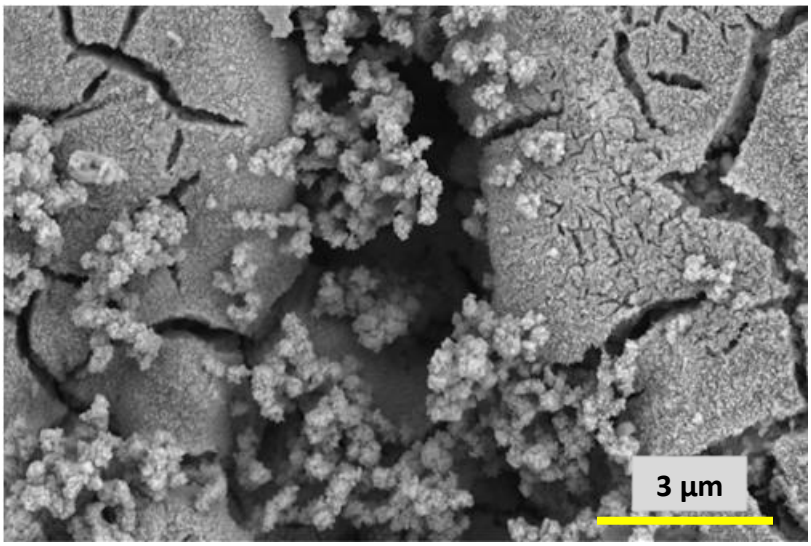

Figure 6.12: Formation of a thick altered layer with microcracks over the leached (U, Ce)O_2 surface (*x30000*)

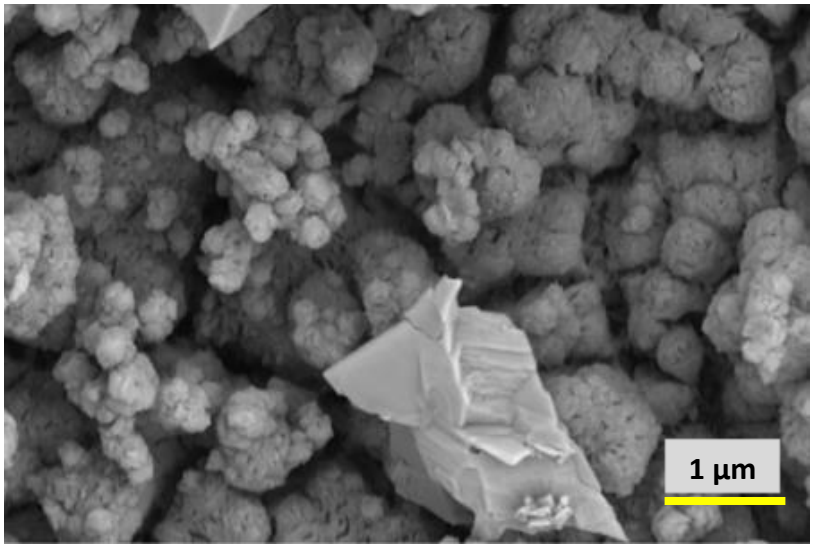

Figure 6.13: Higher magnification SEM image of the leached surface showing the compact secondary phases structures *(x60000)*

6.2.5.4 *Ex situ* Raman mapping of leached (U, Ce)O_2 surface

From the UO_2 electron irradiation experiment (Chapter 4), it was evidenced that the long exposure of irradiated UO_2 disk in ambient-air conditions leads to its rapid oxidation. The latter was mainly due to the role of oxygen vacancies near the UO_2 surface-air boundary interface which leads to an increase in the oxygen mobility.

In regards to the leached (U, Ce)O_2 disk, the presence of the defect-induced LO-mode band gave indication to suggest that the sample still contained an important concentration of oxygen vacancies at the end of the leaching experiment. Therefore this study was extended to further investigate the role of oxygen vacancies during the exposure of irradiated (U, Ce)O_2 disk in ambient-air. The obtained findings will be used to confirm the proposed mechanisms for the rapid oxidation of irradiated UO_2 disk.

Post-irradiation, the leached (U, Ce)O_2 disk was left in ambient-air conditions for about 6 months and then analyzed by the Renishaw Invia Raman spectroscopy. For an independent quantitative analysis of the Ce-rich phase, U-rich phase and the intermediate solid solution phase, Raman spectrometry was used to identify a suitable region on the (U, Ce)O_2 surface which was not covered by the studtite secondary phase. The microscope image of the selected (U, Ce)O_2 region for the analysis is shown in Figure 6.14.

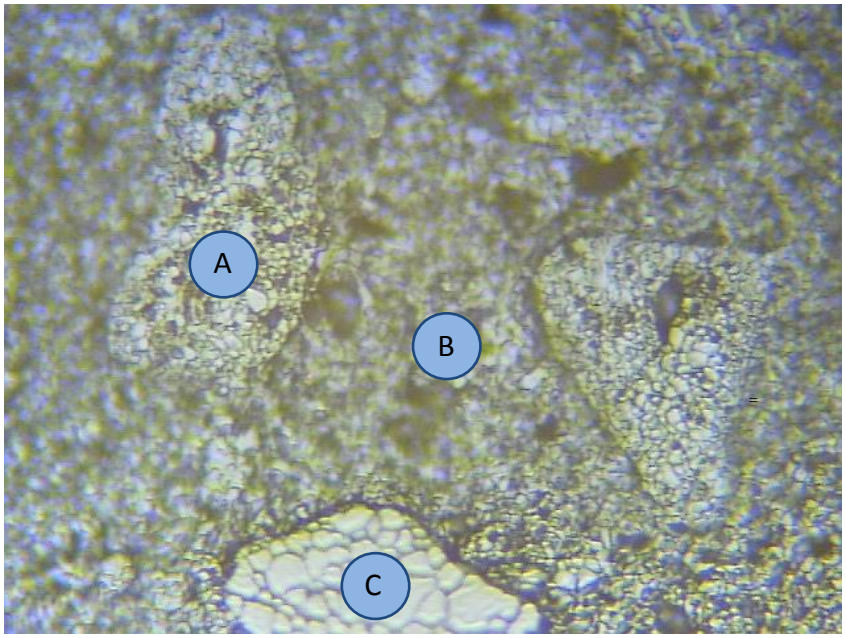

Figure 6.14: Microscope image of the leached surface after air exposure. Three distinct phases that are characteristic to the (U, Ce)O_2 heterogeneous microstructure are designated by **A** (Ce-rich phase), **B** (agglomerate/intermediate phase) & **C** (U-rich phase)

A Raman acquisition was carried out on each of the three distinct phases. The obtained results are presented in Figure 6.15.

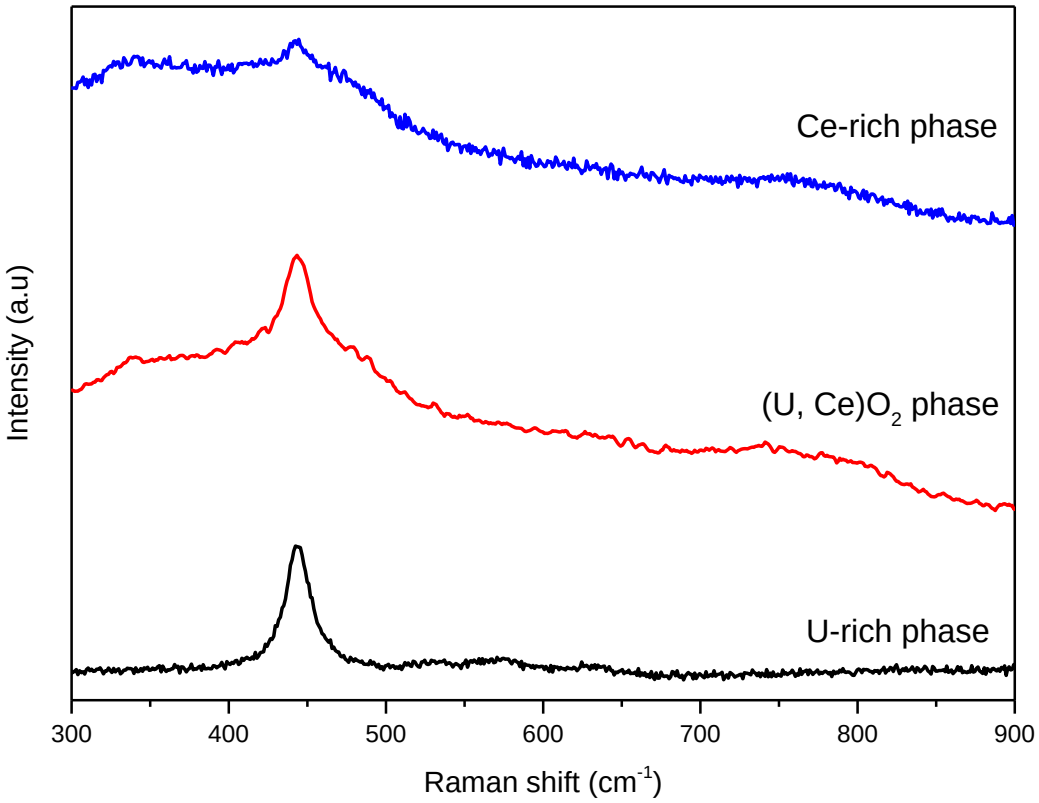

Figure 6.15: Raman acquisition of the three distinct different phases in the irradiated (U, Ce)O_2 disk after 6 months of ambient-air exposure

In regards to irradiation defects, the Raman acquisition put into evidence the presence of the Raman triplet defect bands occurring in the 500-650 cm^{-1} spectral range of the U-rich spectrum. The U1, U2 & U3 bands can clearly be distinguished from Figure 6.16.

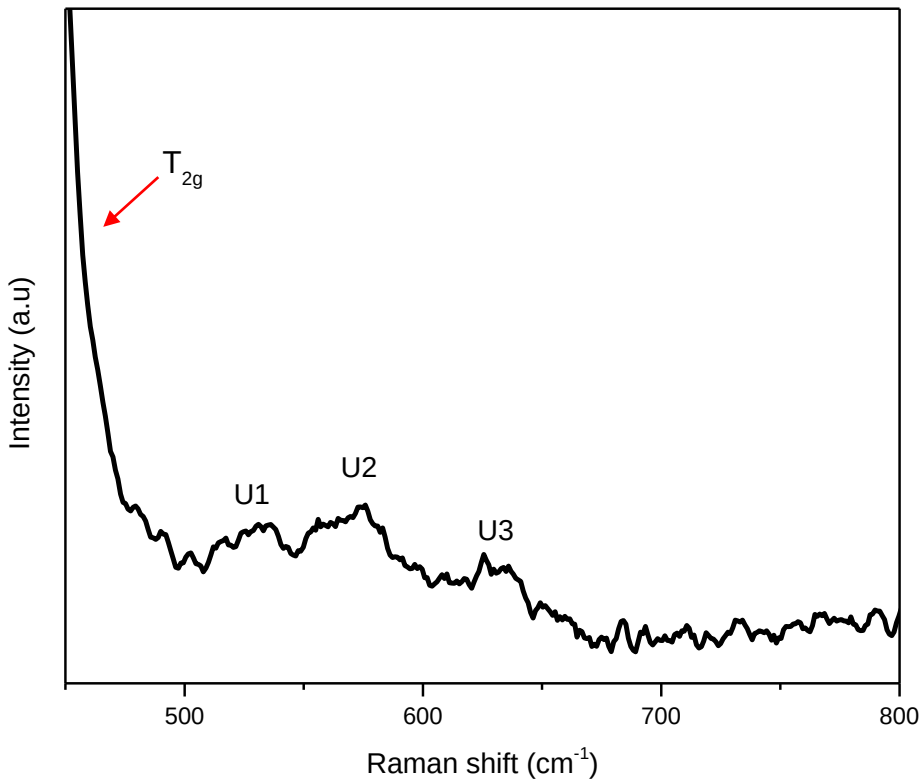

Figure 6.16: Raman acquisition of the U-rich phase in the irradiated (U, Ce)O_2 disk after 6 months of ambient-air exposure

However, no such observation was recorded for the Ce-rich phase. As previously discussed in Section 6.2.1, Grover *et al.* [195] evidenced the presence of the Raman defect bands during the irradiation of pure CeO_2 compounds with heavy swift ions. The irradiation was carried out with 100 MeV silver ions and a fluence of 1 x 10^{14} ions/cm^2, which corresponds to a total dpa of 8.59.

On the other, no relevant data regarding the Raman analysis of alpha-irradiated CeO_2 have been reported. Thus to explain the absence of the defect bands in the Ce-rich phase, an experiment was carried out whereby a pure CeO_2 disk was irradiated with a 45 MeV alpha beam to reach a final fluence of 7.07 x 10^{15} alpha/cm^2. The Raman measurements of the virgin and irradiated CeO_2 sample were performed and the obtained findings are presented in Figure 6.17.

From the figure, it can be observed that the alpha irradiation does not induce the apparition of the Raman triplet defect bands. In contrast to heavy ion irradiation, it can be concluded that the irradiation damages resulting from the 45 MeV alpha ions (dpa: 0.0465) are not sufficient enough to cause a local symmetry lowering in CeO_2 lattice in order to be detected by Raman spectroscopy.

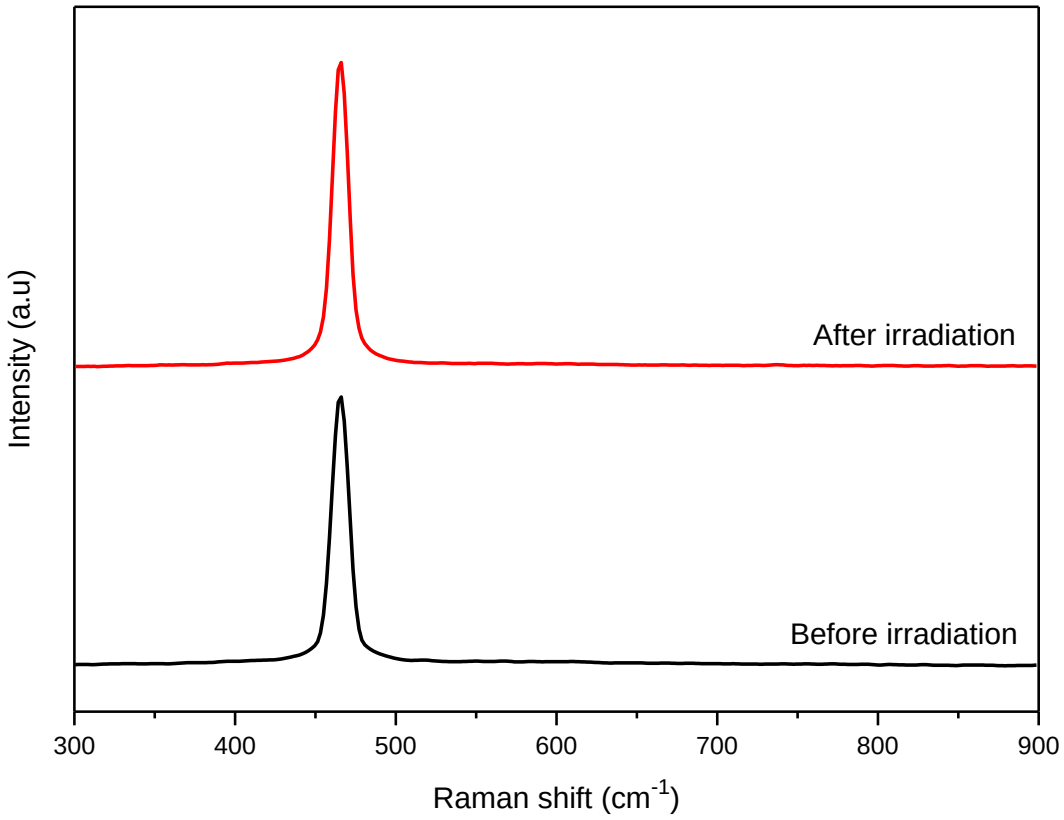

Figure 6.17: Comparison of the Raman spectra of pure CeO_2 sample before and after alpha irradiation

In regards to the (U, Ce)O_2 intermediate phase, it is to be noted that the continuous ambient-air exposure of the irradiated (U, Ce)O_2 causes a significant decrease in the initial LO-mode band intensity that was attributed to intrinsic oxygen vacancies. The disappearance of the LO-mode might indicate the surface oxidation of the irradiated sample which anneals the intrinsic oxygen vacancies. Such observation is consistent with the proposed mechanisms involving the enhanced oxygen mobility to explain the rapid oxidation of samples containing defects as previously detailed in Chapter 4.

Therefore this study confirmed the presence of the Raman triplet defect bands in the U-rich region but the latter do not occur in the Ce-rich phase. In regards to the (U, Ce)O_2 intermediate phase, the defect bands can also be expected by consideration the low concentration of cerium dopants (refer to Table 6.1) but no such findings were evidenced.

Thus, the irradiation response of the intermediate phase suggests that the apparition of the Raman triplet defect bands might be influenced by fuel chemistry. This study was therefore extended to investigate the behavior of several (U, Th)O_2 compounds under alpha irradiation.

6.3 Homogeneous microstructure: UO_2 doped with Thorium

In this section, the irradiation response of homogeneous $(U_xTh_{1-x})O_2$ disks was investigated. Thorium was used as the dopant because it shares the same fluorite crystal structure (Fm3m) as UO_2. The thorium atoms are arranged in a simple cubic structure surrounded by oxygen atoms in a FCC structure. Unlike UO_2, ThO_2 exhibits a white appearance and becomes dark when melted in reducing conditions [199]. ThO_2 has been the main subject of interest due to the absence of 5f electrons, which in UO_2 represents the main features of properties such as electrical conductivity, among others. The absence of these low energy electrons in the valence bands is mainly responsible for the transparent nature of ThO_2.

Kelly *et al.* [200] reported a maximum oxidation state of +4 for thorium indicating that they tend to form stoichiometric oxides as illustrated by its phase diagram in Figure 6.18.

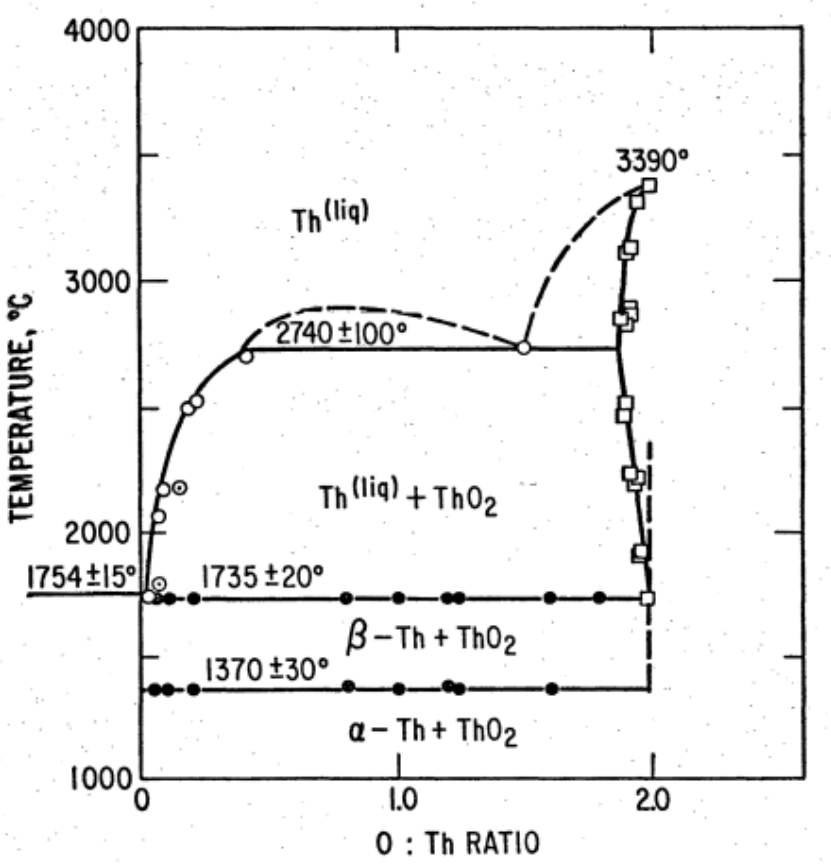

Figure 6.18: Phase diagram of oxygen-thorium system [201]

6.3.1 Irradiation response of ThO_2

The behavior of thoria under irradiation has been subject of intensive experimental research. It has been reported that irradiation induces a change in the physical appearance of ThO_2 sample. For instance, we have reported that the initially white ThO_2 pellets turn into a blue color as a result of alpha irradiation [104]. Childs *et al.* [202] investigated the effect of low-exposure gamma radiation on thoria. The authors reported that the color change was due to an effect involving impurity atoms and oxygen vacancies. A similar observation was reported by Tracy *et al.* [203].

Since ThO_2 share similar physico-chemical properties with UO_2 (same fluorite-type crystal structure, similar mass and number of electrons), both are expected to have a similar behavior under irradiation. However compared to irradiated UO_2, it has recently been reported that the Raman triplet defect bands is masked by the presence of luminescence signals on the Raman spectrum of irradiated ThO_2 [104]. An improved time-resolved Raman set-up is required to differentiate between the Raman triplet defect bands and the luminescence signals. Figure 6.19 shows the time-resolved Raman spectra of a ThO_2 disk irradiated with a 25 MeV alpha beam.

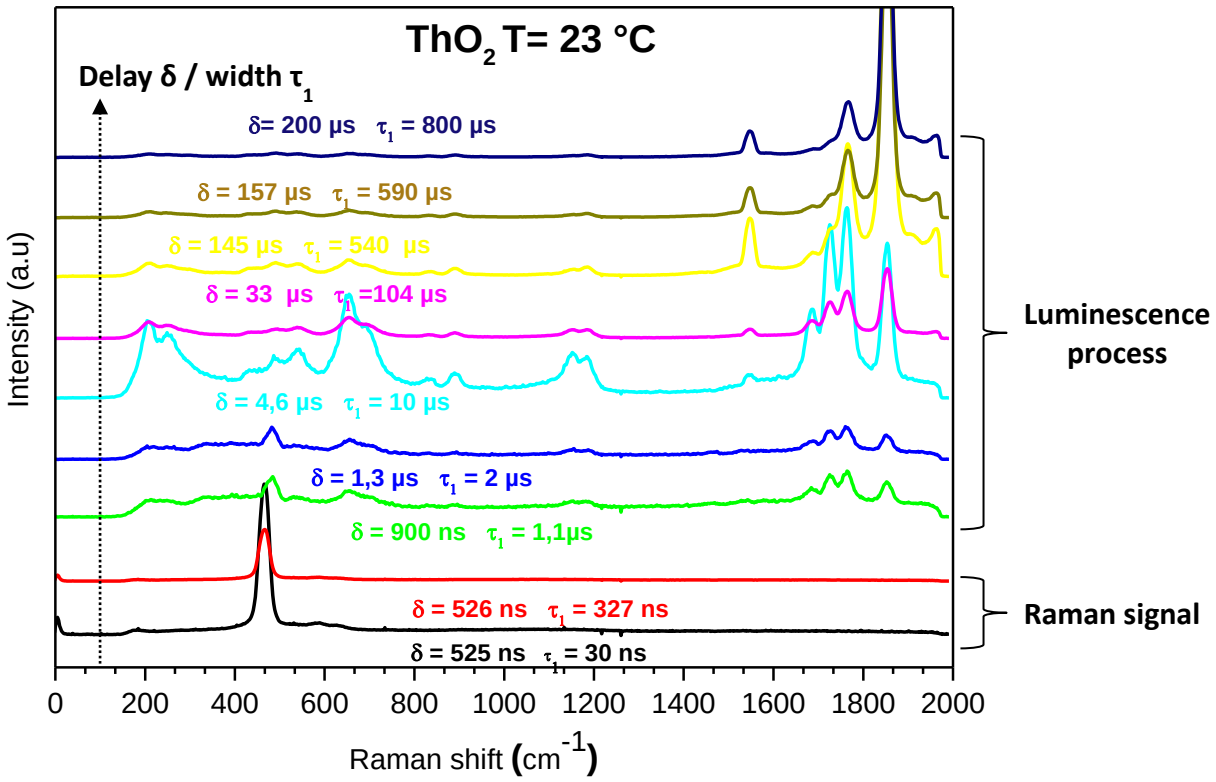

Figure 6.19: Time-resolved Raman spectra of 25 MeV alpha irradiated ThO_2 which allow to separate the Raman defect bands from the luminescence signals

Figure 6.20 shows the Raman triplet defects bands in ThO_2 samples that have been irradiated with 92 MeV krypton ions and 25 MeV alpha ions on their respective spectra collected during the first nanoseconds of the time-resolved acquisitions. However in regards to a 2.5 MeV electron-irradiated ThO_2, the Raman defect bands do not appear on its spectrum. This can be attributed to the low defect concentration associated with electron irradiation experiments.

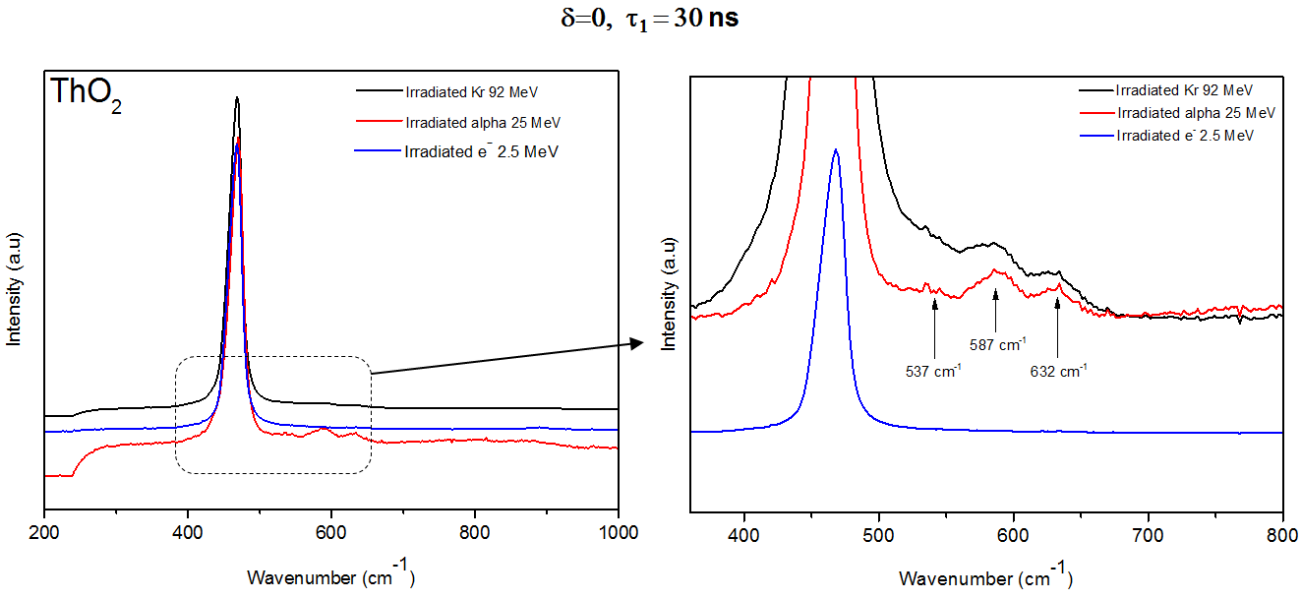

Figure 6.20: Evidence of the Raman triplet defect bands in irradiated ThO_2

6.3.2 Irradiation and characterization of $(U_xTh_{1-x})O_2$ disks

The irradiation of the different $(U_xTh_{1-x})O_2$ solid solutions was carried out at the CEMHTI cyclotron facility in the Dispositif d'Irradiation Appliqué aux MAtériaux du Nucléaire en Température (DIAMANT). The DIAMANT set-up is mainly used for irradiation at various temperatures ranging from -120°C to 1200°C. However, considering the presence of uranium in the solid solutions, it was deemed as more appropriate to carry out the implantation under vacuum and at room temperature to limit the risk of pellet oxidation.

Figure 6.21 illustrates the experimental installation used in this study. The latter comprises of a Raman probe head installed next to the DIAMANT installation. During irradiation, the pellets are loaded in DIAMANT set-up facing the incoming alpha beam. Immediately after irradiation, the sample holder is rotated 90° in the clockwise direction allowing the Raman probe head to have a direct access of the irradiated pellet surface.

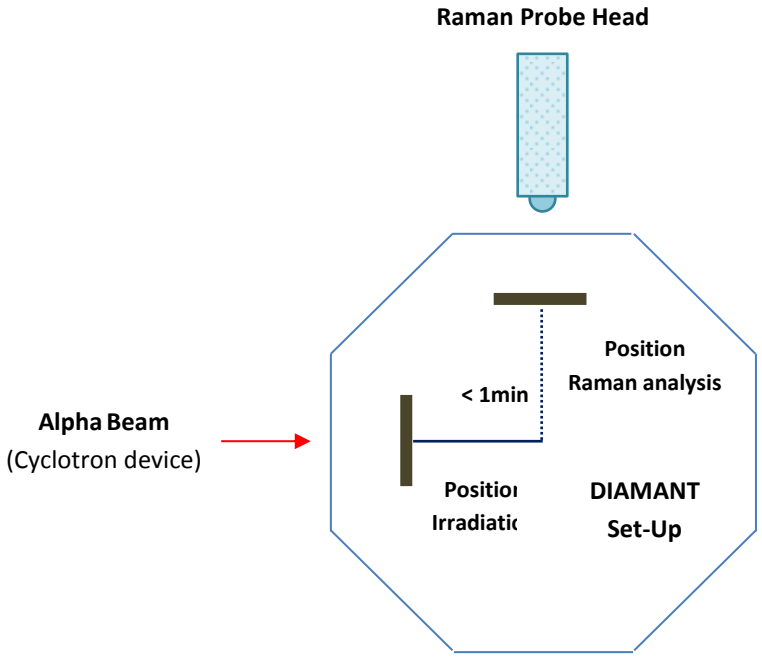

Figure 6.21: Top view of the DIAMANT installation illustrating the configuration of the disks during irradiation followed by *in situ-post irradiation* Raman measurement

The irradiation of the different homogeneous $(U_xTh_{1-x})O_2$ solid solutions was carried out using a 21 MeV alpha beam and a 50 nA ion flow to reach a final fluence of 7.07 x 10^{15} He/cm^2. The SRIM software was used to calculate the damages induced by the alpha ions using the displacement threshold energy (Ed) of 53.5 eV for Th [204], while the Ed values of 40 eV and 20 eV were considered for U and O respectively [124]. The obtained findings are presented in Table 6.2.

Table 6.2: Comparaison of the *(a)* position of the Bragg's peak, *(b)* Nuclear stopping power (Sn), *(c)* Electronic stopping power and *(d)* irradiation damages resulting from the implantation of the 21 MeV alpha ions in the different samples.

Mixed oxide sample	Position of Bragg's peak (µm)	Sn (keV/µm)	Se (keV/µm)	dpa
UO_2	105.25	0.07339	124.50	0.295
$(U_{0.8}Th_{0.2})O_2$	107.94	0.07151	121.30	0.301
$(U_{0.6}Th_{0.4})O_2$	107.83	0.07158	121.40	0.297
$(U_{0.4}Th_{0.6})O_2$	107.69	0.07168	121.50	0.292
$(U_{0.2}Th_{0.8})O_2$	107.05	0.07202	122.10	0.282

Raman acquisitions were performed before and after irradiation. As described in Chapter 3, the (U, Th)O_2 solid solutions were irradiated in the form of half-disks. The Raman probe head of the RA-100 spectrometer was initially used to characterize the irradiated surfaces of the samples immediately after irradiation. The irradiated samples were then removed from the sample holder and a line scanning was then performed using the Renishaw Invia spectrometer on the inner slice surface of each half-disk. This allows to probe the zone on the sample surface where the maximum energy was deposited.

As an example, Figure 6.22 shows the 21 MeV alpha energy deposition profile in the ($U_{0.8}Th_{0.2}$)O_2 mixed oxide. Zone A corresponds to the irradiated area that was analyzed by the RA-100 spectrometer. On the other hand, Renishaw Invia spectrometer was used for the Raman analysis of the point corresponding to the Bragg's peak position (Zone B).

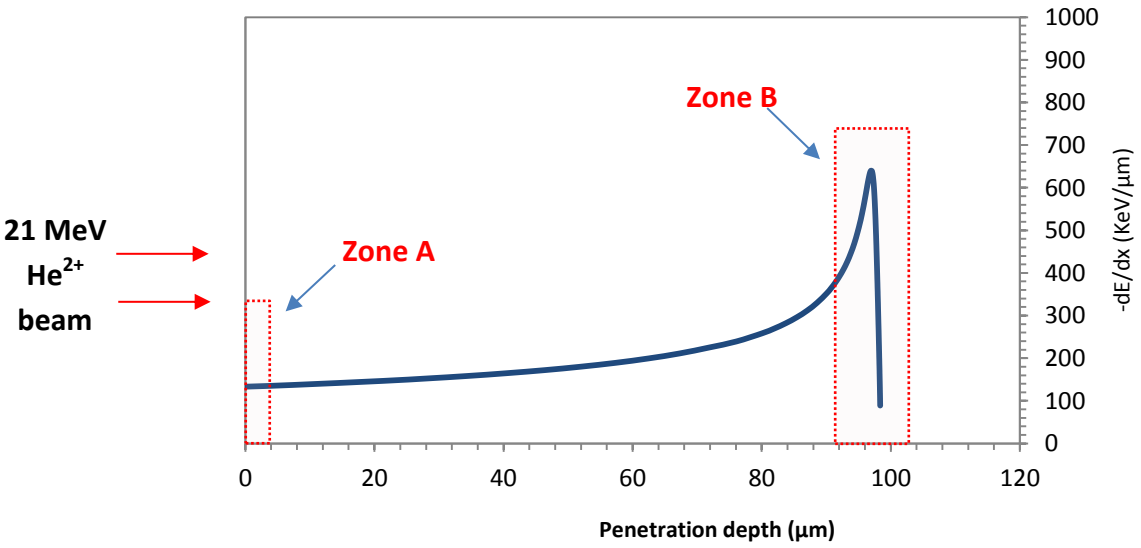

Figure 6.22: SRIM calculated energy deposit depth profile (-dE/dx) for the implantation of 21 MeV alpha ions in ($U_{0.8}Th_{0.2}$)O_2

6.3.3 Experimental results

This section is devoted to present the experimental results to understand the influence of alpha irradiation on the (U, Th)O_2 pellets. The Raman characterizations of the as-prepared mixed oxides pellets are firstly discussed and compared with a pure a UO_2 compound. The obtained results for the irradiated pellets are then interpreted and compared with their corresponding virgin samples.

6.3.3.1 Raman spectra of virgin $(U_xTh_{1-x})O_2$ disks

The initial Raman characterization of a pure UO_2 sample and the different virgin $(U_xTh_{1-x})O_2$ mixed oxides are presented in Figure 6.23. The fluorite crystal structure of the mixed oxides pellets is confirmed owing to the triply degenerate T_{2g} Raman-active vibration mode.

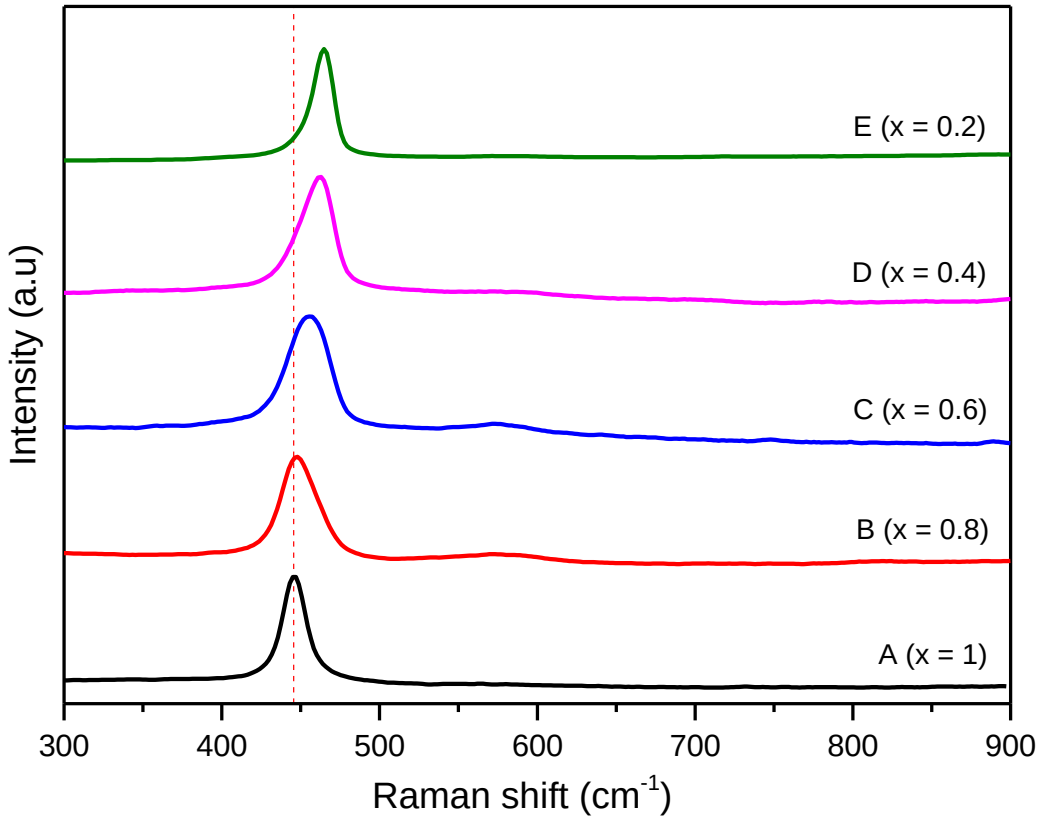

Figure 6.23: Raman spectra of as prepared UO_2 and $(U_x Th_{1-x})O_2$ disks at different Th doping level

The T_{2g} Raman-active vibrational mode of pure stoichiometric UO_2 can be seen to occur at 445 cm^{-1}. The effect of adding thorium causes a shift in the positioning of the T_{2g} band towards that of pure ThO_2 (465 cm^{-1}) [104].

Th-doping was also seen to affect the width of the T_{2g} band. Figure 6.24 shows that the peak broadening reaches its maximum when the thorium content was up to 40% but further addition causes the width to shrink. The T_{2g} broadening can be attributed to an increased frequency distribution of the U-O and Th-O vibrations and could arise from the local disorder caused by the addition of thorium cations.

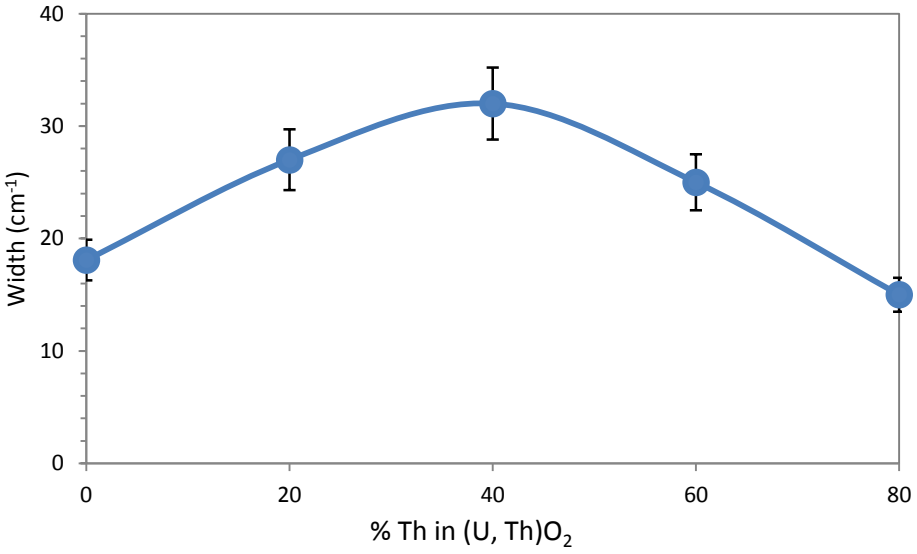

Figure 6.24: Variation of the T_{2g} width as a function of increasing Th content in (U, Th)O_2 mixed oxides

The thorium doping induces intrinsic defects and causes the distortion of the translation symmetry and relaxes the selection rules, thus making several dipole-forbidden optical transition modes observable in some compounds. This can be attributed to the weak feature occurring at around 575 cm^{-1} which corresponds to the dipole-forbidden longitudinal optical (LO) mode. The latter was observed to be more prominent in oxides containing 20% and 40% thorium respectively, i.e. sample B and C, as illustrated in Figure 6.25. The figure also shows that the intensity of the 575 cm^{-1} band decreases significantly above 40% thorium. In a similar study performed by Rao *et al.* [205], the authors assigned the LO mode to the presence of point defects.

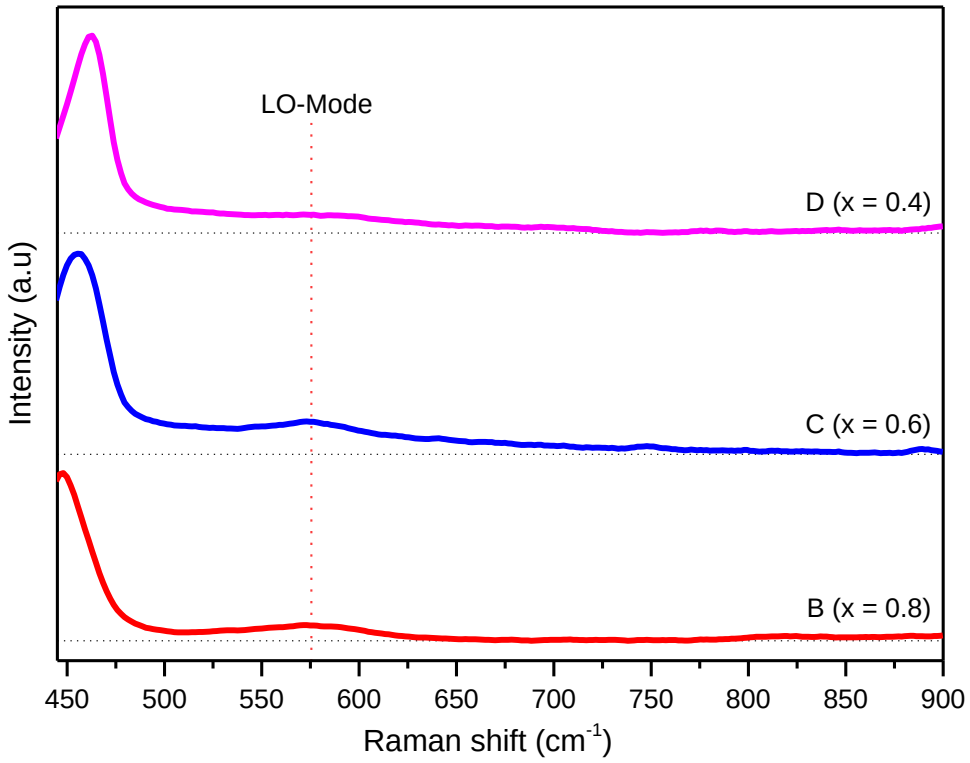

Figure 6.25: Raman spectra of virgin (U, Th)O_2 mixed oxides indicating the presence of the LO-mode

A fit of the different peaks appearing on the Raman spectra of the different mixed oxides was also carried out to investigate the change in their initial positions as a function of Th-doping. Figure 6.26 shows that the asymmetry T_{2g} band vary almost linearly with change in compositions and shifts towards higher wavenumbers at a rate of 0.267 cm^{-1} per ThO_2 percentage. The forbidden LO mode exhibits a similar behavior with a 0.25 cm^{-1} shift per ThO_2 percentage. The quantitative analysis of the Raman bands offers the possibility to deduce the composition of any $(U_xTh_{x-1})O_2$ solid solutions based on the T_{2g} and LO band positions respectively.

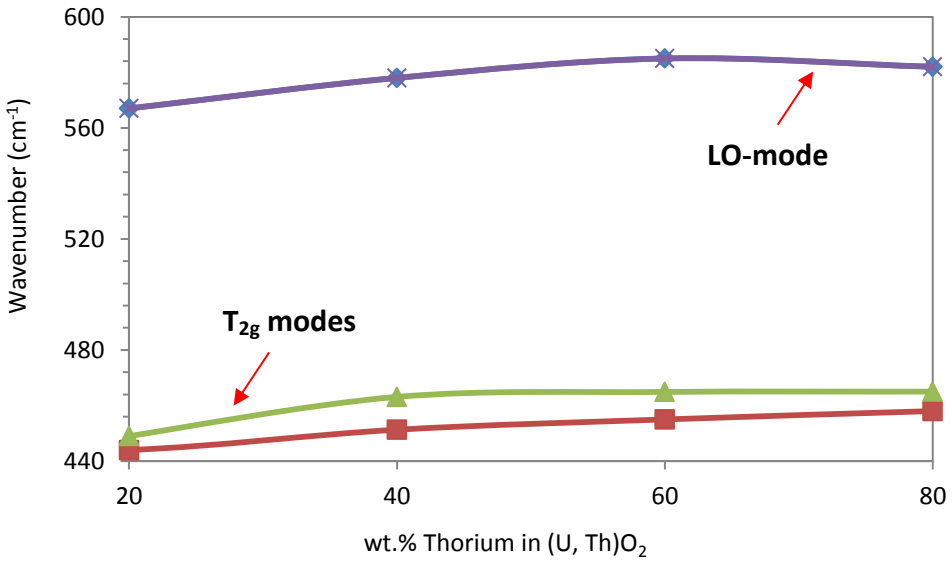

Figure 6.26: Variation of Raman mode wavenumber with composition of UO_2–ThO_2 system

6.3.3.2 Raman spectra of irradiated $(U_xTh_{1-x})O_2$ disks: Surface characterizations

Immediately after irradiation, the surface of the irradiated pellets were analyzed inside the DIAMANT using the Raman probe head of the RA-100 spectrometer as previously described in Section 6.3.2. For a much better visual interpretation, the obtained findings for the different nuclear fuels are independently compared with their corresponding virgin spectra and are illustrated in the figures below.

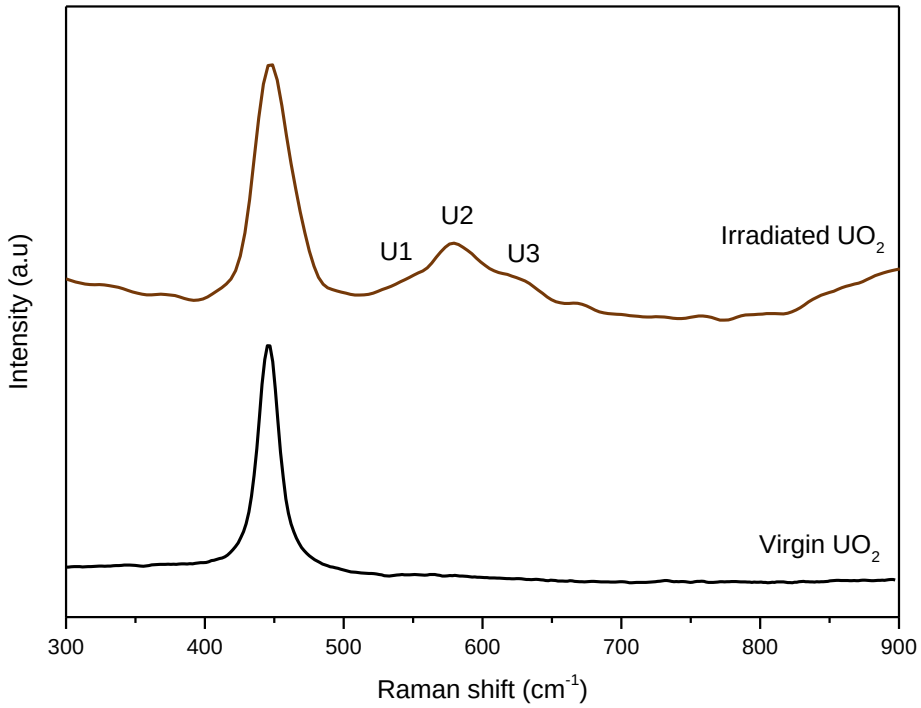

Figure 6.27: Comparison between the virgin and irradiated UO_2 spectra acquired using the RA-100 spectroscopy

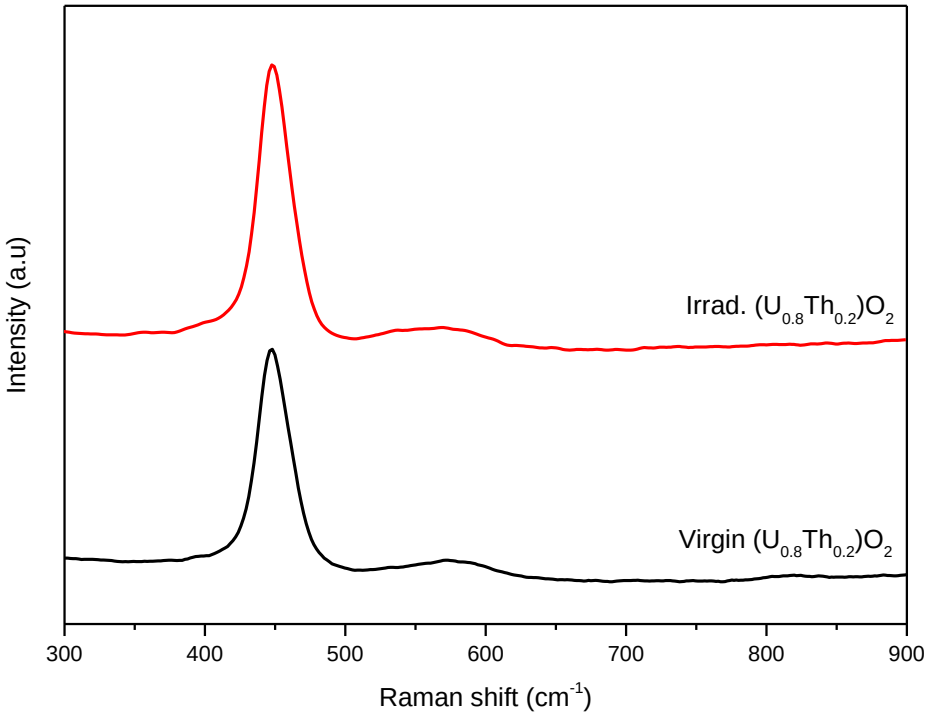

Figure 6.28: Comparison between the virgin and irradiated $(U_{0.8}Th_{0.2})O_2$ spectra acquired using the RA-100 spectroscopy

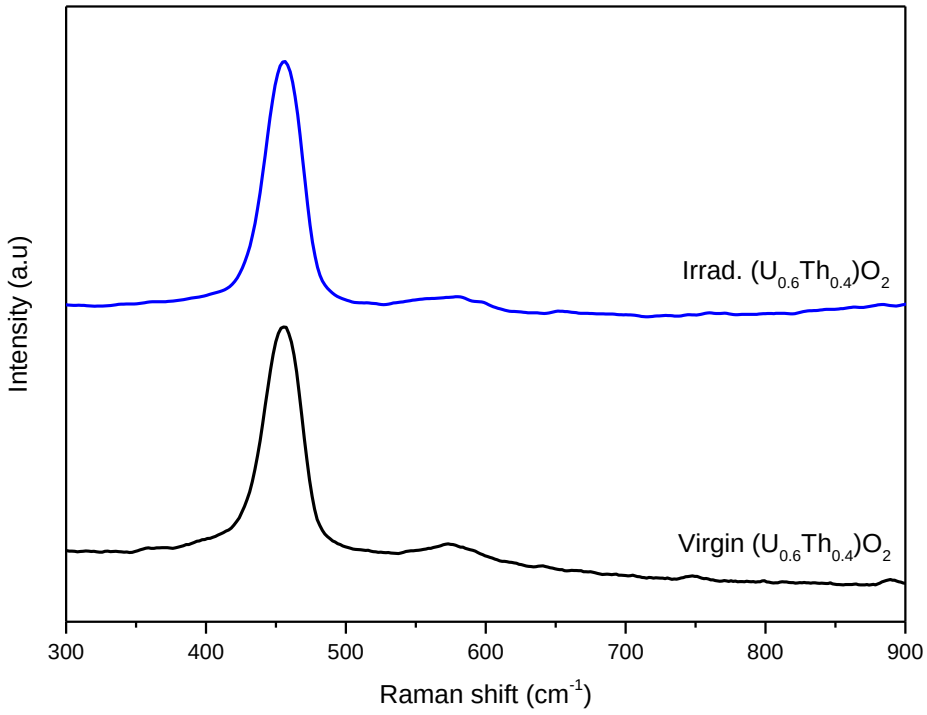

Figure 6.29: Comparison between the virgin and irradiated $(U_{0.6}Th_{0.4})O_2$ spectra acquired using the RA-100 spectroscopy

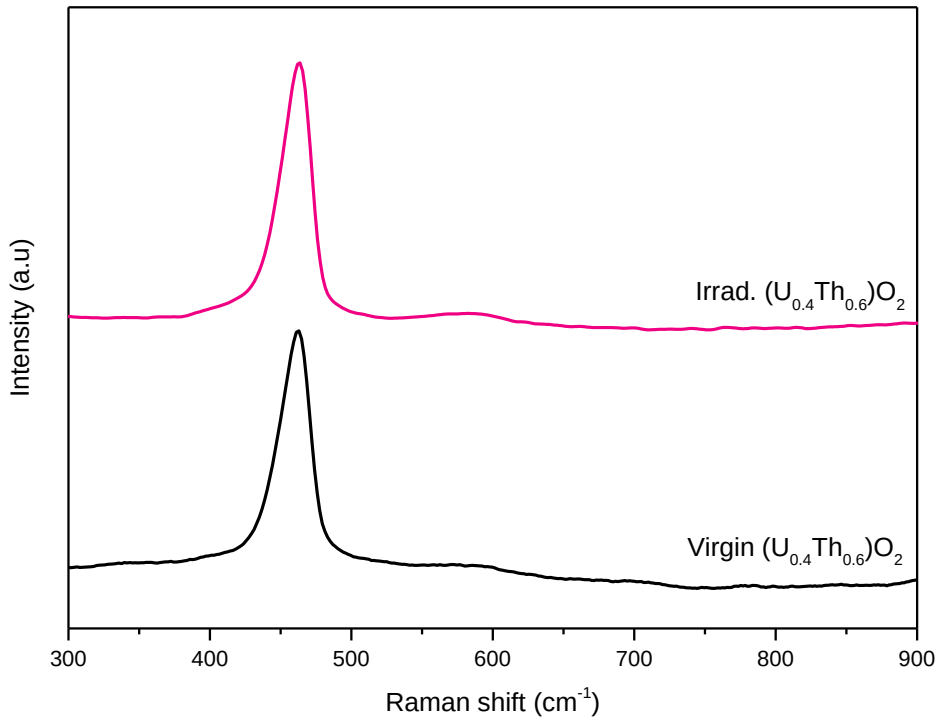

Figure 6.30: Comparison between the virgin and irradiated $(U_{0.4}Th_{0.6})O_2$ spectra acquired using the RA-100 spectroscopy

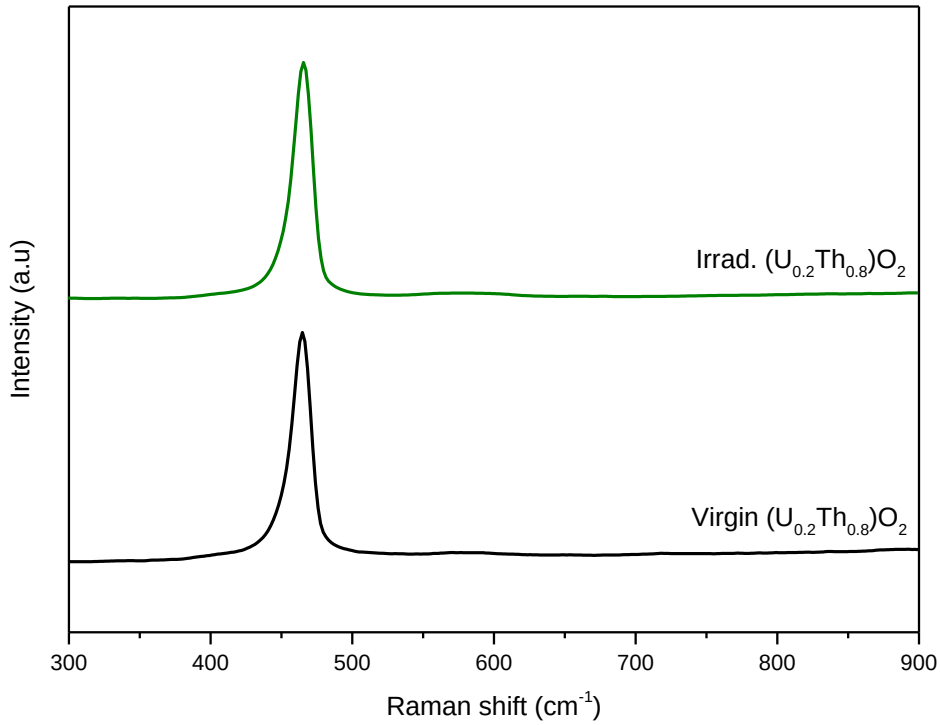

Figure 6.31: Comparison between the virgin and irradiated $(U_{0.2}Th_{0.8})O_2$ spectra acquired using the RA-100 spectroscopy

Figure 6.27 shows clearly shows that the alpha ion beam induces the apparition of the triplet defect bands (U1, U2 & U3) on the spectra of the irradiated pure UO_2 sample. In regards to different (U, Th)O_2 mixed oxides, a similar behavior was expected since the alpha ions induce a similar concentration of defects in all the mixed oxides which is compared to that induced in the pure UO_2 sample.

However the comparison of the virgin and irradiated spectra of the (U, Th)O_2 samples indicate that the alpha irradiation does not cause significant modifications on their corresponding Raman spectra, which were all marked by the absence of the Raman triplet defect bands. As discussed in Section 6.3.1, luminescence signals appear on the Raman spectra of irradiated pure ThO_2. However, such observations were not recorded in regards to the mixed oxides that contained significant Th-content (refer to Figure 6.30 and Figure 6.31).

Thus, due to the non-apparition of the Raman defect bands from the irradiated surfaces analysis, an in-depth characterizations were carried out in order to analyze the regions which suffered the highest damage level, i.e., where the maximum energy loss of the alpha ions was deposited.

6.3.3.3 Raman spectra of irradiated $(U_xTh_{1-x})O_2$ disks: In-depth profile analysis

After the initial post-irradiation measurements, the Renishaw Invia Raman spectroscopy was then employed to analyze one half disk of each corresponding sample. A line-scanning Raman measurement was conducted over the entire inner edge surface and the spectra corresponding to the zone where the 21 MeV alpha ions deposit their maximum energy were considered. The obtained findings are illustrated in the figures below.

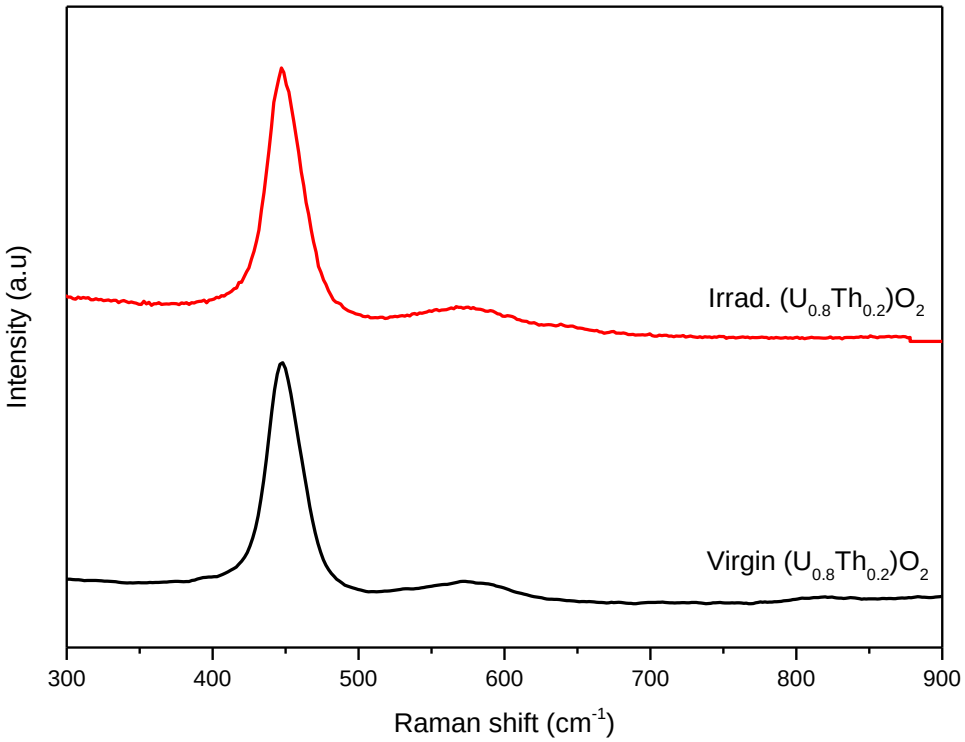

Figure 6.32: Comparison between the virgin and irradiated $(U_{0.8}Th_{0.2})O_2$ spectra corresponding to the maximum damaged zone

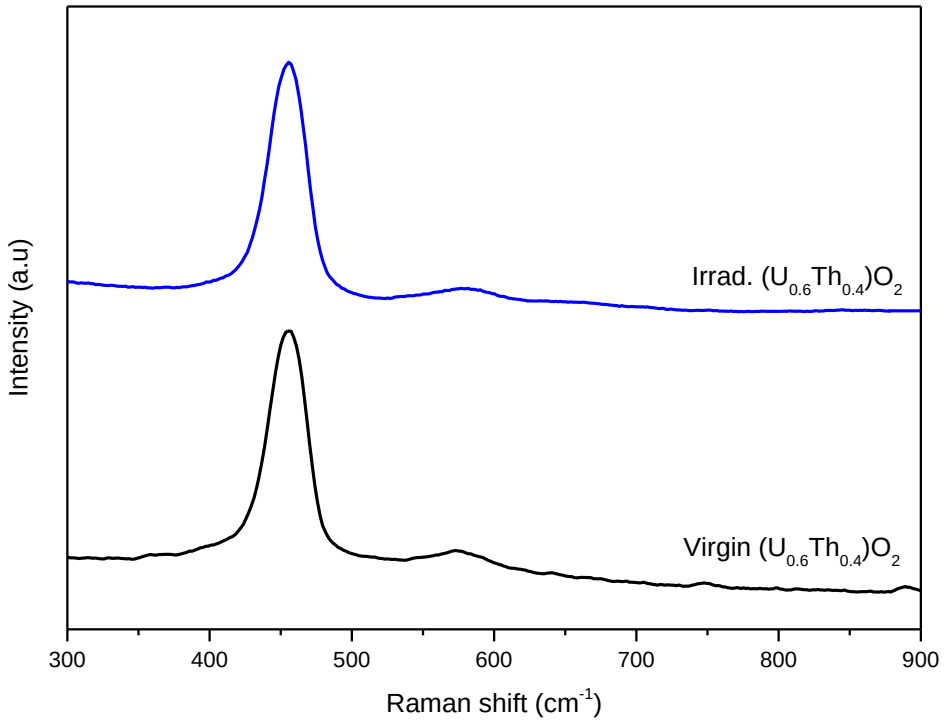

Figure 6.33: Comparison between the virgin and irradiated $(U_{0.6}Th_{0.4})O_2$ spectra corresponding to the maximum damaged zone

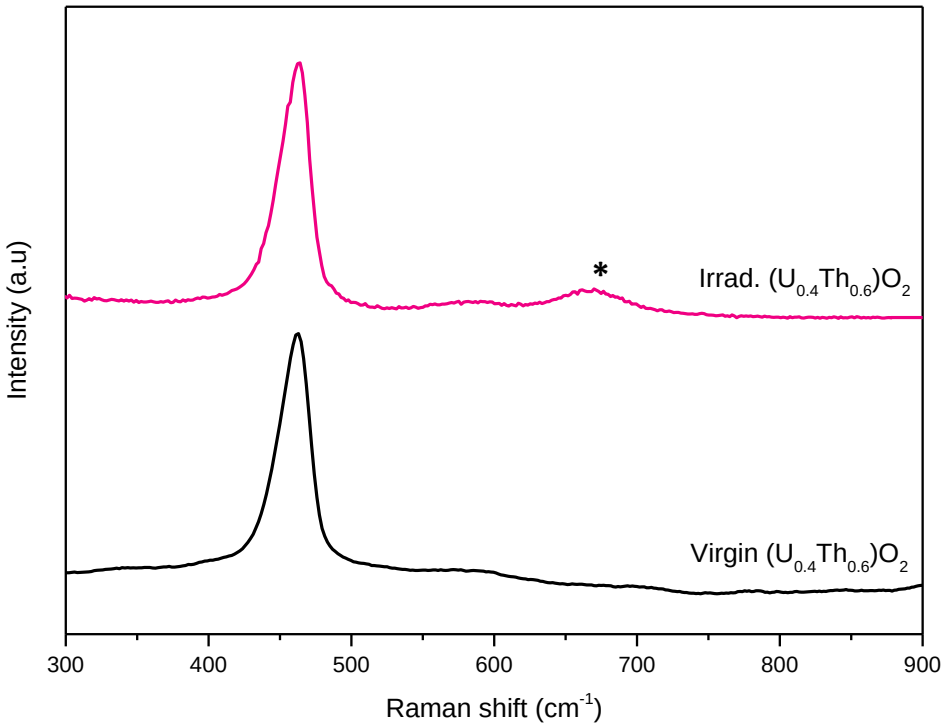

Figure 6.34: Comparison between the virgin and irradiated $(U_{0.4}Th_{0.6})O_2$ spectra corresponding to the maximum damaged zone

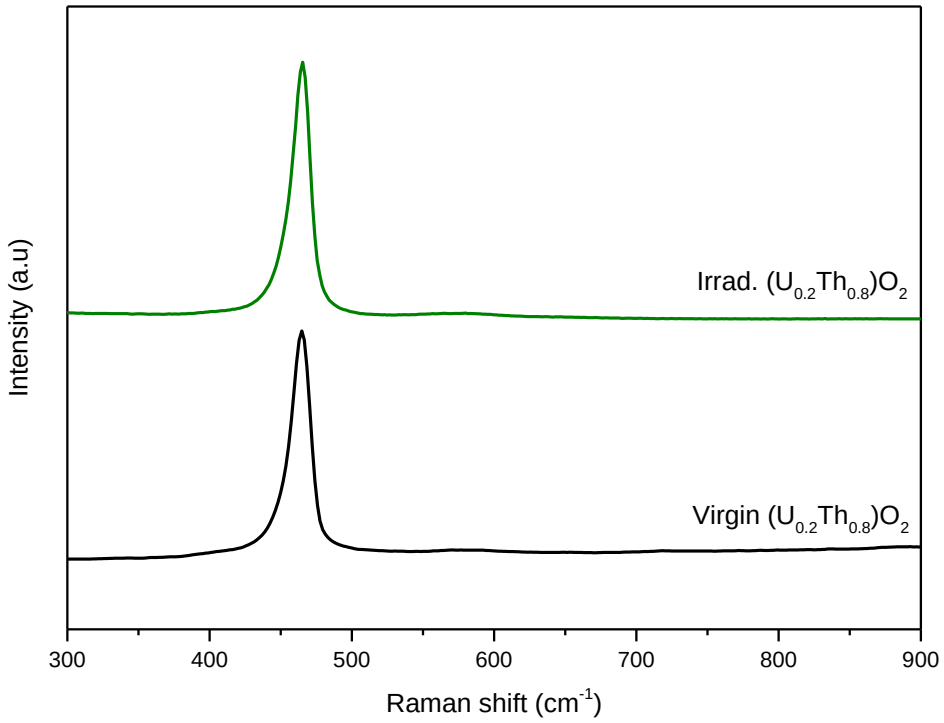

Figure 6.35: Comparison between the virgin and irradiated $(U_{0.2}Th_{0.8})O_2$ spectra corresponding to the maximum damaged zone

The in-depth measurement shows that the spectra acquired at the maximum damaged zones are similar to the findings obtained during the irradiated surface analysis. These observations provide sufficient evidences to suggest that the Raman triplet defect bands do not occur on irradiated nuclear fuels containing significant dopant concentration. These results, together with those obtained during the surface analysis, lead to the conclusion that chemical doping might influence the apparition of the Raman triplet defect bands.

One particular attention can however be drawn from Figure 6.34, i.e. the sample with 60% Th. A slight band occurring at 670 cm^{-1} indicates the pellet oxidation due to continuous air exposure. Indeed after its irradiation, the $(U_{0.4}Th_{0.6})O_2$ sample showed a relatively high radioactivity level compared to the other irradiated samples. Thus, the irradiated $(U_{0.4}Th_{0.6})O_2$ sample was left in ambient-air for more than 4 months in order to allow its radioactivity to reach a suitable threshold so that its measurement can be performed. The oxidation of the irradiated $(U_{0.4}Th_{0.6})O_2$ sample under continuous air exposure is consistent with the oxidation of the electron-irradiated UO_2 as reported in Chapter 4.

6.3.4 Discussion and Conclusions

This chapter was devoted to investigate the behavior of MOX-surrogate compounds under alpha irradiation in laboratory conditions. The objective of this study was to determine the effect of microstructure and doping on the apparition of the Raman triplet defect bands. The irradiation response of heterogeneous (U, Ce)O_2 pellets under chemically inert (Ar) and reactive (H_2O) environments were initially investigated. On the other hand, several (U, Th)O_2 doped samples were also used to study the effect of homogeneous microstructure.

The initial surface characterization of the (U, Ce)O_2 samples put into evidence the presence of three distinct phases, namely; a U-rich phase, a Ce-rich phase and an intermediate agglomerate (U, Ce)O_2 with a uranium content in between the U-rich phase and Ce-rich phase. The heterogeneous microstructure of the (U, Ce)O_2 sample is in good agreement with the microstructure of actual MOX fuels. The initial Raman analysis showed that the (U, Ce)O_2 samples retained their fluorite crystallographic structure mainly due to the presence of the T_{2g} band in all the three phases. However, the intense defect-induced LO-mode occurring in the 500-600 cm^{-1} spectral range indicated a significant concentration of oxygen vacancies in the mixed oxides.

The Raman analysis of the leached (U, Ce)O_2 disk under alpha irradiation showed the presence of the studtite phase on fuel surface. The characteristic double peaks of the altered layer appeared at the same wave numbers (ν_1: 819 cm^{-1}) and (ν_2: 865 cm^{-1}) as those previously observed during the leaching of pure UO_2 under alpha irradiation. This finding indicates that the positioning of the peaks corresponding to the studtite secondary phase is not influenced by the presence of Cerium.

In regards to the irradiation-induced defect bands, a Raman surface mapping of the leached (U, Ce)O_2 disk put into evidence the Raman triplet defect bands in the U-rich phase. However, no such observation was recorded on the Ce-rich phase. Reported data from the literature showed the existence of the defect bands on the Raman spectra of CeO_2 irradiated with swift heavy ion irradiation (dpa: 8.59). This suggests that Raman spectroscopy is not sensitive enough to detect the small concentration of irradiation defects that are induced by alpha ions in the Ce-rich phase (dpa: 4.65 x 10^{-2}). The Raman defect bands were also not observed in the intermediate agglomerate (U, Ce)O_2 phase.

It was also observed that the continuous ambient-air exposure of the irradiated (U, Ce)O_2 causes a significant decrease in the initial LO-mode band intensity that appeared on the spectra of virgin (U, Ce)O_2 due to intrinsic oxygen vacancies. The disappearance of the LO-mode was attributed to the surface oxidation of the irradiated sample thus decreasing the oxygen vacancy

concentration. Such observation is consistent with the proposed mechanisms to describe the rapid oxidation of electron-irradiated UO_2 disk as detailed in Chapter 4.

Finally, the study was extended to investigate the effect of fuel chemistry on the Raman triplet defect bands through the use of several (U, Th)O_2 mixed oxides. The experimental findings were marked by the complete absence of the defect bands on the spectra of all the alpha-irradiated mixed oxides. These observations indicated that chemical doping of nuclear fuels might influence the apparition of the Raman triplet defect bands.

Thus, this experiment provided sufficient elements to show the reliability of Raman spectroscopy during the measurements of nuclear fuels. The presence of the Raman triplet defect bands in the U-rich phase (cerium content: ~0.23-0.3 at.%) suggests that Raman spectroscopy can also be used to characterize irradiation damages in nuclear fuels containing relatively small concentration of dopants. However in regards to highly doped nuclear fuels, Raman spectroscopy can be used to provide relevant information about the chemical doping based on the shifts of the Raman-active T_{2g}-mode.

General Conclusions and Perspectives

The motivation of this thesis was to carry an in-depth analysis of the triplet defect bands in order to investigate how this Raman signature can be used to characterize actual spent nuclear fuel stored in pools. For this purpose, separate effect studies were conducted, which were based on the several experiments involving ionic implantation of nuclear fuels, and the subsequent use of Raman spectroscopy for the characterization of irradiation damages.

The first part of this study was devoted to an in-depth analysis of the triplet defect bands that appear on the Raman spectra of irradiated UO_2. The objective was to correlate the **origin of the defect bands** either to the **electronic or nuclear stopping power** of the incident electrons with the target UO_2 atoms. For that purpose, several UO_2 disks were irradiated at the Laboratoire des Solides Irradiés (LSI-Ecole Polytechnique/CEA/CNRS, Palaiseau) using the Pelletron SIRIUS Van de Graaff electron accelerator in the 1.6-2.5 MeV electron energy range (Reference: **Chapter 4**).

- Experimental results showed that the **electron energy threshold** for the apparition of the Raman triplet defect bands lies between 1.8-1.9 MeV, beyond which the intensity of the defect bands showed a continuous increase up to 2.5 MeV. These observations were consistent with PAS measurements.

- The intensity of the defect bands followed the same trend as the nuclear stopping power values in the same electron energy range. This led to specify that the irradiation-induced Raman defect bands are due to the formation of **atomistic defects** resulting from **ballistic interactions**.

- A detailed analysis showed that the Raman bands take their origin from displacements in the **uranium sub-lattice**.

- Considering that Raman spectroscopy is not sensitive to point defects and also the high formation energy of uranium point defects, it was specified that the triplet defect bands result from a quick re-arrangement of the uranium defects in such a way that they invoke **symmetry-breaking spectroscopic features** and thus appear as new lines on the Raman spectra.

- The rapid oxidation of irradiated UO_2 when exposed to ambient-air conditions was also reported. A suitable oxidation mechanism was hence proposed which is driven by the **migration of oxygen vacancies** towards the UO_2 surface leading to an **enhanced chemical reactivity** of the fuel surface-air boundary layer.

The second part of this study aimed to investigate the **formation kinetics** of irradiation defects in UO_2 when exposed to different (reactive and inert) interfaces through the use of a newly developed ***in-situ* Raman installation**. The incidental scenario of a possible "*Fuel Matrix-Water interaction*" was simulated under laboratory conditions by considering a UO_2/aerated system under alpha irradiation. For a better interpretation of the experimental data, the results were compared to a reference UO_2/Ar system. The irradiation campaigns were carried out at the (CEMHTI, CNRS) on the Cyclotron facility (Reference: **Chapter 5**).

- The formation kinetics of irradiation defects for both UO_2/H_2O and UO_2/Ar systems were found to follow a unique kinetic which can be expressed by a **simple direct impact (DI) model** but are fitted with different numerical values.

- Compared to the reference UO_2/Ar, the UO_2 leaching study highlighted that the presence of a reactive contact medium accelerates the annealing of irradiation defects. The latter was attributed to **oxygen vacancies-enhanced chemical reactions** near the fuel surface-H_2O interface. Thus, this experiment provided additional elements to validate the **role of oxygen vacancies**.

- Although Raman spectroscopy does not enable to characterize the defects that are principally involved near the UO_2-H_2O interface, it has been shown that it provides an alternative method through which the mechanisms of irradiation defects during UO_2 leaching under alpha irradiation can be interpreted.

- The alteration mechanism of UO_2 matrix was also investigated. The irradiated water solution was found to contain sufficient radiolytic H_2O_2 and dissolved uranium to allow the precipitation of secondary altered phases in the form of **studtite phase** ($UO_2(O_2).4H_2O$).

Finally, the study was extended to investigate the relevant information that Raman spectroscopy can provide in regards to MOX fuels. Considering the highly complex microstructure of MOX fuels, the objective of this experiment was to study the effect of microstructure and doping on the Raman triplet defect bands. However due to radiological restrictions, actual MOX fuels were not adapted to be used in the newly develop *in-situ* Raman installation. Thus, it was deemed as more suitable to use surrogate compounds to simulate MOX fuels under laboratory conditions (Reference: **Chapter 6**).

- Heterogeneous (U, Ce)O_2 mixed oxides were initially manufactured to replicate MOX fuels, such that they can be characterized by three distinct phases; a **U-rich matrix**, **Ce-rich phase** and an **intermediate (U, Ce)O_2 agglomerate** with a uranium content intermediate between the U-rich matrix and Ce-rich phase.

- An initial Raman analysis revealed a heavy concentration of oxygen vacancies in the virgin samples which appear as an intense **defect-induced LO peak** occurring at 566 cm^{-1}.

- The leaching of (U, Ce)O_2 under alpha irradiation also revealed the formation of the studtite structure. However, it was evidenced that Ce-dopant does not influence the positioning of the Raman peaks characteristics to the secondary phase.

- The Raman triplet defect bands were observed to occur solely in the **U-rich matrix**. The alpha irradiation did not induce sufficient damages for the defect bands to appear in the **Ce-rich region**.

- Several homogeneous (U, Th)O_2 samples doped at 20% Th interval level were irradiated with alpha ions to further investigate the non-apparition of the defect bands in the **intermediate (U, Ce)O_2 agglomerate.** The findings obtained showed that Raman spectroscopy provides information about irradiation defects when the dopant concentration is relatively low (< 0.3 at.%). However, Raman spectroscopy can be used to study the effect of chemical doping in **highly-doped** nuclear fuels.

- A decrease of the oxygen vacancy-induced LO peak intensity was measured after the irradiated (U, Ce)O_2 was exposed to ambient-air conditions. This observation is consistent with the increase in the **oxygen mobility in nuclear fuels** when exposed to an aerated environment due to the presence of oxygen vacancies near the fuel surface-air boundary layer.

As shown throughout this thesis, Raman spectroscopy is an excellent tool for the study of the nuclear fuel matrix alteration mechanism and the formation of secondary altered phases. Furthermore, quantitative information about the changes occurring at the **microscopic level** in nuclear fuels can also be extracted by this characterization method. For instance, in regards to the heterogeneous microstructure of MOX fuels, the following chemical and structural information can be expected;

- **The plutonium-rich (~38% Pu) aggregate**

Considering the high Pu content, Raman spectroscopy is less likely to reveal relevant information regarding irradiation defect in terms of the Raman triplet defect bands. However,

Raman spectroscopy can be useful to gather important information such as the chemical composition (based on the T_{2g} shift) and stoichiometry (presence of U1 and U3 band on the spectrum) of the nuclear fuel.

- **The coating UO_2-PuO_2 (~7% Pu) matrix**

The low Pu-content suggests that the Raman triplet defect bands might exists in the (U, Pu)O_2 agglomerate phase. In due course, it will be interesting to carry out additional studies devoted to determine the doping threshold for the apparition of the defect bands.

- **The UO_2 (~2.7% Pu) matrix**

As it has been reported in this study, one can expect the Raman defect bands in the U-rich matrix which can be attributed to the low dopant content. However, the effect of burn up should be considered because it remains one of the key factors that determine the final composition of spent nuclear fuels.

Finally, it is worthy to note that this thesis revealed the **unexpected rapid oxidation** of irradiated nuclear fuels when exposed to ambient-air conditions. This observation needs to be considered in experiments devoted to the quantification of irradiation-induced defects and suitable precautions need to be adopted to avoid fuel oxidation. In regards to the actual defective spent nuclear fuel rod, it is more advisable to store the sample specimen in a non-reactive environment in-between the different stages of characterization campaigns.

To conclude, this study has demonstrated that Raman spectroscopy is a viable tool that can provide relevant information regarding irradiation defects in nuclear fuels and also the experimental findings obtained can be used as a reference database for the characterization of an actual defective spent nuclear fuel rod stored in pool conditions.

Annex A: Improvements of the current *in situ* leaching experimental installation

In regards to the leaching of nuclear fuels under alpha irradiation, an improved experimental installation has been designed such that the previous irradiation cell has been replaced by a new sample holder made up of an aluminium anodized material. The use of the new sample holder aims to restrict the release complexing ions (chloride and fluoride ions) in order to allow the leaching study to be carried out under conditions that are representative to interim wet storage conditions. A schematic representation of the new aluminium anodized irradiation cell is presented in Figure A.1.

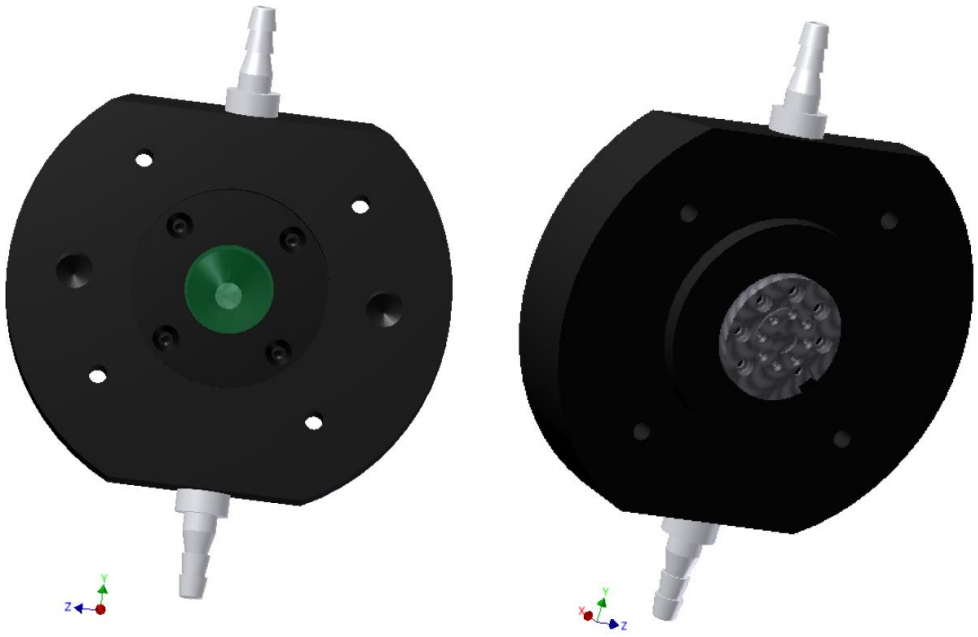

Figure A.1: Newly designed irradiation cell *(a)* back view showing the green window through which the *in situ* Raman probe head is allowed to characterize the fuel surface exposed to water *(b)* front surface indicating the positioning of the fuel sample in the direction of the incoming alpha irradiation beam

In addition, for a better continuous *in situ* Raman acquisition of the nuclear samples during irradiation, it is deemed necessary to evacuate the water bubbles that result due to alpha-induced water radiolysis. Thus, integrating a small peristatic pump in the piping system of the experimental installation such as to continuously recirculate the water solution continuously in a closed loop (no water renewal) will eventually allow the bubbles to escape from the top of the irradiation cell. Therefore, a better *in situ* Raman acquisition of the fuel-water interface can be conducted under alpha irradiation.

It is to be noted that a preliminary testing of the improved experimental installation, comprising of the aluminium anodized irradiation cell and the peristatic pump, has already been performed. Although some upgradings are still required, a significant improvement in the *in situ* acquisitions was recorded.

List of Figures

Chapter 1

Chapter 2

Chapter 3

Chapter 4

Chapter 5

Chapter 6

List of Tables

Bibliography

[1] R. Ewing, "Long-term storage of spent nuclear fuel," *Nature Materials,* vol. 14, pp. 252-257, 2015.

[2] M. Schneider and Y. Marignac, "Spent Nuclear Fuel Reprocessing in France," *International Panel on Fissile Materials,* 2008.

[3] D. Greneche, "Reprocessing and Recycling of Used Nuclear Fuels: The French Feedback Experience and International Aspects," in *IAEA - INPRO meeting: International aspects of reprocessing and recycling*, Vienna, Austria, 2010.

[4] W. Travers, "Mixed-Oxide Fuel use in commercial light water reactors," Nuclear Regulatory Commission, United States, 1999.

[5] J. Provost, "MOX use in PWRs EDF operation experience," *Nuclear Operation Division EDF-Generation* , France, 2011.

[6] M. Debes, "Sustainable Nuclear production in France EDF Nuclear Fuel Cycle," *Nuclear Operation Division EDF-Generation*, France, 2009.

[7] M. Kazimi and al., "The Future of the Nuclear Fuel Cycle: An Interdisciplinary MIT Study," *Massachusetts Institute of Technology*, United States, 2011.

[8] P. Pradel and al., "Nuclear Fuels," CEA Saclay, Paris, France, 2009.

[9] D. Staicu, T. Wiss, Rondinella, R. Konings and C. Ronchi, "Impact of auto irradiation on the thermophysical properties of oxide nuclear reactor fuels," *J. Nucl. Mater.,* vol. 397, pp. 8-18, 2010.

[10] Areva., "Fabrication of recycled fuel".

Retrieved from http://www.areva.com/EN/operations-1173/the-fabrication-of-mox-fuel-recycled-nuclear-power.html [Assessed on 9 Feb 2016]

[11] H. Feiveson, Z. Mian, M. Ramana and F. Von Hippel., "Managing Spent Fuel from Nuclear Power Reactors Experience and Lessons from Around the World," *International Panel on Fissile Materials*, IPFM, 2011.

[12] G. Oudinet, I. Munoz-Viallard, L. Aufore and al., "Characterization of plutonium distribution in MIMAS MOX by image analysis," *J. Nucl. Mater.,* vol. 375, pp. 86-94, 2008.

[13] A. Bouloré, L. Aufore, E. Federici, P. Blanpain and R. Blachier, "Advanced characterization of MIMAS MOX fuel microstructure to quantify the HBS formation," *Nuclear Engineering and Design,* vol. 281, p. 79–87, 2015.

[14] J. Wiktor, "Identification of equilibrium and irradiation-induced defects in nuclear ceramics: electronic structure calculations of defect properties and positron annihilation characteristics," PhD thesis, Aix-Marseille University, 2015.

[15] P. Blackburn, J. Weissbart and E. Gulbransen, "Oxidation of Uranium Dioxide," *J. Phy. Chem.,* vol. 62, pp. 902-908, 1958.

[16] G. Leinders, J. Pakarinen, D. R., T. Cardinaels, K. Binnemans and M. Verwerft, "Low-Temperature Oxidation of Fine UO_2 Powders: A Process of Nanosized Domain Development," *Inorg. Chem.,* vol. 55 , p. 3915–3927, 2016 .

[17] H. Hoekstra, A. Santorot and S. Siegel, "The low temperature oxidation of UO_2 and U_4O_9," *J. lnorg. Nucl. Chem.,* vol. 18, p. 166 to 178, 1961.

[18] L. Thomas, R. Einziger and H. Buchanan, "Effect of fission products on air-oxidation of LWR spent fuel," *J. Nucl. Mat.,* vol. 201 , pp. 310-319, 1993.

[19] R. McEachern and P. Taylor, "A review of the oxidation of uranium dioxide at temperatures below 400°C," *J. Nucl. Mater.,* vol. 254, p. 87, 1998.

[20] L. Desgranges, G. Baldinozzi, D. Simeone and E. Fischer, "Structural changes in the local environment of uranium atoms on the three phases of U_4O_9," *Inorg. Chem. ,* vol. 55, pp. 7485-7491, 2016.

[21] F. Garrido, R. Ibberson, L. Nowicki and B. Willis, "Cuboctahedral oxygen cluster in U_3O_7," *J. Nucl. Mater. ,* vol. 322, pp. 87-89, 2003.

[22] E. Westrum and F. Gronvold, "Triuranium heptaoxides: heat capacities and thermodynamic properties of α- and β-U_30_7, from 5 to 350°K," *J. Phys. Chem. Solids. ,* vol. 23, pp. 39-53, 1962.

[23] F. Zhang, M. Lang, J. Wang, W. Li, K. Sun, V. Prakapenka and R. Ewing, "High-pressure U_3O_8 with the fluorite-type structure," *J. Solid State Chem.,* vol. 213 , p. 110–115, 2014.

[24] J. Morrell and M. Jackson, "Uranium Processing and Properties," *New York: Springer science+business media*, 2013.

[25] J. Ziegler, SRIM software, URL: http://www.srim.org, 2013.

[26] F. Smith, "A primer in applied radiation physics," *London: World Scientiifc Publishing Co. Pte. Ltd*, 2000.

[27] D. Olander, "Fundamental Aspects of Nuclear Reactor Fuel Elements," *Technical Information Center, Office of Public Affairs, Energy Research and Development Administration, United States*, 1976.

[28] A. Putnis, "Introduction to mineral sciences," *Cambridge University Press*, 1992.

[29] P. Li and Z. Zhang, "Standing wave effect and fractal structure in dislocation evolution," *Scientific report,* vol. 7 , p. 4062, 2017.

[30] C. Onofri, C. Sabathier, C. Baumier, C. Bachelet, H. Palancher and M. Legros, "Evolution of extended defects in polycrystalline Au-irradiated UO_2 using in situ TEM: Temperature and fluence effects," *J. Nucl. Mat.,* vol. 482, pp. 105-113, 2016.

[31] A. Michel, C. Sabathier, G. Carlot, M. Cabié, S. Bouffard and P. Garcia, "A TEM study of bubbles growth with temperature in Xenon and Krypton implanted Uranium Dioxide," *Defect and Diffusion Forum,* Vols. 323-325, pp. 191-196, 2012.

[32] P. Jansson, A. Hakansson and A. Backlin, "Gamma-ray measurements of spent PWR fuel and determination of residual power," *Internal report, Uppsala University*, 1997.

[33] C. Ferradini and J. Jay-Gerin, "La radiolyse de l'eau et des solutions aqueuses: historique et actualité," *J. Chem.,* vol. 77, pp. 1542-1575, 1999.

[34] I. Obodovskiy, "Fundamentals of Radiation and Chemical Safety," *Amsterdam, The Netherlands : Elsevier Publication*, 2015.

[35] S. Le Caër, "Water Radiolysis: Influence of Oxide Surfaces on H_2 Production under Ionizing Radiation," *Water,* vol. 3, pp. 235-253, 2011.

[36] G. Baldacchino, "Water radiolysis with heavy-ion beams at GANIL. Back to 20 years of investigations," *J. Phy: Conference Series,* vol. 629, p. 012009, 2015.

[37] J. Spinks and R. Woods, "An Introduction to Radiation Chemistry," *New York, USA : Wiley-*

Interscience publication, 1990.

[38] D. Shoesmith, S. Sunder and W. Hocking, "Electrochemistry of UO_2 nuclear fuel: Electrochemistry of Novel Materials," *VCH Publishers, New York*, 1994.

[39] S. Sunder and D. Shoesmith, "Chemistry of UO_2 fuel dissolution in relation to the disposal of used nuclear fuel," *Atomic Energy of Canada Limited, Canada*, 1991.

[40] Abhilash. and B. Pandey, "Microbially Assisted Leaching of Uranium: A Review," *Mineral Processing & Extractive Metall. Taylor and Francis.,* vol. 34, p. 81–113, 2013.

[41] G. Thomas and G. Till, "The dissolution of unirradiated UO_2 fuel pellets under simulated disposal conditions," *Nucl. Chem. Waste Manage.,* vol. 5, pp. 141-147, 1984.

[42] M. Magnin, C. Jégou, V. Broudic and C. Marques, "Les mécanismes d'altération des combustibles MOX en entreposage sous eau," *CEA report, Marcoule*, 2014.

[43] F. Clarens, J. de Pablo, I. Díez-Pérez, I. Casas, J. Giménez and M. Rovira, "Formation of studtite during the oxidative dissolution of UO_2 by hydrogen peroxide: a SFM study," *Environ Sci Technol.,* vol. 38, pp. 6656-6661, 2004.

[44] S. Nilsson and M. Jonsson, "H_2O_2 and radiation induced dissolution of UO_2 and SIMFUEL pellets," *J. Nucl. Mater.,* vol. 410, pp. 89-93, 2011.

[45] R. Pehrman, M. Trummer, C. Lousada and M. Jonsson, "On the redox reactivity of doped UO_2 pellets-Influence of dopants on the H_2O_2 decomposition mechanism," *J. Nucl. Mater.,* vol. 430 , pp. 6-11, 2012.

[46] M. Trummer, B. Dahlgren and M. Jonsson, "The effect of Y_2O_3 on the dynamics of oxidative dissolution of UO_2," *J. Nucl. Mater.,* vol. 407, pp. 195-199, 2010.

[47] M. Trummer, S. Nilsson and M. Jonsson, "On the effects of fission product noble metal inclusions on the kinetics of radiation induced dissolution of spent nuclear fuel," *J. Nucl. Mater.,* vol. 378, pp. 55-59, 2008.

[48] M. Jonsson, E. Ekeroth and O. Roth, "Dissolution of UO_2 by one- and two-electron oxidants," in *Materials Research Society Symposium Proceedings*, 2004.

[49] E. Hayon and A. Allen, "Evidence for two kinds of "H atoms" in the radiation chemistry of water," *J. Phys. Chem.,* vol. 65, pp. 2181-2185, 1961.

[50] B. De Vivo, C. G. Ippolito and P. Simpson, "Uranium Geochemistry, Mineralogy, Geology, Exploration and Resources, " *England: Stephen Austin/Hertford*, 1984.

[51] R. Finch, M. Cooper, H. F.C. and R. Ewing, "The crystal structure of schoepite, $[(UO_2)8O_2(OH)_{12}](H_2O)_{12}]$," *The Canadian Mineralogist,* vol. 34 , pp. 1071-1088, 1996.

[52] R. H. F. Finch and R. Ewing, "Structural relations among schoepite, metaschoepite, and dehydrated schoepite," *The Canadian Mineralogist,* vol. 36, pp. 831-845, 1998.

[53] T. Forbes, P. Horan, T. Devine, D. Mclnnis and P. Burn, "Alteration of dehydrated schoepite and soddyite to studtite," *The American Mineralogist,* vol. 96 , pp. 202-206, 2011.

[54] L. Morss, N. Edelstein and J. Fuger, The Chemistry of the Actinide and Transactinide Element, The Netherlands: Springer, 2010.

[55] P. Burns and K. Hughes, "Studtite, $[(UO_2)(O_2)(H_2O)_2](H2O)_2]$: The first structure of a peroxide mineral," *American Mineralogist,* vol. 88, p. 1165–1168, 2003.

[56] X. Guo, S. Ushakov, S. Labs, H. Curtius, D. Bosbach and A. Navrosk, "Energetics of metastudtite and implications for nuclear waste alteration," *Proc. Natl. Acad. Sci. ,* vol. 111, p. 17737–17742, 2014.

[57] D. Shoesmith and S. Sunder., "An electrochemistry-based model for the dissolution of UO_2," Atomic Energy of Canada Report, Canada, 1991.

[58] M. Yang, A. Fidalgo, S. Sundin and M. Jonsson, "Inhibition of radiation induced dissolution of UO2 by sulfide – A comparison with the hydrogen effect," *J. Nucl. Mater.,* vol. 434, pp. 38-42, 2013.

[59] A. Rey, I. Casas, J. Gimenez, J. Quinones and J. De Pablo, "Effect of temperature on Studtite stability: Thermogravimetry and differential scanning calorimetry investigations," *J. Nucl. Mater.,* vol. 385, pp. 467-473, 2009.

[60] P. Debets, "X-ray diffraction data on hydrated uranium peroxide," *J. Inorganic & Nucl. Chem.,* vol. 25, pp. 727-730, 1963.

[61] C. Rocchicc, "Etude par Thermogravimetrie analyse thermique differentielle et spectrographie d'absorption infrarouge des hydrates du peroxyde d'uranium," *Cr Acad Sci B Phys,* vol. 263, p. 1061–1063, 1966.

[62] R. Ewing and W. C. J. F. Weber, "Radiation effects in nuclear waste forms for high-level

radioactive waste," *Progress in Nuclear Energy,* vol. 29, pp. 63-121, 1995.

[63] V. Gromov, "Dissolution of uranium oxides in the gamma-radiation field," *Radiation Phys Chem.,* vol. 18, pp. 135-146, 1981.

[64] S. Sunder, D. Shoesmith, H. Christensen and N. Miller, "Oxidation of UO_2 fuel by the products of gamma radiolysis of water," *J. Nucl. Mater.,* vol. 190, pp. 78-86, 1992.

[65] C. Jégou, B. Muzeau, V. Broudic, S. Peuget, A. Poulesquen, D. Roudil and C. Corbel, "Effect of external gamma irradiation on dissolution of the spent UO_2 fuel matrix," *J. Nucl. Mater.,* vol. 341, p. 62–82, 2005.

[66] F. Clarens, J. Giménez, J. De Pablo, I. Casas, M. Rovira, J. Dies, J. Quiñones and A. J. Martínez Esparza, "Influence of beta-radiation on UO_2 dissolution at different pH values," *Radiochim. Acta,* vol. 93, pp. 533-538, 2005.

[67] M. B. Carver, D. V. Hanley and K. R. Chaplin, "Maksima-Chemist: A program for mass action kinetics simulation by automatic chemical equation manipulation and integration using stiff techniques," *Atomic Energy of Canada Ltd., Chalk River*, 1979.

[68] K. Lundgren and H. Christensen, "Model calculations of water radiolysis in the primary coolant circuit of the Barseback-1 BWR," *Water Chemistry of Nuclear Systems ,* vol. 7, 1996.

[69] R. Watts, M. Foget, K. S.H. and A. Teel, "Hydrogen peroxide decomposition in model subsurface system," *J. Hazard Mater. B.,* vol. 69, pp. 229-243, 1999.

[70] D. W. S. S. ". Shoesmith, "The prediction of nuclear fuel (UO_2) dissolution rates under waste disposal conditions," *J. Nucl. Mater.,* vol. 190, pp. 20-35, 1992.

[71] B. Grambow, A. Loida, P. Dressier, H. Geckeis, J. Gago, I. Casas, J. de Pablo, J. Gimenez and M. E. Torrero, "Chemical reaction of fabricated and high burn-up spent UO_2 fuel with saline brines," *Final Report EUR., European Commission,* 1997.

[72] B. Grambow, "Spent fuel dissolution and oxidation: An evaluation of literature data," *SKB Technical Report , Sweden*, 1989.

[73] T. E. Eriksen, U. B. Eklund, L. Werme and J. Bruno, "Dissolution of irradiated fuel: a radiolytic mass balance study," *J. Nucl. Mater.,* vol. 227, pp. 76-82, 1995.

[74] G. Sattonnay, C. Ardois, C. Corbel, J. F. Lucchini, M. F. Barthe, F. Garrido and D. Gosset, "Alpha-radiolysis effects on UO_2 alteration in water," *J. Nucl. Mater.,* vol. 288, pp. 11-19,

2001.

[75] C. Corbel, G. Sattonnay, J. Lucchini, C. Ardois, M. Barthe, F. Huet, P. Dehaudt, B. Hickel and C. Jégou, "Increase of the uranium release at an UO_2/H_2O interface under He^{2+} ion beam irradiation," *Nucl. Instrum. Methods Phys. Res. B.,* vol. 179, p. 225–229, 2001.

[76] W. Gray, "Effect of surface oxidation, alpha radiolysis and salt brine composition on spent fuel and UO_2 leaching performance," PNL Technical Report , PNL/SRP-6689, 1988.

[77] V. Rondinella, H. Matzke, J. Cobos and T. Wiss, "alpha-radiolysis and alpha-radiation damage effects on UO_2 dissolution under spent fuel storage conditions," *Mater. Res. Soc. Symp. Proc. ,* vol. 556, p. 447–454, 1999.

[78] V. Rondinella, H. Matzke, J. Cobos and T. Wiss, "Leaching behaviour of UO_2 containing alpha-emitters actinides," *Radio. Acta.,* vol. 88, p. 527–531, 2000.

[79] J. Cobos, L. Havela, V. Rondinella, J. De Pablo, T. Gouder, J. Glatz, P. Carbol and H. Matzke, "Corrosion and dissolution studies of UO_2 containing alpha-emitters," *Radio. Acta. ,* vol. 90, p. 597–602, 2002.

[80] M. Bailey, L. Johnson and D. Shoesmith, "The Effects of the Alpha-Radiolysis of Water on the Corrosion of UO_2," *Corros. Sci.,* vol. 25, pp. 233-238, 1985.

[81] C. Corbel, G. Sattonnay, S. Guilbert, F. Garrido, M. Barthe and C. Jégou, "Addition versus radiolytic production effects of hydrogen peroxide on aqueous corrosion of UO_2," *J. Nucl. Mater.,* vol. 348, pp. 1-17, 2006.

[82] C. Jégou, B. Muzeau, V. Broudic, A. Poulesquen, D. Roudil, F. Jorion and C. Corbel, "Effect of alpha irradiation on UO_2 surface reactivity in aqueous media," *Radiochim. Acta.,* vol. 93, p. 35–42, 2005.

[83] P. Tucker, "The effect of oxygen partial pressure on the kinetics of unirradiated UO_2 oxidation," *Chemical Reactivity of Oxide Fuel and Fission Product Release Proc.,* pp. 49-84, 1987.

[84] S. Stroes-Gascoyne, F. Garisto and J.S. Betteridge, " The effects of alpha-radiolysis on UO_2 dissolution determined from batch experiments with 238Pu-doped UO_2," *J. Nucl. Mater., vol. 346, pp. 5-15, 2005.*

[85] J. Lucchini, G. Sattonnay, C. Ardois, C. Jégou and C. Corbel, "Effects of water alpha radiolysis on the spent fuel matrix corrosion," *CEA report, France*, 2004.

[86] C. Poinssot, C. Ferry, B. Kelm, B. Grambow, A. Martinez-Esparza, L. Johnson and al., "Final report of the European project Spent Fuel Stability under Repository Conditions," *European Commission Report CEA-R-6093*, 2001.

[87] S. Sunder, N. Milner and D. Shoesmith, "Corrosion of uranium dioxide in hydrogen peroxide solutions," *Corrosion Science,* vol. 46, p. 1095–1111, 2004.

[88] M. Trummer, B. Dahlgren and M. Jonsson, "The effect of Y_2O_3 on the dynamics of oxidative dissolution of UO_2," *J. Nucl. Mater.,* vol. 407, pp. 195-199, 2010.

[89] M. Amme, B. Renker, B. Schmid, M. Feth, H. Bertagnolli and W. Dobelin, "Raman Microspectrometric Identification of Corrosion products formed on UO_2 Nuclear Fuel during leaching experiments," *J. Nucl. Mater.,* vol. 306, pp. 202-212, 2002.

[90] B. Hanson, B. McNamara, E. Buck, J. Friese, E. Jenson, K. Krupka and B. Arey, "Corrosion of Commercial Spent Nuclear Fuel: Formation of Studtite and Metastudtite," *Radiochimica Acta.,* vol. 93 , pp. 159-168, 2005.

[91] K. Walenta, "On studtite and its composition," *The American Mineralogist.,* vol. 59, pp. 166-171, 1974.

[92] C. Jégou, B. Muzeau, V. Broudic, D. Roudil and X. Deschanels, "Spent fuel UO_2 matrix alteration in aqueous media under oxidizing conditions," *Radiochim. Acta.,* vol. 95, p. 513–522, 2007.

[93] H. Szymanski, "Raman spectroscopy: Theory and Practice," *New York: Plenum Press,* 1970.

[94] Y. Yun, D. Legut and P. Oppeneer, "Phonon spectrum, thermal expansion and heat capacity of UO_2 from first-principles," *J. Nucl. Mater.,* vol. 426 , pp. 10-114, 2012.

[95] T. Livneh, "Coupling of multi-LO phonons to crystal-field excitations in UO_2 studied by Raman spectroscopy," *J. Phys.: Condens. Matter,* vol. 20, p. 085202, 2008.

[96] L. Desgranges, G. Baldinozzi, P. Simon, G. Guimbretière and A. Canizarès, "Raman spectrum of U_4O_9: a new interpretation of damage lines in UO_2," *J. Raman Spec.,* vol. 43, pp. 455-458, 2012.

[97] R. Böhler, A. Quainic and al., "The solidification behaviour of the UO_2–ThO_2 system in a laser heating study," *J. Alloys & Compounds.,* vol. 616, pp. 5-13, 2014.

[98] S. Senanayake, R. Rousseau, D. Colegrave and H. Idriss, "The reaction of water on polycrystalline UO_2: Pathways to surface and bulk oxidation," *J. Nucl. Mater.,* vol. 342 , p.

179–187, 2005.

[99] P. Graves, "Raman microprobe spectroscopy of uranium dioxide single crystals and ion implanted polycrystals," *Appl. Spectrosc.,* vol. 44, pp. 1665-1667, 1990.

[100] G. Allen, "Characterization of uranium oxides by micro-Raman spectroscopy," *J. Nucl. Mater.,* vol. 144, pp. 17-19, 1987.

[101] D. Manara and B. Renker, "Raman spectra of stoichiometric and hyper-stoichiometric uranium dioxide," *J. Nucl. Mater.,* vol. 321, p. 233–237, 2003.

[102] G. Sarau, A. Bochmann, R. Lewandowska and S. Christiansen, "From Micro to Macro Raman Spectroscopy: Solar Silicon for a Case Study," *Intech Open Access Publisher*, 2012.

[103] G. Guimbretière, L. Desgranges, A. Canizarès, G. Carlot, R. Caraballo, C. Jégou, F. Duval, N. Raimboux, M. Ammar and P. Simon, "Determination of in-depth damaged profile by Raman line scan in a pre-cut He^{2+} irradiated UO_2," *Appl. Phys. Lett.,* vol. 100 , p. 251914, 2012.

[104] R. Mohun, L. Desgranges, J. Léchelle, G. Guimbretière, A. Canizarès, P. Simon and al., "Charged defects during alpha-irradiation of actinide oxides as revealed by Raman and luminescence spectroscopy," *Nucl. Instrum. Methods B.,* vol. 374, pp. 67-70, 2016.

[105] G. Guimbretière, A. Canizarès, L. Desgranges, N. Raimboux, P. Desgardin, C. Jégou, J. Joseph and P. Simon, "High temperature Raman study of UO_2: A possible tool for in situ estimation of irradiation-induced heating," *J. Raman Spectrosc.,* vol. 46, pp. 418-420, 2015.

[106] G. Guimbretière, A. Canizarès, L. Desgranges, R. Caraballo, F. Duval and al., "In situ Raman monitoring of He^{2+} irradiation induced damage in a UO_2 ceramic," *Appl. Phys. Lett.,* vol. 103, p. 041904, 2013.

[107] W. Weber, "Ingrowth of lattice defects in alpha irradiated UO_2 single crystals," *J. Nucl. Mater. ,* vol. 98, p. 206–215, 1981.

[108] L. Desgranges, G. Guimbretière, P. Simon, F. Duval, A. Canizarès, R. Omnee, C. Jégou and R. Caraballo, "Annealing of the defects observed by Raman spectroscopy in UO_2 irradiated by 25 MeV He^{2+} ions," *Nucl. Instrum. Methods B.,* vol. 327, p. 74–77, 2014.

[109] H. Labrim, M. Barthe, P. Desgardin, T. Sauvage, C. Corbel, G. Blondiaux and J. Piron, "Thermal evolution of the vacancy defects distribution in 1 MeV helium implanted

sintered UO_2," *Nucl. Instr. Methods B.,* vol. 261, p. 883–887, 2007.

[110] J. Weber, "Alpha-irradiation damage in CeO_2, UO_2 and PuO_2," *Radiation effects,* vol. 83, pp. 145-156, 1984.

[111] J. Weidlein, U. Müller and K. Dehnicke, "Vibrational Spectroscopy: An Introduction," *Stuttgart: Georg Thieme Verlag.*, 1988, p. 228.

[112] S. Hubert, J. Purans, G. Heisbourg, P. Moisy and N. Dacheux, "Local Structure of Actinide Dioxide Solid Solutions $Th_{1-x}U_xO_2$ and $Th_{1-x}Pu_xO_2$," *Inorg. Chem. ,* vol. 45, p. 3887−3894, 2006.

[113] M. Guo, J. Lu, Y. Wu, Y. Wang and L. M., "UV and Visible Raman Studies of Oxygen Vacancies in Rare-Earth-Doped Ceria," *Am. Chem. Soc.,* vol. 27, p. 3872–3877, 2011.

[114] N. Nakae, A. Harada and T. Kirihara, "A laser heating study of the CeO_2 solid/liquid transition: challenges related to a refractory compound with a very high oxygen pressure," *J. Nucl. Mat. ,* vol. 71, pp. 314-319, 1978.

[115] S. Minamoto, M. Kato, K. Konashi and Y. Kawazo, "Calculations of thermodynamic properties of PuO_2 by the first-principles and lattice vibration," *J. Nucl. Mater.,* vol. 385 , p. 18–20, 2009.

[116] M. Benedict, T. Pigford and H. Levi, "Nuclear chemical engineering," McGraw-Hill, 1981.

[117] W. Lambertson, M. Mueller and F. Gunzel Jr., "Uranium Oxide Phase Equilibrium Systems: IV, UO_2–ThO_2," *J. Am. Ceram. Soc., ,* vol. 36, pp. 397-399, 1953.

[118] L. Capriotti, A. Quaini, R. Böhler, K. Boboridis, L. Luzzi and D. Manara, "A laser heating study of the CeO_2 solid/liquid transition: challenges related to a refractory compound with a very high oxygen pressure," *High Temp-High Pressures.,* vol. 44, pp. 69-82, 2014.

[119] W. Lyon and W. Bailey, "The solid-liquid phase diagram for the UO_2-PuO_2 system," *J. Nucl. Mater. ,* vol. 22, p. 332–339, 1967.

[120] C. Pillai and P. Raj., "Thermal conductivity of ThO_2 and $Th_{0.98}U0_{.02}O_2$," *J. Nucl. Mat. ,* vol. 277, pp. 116-119, 2000.

[121] A. Nelson, D. Rittman, J. White, J. Dunwoody, K. Masato and K. McClellan, "An Evaluation of the Thermophysical Properties of Stoichiometric CeO_2 in Comparison to UO_2 and PuO_2," *J. Am. Ceram. Soc.,* vol. 97 , pp. 3652-3659, 2014.

[122] C. Cozzo, D. Staicu, J. Somers, F. &. A. and R. Konings, "Thermal diffusivity and conductivity of thorium–plutonium mixed oxide," *J. Nucl .Mater. ,* vol. 416 , p. 135–141, 2011.

[123] M. Berger, J. Coursey, M. Zucker and J. Chang, ESTAR: Stopping powers and ranges for electrons calculator, National Institute of Standards and Technology: https://physics.nist.gov/PhysRefData/Star/Text/ESTAR.html.

[124] J. Soullard, "High voltage electron microscope observations of UO_2," *J. Nucl. Mater.,* vol. 315, pp. 190-196, 1985.

[125] Bruker,TOPAS Rietveld Analysis Software, https://www.bruker.com.

[126] G. Holzer, M. Fritsch, M. Deutsch, J. Hartwig and E. Forster, "$K_{\alpha 1,2}$ and $K_{\beta 1,3}$ x-ray emission lines of the 3d transition metals," *Phy. Rev. A ,* vol. 56, pp. 4554-4568, 1997.

[127] M. Barthe, H. Labrim, A. Gentils, P. Desgardin, C. Corbel, S. Esnouf and J. Piron, "Positron annihilation characteristics in UO_2: for lattice and vacancy defects induced by electron irradiation," *Phys. stat. sol.,* vol. 10, p. 3627–3632, 2007.

[128] J. Wiktor, M. Barthe, G. Jomard, M. Torrent, M. Freyss and M. Bertolus, "Coupled experimental and DFT+U investigation of positron lifetimes in UO_2," *Phys. Rev. B.,* vol. 90, p. 184101, 2014.

[129] C. Onofri, C. Sabathier, H. Palancher, G. Carlot, S. Miro, Y. Serruys, L. Desgranges and M. Legros, "Evolution of extended defects in polycrystalline UO_2 under heavy ion irradiation: combined TEM, XRD and Raman study," *Nucl. Instrum. Methods B.,* vol. 374, pp. 51-57, 2016.

[130] H. Palancher, R. Kachnaoui, G. Martin, A. Richard, J. Richaud, C. Onofri, R. Belin, A. Boulle and al., "Strain relaxation in He implanted UO_2 polycrystals under thermal treatment: An in situ XRD study," *J. Nucl. Mat. ,* vol. 476, p. 63–76, 2016.

[131] G. Carlot, C. Sabathier, S. Maillard, A. Michel, G. Martin, E. Gilabert, F. Fortuna and P. Garcia, "Study of Rare Gases Behavior in Uranium Dioxide," *EPJ Web of Conferences,* vol. 115, p. 03003, 2016.

[132] C. Sabathier, G. Martin, A. Michel, G. Carlot, S. Maillard, C. Bachelet, F. Fortuna, O. Kaitasov, E. Oliviero and P. Garcia, "In-situ TEM observation of nano-void formation in UO_2 under irradiation," *Nucl. Instrum. Methods B. ,* vol. 326, p. 247–250, 2014.

[133] H. Chiang, T. Zweifel, H. Palancher, A. Bonnin, L. Beck, P. Weiser, M. Döblinger, C.

Sabathier, R. Jungwirth and W. Petry, "Evidence of amorphous interdiffusion layer in heavy ion irradiated U-8wt%Mo/Al interfaces," *J. Nucl. Mat. ,* vol. 440, p. 117–123, 2013.

[134] S. Maillard, G. Martin and C. Sabathier, "Why a steady state void size distribution in irradiated UO_2? A modeling approach.," *Nucl. Instrum. Methods B. ,* vol. 374, p. 58–66, 2016.

[135] G. Martin, P. Garcia, C. Sabathier, F. Devynck, M. Krack and S. Maillard, "A thermal modelling of displacement cascades in uranium dioxide," *Nucl. Instrum. Methods B. ,* vol. 327, p. 108–112, 2014.

[136] R. Skorek, S. Maillard, A. Michel, G. Carlot, E. Gilabert and T. Jourdan, "Modelling Fission Gas Bubble Distribution in UO_2," *Defect and Diffusion Forum,* vol. 323, p. 209–214, 2012.

[137] G. Martin, P. Garcia, C. Sabathier, L. Van Brutzel, B. Dorado, F. Garrido and S. Maillard, "Irradiation-induced heterogeneous nucleation in uranium dioxide," *Phy. Let. A,* vol. 374, p. 3038–3041, 2010.

[138] J. Crocombette, L. Van Brutzel, D. Simeone and L. Luneville, "Molecular dynamics simulations of high energy cascade in ordered alloys: Defect production and subcascade division," *J. Nucl. Mat. ,* vol. 474, p. 134–142, 2016.

[139] O. Maslova, "Spectroscopie et imagerie Raman de matériaux inhomogènes," PhD thesis, Université d'Orléans, France, 2014.

[140] T. Cardinaels, K. Govers, B. Vos, S. Van den Berghe, M. Verwerft, L. de Tollenaere, G. Maier and C. Delafoy, "Chromia doped UO_2 fuel: Investigation of the lattice parameter," *J. Nucl. Mater.,* vol. 424 , pp. 252-260, 2012.

[141] G. Leinders, T. Cardinaels, K. Binnemans and M. Verwerft, "Accurate lattice parameter measurements of stoichiometric uranium dioxide," *J. Nucl. Mater.,* vol. 459, pp. 135-142, 2015.

[142] V. Alekseyev, L. Ananyeva and R. Rafalskiy, "Effects of Composition on Lattice Parameter of UO_{2+x}," *Internat. Goelogy. Rev.,* vol. 23, pp. 1229-1236, 2010.

[143] Non Ionizing Energy Loss program code, http://www.sr-niel.org/index.php/electrons-niel-calculator.

[144] J. Crawford and L. Slifkin, Point Defects in Solids: Semiconductors and Molecular Crystals, New York: Plenum Press, 1975.

[145] P. Garcia, G. Martin, G. Carlot, C. Sabathier and al., "Experimental investigations of irradiation induced diffusion of He and I in UO_2," in *F-Bridge Project*, 2013.

[146] N. Nakae, Y. Iwata and T. Kirihara, "Thermal recovery of defects in neutron irradiated UO_2," *J. Nucl. Mater.,* vol. 80 , p. 314, 1979.

[147] W. Weber, "Thermal recovery of lattice defects in alpha-irradiated UO_2 crystals," *J. Nucl. Mater. ,* vol. 114 , p. 213, 1983.

[148] M. Iwasawa, Y. Chen, Y. Kaneta, T. Ohnuma, H. Geng and M. Kinoshita, "First-Principles Calculation of Point Defects in Uranium Dioxide," *Mat. Trans. ,* vol. 47, pp. 2651-2657, 2006.

[149] B. Dorado, D. Andersson, C. Stanek, M. Bertolus, B. Uberuaga and G. Martin, "First-principles calculations of uranium diffusion in uranium dioxide," *Phys. Rev. B.,* vol. 86, p. 035110, 2012.

[150] H. He. and D. Shoesmith, "Raman spectroscopic studies of defect structures and phase transition in hyper-stoichiometric UO_{2+x}," *Phys. Chem. Chem. Phys.,* vol. 12, pp. 8109-8118, 2010.

[151] P. Tempest, T. P.M. and J. Tyler, "Oxidation of UO_2 fuel pellets in air at 503 and 543 K studied using X-ray photoelectron spectroscopy and X-ray diffraction," *J. Nucl. Mater.,* vol. 151, pp. 269-274, 1988.

[152] P. Taylor, E. A. Burgess and G. G. Owens, "An X-ray diffraction study of the formation of β-$UO_{2.33}$ on UO_2 pellet surfaces in air at 229 to 275°C," *J. Nucl. Mater.,* vol. 88, p. 153–160, 1980.

[153] J. Elorrieta, L. Bonales, N. Rodriguez-Villagra, V. Baonza and J. Cobos, "A detailed Raman and X-ray study of UO_{2+x} oxides and related structure transitions," *Phys. Chem. Chem. Phys. ,* vol. 18, pp. 28209-28216, 2016.

[154] L. Nowicki, F. Garrido, A. Turos and L. Thome, "Polytypic arrangements of cuboctahedral oxygen clusters in U_3O_7," *J. Phys. Chem. Solids.,* vol. 61 , p. 1789–1804, 2000.

[155] B. Belbeoch, J. Boivineau and P. Perio, "Changements de structure de l'oxyde U_4O_9," *J. Phys. Chem. Solids,* vol. 28, p. 1267, 1967.

[156] L. Desgranges, H. Palancher, M. Gamaléri, J. Micha, V. Optasanu, L. Raceanu, T. Montesin and N. Creton, "Influence of the U_3O_7 domain structure on cracking during the oxidation

of UO_2," *J. Nucl. Mater.,* vol. 402, pp. 167-172, 2010.

[157] Y. Teterin, A. Popel, K. Maslakov, A. Teterin, K. E. Ivanov, S. Kalmykov, R. Springell, T. B. Scott and I. Farnan, "XPS Study of Ion Irradiated and Unirradiated UO_2 Thin Films," *Inorg. Chem. ,* vol. 55, pp. 8059-8070, 2016.

[158] L. Desgranges, M. Ferroud-Plattet, R. Alloncle, I. Aubrun, J. M. Untrau and P. Lhuillery, "Behavior of a defective nuclear fuel rod in dry storage conditions studied with a new experimental setup," *Nucl. Tech.,* vol. 163 , pp. 252-260, 2008.

[159] K. Kim, G. You, D. Min, S. Ro and E. Kim, "Oxidation behavior of unirradiated and irradiated UO_2 in Air at 150-375°C," *J. Korean. Nucl. Soc. ,* vol. 29, pp. 93-98, 1997.

[160] R. McEachern, "A review of kinetic data on the rate of U_30_7 formation on UO_2," *J. Nucl. Mater.,* vol. 245, pp. 238-247, 1997.

[161] B. Dorado, J. Durinck, P. Garcia, M. Freyss and M. Bertolu, "An atomistic approach to self-diffusion in uranium dioxide," *J. Nucl. Mater.,* vol. 400, pp. 103-106, 2010.

[162] F. Gupta, A. Pasturel and G. Brillant, "Diffusion of oxygen in uranium dioxide: A first-principles investigation," *Phys. Rev. B.Phys. Rev. B.,* vol. 81, p. 014110, 2010.

[163] A. Kuksin and D. Smirnova, "Calculation of Diffusion Coefficients of Defects and Ions in UO_2," *Phys. Solid State,* vol. 56, pp. 1214-1223, 2014.

[164] G. E. Norman and V. V. Stegailov, "Stochastic Theory of the Classical Molecular Dynamics Method," *Mat. Model.,* vol. 24, p. 3–44, 2012.

[165] C. Corkhill, D. Bailey, F. Tocino, M. Stennett, J. Miller, J. Provis, K. Travis and N. Hyatt, "Role of Microstructure and Surface Defects on the Dissolution Kinetics of CeO_2, a UO_2 Fuel Analogue," *ACS Appl. Mater. Interfaces,* vol. 8, pp. 10562-10571, 2016.

[166] W. Weber, R. Ewing and al., "Radiation effects in crystalline ceramics for the immobilization of high-level nuclear waste and plutonium," *J. Mater. Res. ,* vol. 13, pp. 1435-1484, 1998.

[167] W. Weber and F. Roberts, "A Review of Radiation Effects in Solid Nuclear Waste Forms," *Nucl. Tech.,* vol. 60, pp. 178-198, 1983.

[168] D. Horlait, N. Clavier and al., "Dissolution of cerium (IV)–Lanthanide (III) oxides: comparative effect of chemical composition, temperature, and acidity," *Inorg. Chem.,* vol.

51, pp. 3868-3878, 2012.

[169] A. Popel, S. Le Solliec and al., "The effect of fission-energy Xe ion irradiation on the structural integrity and dissolution of the CeO_2 matrix," *J. Nucl. Mater.,* vol. 484, p. 332–338, 2017.

[170] D. Olander, "Thermal spike theory of athermal diffusion of fission products due to alpha decay of actinides in spent fuels (UO_2)," Thecnical report, University of Michigan, 2004.

[171] G. Guimbretière, L. Desgranges, A. Canizarès, J. Joseph, N. Raimboux, D. Desgardin, C. Jegou and P. Simon, "High temperature Raman study of UO_2: A possible tool for in-situ estimation of irradiation-induced heating," *J. Raman Spec. ,* vol. 46, pp. 418-420, 2015.

[172] Renishaw Wire Software, http://www.renishaw.com/en/raman-software--9450.

[173] Origin Mathematical tool, "http://www.originlab.com".

[174] R. Baddour-Hadjean and J. Pereira-Ramos, *Chem. Rev. ,* vol. 110, pp. 1278-1319, 2010.

[175] J. Jagielski and L. Thomé, "Damage accumulation in ion-irradiated ceramics," *Vacuum,* vol. 81 , pp. 1352-1356, 2007.

[176] F. Tocino, S. Szenknect and al., "Dissolution of uranium mixed oxides: The role of oxygen vacancies vs the redox reactions," *Nucl. Energy.,* vol. 72, pp. 101-106, 2014.

[177] G. Guimbretière, A. Canizarès, Y. Tobon-Correa, M. Ammar, C. Corbel, P. Simon and M. Barthe, "In-Situ Raman Observation of the First Step of Uranium Dioxide Weathering Exposed to Water Radiolysis," *Spectroscopy Letters,* vol. 44, pp. 570-573, 2011.

[178] G. Hochanadel, *J. Phys. Chem.,* vol. 56 , pp. 587-594, 1952.

[179] K. Kubatko, K. Helean, N. A. and P. Burns, "Stability of peroxide-containing uranyl minerals," *Science ,* vol. 302, pp. 1191-1193, 2003.

[180] M. E. Torrero, E. Baraj, J. De Pablo, J. Giménez and I. Casas, "Kinetics of corrosion and dissolution of uranium dioxide as a function of pH," *Int. J. Chem. Kinetics,* vol. 29, pp. 261-267, 1997.

[181] A. Trovarelli and P. Fornasiero, Catalysis by Ceria and Related Materials, London, UK: 2nd ed.; Imperial College Press, 2013.

[182] R. Courtel and J. Loriers, *Comptes Rendus Acad. Sci. (Paris),* vol. 230, p. 735, 1950.

[183] D. Bevan and J. Kordis, "Mixed oxides of the type MO_2 (fluorite)—M_2O_3—I oxygen dissociation pressures and phase relationships in the system CeO_2-Ce_2O_3 at high temperatures," *J. Inorg. Nucl. Chem. ,* vol. 26, pp. 1509-1523, 1964.

[184] H. Tuller and A. Nowick, "Defect Structure and Electrical Properties of Nonstoichiometric CeO_2 Single Crystals," *J. Electrochem. Soc. ,* vol. 126, pp. 209-217, 1979.

[185] A. Tyaki, B. Ambekar and M. Mattews, "Simulation of lattice thermal expansion behavior of $Th_{1-x}Pu_xO_2$ ($0.0 \leq x \leq 1.0$) using CeO_2 as a surrogate material for PuO_2," *J. Alloys & Compounds.,* vol. 337, p. 277 –281, 2002.

[186] H. Kim, C. Joung, B. Lee, J. Oh, Y. Koo and P. Heimgartner, "Applicability of CeO_2 as a surrogate for PuO_2 in a MOX fuel development," *J. Nucl. Mater.,* vol. 378, p. 98–104, 2008.

[187] K. Yasunaga, K. Yasuda, S. Matsumura and T. Sonoda, "Nucleation and growth of defect clusters in CeO_2 irradiated with electrons," *Nucl. Instrum. Methods B. ,* vol. 250, pp. 144-118, 2006.

[188] K. Yasunaga, K. Yasuda, S. Matsumura and T. Sonoda, "Electron energy-dependent formation of dislocation loops in CeO_2," *Nucl. Instrum. Methods B.,* vol. 266, pp. 2877-2881, 2008.

[189] T. Sonoda, M. Kinoshita, Y. Chimi, N. Ishikawa, M. Sataka and A. Iwase, "Electronic excitation effects in CeO_2 under irradiations with high-energy ions of typical fission products," *Nucl. Instrum. Methods B. ,* vol. 250, pp. 254-258 , 2006.

[190] N. Ishikawaa, Y. Chimib, O. Michikamic, Y. Ohtac, K. Ohharad, M. Lange and N. R., "Study of structural change in CeO_2 irradiated with high-energy ions by means of X-ray diffraction measurement," *Nucl. Instrum. Methods B. ,* vol. 266, pp. 3033-3036, 2008.

[191] T. Sonoda, M. Kinoshita, N. Ishikawa, M. Sataka, M. Chimi, N. Okubo, A. Iwase and K. Yasunaga, "Clarification of the properties and accumulation effects of ion tracks in CeO_2," *Nucl. Instrum. Methods B.,* vol. 266, pp. 2882-2886, 2008.

[192] K. Ohhara, N. Ishikawa, S. Sakai, Y. Matsumoto, O. Michikami and Y. Ohta, "Oxygen defects created in CeO_2 irradiated with 200 MeV Au ions," *Nucl. Instrum. Methods B. ,* vol. 267, pp. 973-975, 2009.

[193] K. Shimizu, S. Kosugi, K. Yasunaga, Y. Kaneta, N. Ishikawa, F. Hori, T. Matsui and A. Iwase,

"Change in magnetic properties induced by swift heavy ion irradiation in CeO_2," *Nucl. Instrum. Methods B. ,* vol. 286, pp. 291-294, 2012.

[194] A. Iwase, H. Ohno, N. Ishikawa, Y. Baba, N. Hirao, T. Sonoda and M. Kinoshita, "Study on the behavior of oxygen atoms in swift heavy ion irradiated CeO_2 by means of synchrotron radiation X-ray photoelectron spectroscopy," *Nucl. Instrum. Methods B.,* vol. 267, pp. 969-972, 2009.

[195] V. Grover, R. Shukla, R. Kumari, P. Mandal, P. Kulriya, K. Srivastava, S. Ghosh, A. Tyagi and D. Avasthi, "Effect of grain size and microstructure on radiation stability of CeO_2: an extensive study," *Phy. Chem. Chem. Phys. ,* vol. 16, p. 27065, 2014.

[196] M. L. J. Guo, J. Wu., Y. Wang and M. Luo, "Effect of grain size and microstructure on radiation stability of CeO_2: an extensive study," *Am. Chem. Soc.,* vol. 27, pp. 3872-3877, 2011.

[197] A. Westermann, C. Geantet, P. Vernoux and S. Loridant, "Defects band enhanced by resonance Raman effect in praseodymium doped CeO_2," *J. Raman Spectrosc. ,* vol. 47 , p. 1276–1279, 2016.

[198] A. Nakajima, A. Yoshihara and M. Ishigame, "Defect-induced Raman spectra in doped CeO_2," *Phys. Rev. B. ,* vol. 50, p. 13297, 1994.

[199] F. Cappia, "High temperature investigation of nanostructured actinide oxides," PhD thesis: Politecnico di Milano, 2013.

[200] P. Kelly and M. Brooks, "Electronic structure and ground-state properties of the actinides dioxides," *J. Chem. Soc. ,* vol. 83 , pp. 1189-1203, 1987.

[201] R. Ackermann and M. Tetenbaum, "High temperature thermodynamic properties of the thorium-oxygen system," in *International colloquium on materials for high-temperature energy*, Toronto, Canada, 1979.

[202] B. Childs, P. Harvey and J. Hallett, "Color centers and point defects in irradiated Thoria," *J. American Ceramic Soc.,* vol. 53, pp. 431-435, 1970.

[203] C. Tracy, J. Pray, M. Lang, C. Park, C. Trautmann and R. Ewing, "Defect Accumulation in ThO_2 irradiated with swift heavy ions," *Nucl. Instruments and Methods B.,* vol. 326, pp. 169-173, 2014.

[204] H. Xiao, Y. Zhang and W. Weber, "Ab initio molecular dynamics simulations of low-energy

recoil events in ThO_2, CeO_2 and ZrO_2," *Phys. Rev. B,* vol. 054109, p. 86, 2012.

[205] R. Rao, R. Bhagat, N. Salke and A. Kumar, "Raman spectroscopic investigation of thorium dioxide-uranium dioxide (ThO_2-UO_2) fuel materials," *Appl. Spectrosc. ,* vol. 68, pp. 44-48, 2014.

Résumé en français

APPORT DE LA SPECTROSCOPIE RAMAN POUR LA CARACTERISATION DES COMBUSTIBLES NUCLEAIRES DEFECTUEUX EN CONDITIONS D'ENTREPOSAGE SOUS EAU

Introduction

La gestion des combustibles nucléaires usés reste l'un des principaux enjeux auxquels fait face l'industrie nucléaire. Cette industrie cherche à proposer, au niveau international, une gestion optimisée et sûre des combustibles usés. Cette gestion dépend du type de cycle du combustible, qui peut être soit ouvert ou fermé. Dans le cycle ouvert, les combustibles irradiés ne sont pas repris afin être réutilisé dans les réacteurs nucléaires. Au contraire, une fois leur radioactivité suffisamment réduite, ils finissent leur vie dans des sites de stockage. Le cycle du combustible ouvert ne fait partie d'une démarche de développement durable car les combustibles usés contiennent encore 98% de matières fissiles réutilisables.

En revanche, le cycle fermé vise à la réutilisation des matières qui ont toujours une valeur énergétique et qui permet aussi de limiter la quantité des déchets nucléaires qui doivent être stockés dans des sites géologiques. Ainsi, les isotopes fertiles (U-238) et fissiles (U-235 et Pu-239) issus du combustible d'oxyde d'uranium (UOX) sont récupérés et réutilisés pour la fabrication de combustibles d'oxydes mixtes, dit MOX (pour Mélange d'OXyde de plutonium et d'uranium). Le cycle du combustible fermé a été adopté au tout début du programme nucléaire en France, motivé par le manque de réserve d'uranium naturel et aussi la volonté de développer une stratégie énergétique indépendante.

L'utilisation du MOX comme combustibles dans les réacteurs s'est étendue après le « Projet : MOX Parity Fuel Management » qui a permis d'avoir le même taux de combustion de déchargement entre le MOX et l'UOX. Ainsi en France, l'industrie nucléaire s'est fortement engagée dans la politique du recyclage dont elle maîtrise toutes les étapes. La politique industrielle d'EdF conduit à entreposer sous eau des assemblages de combustibles MOX irradiés non retraités pendant plusieurs décennies, jusqu'à ce qu'ils soient recyclés dans les réacteurs à neutrons rapides de quatrième génération, qui sont essentiellement des projets à long terme. Cette stratégie nécessite d'évaluer le comportement à long terme des UOX et MOX en conditions de stockage en piscines.

L'entreposage de longue durée des combustibles usés ne pose pas de problème majeur, néanmoins un scénario incidentel correspondant à la présence d'un défaut débouchant

au niveau de la gaine n'est pas à négliger. L'interaction entre la matrice du combustible et l'eau, ainsi que les conditions physico-chimiques des piscines conduisent à la formation d'espèces radiolytiques et notamment de peroxyde d'hydrogène (H_2O_2). Ces produits radiolytiques induisent une altération de la surface du combustible, accélèrent la vitesse de dissolution oxydante et peuvent engendrer la précipitation de phases secondaires à base de U(VI) (précipitation de phases secondaires gonflantes pouvant contraindre le défaut).

La dissolution oxydante de l'UO_2 et des MOX en présence d'irradiation (alpha, beta et gamma) a fait l'objet d'études antérieures. Cependant les mécanismes correspondants restent encore à préciser. Les études précédentes se sont focalisées sur l'oxydation de la matrice, le taux de relâchement de l'uranium et du plutonium en solution et l'effet de l'H_2O_2 sur la dissolution, mais il existe peu de données qui permettent de comprendre le comportement des défauts d'irradiation à l'intérieur du combustible irradié lors d'une interaction chimique avec les produits de la radiolyse de l'eau.

Le but de notre étude est d'évaluer le rôle des dommages d'irradiation pendant la dissolution des combustibles en utilisant la spectroscopie Raman. La spectroscopie Raman a récemment mis en évidence l'existence d'une signature spécifique des dommages d'irradiation dans le dioxyde d'uranium, dénommé le « triplet de défauts (U1, U2 & U3) », comme le montre la figure ci-dessus.

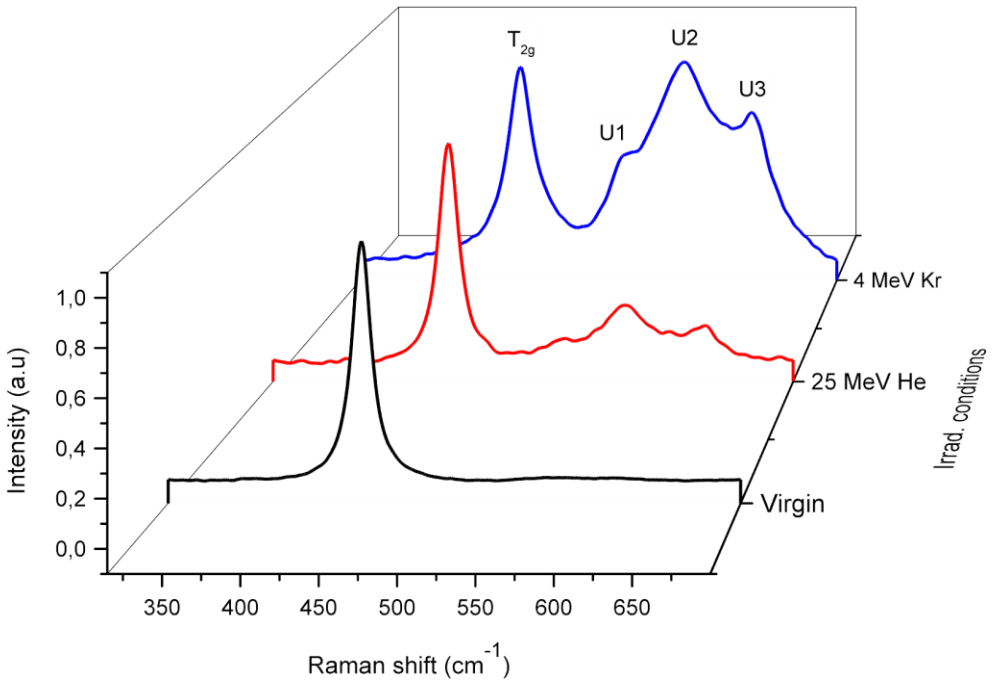

Figure B.1: Evolution du spectre Raman d'un UO_2 en fonction des différentes conditions d'irradiations

Bien que plusieurs études ont été consacrées à caractériser le triplet de défauts, une interprétation unanime de leur origine exacte manque toujours. Le but de cette étude est d'effectuer une analyse en profondeur du triplet de défauts afin d'étudier comment cette signature Raman peuvent être utilisée pour caractériser les combustibles nucléaires entreposés dans des piscines. Dans ce contexte, trois grands domaines d'études ont été identifiés, à savoir:

4. Identifier le type de défauts d'irradiation responsables de l'apparition du triplet de défauts
5. Étudier le comportement du triplet de défauts au cours de la lixiviation de l'UO_2 sous conditions oxydantes
6. Étudier l'effet de dopage chimique et de la microstructure sur le triplet de défauts

OBJECTIF 1: IDENTIFICATION DE DEFAUTS D'IRRADIATION RESPONSABLES DE L'APPARITION DU TRIPLET DE DEFAUTS

Cette partie a pour but de fournir des informations détaillées sur le triplet de défauts. Pour ce faire une expérience d'irradiation avec des électrons a été menée sur des disques frittés d'UO_2. Au cours de l'irradiation, les électrons perdent la plupart de leur énergie par collisions inélastiques mais ils peuvent aussi interagir de façon élastique et déplacer les atomes hors de leur position initiale dans le réseau cristallin d'UO_2.

Plusieurs échantillons UO_2 ont été irradiés dans l'installation SIRIUS (LSI, École Polytechnique), avec des électrons ayant une énergie dans la gamme de 1.6 à 2.5 MeV. Cette gamme d'énergie se justifie par le fait que le pouvoir d'arrêt électronique est constant alors que le pouvoir d'arrêt nucléaire est caractérisé par une forte augmentation en fonction de l'énergie des électrons comme le montre la Figure B.2.

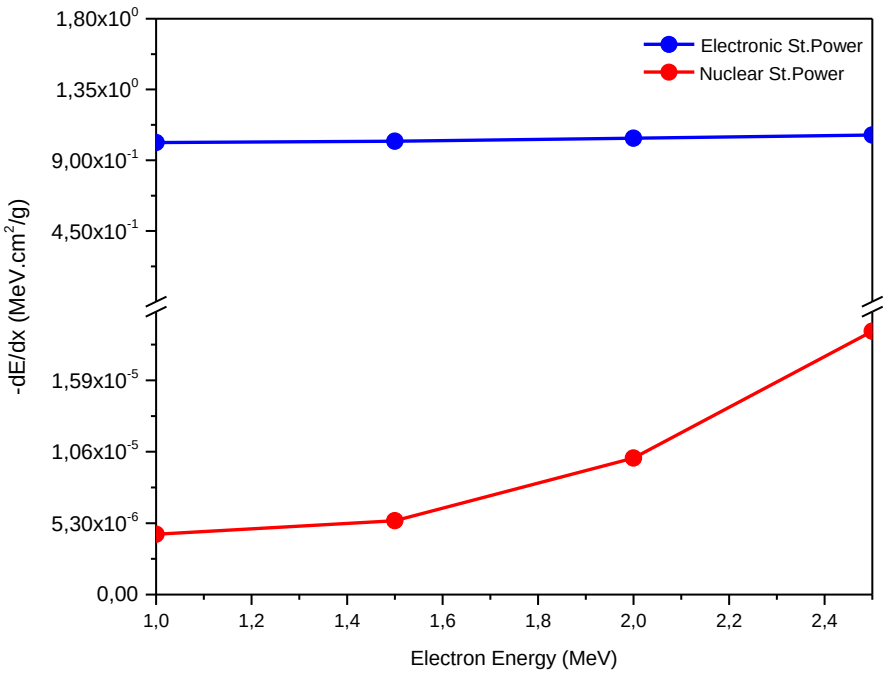

Figure B.2: Comparaison entre les pouvoirs d'arrêts électronique et nulcéaire des électrons dans UO_2 dans la gamme 1.0-2.5 MeV

L'évolution de l'intensité du triplet de défauts a été étudiée en fonction de l'énergie des électrons par deux approches différentes : à savoir la caractérisation Raman de la surface des disques irradiés et la caractérisation Raman de sections de disques irradiés. La Figure B.3 montres que l'énergie des électrons seuil pour l'apparition du triplet de défauts se situe entre 1.8 et 1.9 MeV. L'intensité du triplet de défauts augmente ensuite avec l'énergie des électrons jusqu'à 2.5 MeV. Cette observation est conforme à l'évolution de la puissance d'arrêt nucléaire dans la même gamme d'énergie. Ainsi, les résultats obtenus ont conduit à la conclusion que le triplet de défauts a pour origine des collisions balistiques entre électrons incidents et des atomes de l'UO_2.

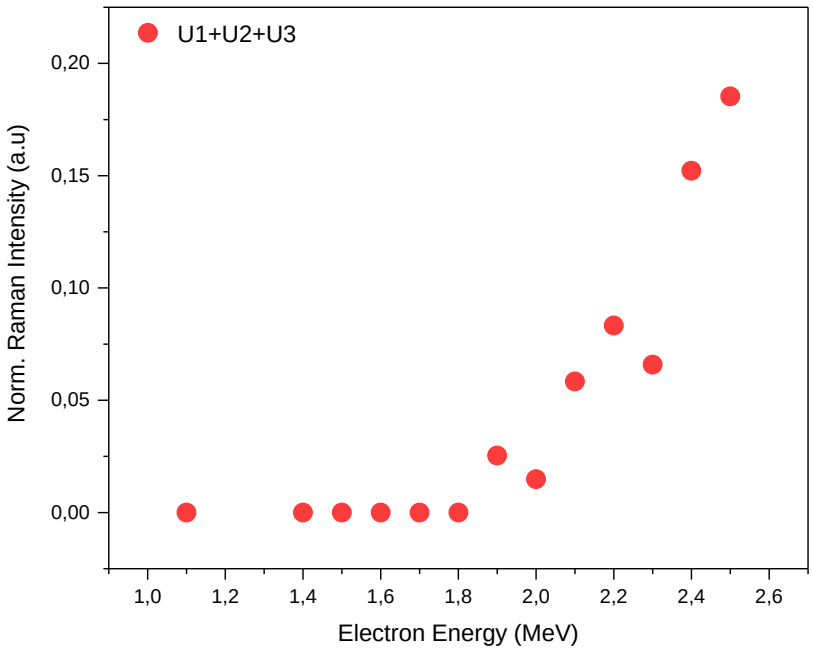

Figure B.3: Evolution de l'intensité du triplet de défauts en fonction de l'energie des électrons incidents

La présence de défauts ponctuels dans le combustible UO_2 irradiés a été confirmée par la spectroscopie d'annihilation des positons et les mesures de diffraction. La nature des défauts ponctuels associés au triplet de défauts a ensuite été déterminée. La concentration des défauts ponctuels sur les sous-réseaux uranium et oxygène a été calculée en utilisant les valeurs des sections efficaces publiées dans la littérature. Il est observé que le seuil d'énergie pour l'apparition du triplet de défauts correspond à l'énergie électronique minimale nécessaire pour induire des déplacements dans le sous-réseau uranium (1.6 MeV), alors que l'énergie minimale nécessaire pour induire des déplacements dans le sous-réseau oxygène est de 0.5 MeV. Le calcul de la concentration en défauts sur le sous-réseau uranium montre la même tendance que l'intensité du triplet de défauts dans la gamme de 1.6 à 2.5 MeV. Ces observations indiquent que le triplet de défauts Raman dû à l'irradiation correspond à des déplacements atomiques dans le sous-réseau uranium.

De plus, le vieillissement de disques UO_2 vierges et irradiés stockés à l'air ambiant a été étudié. Il a été observé que la présence de défauts d'irradiation accélère l'oxydation de l'UO_2. Un mécanisme d'oxydation a été proposé. Il est basé sur des réactions chimiques se produisant près de l'interface UO_2-air en raison de la migration de lacunes d'oxygène de l'UO_2 vers la surface. Il a également été signalé que le mécanisme d'oxydation ne se manifeste pas immédiatement après l'irradiation, mais se produit graduellement tout au long de l'exposition à l'air.

OBJECTIF 2 : ÉTUDE DU COMPORTEMENT DU TRIPLET DE DEFAUTS AU COURS DE LA LIXIVIATION DE L'UO_2 SOUS CONDITIONS OXYDANTES

Dans cette étude, une nouvelle installation a été conçue pour caractériser, par spectrométrie Raman *in situ*, le comportement d'un disque d'UO_2 en contact avec de l'eau aérée (UO_2/H_2O) sous un faisceau d'hélium à 45 MeV. L'objectif principal de cette étude était de mesurer la cinétique de formation de défauts d'irradiation et les données ont ensuite été comparées à une expérience de référence où UO_2 était en contact avec un environnement inerte d'Argon (UO_2/Ar). La spectrométrie Raman *in situ* a aussi permis de mesurer la cinétique de formation de phases secondaires, qui se forment sur la surface de l'UO_2 lors de la lixiviation.

La cinétique de formation des défauts d'irradiation pour les conditions UO_2/H_2O et UO_2/Ar suit une loi cinétique unique qui correspond au modèle d'impact direct. Mais l'ajustement numérique des courbes expérimentales avec cette loi cinétique conduit à des valeurs numériques des coefficients différents. En effet la cinétique de formation du triplet de défauts est plus rapide pour l'interface chimiquement réactive UO_2/H_2O que pour l'interface chimiquement neutre UO_2/Ar (Figure B.4). Cet effet a été attribué à la migration des lacunes d'oxygène vers la surface et un modèle qualitatif a été proposé pour interpréter les résultats expérimentaux. Ainsi, cette expérience a fourni des éléments supplémentaires pour valider le rôle des lacunes d'oxygène à l'interface UO_2-air.

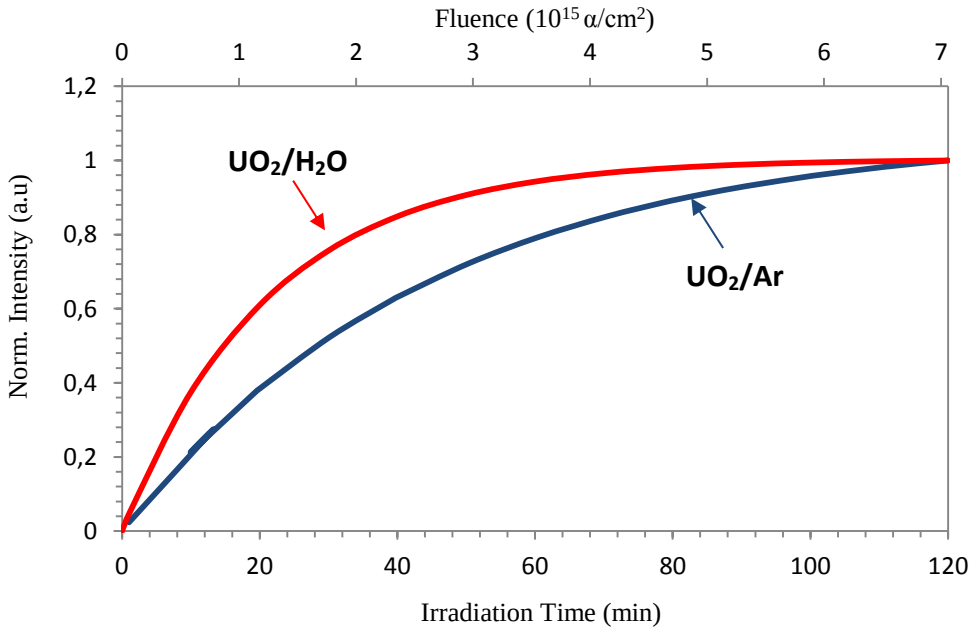

Figure B.4: Comparaison des intensités du triplet de défauts mesurées *in situ* pour les systèmes UO_2/Ar (ligne bleue) et UO_2/H_2O (ligne rouge)

Enfin, la solution irradiée a été analysée pour déterminer les mécanismes de la dissolution oxydante d'UO_2. Il a été observé que la concentration en H_2O_2 de radiolyse et en uranium dissous ont été largement suffisantes pour provoquer la précipitation de phases secondaires sous forme de studtite. En outre, le processus de dissolution se produit sans la formation d'une couche oxydée en raison de l'effet combiné des agents complexant, tels que les ions fluorures, et de l'acidité de l'eau irradiée.

OBJECTIF 3 : L'EFFET DU DOPAGE CHIMIQUE ET DE LA MICROSTRUCTURE SUR LE TRIPLET DE DÉFAUTS

Ce chapitre a été consacrée à étudier le comportement du composé simulant le combustible MOX sous irradiation alpha dans des conditions de laboratoire. L'objectif de cette étude était de déterminer l'effet de la microstructure et du dopage sur l'apparition du triplet de défauts. Dans un premier temps un composé (U, Ce)O_2 hétérogène a été soumis à une irradiation alpha avec une interface sous atmosphère inerte (Ar) et une interface réactive (H_2O). Dans un deuxième temps, plusieurs échantillons (U, Th)O_2 homogènes avec différent teneurs en Th (de 0 à 80% par tranche de 20%) ont été également d'étudiés.

La caractérisation de la surface initiale des échantillons (U, Ce)O_2 a mis en évidence la présence de trois phases distinctes, à savoir : une phase riche en U, une phase riche en Ce et une phase d'enrobage avec une teneur en Ce intermédiaire. Cette microstructure hétérogène vise à simuler la microstructure des combustibles MOX. La première analyse a montré que les trois phases ont conservé leur structure cristallographique fluorite, comme le montre la présence de la raie T_{2g} dans l'ensemble des trois phases. Cependant, l'apparition du mode LO dans la gamme spectrale 500-600 cm^{-1} (normalement éteint dans UO_2 parfait), indique une concentration importante de lacunes d'oxygène dans ces oxydes mixtes.

L'analyse Raman des (U, Ce)O_2 irradiés aux alphas sous eau a montré la présence de la phase studtite sur la surface des disques étudiés. Les deux pics caractéristiques de la couche altérée sont apparu aux mêmes nombres d'onde (ν_1 : 819 cm^{-1}) et (ν_2 : 865 cm^{-1}) que ceux observés antérieurement au cours de la lixiviation de l'UO_2 sous irradiation alpha. Ainsi, cette constatation indique que les pics correspondants à la phase studtite ne sont pas influencés par la présence du cérium.

En ce qui concerne le triplet de défauts, une cartographie Raman de l'échantillon (U, Ce)O_2 lixiviés a mis en évidence la bande de défauts dans la phase riche en U, mais pas dans la phase riche en Ce. L'existence du triplet de défauts a été précédemment observé dans des CeO_2 irradiés aux ions lourds (dpa : 8.59). Ainsi, ceci pourrait suggérer que la spectroscopie Raman n'est pas assez sensible pour détecter la faible concentration de défauts d'irradiation qui sont induits par les ions alpha dans la phase riche en Ce (dpa : 4.65 x 10^{-2}). Il est aussi à noter

que le triplet de défauts n'a pas été observé sur la phase d'enrobage. Les acquisitions Raman après l'irradiation obtenues sur les trois phases distinctes sont rassemblées en Figure B.5.

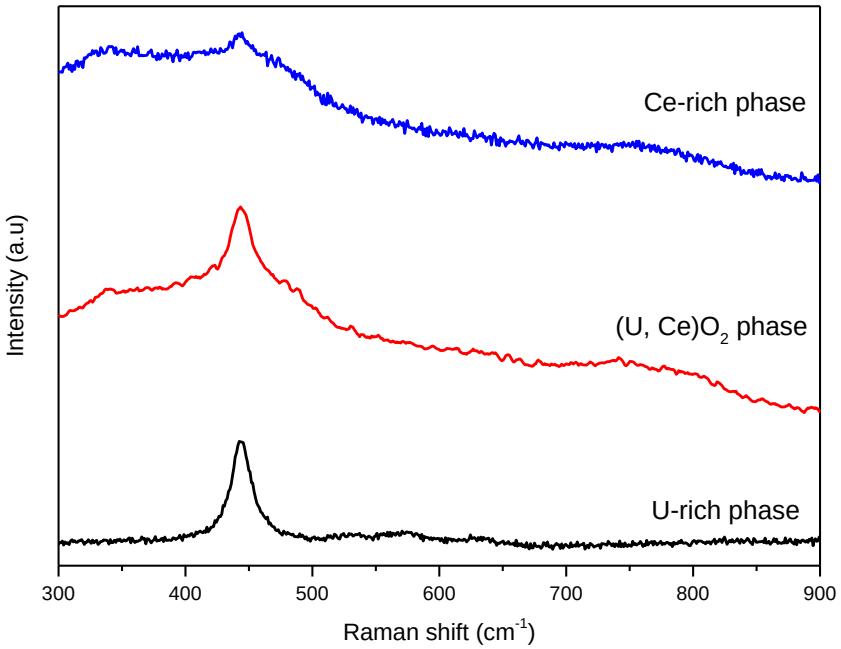

Figure B.5: Spectre Raman des trois phases dans le disque (U, Ce)O_2 irradié sous eau et entreposé 6 mois sous air

En outre, on remarquera que l'exposition en continu de l'air ambiant de l'échantillon (U,Ce)O_2 irradié provoque une diminution significative de l'intensité de la bande en mode LO sur le spectre de la phase riche en U. La disparition du mode LO a été attribuée à une augmentation de la mobilité de l'oxygène ce qui conduit à une diminution de la concentration en lacunes d'oxygène. Cette observation est cohérente avec les mécanismes proposés pour décrire l'oxydation rapide des UO_2 irradiés aux électrons.

Enfin, l'étude a été étendue pour étudier l'effet du dopage du combustible sur le triplet de défauts par l'utilisation de plusieurs oxydes mixtes (U, Th)O_2. Les résultats expérimentaux ont été marqués par l'absence complète du triplet de défauts sur tous les oxydes mixtes irradiés aux alphas. Ces observations indiquent que le dopage chimique des combustibles nucléaires influent sur l'apparition du triplet de défauts dans des combustibles nucléaires irradiées.

Ainsi, ces expériences ont fourni suffisamment d'éléments pour conclure que la spectroscopie Raman peut être utilisée pour étudier les défauts d'irradiation dans des combustibles nucléaires. La présence du triplet de défauts dans la phase riche en U (concentration en dopant : ~0.23-0.3 at.%) suggère que la spectroscopie Raman peut caractériser les dommages d'irradiation dans des combustibles nucléaires ayant une faible concentration en dopants.

Cependant en ce qui concerne les combustibles nucléaires fortement dopés, la spectroscopie Raman apporte des informations pertinentes sur le dopage chimique en utilisant les modifications de la raie T_{2g}.

Conclusion

Comme indiqué tout au long de cette thèse, la spectroscopie Raman est un excellent outil pour l'étude de l'altération de la matrice du combustible nucléaire et les mécanismes de formation des phases secondaires. En outre, une information quantitative sur les changements qui se produisent au niveau atomique dans les combustibles nucléaires peut également être extraite par cette méthode de caractérisation. Par exemple, en ce qui concerne l'hétérogénéité de la microstructure des combustibles MOX, les informations structurelles et chimiques suivantes peuvent être discutées :

- **Pour la phase riche en Pu**

Compte tenu de la forte teneur en Pu, la spectroscopie Raman est moins susceptible de révéler des informations pertinentes concernant le triplet de défauts. Cependant, elle peut être utile pour recueillir des informations importantes, telles que la composition chimique (déduite du décalage en nombre d'onde de la raie T_{2g}) et la stœchiométrie en oxygène (déduite des raies U1 et U3 du triplet de défauts).

- **L'enrobage UO_2-PuO_2**

La faible teneur en Pu-suggère que le triplet bandes Raman défaut pourrait exister dans la phase d'enrobage (U, Pu)O_2. En temps voulu, il sera intéressant de mener des études supplémentaires consacrées à déterminer le seuil en dopage pour l'apparition du triplet de défauts.

- **La phase riche en U**

Comme il a été rapporté dans cette étude, on peut s'attendre à ce que le triplet de défauts soit observable, ce qui peut être attribué à la faible teneur en dopant. Cependant, l'effet de taux de combustion doit aussi être considéré car c'est l'un des principaux facteurs qui déterminent la composition finale des combustibles nucléaires usés.

Enfin, il convient de noter que cette thèse a révélé l'oxydation rapide et inattendue de combustibles nucléaires irradiés lors de l'exposition à l'air. Cette observation doit être prise en compte dans les expériences consacrées à la quantification des défauts causés par l'irradiation et des précautions adéquates doivent être prises pour éviter l'oxydation du combustible. En ce qui concerne les combustibles nucléaire usés défectueux, il est préférable de stocker l'échantillon dans un environnement non réactif entre les différentes campagnes de caractérisation.

Pour conclure, cette thèse a démontré que la spectroscopie Raman est un outil viable qui peut fournir des informations pertinentes concernant les défauts d'irradiation dans les combustibles nucléaires et aussi les résultats expérimentaux obtenus peuvent être utilisés comme base de référence pour la caractérisation d'un combustible nucléaire défectueux en piscine.

Raman spectroscopy for the characterization of defective spent fuels during interim storage in pool

A specific signature characteristic of irradiation damages in uranium dioxide, the most used nuclear fuel, referred as « triplet defect bands» has recently been evidenced by Raman Spectroscopy. The objective of this study is to determine how this signature can be used to characterize actual spent nuclear fuel stored in pools. For that purpose, three separate effect studies were carried out. Firstly, an electron irradiation experiment shows that the triplet defect bands are due to ballistic interactions and result from the formation displacements in the uranium sub-lattice. Post electron irradiation, the enhanced oxidation of UO_2 samples is observed and attributed to the migration of irradiation induced oxygen vacancies towards the surface. The formation kinetics of the triplet defect bands in UO_2 when exposed to a chemically inert (Ar) and a reactive (aerated water) contact medium is then investigated through the use of an *in situ* Raman installation. Both kinetics can be fitted using a direct impact model, but with different numerical values. Finally, to simulate actual spent nuclear fuels in laboratory conditions, the study of different mixed oxide compounds shows that chemical doping impacts the apparition of the Raman triplet defect bands. The experimental results obtained in this work will be used as complementary data for the interpretation of Raman results of actual defective spent nuclear fuels stored in pool conditions.

Keywords : Uranium dioxide, irradiation damages, Raman spectroscopy, uranium sub-lattice

Apport de la spectroscopie Raman pour la caractérisation des combustibles nucléaires défectueux en conditions d'entreposage sous eau.

Une signature spécifique des dommages d'irradiation dans le dioxyde d'uranium, dénommé « triplet de défauts » a été récemment mis en évidence par spectroscopie Raman. Ce travail vise à savoir comment cette signature peut être utilisée afin de caractériser les combustibles nucléaires irradiés qui sont entreposés sous eau. Pour cela, trois études à effets séparés sont menées. Tout d'abord, une expérience d'irradiation aux électrons montre que le triplet de défauts est dû à des interactions balistiques et est associé aux déplacements dans le sous-réseau d'uranium. Après l'irradiation aux électrons, l'échantillon d'UO_2 s'oxyde de manière accélérée, ce qui a été attribué à la migration des lacunes d'oxygène créées par l'irradiation vers la surface. Ensuite, la cinétique de formation du triplet de défauts dans de l'UO_2 exposé à des environnements inerte (Ar) et réactif (eau aérée) a été mesurée grâce à un dispositif Raman *in situ*. Dans tous les cas, la cinétique peut être décrite par un modèle d'impact direct, mais avec des coefficients numériques différents. Enfin, de manière à simuler le combustible irradié industriel en laboratoire, l'étude de différents composés d'oxydes mixtes a montré le rôle du dopage chimique sur la formation du triplet de défauts. Ces informations seront mises à profit dans les études futures de combustibles défectueux entreposés sous eau.

Mots clés : dioxyde d'uranium, dommages d'irradiation, spectroscopie Raman, sous-réseau uranium

Laboratoire des Lois de Comportement du combustible – CEA, DEN, DEC, Centre de Cadarache